Coupling colloidal chemistry with coordination chemistry:

Design of hybrid nanomaterials by the assembly of plasmonic nanoparticles and functional coordination complexes

Universitat de València

Paterna, March 2021

Roger Sanchis Gual

Ph.D. Thesis in Nanoscience and Nanotechnology

Supervised by:

Prof. Dr. Eugenio Coronado Miralles and Dr. Marc Coronado Puchau

Coupling colloidal chemistry with coordination chemistry:

Design of hybrid nanomaterials by the assembly of plasmonic nanoparticles and functional coordination complexes

Instituto de Ciencia Molecular (ICMol)
Universitat de València

****

Memoria presentada por Roger Sanchis Gual para aspirar al grado de Doctor en Nanociencia y Nanotecnología

****

Dirigida por:
Prof. Eugenio Coronado Miralles
Dr. Marc Coronado Puchau

Marzo 2021

D. EUGENIO CORONADO MIRALLES, catedrático del Departamento de Química Inorgánica de la Universitat de València y D. MARC CORONADO PUCHAU, doctor por la Universidad de Vigo y actualmente investigador del Instituto de Ciencia Molecular, de la Universitat de València.

CERTIFICAN:

Que la memoria presentada por D. Roger Sanchis Gual con el título “Coupling colloidal chemistry with coordination chemistry: Design of hybrid nanomaterials by the assembly of plasmonic nanoparticles and functional coordination complexes” corresponde a su Tesis Doctoral y ha sido realizada bajo su dirección en el Instituto de Ciencia Molecular, autorizando mediante este escrito la presentación de la misma para optar al grado de Doctor.

En Paterna, a 4 de Marzo de 2021

Dr. Eugenio Coronado Miralles Dr. Marc Coronado Puchau

"The science of today is the technology of tomorrow."

Edward Teller

Agradecimientos

En primer lugar, quiero aprovechar para agradecer a Eugenio por darme la oportunidad de realizar la tesis doctoral en su grupo de investigación. Y es que no todos tienen la suerte de poder trabajar en un grupo tan talentoso y con tan gran científico. Hay que saber valorar el tremendo trabajo que supone tener un excelente grupo con tantas líneas de investigación y tantos equipos disponibles y, pese a ello, tener las puertas de su despacho siempre abiertas (literalmente). Además, pienso que salir de mi zona de confort para trabajar en nanopartículas ha resultado ser enormemente positivo. Siento que me voy formado y con ganas de enfrentarme al próximo reto. Del mismo modo, quiero agradecer a Marc por su apoyo, consejos y orientación, fundamentales para la conclusión de este trabajo.

Por supuesto, quiero dar mi agradecimiento a Gonzalo. Valoro mucho tu apoyo en los momentos más difíciles y darme la oportunidad de poder retomar la electroquímica. Ha sido un verdadero placer poder colaborar contigo.

Quiero mencionar la valiosa ayuda de Mónica. No sabes cuánto aprecio tu incalculable dosis de ilusión, motivación y ánimo que brindas cada día. También el gran apoyo de Elena Pinilla durante mi doctorado. Lo cierto es que las medidas de Raman que hicimos en el NTC con tanto sufrimiento en plena oscuridad fueron inolvidables. Igualmente, dar las gracias a Alicia. Recuerdo cuando me explicaste como interpretar las medidas magnéticas. Las notas que tomé las utilizo siempre que he de enfrentarme a ellas. Agradecer también a Josep por su apoyo con todo lo relacionado con la plasmónica, a Toribio por las excelentes charlas electroquímicas que me ha brindado, a Guillermo por su ayuda en rayos x, a Alejandra por sus innumerables medidas en el HTS, a Jose Usagre por los innumerables pedidos, a Paco y a Ruth por la innumerable lista de papeleo. Por supuesto, hablando de innumerables cosas no puede faltar Ángel. También, a Cristian por su gran dedicación. A Said y sus “qué maravilla” cuando veía las nanopartículas de oro en el HR-TEM. Asimismo, al resto de técnicos y administrativos por las innumerables veces que me han ayudado.

Durante este periodo he podido trabajar en el UIMM, un grupo que me ha hecho sentirme como en casa. Primero, darle las gracias a Jorge por su recibimiento. Los primeros meses fueron más sencillos por tu integración, apoyo y divertidos momentos. Jamás olvidaré las bromas (¡ni tus ronquidos!). A Néstor (al viejo y al nuevo) por su certera donación a mi tesis. Se te echa de menos y no sabes cuánto. Creo que la botella pegada a tu mesa es mi historia favorita del ICMol. A Javi Castells por ser personalmente y científicamente extraordinario. ¡Tenemos pendiente ir alguna vez más a nadar! A Víctor García (¡oh Vic!) por su relación con un tal Ramon(cín). Ahora en serio, Vic eres una persona genial. A Iván y a Isaac (Ivaac e Isan) por ser unos grandes compañeros de pecera con un gran sentido del humor. Por si fuera poco, Isaac, siempre has sido un buen compañero al que vender a buen precio. A Yan Duan por ser mi hermana china mayor (¡Nǐ hǎo!). ¡Cómo te echo de menos, cheee! A Eugenia por su profundo amor gatuno y su enorme perseverancia. Estoy seguro de que tu constancia acabará dando sus frutos. A Miguel Gavara por ser un gran compañero docente con un gran sentido del humor. Tus historias en Aliaga aún atormentan mi pobre mente.

Quiero también nombrar a mucha gente del UIMM que ha contribuido a este buen clima: Alejandro Núñez, Alejandro Lumbreras, Alex Gaita, Álvaro, Azeem, Camilo, Carla, Chandan, Christian, Dani, Eduardo (de la Cierva), Edurne, Eleni, Estrella, Garin, Helena Prima, Javi López, Jose Jaime, Lorena, Luis, Manel, Marc Morant, María, Mario, Marta (y tu inolvidable risa), Mhamed, Michelle, Miguel Clemente, Modesto, Paco, Pascual, Rosa, Safaa, Salva, Samuel, Silvia, Thibaut, Vero, Víctor Oestreicher y muchos más que me dejo. Con todos vosotros es mucho más fácil trabajar y ser feliz, gracias.

Al grupo de García-España (Alberto, Alexis y Elena) por los buenos momentos y las charlas tan graciosas que pasamos en las comidas. Estoy muy agradecido por vuestro recibimiento y me alegro mucho de haberos conocido. También al grupo de Henk (en particular a Dani, Laura y Jorge) por las numerosas, divertidas e interesantes conversaciones que hemos tenido durante estos años. En especial quiero nombrar a Isidora, una persona estupenda y alegre con la que me siento muy orgulloso de haber trabajado. De igual manera, al grupo de Carlos Martí (Victor Rubio, Belén, María, etc) por los mil y un momentos divertidos.

A Josena. No sabes cuánto echaré de menos tu risa malvada y ver como se te iluminan tus ojos cuando ves agitarse un yogur. Fue muy divertido compartir pecera contigo y ser testigo de tu humor (¿humor?) infinito. Pase lo que pase, siempre te seguiré…en Scopus.

A Katia. Oh K. Te mereces un monumento por todas tus labores en el laboratorio. Cuando dejaste nuestra vitrina fue horrible, una muestra más de lo vital que eres. Y es que en el RKR eres la que sostiene las erres. ¿Quién se reirá ahora de mis bromas? Jo… Te echaré mucho de menos.

A Jose. Ha sido un verdadero placer conocerte en algún lugar del 2.7 y trabajar contigo. Durante estos años hemos hablado de todo lo posible y, a pesar de ello, aún nos queda mucho de lo que hablar (¡y que hablaremos!). El *paper de la amistad* me mostró que eres un buen amigo, pero el *stibium* me demostró que eres un gran amigo. Por eso solo me queda decirte que hasta pronto braven-maníaco… 3 info.

A Ramón. Parece que el doblete ha de transformarse en dos singletes… Ojalá podamos volver a trabajar una vez más juntos en el futuro. Quién sabe… la vida da muchas vueltas, tantas que a veces algunos hasta se vuelven **rubios**. Fuera bromas, estos años en el ICMol han sido de los mejores en parte gracias a ti. En mi retina quedan grabados momentos tan épicos como el salto mortal, la canción de mi gran noche, tu nasofilia y tu amor incondicional a los franceses. Eres un científico y una persona increíble. Que dios te lo pague con príncipes. Ciao amigo.

A los integrantes del Laboratorio de Electroquímica del departamento de Química Física (Alex, David, Jero, Juan y Paco) con los que realicé el máster e inicié mi etapa investigadora. Aprendí muchísimo y viví momentos geniales con vosotros (mención especial al congreso de Vigo).

Dar las gracias a mis amigos del Liceo, en especial a César y a Mika con los que me alegro de no haber perdido nunca el contacto. Además, comer en nuestro sagrado templo (el Manolo) es siempre una excelente excusa para reunirnos. También a amigos que conocí durante la carrera como es el Rub, una persona magnifica y con una estupenda forma de ser. De la misma forma, a Héctor y Marino a quienes quiero también agradecer su preciada amistad. Son tantas aventuras y anécdotas vividas con vosotros que no sabéis cuanto valoro.

Agradecer a Elia y Waldo, por vuestro afecto. Que ganas tengo de que volvamos a comer en el Famós. A mis tíos Fina y Chimo y a mi prima Anna que siempre me han otorgado un gran cariño. A mis primos Carlos y Pablo por los grandes momentos en nuestra infancia. A mis hermanos, Migue y Nico, que son personas inteligentes, trabajadoras, cultas y por encima de todo, cariñosas. Guardo grandes recuerdos de cuando nos juntábamos con los “Carlitos”. Por supuesto, agradecer a mis padres que han sido la base de mi educación y, sobretodo, un espejo en el que mirarse. No sabéis cuanto os admiro.

Por último, agradecer a la persona más maravillosa. Soy muy afortunado de haberte conocido durante la carrera de Química. ¡Si es que entre nosotros siempre ha habido mucha química! Tu ánimo y tu alegría siempre han sido esenciales para mí. Me has dado fuerzas e ilusión para comenzar, continuar y terminar este trabajo. Sin ti, Miri, esta tesis carece de sentido.

Table of Contents

Abbreviations

AFM	Atomic Force Microscopy
APTES	(3-aminopropyl)triethoxysilane
ATR-FTIR	Attenuated Total Reflectance Fourier-Transform Infrared
CP	Coordination Polymer
CPE	Constant Phase Element
CTAB	Cetyltrimethylammonium Bromide
CTAC	Cetyltrimethylammonium Chloride
CV	Cyclic Voltammetry
DLS	Dynamic Light Scattering
DSC	Differential Scanning Calorimetry
ECSA	Electrochemical Surface Area
EDX	Energy Dispersive X-ray Analysis
EIS	Electrochemical Impedance Spectroscopy
FWHM	Full Width at Half Maximum
HR-TEM	High Resolution Transmission Electron Microscopy
HS	High Spin
Htrz	Triazole
ICP-MS	Inductively Coupled-Plasma Mass Spectrometry
j	Current Density
LS	Low Spin
LSPR	Localized Surface Plasmon Resonance
LSV	Linear Sweep Voltammetry

MO	Magneto-Optics
MOF	Metal-Organic Framework
NIR	Near-Infrared
NP	Nanoparticle
NR	Nanorod
NS	Nanostar
η	Overpotential
OER	Oxygen Evolution Reaction
PB	Prussian Blue
PBA	Prussian Blue Analogue
PEG	Poly(ethylene glycol)
PPMS	Physical Properties Measurements System
PVP	Polyvinylpyrrolidone
PXRD	Powder X-ray Diffraction
R	Resistance
RHE	Reversible Hydrogen Electrode
rpm	Revolutions Per Minute
SCO	Spin-Crossover
SEM	Scanning Electron Microscopy
SERS	Surface Enhanced Raman Spectroscopy
TEM	Transmission Electron Microscopy
UV-Vis	Ultraviolet-Visible
XPS	X-ray Photoelectron Spectroscopy
Z	Impedance

Goals and structure of the thesis

Nanotechnology involves the design, characterization, production and application of structures, devices and systems by the control of the shape and size at the nanometer scale involving different fields. In the last decade, nanotechnology development has boosted the interest in hybrid nanomaterials. These materials are a complimenting combination of two (or more) nanoparticles (NPs) with enhanced performance characteristics that offer exciting opportunities. It allows the possibility of integrating materials with different physical and chemical properties to widen the range of practical applications.

In this context, Au NPs have recently attracted a lot of attention due to the great opportunities that Au offers at the nanoscale. In fact, their facile synthesis and functionalization can be exploited for constructing hybrid nanoparticles showing multi-functionality. In this manner, different Au hybrid nanostructures have been developed exhibiting diverse sizes, shapes and compositions displaying novel physicochemical properties, opening the door to potential new applications.

On the other hand, Coordination Polymers (CPs) possess besides interesting electronic properties, potential advantages over conventional inorganic nanomaterials such as structural and chemical versatility, high specific area and biodegradability, among others. Therefore, the integration of both Au and CPs in a single heterostructure has emerged as an appealing topic. However, suitable chemical design appears as one of the key factors to improve their applicability.

The work described in this thesis is motivated by the purpose of designing and studying novel hybrid nanostructures formed by combining Au NPs with different CPs: i) Prussian Blue and its Analogues (PB and PBA), ii) Spin-Crossover compounds (SCO) and iii) Metal-Organic Frameworks (MOF). Taking into account the numerous possible heterostructures, it will be discussed why these tailored hybrid NPs are the most appropriate for magneto-optical, electrochemical and electrical applications.

In chapter 1, it is described the optical properties and the synthesis of Au NPs as well as the main research efforts that have been made to combine CPs incorporating Au functionalities within the overall hybrid nanomaterials.

The main results of this thesis are divided into three parts depending on the potential applications: magneto-optics, electrochemistry and electrical conductivity.

Chapter 2 deals with the preparation of hybrid systems formed by metallic NPs decorated by electrostatic attraction onto PBA NPs of different sizes and nature. In this approach, the capping agent of the plasmonic NP is modified, thus, allowing to select the plasmonic NP (isotropic or anisotropic) and, therefore, to tune the plasmon band position in a broad range of the visible spectrum. The heterostructure keeps its plasmonic and magnetic properties becoming a suitable hybrid material for magneto-optical applications.

In chapter 3, different heterostructures composed of Au and PBA (of NiFe and CoFe) are synthesized and evaluated as electrocatalysts for the oxygen evolution reaction. The core@shell heterostructures are found to be the most appropriate to exploit the Au properties (conductivity and electronegativity). In this way, through a suitable chemical design it can be greatly enhanced the electrochemical activity and stability of the electroactive PBA.

In chapter 4, a straightforward protocol is carried out to overgrow a thin SCO over different plasmonic NPs. Moreover, this synthetic route was extended to MOF. It is observed that thanks to the metallic core and the naked surface of the ultrathin SCO/MOF shell, these core@shell NPs are more conductive than the pristine SCO NPs when contacted to electrodes. In future work, further development will be done by taking advantage of the plasmon properties of the plasmonic core to get a light-induced spin transition (SCO) and to promote the adsorption/desorption of guest molecules (MOF) to obtain advanced sensing devices.

This Ph.D. thesis is expected to represent a significant advancement in the development of novel heterostructures as a result of the incorporation of Au NPs to CPs.

The work described here has given rise to the following publications:

"Design of Bistable Gold@Spin-Crossover Core–Shell Nanoparticles Showing Large Electrical Responses for the Spin Switching" R. Torres-Cavanillas, R. Sanchis-Gual, J. Dugay, M. Coronado-Puchau, M. Giménez-Marqués, E. Coronado. *Adv. Mater.* **2019**, 31(27), 1900039.

"The design of magneto-plasmonic nanostructures formed by magnetic Prussian Blue-type nanocrystals decorated with Au nanoparticles" R. Sanchis-Gual, I. Susic, R. Torres-Cavanillas, D. Arenas-Esteban, S. Bals, T. Mallah, M. Coronado-Puchau, E. Coronado. *Chem. Commun.* **2021,** 57, 1903 - 1906.

"Improving the OER electrocatalitic activity and stability of Prussian Blue Analogues through the introduction of Au nanoparticles in a core@shell heterostructure" R. Sanchis-Gual, T. F. Otero, M. Coronado-Puchau, E. Coronado. *Submitted.*

"*Plasmon-assisted spin transition in gold nanostar@Spin Crossover heterostructures*" R. Sanchis-Gual, R. Torres-Cavanillas, M. Coronado-Puchau, M. Giménez-Marqués, E. Coronado. *Manuscript in preparation.*

Other publications to which the author has contributed during his PhD work are the following:

"Prussian Blue@MoS_2 Layer Composites as Highly Efficient Cathodes for Sodium- and Potassium-Ion Batteries" M. Morant-Giner, R. Sanchis-Gual, J. Romero, A. Alberola, L. García-Cruz, S. Agouram, M. Galbiati, N. M. Padial, J. C. Waerenborgh, C. Martí-Gastaldo, S. Tatay, A. Forment-Aliaga, E. Coronado. *Adv. Funct. Mater.* **2018**, 28, 1706125.

"Liquid phase exfoliation of carbonate-intercalated layered double hydroxides" J.A. Carrasco, A. Harvey, D. Hanlon, V. Lloret, D. McAteer, R. Sanchis-Gual, A. Hirsch, F. Hauke, G. Abellán, J. N. Coleman, E. Coronado. *Chem. Commun.* **2019,** 55(23), 3315-3318.

"Influence of the Interlayer Space on the Water Oxidation Performance in a Family of Surfactant-Intercalated NiFe-Layered Double Hydroxides" J.A. *Carrasco,* R. Sanchis-Gual, A. Seijas-Da Silva, G. Abellan, E. Coronado. *Chem. Mater.* **2019**, 31(17), 6798-6807.

"Liquid phase exfoliation of antimonene: systematic optimization, characterization and electrocatalytic properties" C. Gibaja, M. Assebban, I. Torres, M. Fickert, R. Sanchis-Gual, I. Brotons, W. S. Paz, J.J. Palacios, E. G. Michel, G. Abellán, F. Zamora. *J. Mater. Chem. A.* **2019**, 7(39), 22475-22486.

"Boosting the supercapacitive behavior of CoAl-layered double hydroxides via tuning the metal composition and interlayer space" A. Seijas-Da Silva, R. Sanchis-Gual, J.A. Carrasco, V. Oestreicher, G. Abellán, E. Coronado. Batter. Supercaps. **2020**, 3, 499-509.

"Reinforced room temperature spin filtering in chiral paramagnetic metallopeptides" R. Torres-Cavanillas, G. Escorcia-Ariza, I. Brotons-Alcazar, R. Sanchis-Gual, P. Chandra Mondal, L.E. Rosaleny, S.M. Giménez-Santamarina, M. Sessolo, M. Galbiati, S. Tatay, A. Gaita-Ariño, A. Forment-Aliaga, S. Cardona-Serra. *J. Am. Chem. Soc.* **2020**, 142, 17572−17580.

"Continuous-flow synthesis of high-quality few-layer antimonene hexagons" I. Torres, M. Alcaraz, R. Sanchis-Gual, J.A. Carrasco, M. Fickert, M. Assebban, C. Gibaja, C. Dolle, D. A. Aldave, C. Gómez-Navarro, E. García Michel, M. Varela, J. Gómez-Herrero, G. Abellán, F. Zamora. *Adv. Funct. Mater.* **2021**, 2101616.

"Improving the onset potential and Tafel slope determination of earth-abundant water oxidation electrocatalysts" R. Sanchis-Gual, A. Seijas-Da Silva, M. Coronado-Puchau, T. F. Otero, G. Abellán, E. Coronado. *Electrochim. Acta*. **2021**, 388, 138613.

Chapter 1

General introduction

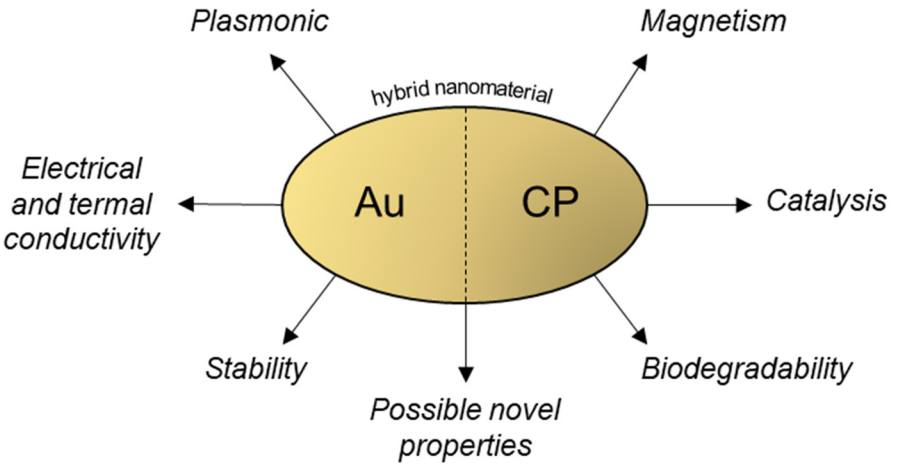

1.1 Gold nanoparticles

Nanoparticles (NPs) are a wide class of materials that in general include particles with dimensions of less than 100 nm. Among all the different types of NPs, noble metal NPs, especially gold (Au) and silver (Ag), have received much attention worldwide throughout human history. Colloidal Au and Ag NPs have been known since ancient times and they were commonly used for producing highly colored glasses. For instance, red or mauve glasses were highly valued by the Romans. Also, the alchemists believed in the existence of a potion called the “elixir of life” consisting of a soluble form of Au which, if ingested, would lead to eternal life.[1] In 1857, Michael Faraday discovered for the first time the Au nanoparticles (Au NPs) based on the observation of a ‘‘beautiful ruby fluid’’ due to the formation of a deep-red-colored colloidal Au by the reduction of an aqueous solution of gold chloride ($AuCl_4^-$).[2] This synthesis is considered to be an important milestone in the development of nanotechnology. Interestingly, about forty years later, motivated by Faraday’s discovery, Richard Zsigmondy introduced the procedure called the “seed-mediated method” which is still used nowadays in the synthesis of several NPs.[3]

Faraday was the first to realize that the color was caused by the small size of the Au particles. He supposed that the metallic particles in the colloids should be very small because they could not be observed with the best available microscopes. He also noted that their colors ranged from ruby, green, violet and blue depending on the metallic particle. Approximately a century later, the shorter wavelengths generated in electron microscopes evidenced that Faraday’s Au colloids had diameters from 3 to 30 nm.[1] At the beginning of the 20th century, Gustav Mie, using Maxwell's electromagnetic theory, was the first to provide a general theory for scattering and absorption of light by spherical metallic particles.[4] In 1912, Richard Gans generalized Mie’s result to ellipsoidal particles of any aspect ratio in the small particle approximation.[5] In addition to this, the improvements of electron microscopy to study the morphology of metal colloids have led to an important renaissance in the study of metal colloids and these studies have led to the investigation and exploitation of their properties.

1.1.1 Physical properties of metallic nanoparticles

Physical properties at the nanoscale are notably different from those observed in bulk (macroscopic). Along this front, reducing the size of metallic particles and entering into the nanometric scale produce drastic changes in the optical behavior, hardly achievable in other optical materials. This exceptional characteristic is due to the surface plasmon resonance. The Lycurgus cup from the 4th century AC is probably the most famous example of the use of surface plasmon in ancient times, exhibiting different coloration when observed upon illumination inside or outside of the cup.[6] This development was empirically achieved without knowing the origin of these surprising optical effects.

A plasmon is a quantum oscillation of the free electron cloud with respect to the fixed positive ions in a metal. It plays an important role in the optical properties of metals and semiconductors. Plasmons that are confined on surfaces and strongly interacting with light are called surface plasmons. Localized surface plasmon resonance (LSPR) is a phenomenon that takes place in Au NPs. In general, when the electromagnetic radiation of an appropriate wavelength interacts with a metallic nanostructure, the electrons near a metal-dielectric interface will be excited (Figure 1.1). They will undergo a collective oscillation relative to the fixed positive nuclei, with the frequency of the incoming light. A momentary electric field is generated on the surface of the NP as a result of the oscillations. This effect can be extended into the dielectric over nanometer lengths and giving an enhancement of the incident field of several orders of magnitude. This phenomenon happens with a size of the metallic NP smaller than the wavelength of light used to excite the plasmon and it is influenced by various factors such as the size, the shape or the surrounding media of the NPs.[7–9]

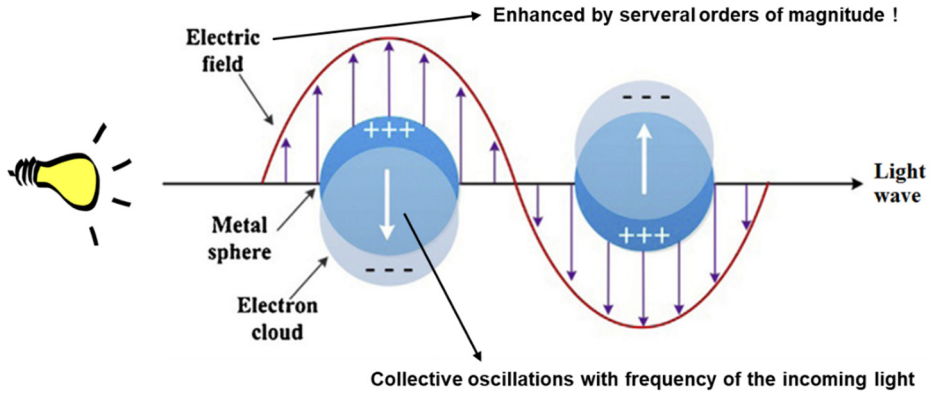

Figure 1.1 Schematic illustration of a plasmon oscillation in a metallic sphere, showing the oscillations of the conduction electron cloud relative to the positive nuclei.

According to Mie's theory, spherical particles with a radius much smaller than the wavelength of light exhibit different absorption peaks depending on the NP size (*i.e.* the particle diameter). Indeed, the size effect also influences both the width and intensity of the resonance band. The increase in the particle size for nanospheres induces undesirable line broadening of the plasmon resonance peak. Moreover, the size dispersion affects the absorption band as well, in such a way that for obtaining the narrow band, smaller size dispersion is desirable.[10]

Furthermore, particle shape and geometry play an important role in the LSPR (Figure 1.2). A typical example is the metallic nanorods (NRs). Unlike nanospheres (which have only one well-defined plasmon resonance peak), NRs display two plasmon bands in the visible/near-infrared (NIR) regions due to longitudinal surface plasmon oscillations along the rod axis and transverse surface plasmon oscillations perpendicular to the long axis. For other anisotropic NPs such as nanostars (NSs), the UV-Vis can be seen as the result of a LSPR hybridization of the core and the tips. In general, deviation from sphericity shifts the resonance towards larger wavelengths.[7,11,12]

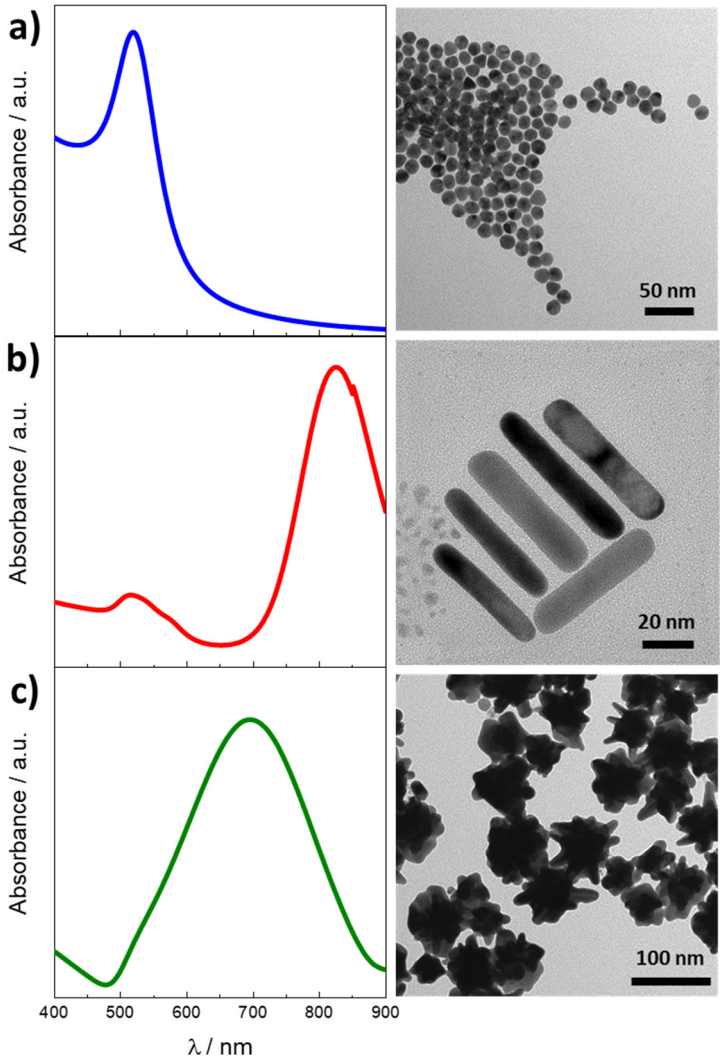

Figure 1.2 a) Absorption spectra and their corresponding TEM images of a) spherical Au NPs, b) AuNRs and c) AuNSs.

Another noteworthy factor is the dielectric constant of the surrounding media around the NP surface, moving the resonant band towards larger wavelengths as its value increases. Therefore, the solvent, the capping agents that are stabilizing the NPs and the presence of a shell may have a considerable impact on the surface plasmon resonance phenomenon.[11,13]

1.1.2 Synthesis of Au nanoparticles

Among noble metals, Au is by excellence the element that has motivated more interest throughout history because of its importance in many areas of human existence. At the nanoscale, its appreciated features, such as the optical properties, the amenable surface functionalization, the high stability, and the electrical and thermal conductivity, open the possibility to develop successful applications in materials science or biomedicine, to mention a few.[1,14–16]

The design of generic methods that allow the preparation of Au nanostructures with a broad range of narrow size and well-defined morphologies is needed to fully exploit their unique properties. In general terms, chemical methods for the synthesis of nanomaterials are made starting from atoms generated from ions, in solution, and are assembled to make NPs. As the synthesis initiates from atoms, these methods are also called bottom-up approaches. This is the case of Au NPs. A typical Au NP obtained by chemical synthesis in liquid phase comprises three parts, namely inner Au atoms (central atoms), atoms exposed to the surface (surface atoms) and surface-protecting organic ligands or surfactants. The central Au atoms determine the crystallinity of the structure, whereas the geometry of the surface atoms form surface facets and edges that will dominate its reactivity, including the catalytic activity. The surfactant is anchored on the surface atoms, stabilizing them and providing surface functionality. Today, most of the colloidal synthetic methods for preparing Au NPs follow a similar strategy: an Au salt is reduced in aqueous solution by surface capping ligands which prevent aggregation of the particles by electrostatic and/or steric repulsion.[14]

The first achievement in the field of Au NPs was the preparation of spherical Au and later on, various anisotropic shapes were obtained such as nanorods, nanoshells, and nanocages. In the past decades, numerous solution-based approaches have been developed to control the size, shape, and surface functionality of Au NPs.[16–21] In 1951, Turkevich and coworkers established a synthetic method for creating Au NPs by treating hydrogen tetrachloroaurate ($HAuCl_4$) with citric acid in boiling water, where the citrate acted as both reducing and stabilizing agent.[22] Later on, in 1973, Frens extended this protocol by changing

the Au:citrate ratio to control the NP size.[23] This protocol has been widely employed in order to prepare diluted solutions of moderately stable spherical Au NPs with diameters ranging from 10 to 20 nm, where larger NPs up to 100 nm can also be synthesized.[15]

Interest in the shape-controlled synthesis of Au nanostructures started in the early 1990s when Masuda *et al.* and Martin prepared AuNRs by electrochemical reduction. These methods produced relatively monodisperse structures, but due to the low yield and large diameter (under 100 nm), the optical response from these NRs was, at that moment, difficult to discern.[14,24,25] A decade after, a colloidal growth route based on a seeded growth method was found to produce high yield monodisperse AuNRs. Seed-mediated growth involves two consecutive steps:

- Firstly, single-crystal seed particles of around 2 nm are produced by the reduction of $HAuCl_4$ with sodium borohydride in the presence of cetyltrimethylammonium bromide (CTAB) that acts as a surfactant.

- Secondly, a controlled amount of seeds is added into an Au(I) growth solution previously prepared by the mild reduction of $HAuCl_4$ with ascorbate in the presence of $AgNO_3$ and CTAB. By controlling these growth conditions in aqueous surfactant media, it was possible to synthesize AuNRs with a tunable aspect ratio (length/width) and thus, with tunable optical properties.[14,26,27]

Indeed, the seed-mediated growth has become the most widely used strategy for the synthesis of anisotropic NPs of different shapes and sizes.[28] For instance, in 2008, Huang and coworkers reported the synthesis of AuNSs by the seed-mediated growth.[29] These nanostructures have plasmon bands that are tunable into the NIR region, and the NP contains multiple sharp branches that act as “hot spots” and greatly enhance the local electromagnetic field.[18,29] Thus, anisotropic NPs are powerful building blocks for the design of new materials exhibiting unusual properties that may afford novel applications.

1.2 Hybrid nanomaterials containing Au nanoparticles

Hybrid materials can be described as an intentional complimenting combination of two or more materials, with the aim of obtaining a combination of properties or new emergent properties. In this line, hybrid nanomaterials, formed by two or more components connected at the nanometer scale, combine the intrinsic characteristics of their individual constituents to afford from a simple co-existence of the properties of their components to the emergence of novel properties due to synergistic effects between them.[30,31] As a result, the properties of hybrid nanomaterials can be tuned by changing their composition and morphology, leading to materials with enhanced performance characteristics, such as high thermal stability, mechanical strength, light emission, electrical conductivity, and new optical properties.[30] Owing to their wide spectrum of accessible properties, hybrid materials are ideal platforms for applications in extremely diverse fields.

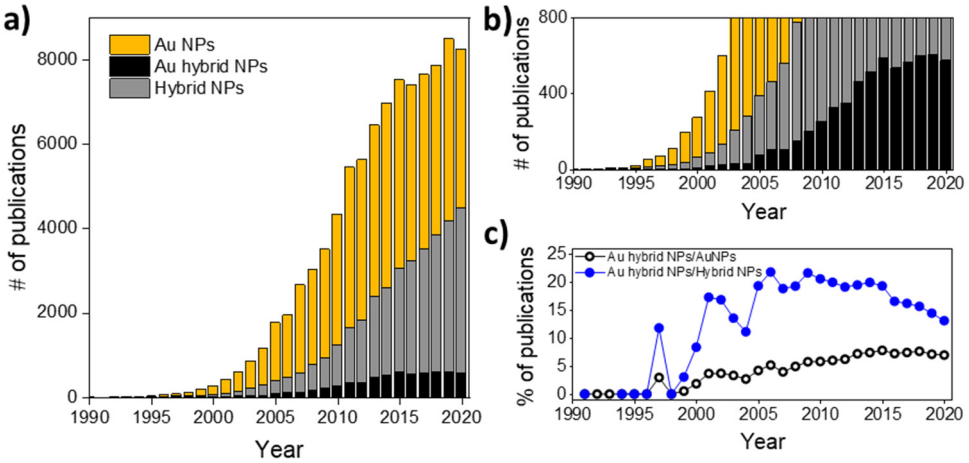

Figure 1.3 a) Number of publications containing the terms “gold nanoparticles”, “hybrid gold nanoparticles” and “hybrid nanoparticles” since 1990. b) Zoom of Figure 3a. c) Percentage of publications of Au-hybrid NPs/Au NPs and Au-hybrid NPs/Hybrid NPs since 1990. Source: Scopus, as assessed in January 2021.

Hybrid NPs have received increasing attention from the scientific community (Figure 1.3a). Thus, this area of research is a burgeoning field with a significant number of publications per year (up to 4000). In the same way, Au NPs have gathered intense interest in the last decade due to the great opportunities that Au offers at the nanometric scale. In this context, the development of hybrid materials containing Au NPs is also attracting widespread attention (Figure 1.3b). Interestingly, in recent years, around 8 % of academic publications involving Au NPs are dedicated to the development of Au hybrid nanostructures and near 20 % of hybrid NPs studies are associated with Au NPs (Figure 1.3c). This noteworthy percentage indicates that Au NPs result of high interest in the preparation of complex multi-component NPs.

1.2.1 Au heterostructures at the nanoscale

Au NPs are one of the most versatile nanomaterials reported to date. Their facile synthesis and functionalization make them an appealing nano-scaffold for constructing hybrid NPs displaying multifunctionality. This has undergone the development of different Au hybrid nanostructures exhibiting diverse sizes, shapes and compositions with novel physicochemical properties paving the way to potential new applications. The incorporation of other functional materials onto Au NPs can lead to the introduction of new properties/functionalities.

The easy surface functionalization has resulted in strong interest especially in Au NPs functionalization by a broad variety of organic matrices and coatings including proteins.[32–34] From an inorganic point of view, other functionalizations, such as the incorporation of a transition metal complex, have been performed, providing new functionalities to the resulting hybrid.[35] Beyond that, Au hybrid NPs composed of two different nanosystems (*i.e.* two different NPs) have recently aroused interest. In fact, the combination of two different nanosystems gives rise to a variety of different heterostructures (core@shell, Au-coated, NP decoration, dumbbell/Janus, *etc.*) with some peculiarities. To have a better scope of the highly diverse Au hybrid nanostructures, a classification is presented in Figure 1.4 based on the most relevant heterostructures. Depending on the desired properties and the application field, a

given hybrid heterostructure will become the most suitable. Besides, the corresponding synthetic strategy must focus on the development of these nanomaterials in a simple, efficient and sustainable way.

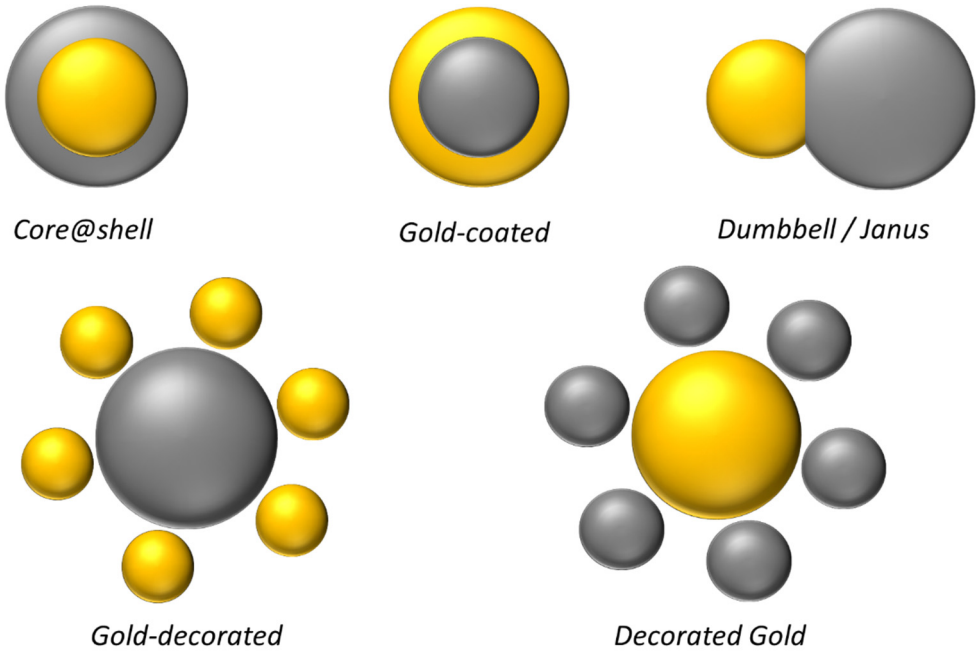

Figure 1.4 Different heterostructures formed by Au hybrid NPs (Au is represented in yellow).

1.2.2 Classification of Au hybrid nanostructures

Colloidal chemistry has become a reliable approach for obtaining high-quality hybrid NPs. A great variety of synthetic approaches have been recently developed in such a way that one can control a wide range of sizes, shapes and compositions of the NPs. In this sense, the most common heterostructures that can be synthesized at the moment are:

i) Core@shell heterostructures: These nanostructures are highly functional materials that exhibit unique properties arising from either the core or the shell. These new properties can be modified by modulating the core/shell size ratio. Thus, many different synthetic approaches have been developed using a plethora of different procedures such as precipitation, grafted polymerization, micro-emulsion, reverse micelle, sol-gel condensation, layer-by-layer adsorption technique and so on. However, it is still difficult to control the thickness and homogeneity of the coating. The shell formation requires highly controlled and sensitive synthesis protocols to ensure complete coverage of core particles with the shell material. In such a way, if this reaction is not properly controlled, it may lead to aggregation of core particles, the formation of separate particles or an incomplete coverage.[36] Interestingly, some synthetic routes permit to achieve core@shell NPs using anisotropic Au NPs (rods, stars, cages, etc)[37,38] and multishell heterostructures[39] (*i.e.* core having several shells around them), thereby, allowing the chemists to modulate the LSPR of the system. Due to the close contact between these two nanosystems, the core@shell structure presents the largest interface area, thus facilitating the interaction between the two components. However, it is important to point out that the Au core is completely covered by the shell leading to a minimal interaction of the Au with the environment.

ii) Au-coated heterostructures: In contrast to the previous one, in this case, Au is used for covering NPs of different nature. Au confers plasmon properties and high chemical and colloidal stability. In addition, as mentioned before, Au exhibits an amenable surface functionalization that results in particular interest in some applications such as biomedicine. These nanoshells can be mainly prepared by two methods: 1) Direct method: the Au precursor is reduced directly onto the chemically modified NP surface having similar crystal lattices. 2) Indirect method: small Au NPs acting as nucleation sites are previously adsorbed on the surface of the NP to facilitate the growth of the Au shell upon the addition of the NPs to the growth solution. This method can be easily controlled, allowing the chemists to synthesize highly monodisperse Au nanoshells with tunable thicknesses.[40] In fact, by modifying the thickness of this Au layer, relative to the size of the core,

the LSPR of the nanoshell can be tuned to a specific wavelength across the visible and infrared range of the electromagnetic spectrum.[41] Nevertheless, in this sort of heterostructure, the core NP stands chemically inert and only the Au shell is able to interact with the environment.

iii) Dumbbell / Janus heterostructures: In such heterostructures, a single NP is attached to another NP offering two functional surfaces. In this manner, the hybrid NP integrates two or more functionalities in an individual entity. Depending on the interactions at the interface, the physical and chemical properties of each component can be retained, enhanced or even weakened. Besides, the break of mirror symmetry can lead to interesting effects. They are commonly obtained by sequential growth of a second component on the preformed seeds. The successful synthesis relies on promoting heterogeneous nucleation while suppressing the homogeneous nucleation (*i.e*. the formation of separate NPs of the second component).[42] When Au NPs are used, these NPs can also display LSPR in a wide range of the visible spectrum.[43,44] However, the principal disadvantages are related to the lack of simple synthetic procedures and difficulties to characterize and unambiguously verify their formation. Moreover, the contact area between both nanosystems is smaller than that of core@shell heterostructure.

iv) Au-decorated heterostructures: This structure is the result of linking a large number of small Au NPs to the surface of another NP. Frequently, negatively charged satellite Au NPs are immobilized on a positively charged NP *via* electrostatic interactions or by using a polymer anchored to both NPs. Then, this route relies on surface functionalization that governs the interaction between NPs. In this way, the distance between both NPs can be adjusted. Another strategy to obtain these heterostructures involves the *in situ* formation of Au NP seeds on the surface of NPs *via* the reduction of $HAuCl_4$ in a way that the total specific area is enhanced.[40,45] However, this heterostructure exhibits a lower contact between both NPs compared to the above-mentioned nanostructures.

v) Decorated Au NPs: It represents an analogous case to the previous one but in this case, big Au NPs are decorated by smaller NPs of different nature. In this approach, the small NPs are linked *via* electrostatic interaction to a previously

prepared bigger Au NP. Therefore, the decoration of Au NP permits to work with big Au NPs such as rods, triangles and stars. As in the core@sell heterostructure, this heterostructure also exhibits a high total specific area but a less intense contact between both NPs.

1.2.3 Au and Fe_3O_4: the reported combinations

The combination of iron oxides and Au NPs have attracted a lot of attention due to their magnetic and optical properties that open a plethora of different applications in the fields of magnetic resonance imaging, hyperthermia treatment, drug delivery, DNA-based biosensors, and catalysis.[46] Some examples of the possible heterostructures are the following (Figure 1.5):

- Core/shell structures. When comparing Au@Fe_3O_4 with Fe_3O_4@Au, it is found that Au@Fe_3O_4 have been much less investigated mainly due to the challenge that represents its synthetic process and the alleged quenching of the Au when covered by Fe_3O_4.[47] However, it is found that, in Au@Fe_3O_4, the surface of the Au core is inactivated but still keeps its optical properties. In addition, it is important to mention that its initial morphology does not necessarily need to be spherical, leading to very intense optical absorption bands in the whole visible spectrum. Then, the advantage of this structure seems to be that it exhibits higher magnetization and higher blocking temperatures because of the lower amount of Au. In contrast, Au coated iron oxides exhibit lower magnetization due to a higher diamagnetic contribution of Au, but improved stability and biocompatibility in aqueous media.[48] Indeed, in Fe_3O_4@Au, the Fe_3O_4 cores are fully covered by Au, making them chemically inert, even in some corrosive environments (*i.e.* blood serum).[49] Furthermore, anisotropic Au shells have been achieved, thereby permitting the controlled tuning of the LSPR Au response from visible to near-infrared region.[50]
- Dumbell-like heterostructures. These nanostructures present optimized magnetic and optical properties that can be modulated by controlling the size of either the Au NP or the Fe_3O_4 NP. In addition, the presence of Au and Fe_3O_4 allows one to functionalize their surface with different chemical functionalities

such as biological molecules. Due to the advantages of these heterostructures over single component NPs or conventional core@shell nanostructures, dumbbell-like Au-Fe_3O_4 provides a promising integrated theranostic nanoplatform.[51]

- Decorated heterostructures. One can synthesize single Au NPs decorated by many Fe_3O_4 NPs or *vice versa*, *i.e.* a single Fe_3O_4 NP decorated by many Au NPs. The main advantage of such morphology is to provide a high Au (or iron oxide) specific area and to offer the possibility of a further functionalization of the uncovered iron oxide (or Au) surface.[47] Despite the simplicity of this heterostructure formation, the important polydispersity due to aggregation has hampered its use. However, when this limitation is overcome, the integration of these two functional components, with the high surface area provided by the satellite NPs, can be very useful for catalytic applications.[47]

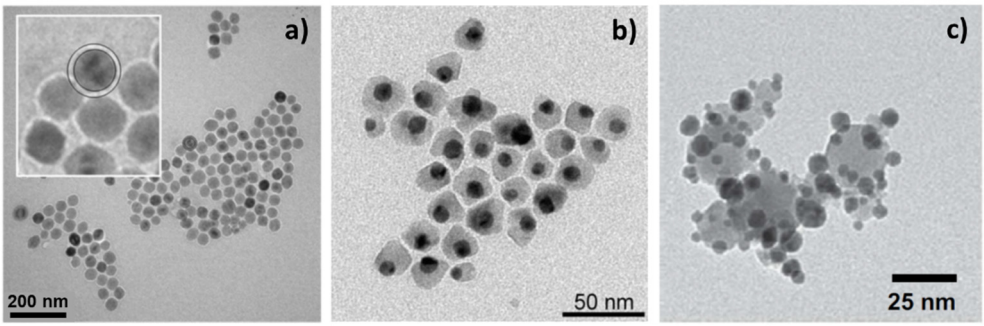

Figure 1.5 a) Core@shell NPs of Fe_3O_4@Au. b) Dumbbell Au-Fe_3O_4 NPs and c) Au decorated Fe_3O_4 NPs. Adapted from 52–54.

1.3 Combination of Coordination Polymers and Au NPs

For a long time, many groups have studied different synthetic approaches and possible applications of hybrid Au-iron oxide nanostructures.[47,48,55] Compared to this, Au hybrid materials composed of coordination complexes as functional components represent a nascent field.[56] In this context, Coordination Polymers (CPs) possess besides interesting electronic properties, potential advantages over conventional inorganic nanomaterials such as structural and chemical versatility, high specific area, biodegradability and so on. Moreover, CPs have, among other exciting advantages, the facility to be nanoprocessed.[57] Therefore, the integration of both Au and CPs in a single heterostructure represents a topic that could be very interesting in terms of developing new properties and novel applications.

Even if the term “Coordination Polymer” started to appear in the early 20th century, the current extensive interest in CPs was triggered after the reports of Robson, Hoskins and coworkers in the early 1990s.[58,59] These authors proposed that the new materials could be deliberately engineered through describing crystal structures in terms of nets which was proposed in 1977 by Wells.[60]

A CP is an organometallic polymer structure built from the association of metal ions and bridging organic linkers (ligands). The wide variety of metal cations, ligands, and structures affords a vast number of possible combinations. Metal cations, often called nodes or hubs, are bonded to a specific number of ligands at well-defined angles. Regarding the ligands, they donate a lone pair of electrons to a node and form a coordination complex *via* a Lewis acid/ base interaction. Ligands that can form one coordination bond are referred to as monodentate, but those which form multiple coordination bonds, which could lead to CPs are called polydentate; these are particularly important because it can connect multiple nodes, leading to the formation of infinite arrays. It is important to remark that polydentate ligands can also act as chelates forming multiple bonds to a single node. CPs are formed when a ligand can form multiple coordination bonds and act as a bridge between multiple nodes. The number of ligands bound to a node is known as the coordination number, while the connection between nodes determines the dimensionality of the structure. Thus, a structure linked by coordination bonds in one direction and supramolecular

interactions in two other directions is a one-dimensional CP; a structure linked by coordination bonds in two directions and supramolecular interactions in another direction is a two-dimensional CP, and a structure linked by coordination bonds in three directions is a three-dimensional CP (Figure 1.6). The coordination behaviors of both nodes and ligands play a critical role in the self-assembly of CPs since the coordination bonding is a kind of directional and strong interaction in the process. Therefore, its judicious choice is crucial for a targeted structure.[61–63]

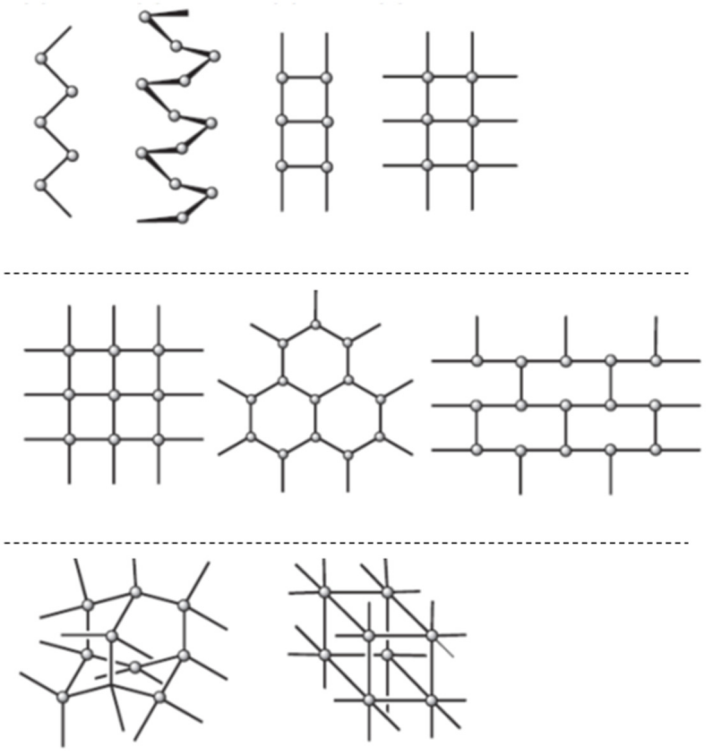

Figure 1.6 Examples of different CP nets: first row correspond to 1D, second row to 2D and third row to 3D. Adapted from 61.

The metal ions are usually d-transition metals and/or lanthanides. Generally, d-transition metals have been more popular due in part to the more predictable nature of their coordination geometries. Besides, a large range of accessible properties are displayed by d-transition metals and they can be conveniently used in CPs because

their chemistry is well understood. For d-transition metals, the field is dominated by the first-row elements (plus Zn, Cd, Hg, Ag and, to a less extent, Au, Pd, Pt). Their low cost, earth abundance, kinetic lability and stability explain why the research in these d-transition metal-containing CPs is predominant compared to the rest.[63]

The sizes of CPs can be carefully controlled to be uniform and below several hundred nanometers.[62] In addition to this, they can exhibit different magnetic, electronic, optical, and catalytic properties associated by tailoring the wide choice of metallic and ligand elements they can contain.

Current research on CPs is not only focused on their synthesis at the nanoscale but also on combining these polymers with other materials. Therefore, the design of heterostructures is a promising way towards multifunctional nanomaterials that combine multiple properties in a single nanosystem. These heterostructures can feature a simple combination of the physical and chemical properties of both components or display novel properties that are due to the mutual interactions. In addition, the functional components can lead to unique synergy induced properties of the resultant hybrid materials.[64,65]

Several heterostructured systems that combine inorganic materials with CPs have been investigated because of their enhanced catalytic activity or because of an association of the magnetic or optical properties of the inorganic NPs with the porosity,[66] electrochemical[67] or magnetic properties[68] of the CPs. Therefore, the controllable integration of metallic NPs and CPs into advanced hybrid materials with targeted functions can extend the scope of the utilization of these materials. This thesis will focus on the integration of Au NPs in three different categories of CPs forming novel heterostructures with interesting multifunctionalities.

1.3.1 Bimetallic cyanide complexes with the Prussian Blue structure

Prussian Blue (PB) is an early example of functional CP. It was made by accident in the early 18th century and used as a pigment. The structure of PB is illustrated in Figure 1.7 where iron centers are octahedrally coordinated by bridging cyanide ligands into an infinite 3D network. The structure is cubic with a face-centered cubic

(fcc) unit cell alternating Fe^{III} and Fe^{II} bridged by the cyanide ligands and with general formula $A_aFe_x[Fe(CN)_6]_y \cdot nH_2O$ (A = alkali cation). PB is comprised of both Fe^{II} and Fe^{III} centers and the intense blue color located around 700 nm that gives rise to its use as a pigment is due to an intervalence charge transfer band associated with the Fe^{II}-CN-Fe^{III}. On the other hand, PB is also the first example of a synthetic CP with functionality derived from its electronic properties that can potentially be exploited in devices and hybrid materials.[63,69,70]

Replacing Fe^{III} or Fe^{II} by other transition metal ions gives rise to Prussian Blue Analogues (PBAs) of general formula $A_aB_x[D(CN)_6]_y \cdot nH_2O$ (A = alkali cation, B and D = transition metal ions), which possess the same cubic structure (Figure 1.7). As well as in PB structure, it could exist a vacancy on the $[D(CN)_6]^{d-}$ site. Vacancies are usually filled by water molecules, which complete the coordination sphere of the neighboring metallic ions. The term 'vacancy' is used to encompass the possible occupancy of the M′ site with water.[63,71] These vacancies have an important role and their manipulation has been proven as an interesting strategy in order to modulate the PBA properties.[72,73]

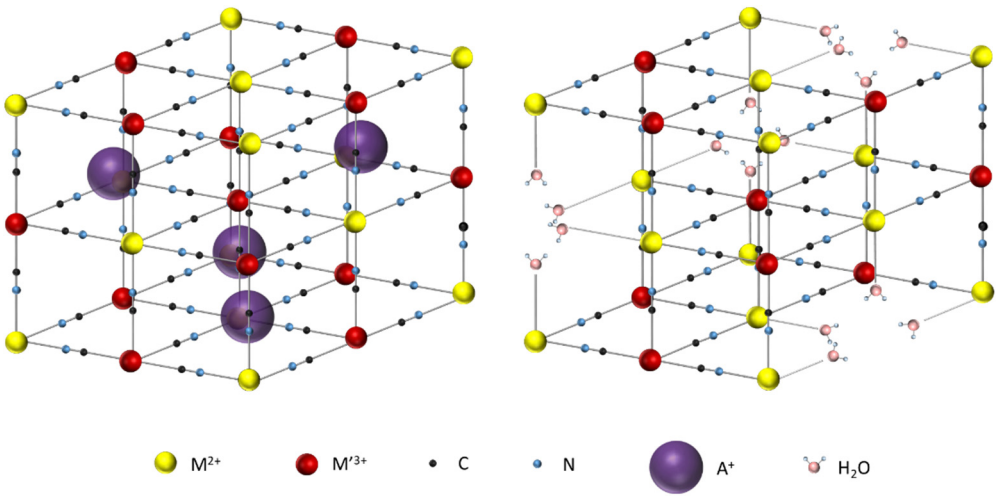

Figure 1.7 Illustrations of the cubic structure of the PBA (left) and the PBA with random site defects (right). The appearance of defects leads to a lower amount of alkali metals due to charge balance. The PB structure is identical but Fe^{II} centers are connected to C atoms while Fe^{III} centers are connected to N atoms.

PBAs offer several advantages in comparison to other conventional inorganic materials and semiconductors because of their different magnetic and optical properties, processability and chemical versatility.[70] In fact, PB and their PBA can easily be synthesized by the simple reaction of hexacyanometalates $[D(CN)_6]^{d-}$ with a transition metal Lewis acid B^{b+} in water to give neutral 3D networks. Hexacyanometalate anions are known for many of the transition metal elements, and thus PBA can be prepared with a variety of metals. Furthermore, it is possible to control the synthesis to obtain individualized NPs over a large size range (2 - 200 nm). Also, these NPs can be formed in "soluble" colloidal solutions or powders depending on the synthetic conditions.[69] This versatility has allowed producing PBAs in various shapes and sizes including individual NPs,[69] films,[74] wires[75] and even core@shell particles formed by the combination of two different PBA or a PBA and another different material.[76] This huge control over the synthesis and its interesting properties makes them key compounds in the field of molecular nanomaterials. Indeed, their high chemical versatility leads to a vast number of different properties that gives rise to many possible applications (Figure 1.8):

- Biomedical applications: PBA and especially the PB have a strong charge-transfer absorption that can be used to undergo a thermal relaxation and can be exploited to generate local hyperthermia by light irradiation. In addition to this, these CPs are fully biocompatible (PB has already been approved by the FDA), biodegradable and easy to be functionalized. These properties make them ideal candidates for biomedical applications.[77]
- Magnetism: most PBAs are magnets thanks to the magnetic interactions between the spin carriers mediated by the cyanide bridge, their high dimensionality (3D) and connectivity of the magnetic lattice.[78,79] Additionally, the versatility of their chemistry has allowed the magnetic ordering temperature to be pushed from 5 K in the classical PB to room temperature in a VCr PBA.[70] Furthermore, some PBA exhibit also photomagnetism due to a metal-to-metal charge transfer that was evidenced for the first time in a CoFe PBA.[80]
- Energy storage: the PBA open framework offers a large interstitial space to host big ions like sodium and potassium. The existing bond between the alkali metal and cyanide is considerably weaker than the bond existing in oxide materials,

facilitating the alkali intercalation in the PBA structure.[81] In addition to this, the combination of PBA and other compounds in hybrid heterostructures has been demonstrated as an efficient strategy to develop novel batteries.[82]

- Catalysis: PBAs exhibit open framework structures, large specific surface areas, adjustable metal active sites, uniform catalytic centers and also they are electrochemically stable in a large pH range making them promising materials for electrocatalytic water splitting. In fact, the PBAs based on the first transition metals (such as Co, Ni, Cr and Fe) have been proven as excellent catalyzers with electrochemical activities comparable to those of metal oxides for the oxygen evolution reaction.[67,83]

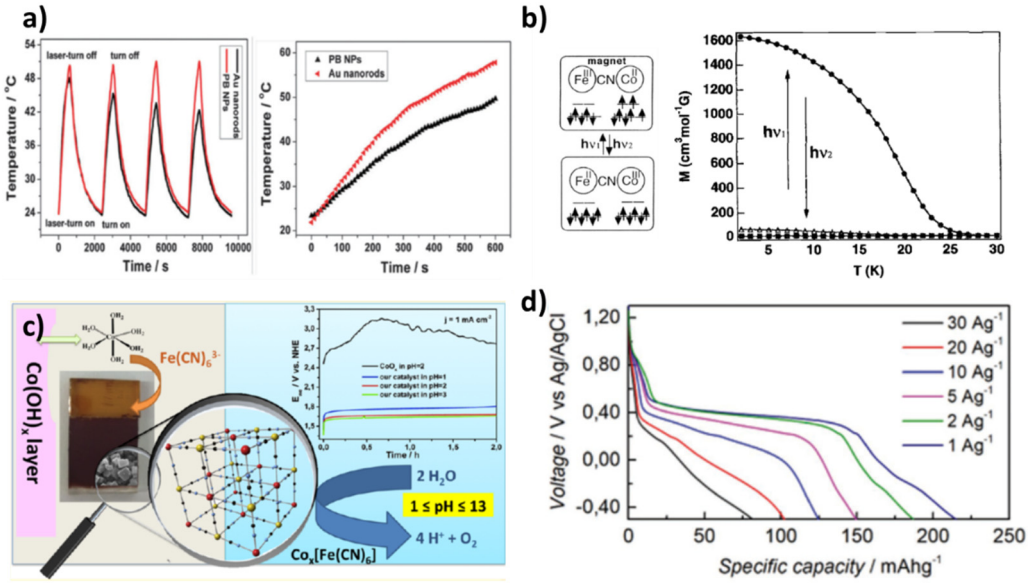

Figure 1.8 a) Temperature variations of PB NPs and AuNRs under the continuous irradiation of 808 nm laser for 4 cycles and the continuous irradiation for 10 min. b) Charge transfer of the reversible photo-induced magnetization. Field-cooled magnetization vs. temperature curves at H = 5 G. ($h\nu_1$ corresponds to visible light illumination while $h\nu_2$ corresponds to near-IR light illumination). c) Highly active phase of CoFe-PBA able to promote water oxidation under neutral, basic (pH < 13), and acidic conditions (pH > 1). d) Galvanostatic discharge curves at different current densities of a PB heterostructure measured in a typical three-electrode cell using 0.5 m K_2SO_4 aqueous solution. Adapted from 82–85.

The current emerging challenges in the field of PB NPs consist of designing multifunctional hybrid nanomaterials combining metals or metal oxides with PB in various heterostructures but especially as core@shell or decorated NPs. Such nanomaterials combine the properties of each component in a single nanosystem exhibiting diverse physical responses. Regarding the heterostructures formed by Au and PB/PBA, first combinations were achieved through electrochemical deposition of PB where the resulting nanocomposite films were applied for biosensing and electrocatalytic reduction of H_2O_2.[86–89] Nevertheless, the achieved hybrid material is deposited in an electrode as a film, limiting their applications. Later on, PB coating Au NPs were for the first time synthesized by a simple colloidal method by the group of Xia.[90] In this case, the nanohybrid was also used in electrocatalysis. In this synthetic method, the key step is the reduction of ferric ions catalyzed by Au NPs, which determines the formation rate of PB. Therefore, colloidal chemistry has enabled the control of the nanostructures constituted of both compounds opening a wide range of new applications.

Initially, the method to decorate PB NPs with Au NPs consisted of using albumina as a linker between the two components. This hybrid system was used as electrochemical sensor.[91] However, this protein coverage avoids contact between both systems. In addition, a similar approach, using different organic polymers as linkers, was developed for *in vivo* computing tomography and photo-thermal therapy.[92] More recently, a new strategy was performed to obtain very small core@shell NPs by growing a PB shell onto a citrate-stabilized Au core through the addition of Fe^{3+} and ferricyanide in the presence of citric acid.[93] The combination of plasmonic properties of Au and photo-thermal/magnetic properties of PB was used in this case for biomedical applications. In this line, Marin-Pasturel *et al.* developed another core@shell heterostructure consisting of a double shell of PBA in Au spherical core, where the core and the shell size can be modulated, therefore exhibiting different magnetic and plasmonic properties. They synthesized for the first time different Au@PBA@PBA' using an elegant approach based on the synthesis of cyanide-stabilized Au NPs in water through reduction of the precursor $[Au(CN)_2]^-$ with sodium borohydride followed by the sequential growth of one or more PBA shells (Figure 1.9).[68,94,95] However, following this approach, a first weak magnetic

shell located between the magnetic and the plasmonic particles is necessary, thus reducing the electronic interaction between the plasmonic and the magnetic components.

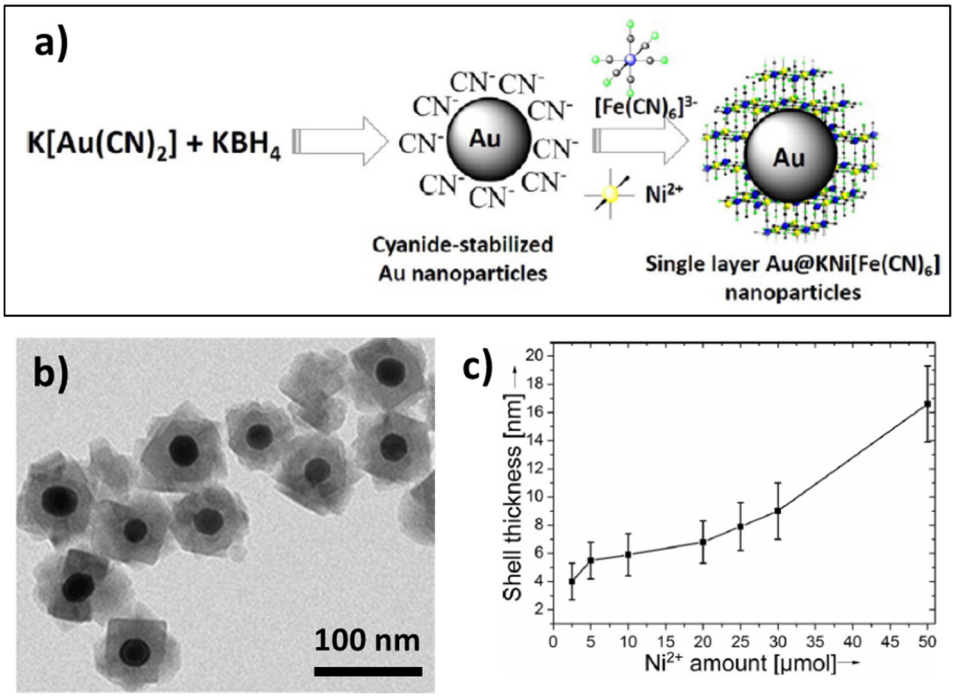

Figure 1.9 a) Schematic representation of the approach used for the synthesis of Au@KNi[$Fe^{II}(CN)_6$] core@shell NPs. b) TEM image of Au@PBA NPs. c) Thickness of the KNi[$Fe^{II}(CN)_6$] shell *versus* the amount of Ni^{2+} added. Adapted from 94.

1.3.2 Spin-Crossover compounds

A category of CPs that are of special interest is those that display Spin-Crossover (SCO). The SCO phenomenon may provide one of the most spectacular examples of molecular bistability. The bistability arises from their ability to be switched between two electronic states, the high spin (HS) and the low spin (LS) in a readily detectable and reversible way. The transition between these two states may be typically induced

by means of a variation of temperature, pressure, or by light irradiation. The transition metal compounds that may present a spin-crossover are generally octahedrally coordinated and have a d^4 to d^7 electronic configuration (see Figure 1.10). SCO induces changes in metal-to-ligand bond distances due to the population or depopulation of the e_g orbitals that have a slight antibonding character.[96–98] Therefore, this spin transition involves a compression/expansion of the coordination site. Reversible changes in their optical, magnetic, mechanical, and electrical properties are also occurring, making these compounds promising as molecular switches,[99] optoelectronic devices,[100] actuators,[101] and sensors.[102]

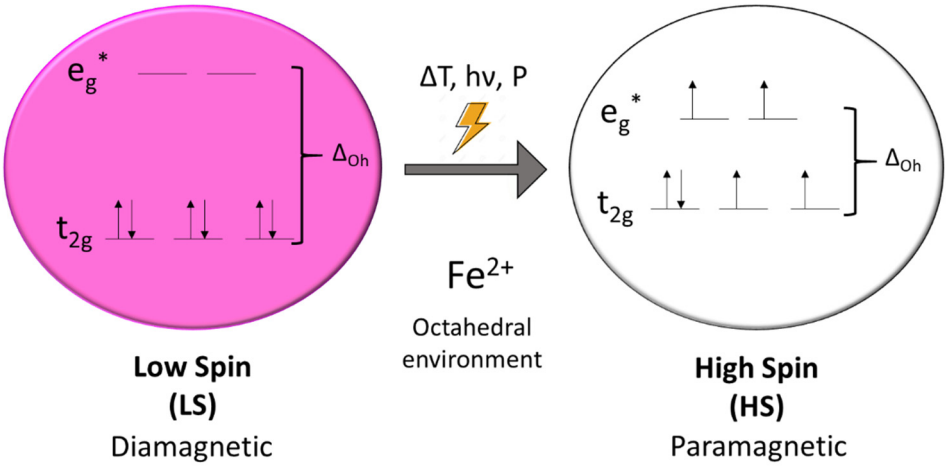

Figure 1.10 Example of the SCO phenomenon for a Fe^{II} compound in an octahedral environment. The spin transition involves switching from a diamagnetic (LS) to a paramagnetic (HS) state.

One of the best-known class of SCO compounds features the d^6 Fe^{II} ion, where the transition is typically induced by varying the temperature. Depending on the selected ligands, there are several examples of SCO CPs, comprising 1D chains,[103] 2D nets[104] and 3D networks.[105] The design of ligands is crucial because they not only provide the correct strength of the crystal field (Δ_O) for the SCO phenomenon but also enhance the cooperative elastic interactions between the SCO centers in the crystal, thus favoring undergo an abrupt and/or hysteretic spin transitions.[98] Kahn

et al. identified a 1D CP exhibiting SCO with the formula $[Fe(Htrz)_2(trz)](BF_4)$.[96] This SCO complex is usually selected owing to its large and abrupt hysteresis that takes place above room temperature and its well-established miniaturization protocol,[106] permitting the maintenance of cooperative behavior even in very small NPs.[107]

Recently, diverse pathways have been established for the production of SCO nanomaterials as colloidal suspensions, thin films and other types of nanoscale assemblies using different approaches in order to control the size, shape and even the organization of SCO compounds. Hybrid nanostructures that involve SCO in complex structures reveal unique functionalities due to the synergy between the SCO properties and the physical properties (magnetic, photonic, charge transport, etc.) of the surrounding matter. Indeed, many strategies to access the multifunctional potential of novel nanomaterials were developed by creating nanohybrids or nanocomposites that can combine different materials with different properties. In this context, the SCO combination with Au NPs has opened some promising perspectives for new physical properties in SCO materials, including plasmonic effects.[108]

Combinations of SCO entities and Au NPs in hybrid heterostructures are typically overtaken following a decoration protocol. In this context, attachment of Au NPs on the surface of $[Fe(NH_2trz)_3](Br)$ was firstly reported in 2008 in order to evidence the presence of the amino groups on the SCO surface.[109] Later on, in 2012, the first attempt to study the synergy between both systems was described by preparing the well-known $[Fe(Htrz)_2(trz)](BF_4)$ polymeric complex covered by Au using thermal evaporation deposition.[110] The resulting film was analyzed and the authors confirmed the persistence of the spin-crossover properties of the Au coated particles. In 2014, Suleimanov and coworkers obtained a hybrid to induce the SCO transition, reducing the energy needed through the photo-thermal from the LSPR.[111] In this case, $[Fe(Htrz)_2(trz)](BF_4)$ was decorated with ultra-small Au NPs of ~2 nm. These NPs were attached to silica shell SCO NPs that were firstly synthesized using the reverse micelle technique. By exciting the nanocomposite at different laser wavelengths, a full switching was carried out and a notable photo-thermal effect was noticed. Indeed, the laser power required to complete the spin transition was reduced by around 70 % in the presence of the Au NPs. Au size was increased by

the addition of further $AuCl_4^-$ precursor, giving rise to ~15 nm NPs. Nevertheless, Raman spectra were not possible to be recorded possibly due to the Surface Enhanced Raman Spectroscopy (SERS) effect associated with the larger Au particles. In the same year, a similar Au decoration was also used by Qiu *et al.,* obtaining analogous nanohybrid material displaying a photo-thermal effect.[112] Later on, in 2016, Moulet *et al.* went one step further and reported direct Au decoration of the $[Fe(Htrz)_2(trz)](BF_4)$ without any silica shell.[113] They developed a simple manner to fix Au by taking advantage of o the Au affinity of nitrogen donor atoms present in triazole molecules at the surface of the SCO particles, which coordinate to the Au surface. Besides, they were able to tune the Au NPs size (from 4 to 45 nm) and ensure good coverage, but no photo-thermal effect was recorded maybe because of the insufficient applied laser power. After, other plasmonic metals such as Ag were used. Li *et al.* decorated Ag nanowires with two SCO NPs: $[Fe(Htrz)_2(trz)](BF_4)$ and $[Fe(pz)\{Pt(CN)_4\}]$ employing an *in situ* growing method.[114] However, although the nanocomposites retained their SCO properties, the electrical conductivity was unaffected by the spin transition. Therefore, after this short overview, one can conclude that even if metal nanocomposite materials have been successfully obtained, the impact coming from the metallic decoration on the physical properties is still ineffective. This limitation is very likely due to an inefficient interaction between the metal and the SCO material. Then, to overcome this limitation, a possible pathway is the preparation of a core@shell heterostructure to ensure an intimate interaction between both nanosystems. On this basis, the coverage of AuNRs by $[Fe(Htrz)_2(trz)](BF_4)$ was undertaken by another group, obtaining well-defined heterostructures.[115] In that work, the resulting nanohybrid displayed a widening of the thermal hysteresis loop compared to the pure SCO NPs of similar size. Besides, it was observed an important reduction of the power laser beam required in order to photo-switch the SCO shell. Furthermore, it was also recorded a strong modulation of the LSPR upon the spin transition of the SCO shell (Figure 1.11). This synergetic effect brings out the importance of chemical engineering for the design of appropriate heterostructures. However, the development of more versatile methods to increase the contact of Au and SCO NPs still remains a challenge.

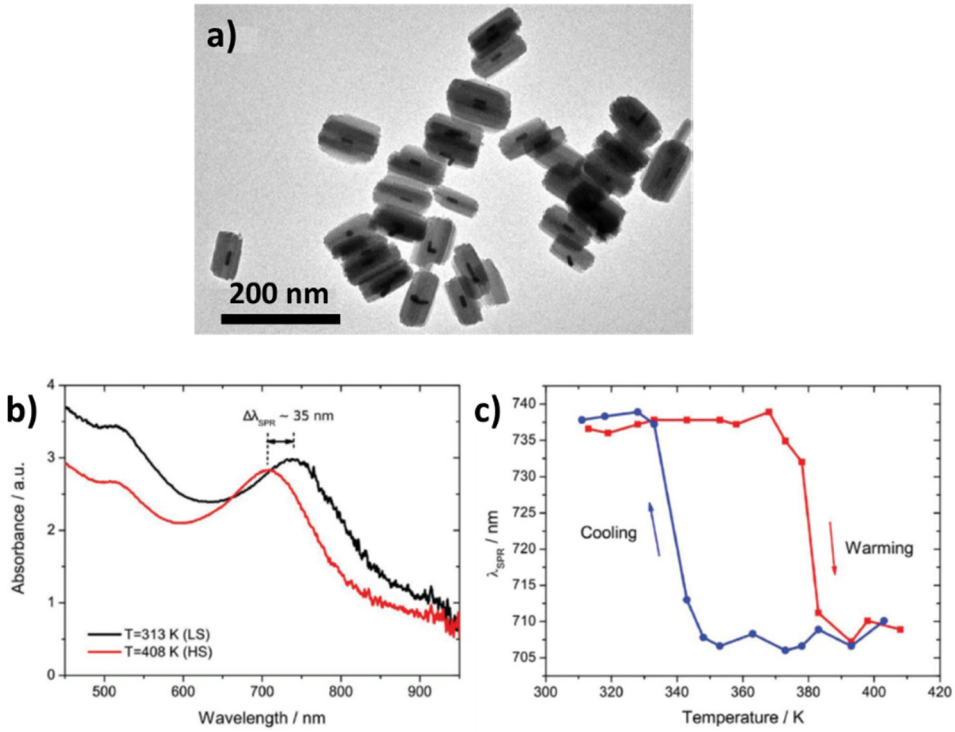

Figure 1.11 a) TEM image of AuNRs@SCO NPs**.** b) Optical spectra of the core@shell recorded at 313 and 408 K, respectively. c) Evolution of the peak of LSPR upon temperature variation in both warming and cooling mode. Adapted from 115.

1.3.3 Metal-Organic Frameworks

Porosity is one of the most widely studied individual properties within the field of CPs. In this context, porous CPs, also known as Metal-Organic Frameworks (MOFs), are a promising class of porous materials where the combination of the metal centers and the organic ligands gives rise to reticular 3D networks with high crystallinity, ultrahigh pore volumes (up to 90% free volume) and extremely large specific surface areas. Thanks to their modular nature, a chemical control over the structure is possible (Figure 1.12), leading to a tunability of the properties and to the development of applications.[116,117] Thus, MOFs have emerged as a significant class of nanoporous materials with potential applications in gas storage, separation,

catalysis, and chemical sensing. Still, porosity is not the only property that can be exploited. The possibility to introduce functional properties in the MOF, such as electrical conductivity, optical properties or magnetism, is also very promising to improve the properties of these materials and to expand the range of applications.[118]

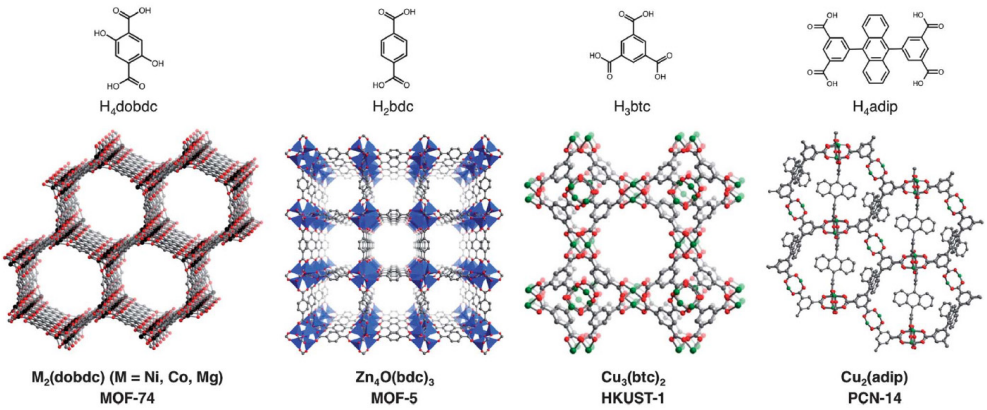

Figure 1.12 Crystal structures and organic bridging ligands for some MOFs, evidencing the structural tunability of these CPs. Adapted from 119.

A hybrid approach in which a functional nanostructure is mixed with the MOF provides a useful way to improve the properties of the MOF. Au NPs have attracted much attention in this context. Indeed, a combination of MOFs with suitable Au NPs could lead to synergetic effects brought by both sides. Hybrid materials consisting of plasmonic NPs and MOFs have become promising nanostructures for several applications, especially in sensing[120] and catalysis.[121] For example, a hybrid material can be designed for chemical sensing of high SERS signal molecules by combining the selectivity and easy adsorption of MOFs with the plasmonic effect provided by the Au NPs.[122] Another example comes from the use of light (*i.e.* photo-thermal effect) to control the adsorption or desorption of molecules carried by these hybrid nanostructures.[123]

These composites can be prepared by different methods. On the one hand, pre-synthesized Au NPs can be either encapsulated into the MOF or attached to the MOF surface and on the other hand, MOF can be directly grown on the Au NP surface. Due to the too high number of publications (more than 250 publications in the last 5 years), only core@shell heterostructures composed by an Au core will be addressed, representing near 60 % of the heterostructures developed in the last decade (source: Scopus).

The first Au loading into MOF was reported in 2005 for MOF-5.[124] However, Au@MOF-5 seemed to be inactive for catalytic CO oxidation. Further investigations extended this system by encapsulating Au NPs in ZIF-8[125] and MIL-101.[126] In the first case, an improvement of the catalytic activity for CO oxidation was observed with increasing Au loadings, and the highest catalytic activity was obtained for 5.0 wt % Au@ZIF-8. In the second case, Gu *et al.* reported Au−Pd clusters adsorbed inside activated MIL-101 using a simple liquid impregnation method. This nanocomposite catalyzes effectively the dehydrogenation of formic acid. However, despite the increasing endeavors to control the size, composition, dispersed nature, spatial distribution and confinement of the incorporated NPs within MOF matrices,[127] obtaining a single Au NP core coated with a uniform MOF shell remained still a challenge. Indeed, although the aforementioned nanocomposites exhibit core@shell structure, they are actually composed of several Au NPs embedded in a MOF matrix rather than a single NP surrounded by a MOF shell. In fact, core@shell particles with individual cores are more difficult to synthesize because they require correct concentrations of Au and MOF precursors as well as a precise control of the reaction kinetics to avoid MOF self-nucleation.[128]

In 2013, a one-pot method was established for the first time for the preparation of single Au NP cores coated with a uniform MOF shell of MOF-5, ZIF-8 and IRMOF-3.[129] Besides, the resulting Au@MOF-5 nanostructure was successfully applied for the detection of CO_2 and other gases by SERS (Figure 1.13).

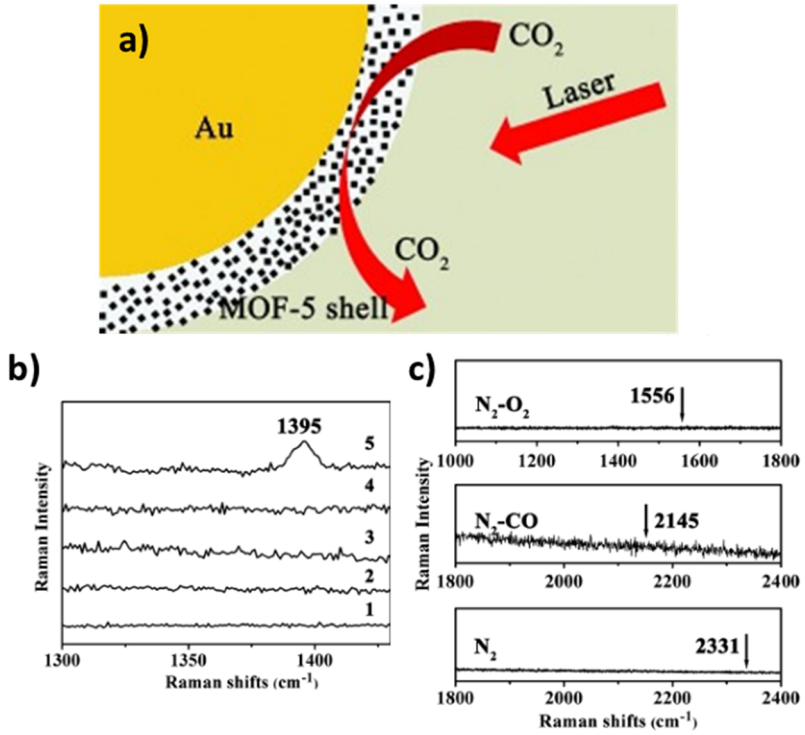

Figure 1.13 a) SERS effect on Au@MOF-5. b) SERS spectra of single Au NPs (trace 1), single MOF-5 spheres (trace 2), and Au@MOF-5 NPs with different shell thickness toward CO_2 in a CO_2/N_2 gas mixture. The thinnest shell (under 4 nm) is the only one active (trace 5). c) SERS spectra of single Au@MOF-5 NPs with a thinner shell toward N_2, CO, and O_2. The arrows point to the characteristic SERS peak positions of N_2, CO, and O_2. Adapted from 129.

Simultaneously, Khaletskaya *et al.* also obtained a core@shell of Au@Al(OH)(1,4-ndc) (1,4-ndc = naphthalenedicarboxylate) composed of individual AuNR cores surrounded by a MOF shell.[130] To ensure the accurate MOF crystal nucleation onto Au rods, the Au was first coated with a hydrated amorphous alumina layer. These Al-modified rods were then used as reactive seeds in such a way that the dissolution of the alumina coating by microwave treatment in the presence of 1,4-ndc promoted the MOF nucleation specifically on the surface of the rods. Besides, in this system, the photo-thermal conversion ability of the NRs acts as an optical switch that enables to remotely release the guest molecules adsorbed within the pores through an increase of molecular mobility. Just after, Hu *et al.* proposed a

surfactant mediated method for the MOF coating of ZIF-8 on single Au octahedral NPs.[131] In this work, instead of using a metal layer, CTAB was added to align the overgrowth of the MOF. This turned out to be essential. Indeed, it was also found that the CTAB adsorbed, even on anisotropic metal surfaces, can efficiently induce ZIF-8 nucleation (and/or adsorption) and its further overgrowth.[132] This new methodology (*i.e.* using other quaternary ammonium as surfactants or polymers such as poly(ethylene glycol) (PEG) allowed researchers to successfully obtain single anisotropic Au NPs coated with a uniform MOF shell. In this line, AuNRs coated by a NU-901 shell were obtained by functionalizing the Au surface with PEG to avoid the aggregation of the Au NPs prior to the MOF shell growth.[133] In addition, it is essential to remark that these core@shell composites have shown high potential for SERS applications.

The synthesis of the aforementioned heterostructures brings out the importance of the high control required in Au surface functionalization prior to the MOF growth. However, it is worth mentioning that the majority of the reported syntheses for overgrowing MOF shells on metallic NPs do not permit a precise control for shell thickness under 10 nm. In order to overcome this limitation, layer-by-layer methods have recently been used. For instance, Hinman and coworkers developed a protocol for accurate control over the thickness of an HKUST-1 shell on AuNRs.[134] Nevertheless, this protocol requires to centrifugate too many times the nanostructures since the centrifugation can easily lead to some aggregation. Therefore, the development of new systematic protocols to easily cover Au NPs of different morphologies with different MOFs remains a challenge.

1.4 References

(1) Mingos, D. M. P. *Gold Clusters, Colloids and Nanoparticles I*; Springer US, **2014**.

(2) Faraday, M. Experimental Relations of Gold (and Other Metals) to Light. *Phil. Trans. R. Soc.* **1857**, *147* (0), 145–181.

(3) Zsigmondy, R. Ueber Wässrige Lösungen Metallischen Goldes. *Justus Liebigs Ann. Chem.* **1898**, *301* (1), 29–54.

(4) Mie, G. Beitrage Zur Optik Truber Medien, Spexiell Kolloidaler Metallosungen. *Ann. Phys.* **1908**, *3*, 377–445.

(5) Gans, R. Über Die Form Ultramikroskopischer Goldteilchen. *Ann. Phys.* **1912**, *342* (5), 881–900.

(6) Freestone, I.; Meeks, N.; Sax, M.; Higgitt, C. The Lycurgus Cup - A Roman Nanotechnology. *Gold Bull.* **2007**, *40* (4), 270–277.

(7) Mayer, K. M.; Hafner, J. H. Localized Surface Plasmon Resonance Sensors. *Chem. Rev.* **2011**, *111* (6), 3828–3857.

(8) Armelles, G.; Cebollada, A.; García-Martín, A.; González, M. U. Magnetoplasmonics: Magnetoplasmonics: Combining Magnetic and Plasmonic Functionalities. *Adv. Opt. Mater.* **2013**, *1* (1), 10–35.

(9) Petryayeva, E.; Krull, U. J. Localized Surface Plasmon Resonance: Nanostructures, Bioassays and Biosensing-A Review. *Anal. Chim. Acta* **2011**, *706* (1), 8–24.

(10) Lee, K. S.; El-Sayed, M. A. Gold and Silver Nanoparticles in Sensing and Imaging: Sensitivity of Plasmon Response to Size, Shape, and Metal Composition. *J. Phys. Chem. B* **2006**, *110* (39), 19220–19225.

(11) Garcia, M. A. Surface Plasmons in Metallic Nanoparticles: Fundamentals and Applications. *J. Phys. D. Appl. Phys.* **2012**, *45* (38), 389501.

(12) Nehl, C. L.; Hafner, J. H. Shape-Dependent Plasmon Resonances of Gold Nanoparticles. *J. Mater. Chem.* **2008**, *18* (21), 2415–2419.

(13) Liz-Marzán, L. M.; Giersig, M.; Mulvaney, P. Synthesis of Nanosized Gold−Silica Core−Shell Particles. *Langmuir* **1996**, *12* (18), 4329–4335.

(14) Dreaden, E. C.; Alkilany, A. M.; Huang, X.; Murphy, C. J.; El-Sayed, M. A. The Golden Age: Gold Nanoparticles for Biomedicine. *Chem. Soc. Rev.* **2012**, *41* (7), 2740–2779.

(15) Yeh, Y.-C.; Creran, B.; Rotello, V. M. Gold Nanoparticles: Preparation, Properties, and Applications in Bionanotechnology. *Nanoscale* **2012**, *4* (6), 1871–1880.

(16) Synthesis, G.; Tepale, N.; Fern, V. A.; Carreon-alvarez, C.; Gonz, V. J.; Luna-flores, A.; Carreon-alvarez, A.; Aguilar, J. Nanoengineering of Gold Nanoparticles : Green Synthesis, Characterization, and Applications. *Crystals* **2019**, *9*, 612.

(17) Grzelczak, M.; Pérez-Juste, J.; Mulvaney, P.; Liz-Marzán, L. M. Shape Control in Gold Nanoparticle Synthesis. *Chem. Soc. Rev.* **2008**, *37* (9), 1783.

(18) Barbosa, S.; Agrawal, A.; Rodríguez-Lorenzo, L.; Pastoriza-Santos, I.; Alvarez-Puebla, R. A.; Kornowski, A.; Weller, H.; Liz-Marzán, L. M. Tuning Size and Sensing Properties in Colloidal Gold Nanostars. *Langmuir* **2010**, *26* (18), 14943–14950.

(19) Sardar, R.; Shumaker-Parry, J. S. Spectroscopic and Microscopic Investigation of Gold Nanoparticle Formation: Ligand and Temperature Effects on Rate and Particle Size. *J. Am. Chem. Soc.* **2011**, *133* (21), 8179–8190.

(20) Ackerson, C. J.; Jadzinsky, P. D.; Kornberg, R. D. Thiolate Ligands for Synthesis of Water-Soluble Gold Clusters. *J. Am. Chem. Soc.* **2005**, *127* (18), 6550–6551.

(21) Hussain, I.; Graham, S.; Wang, Z.; Tan, B.; Sherrington, D. C.; Rannard, S. P.; Cooper, A. I.; Brust, M. Size-Controlled Synthesis of near-Monodisperse Gold Nanoparticles in the 1-4 Nm Range Using Polymeric Stabilizers. *J. Am. Chem. Soc.* **2005**, *127* (47), 16398–16399.

(22) Turkevich, J.; Stevenson, P. C.; Hillier, J. A Study of the Nucleation and Growth Processes in the Synthesis of Colloidal Gold. *Discuss. Faraday Soc.* **1951**, *11* (c), 55.

(23) Frens. © 1973 Nature Publishing Group. *Nat. Phys. Sci.* **1973**, *241*, 20.

(24) Masuda, H.; Tanaka, H.; Baba, N. Preparation of Porous Material by Replacing Microstructure of Anodic Alumina Film with Metal. *Chemistry Letters*. 1990, 621.

(25) Martin, C. R. Template Synthesis of Polymeric and Metal Microtubules. *Adv. Mater.* **1991**, *3* (9), 457–459.

(26) Nikoobakht, B.; El-Sayed, M. A. Preparation and Growth Mechanism of Gold Nanorods Using Seed-Mediated Growth Method. *Chem. Mater.* **2003**, *15* (10), 1957.

(27) Jana, N. R.; Gearheart, L.; Murphy, C. J. Seed-Mediated Growth Approach for Shape-Controlled Synthesis of Spheroidal and Rod-like Gold Nanoparticles Using a Surfactant Template. *Adv. Mater.* **2001**, *13* (18), 1389–1393.

(28) Burrows, N. D.; Vartanian, A. M.; Abadeer, N. S.; Grzincic, E. M.; Jacob, L. M.; Lin, W.; Li, J.; Dennison, J. M.; Hinman, J. G.; Murphy, C. J. Anisotropic Nanoparticles and Anisotropic Surface Chemistry. *J. Phys. Chem. Lett.* **2016**, *7* (4), 632–641.

(29) Wu, H. L.; Chen, C. H.; Huang, M. H. Seed-Mediated Synthesis of Branched Gold Nanocrystals Derived from the Side Growth of Pentagonal Bipyramids and the Formation of Gold Nanostars. *Chem. Mater.* **2009**, *21* (1), 110–114.

(30) Meroni, D.; Ardizzone, S. Preparation and Application of Hybrid Nanomaterials. *Nanomaterials* **2018**, *8* (11), 891.

(31) Díaz, U.; Brunel, D.; Corma, A. Catalysis Using Multifunctional Organosiliceous Hybrid Materials. *Chem. Soc. Rev.* **2013**, *42* (9), 4083–4097.

(32) Nicol, J. R.; Dixon, D.; Coulter, J. A. Gold Nanoparticle Surface Functionalization: A Necessary Requirement in the Development of Novel Nanotherapeutics. *Nanomedicine* **2015**, *10* (8), 1315–1326.

(33) Cobley, C. M.; Chen, J.; Chul Cho, E.; Wang, L. V.; Xia, Y. Gold Nanostructures: A Class of Multifunctional Materials for Biomedical Applications. *Chem. Soc. Rev.* **2011**, *40* (1), 44–56.

(34) Jans, H.; Huo, Q. Gold Nanoparticle-Enabled Biological and Chemical Detection and Analysis. *Chem. Soc. Rev.* **2012**, *41* (7), 2849–2866.

(35) Jeong, H. H.; Choi, E.; Ellis, E.; Lee, T. C. Recent Advances in Gold Nanoparticles for Biomedical Applications: From Hybrid Structures to Multi-Functionality. *J. Mater. Chem. B* **2019**, *7* (22), 3480–3496.

(36) Kalele, S.; Gosavi, S. W.; Urban, J.; Kulkarni, S. K. Nanoshell Particles: Synthesis, Properties and Applications. *Curr. Sci.* **2006**, *91* (8), 1038–1052.

(37) Zhao, J.; Xu, P.; Li, Y.; Wu, J.; Xue, J.; Zhu, Q.; Lu, X.; Ni, W. Direct Coating of Mesoporous Titania on CTAB-Capped Gold Nanorods. *Nanoscale* **2015**, *8*, 5417.

(38) Fales, A. M.; Yuan, H.; Vo-Dinh, T. Silica-Coated Gold Nanostars for Combined Surface-Enhanced Raman Scattering (SERS) Detection and Singlet-Oxygen Generation: A Potential Nanoplatform for Theranostics. *Langmuir* **2011**, *27* (19), 12186–12190.

(39) Prodan, E.; Radloff, C.; Halas, N. J.; Nordlander, P. A Hybridization Model for the Plasmon Response of Complex Nanostructures. *Science.* **2003**, *302* (5644), 419–422.

(40) Das, P.; Fatehbasharzad, P.; Colombo, M.; Fiandra, L.; Prosperi, D. Multifunctional Magnetic Gold Nanomaterials for Cancer. *Trends Biotechnol.* **2019**, *37* (9), 995–1010.

(41) Halas, N. Playing with Plasmons: Tuning the Optical Resonant Properties of Metallic Nanoshells. *MRS Bull.* **2005**, *30* (5), 362–367.

(42) Wang, C.; Xu, C.; Zeng, H.; Sun, S. Recent Progress in Syntheses and Applications of Dumbbell-like Nanoparticles. *Adv. Mater.* **2009**, *21* (30), 3045–3052.

(43) Reguera, J.; Jiménez De Aberasturi, D.; Henriksen-Lacey, M.; Langer, J.; Espinosa, A.; Szczupak, B.; Wilhelm, C.; Liz-Marzán, L. M. Janus Plasmonic-Magnetic Gold-Iron Oxide Nanoparticles as Contrast Agents for Multimodal Imaging. *Nanoscale* **2017**, *9* (27), 9467–9480.

(44) Wang, C.; Yin, H.; Dai, S.; Sun, S. A General Approach to Noble Metal-Metal Oxide Dumbbell Nanoparticles and Their Catalytic Application for CO Oxidation. *Chem. Mater.* **2010**, *22* (10), 3277–3282.

(45) Ruiyi, L.; Juanjuan, Z.; Zhouping, W.; Zaijun, L.; Junkang, L.; Zhiguo, G.; Guangli, W. Novel Graphene-Gold Nanohybrid with Excellent Electrocatalytic Performance for the Electrochemical Detection of Glucose. *Sensors Actuators, B Chem.* **2015**, *208*, 421.

(46) Feygenson, M.; Bauer, J. C.; Gai, Z.; Marques, C.; Aronson, M. C.; Teng, X.; Su, D.; Stanic, V.; Urban, V. S.; Beyer, K. A.; et al. Exchange Bias Effect in Au-Fe_3O_4 Dumbbell Nanoparticles Induced by the Charge Transfer from Gold. *Phys. Rev. B - Condens. Matter Mater. Phys.* **2015**, *92* (5), 054416.

(47) Leung, K. C. F.; Xuan, S.; Zhu, X.; Wang, D.; Chak, C. P.; Lee, S. F.; Ho, W. K. W.; Chung, B. C. T. Gold and Iron Oxide Hybrid Nanocomposite Materials. *Chem. Soc. Rev.* **2012**, *41* (5), 1911–1928.

(48) Nguyen, T. T.; Mammeri, F.; Ammar, S. Iron Oxide and Gold Based Magneto-Plasmonic Nanostructures for Medical Applications : A Review. *Nanomaterials* **2018**, *8* (3), 149.

(49) Pal kaushik. *Hybrid Nanocomposites Fundamentals, Synthesis, and Applications*; **2013**.

(50) Kwizera, E. A.; Chaffin, E.; Shen, X.; Chen, J.; Zou, Q.; Wu, Z.; Gai, Z.; Bhana, S.; Oconnor, R.; Wang, L.; et al. Size- and Shape-Controlled Synthesis and Properties of Magnetic-Plasmonic Core-Shell Nanoparticles. *J. Phys. Chem. C* **2016**, *120* (19), 10530–10546.

(51) Gouma, P.-I. *Hybrid Nanomaterials*; **2009**.

(52) Yang, D.; Pang, X.; He, Y.; Wang, Y.; Chen, G.; Wang, W.; Lin, Z. Precisely Size-Tunable Magnetic/Plasmonic Core/Shell Nanoparticles with Controlled Optical Properties. *Angew. Chem. Int. Ed.* **2015**, *54* (41), 12091–12096.

(53) Fantechi, E.; Roca, A.; Sepúlveda, B.; Torruella, P.; Estradé, S.; Peiró, F.; Coy, E.; Jurga, S.; Bastús, N.; Nogués, J.; et al. Seeded Growth Synthesis of Au–Fe_3O_4 Heterostructured Nanocrystals: Rational Design and Mechanistic Insights. *Chem. Mater.* **2017**, *29* (9), 4022–4035.

(54) Kamei, K.; Mukai, Y.; Kojima, H.; Yoshikawa, T.; Yoshikawa, M.; Kiyohara, G.; Yamamoto, T. A.; Yoshioka, Y.; Okada, N.; Seino, S.; et al. Direct Cell Entry of Gold/Iron-Oxide Magnetic Nanoparticles in Adenovirus Mediated Gene Delivery. *Biomaterials* **2009**, *30* (9), 1809–1814.

(55) Espinosa, A.; Bugnet, M.; Radtke, G.; Neveu, S.; Botton, G. A.; Wilhelm, C.; Abou-Hassan, A. Can Magneto-Plasmonic Nanohybrids Efficiently Combine Photothermia with Magnetic Hyperthermia? *Nanoscale* **2015**, *7* (45), 18872–18877.

(56) Quintana, C.; Cifuentes, M. P.; Humphrey, M. G. Transition Metal Complex/Gold Nanoparticle Hybrid Materials. *Chem. Soc. Rev.* **2020**, *49* (8), 2316–2341.

(57) Vegas, V. G.; Villar-Alonso, M.; Gómez-García, C. J.; Zamora, F.; Amo-Ochoa, P. Direct Formation of Sub-Micron and Nanoparticles of a Bioinspired Coordination Polymer Based on Copper with Adenine. *Polymers (Basel).* **2017**, *9* (11), 565.

(58) Hoskins, B. F.; Robson, R. Design and Construction of a New Class of Scaffolding-like Materials Comprising Infinite Polymeric Frameworks of 3D-Linked Molecular Rods. A Reappraisal of the $Zn(CN)_2$ and $Cd(CN)_2$ Structures and the Synthesis and Structure of the Diamond-Related Framework. *J. Am. Chem. Soc.* **1990**, *112* (4), 1546–1554.

(59) Robson, R.; Abrahams, B. F.; Batten, S. R.; Gable, R. W.; Hoskins, B. F.; Liu, J. Crystal Engineering of Novel Materials Composed of Infinite Two- and Three-Dimensional Frameworks. **1992**, 256–273.

(60) Wells, A. Three-Dimensional Nets and Polyhe. *Bull. Am. Math. Soc.* **1977**, *84* (3), 466.

(61) Chen, X. M. Assembly Chemistry of Coordination Polymers. *Mod. Inorg. Synth. Chem.* **2011**, 207–225.

(62) Dzhardimalieva, G. I.; Uflyand, I. E. Design and Synthesis of Coordination Polymers

with Chelated Units and Their Application in Nanomaterials Science. *RSC Adv.* **2017**, *7* (67), 42242–42288.

(63) Batten, S. R.; Neville, S. M.; Turner, D. R. *Coordination Polymers: Design, Analysis and Application*; Royal Society of Chemistry, **2009**.

(64) Choi, K. M.; Kim, D.; Rungtaweevoranit, B.; Trickett, C. A.; Barmanbek, J. T. D.; Alshammari, A. S.; Yang, P.; Yaghi, O. M. Plasmon-Enhanced Photocatalytic CO2conversion within Metal-Organic Frameworks under Visible Light. *J. Am. Chem. Soc.* **2017**, *139* (1), 356−362.

(65) Rungtaweevoranit, B.; Baek, J.; Araujo, J. R.; Archanjo, B. S.; Choi, K. M.; Yaghi, O. M.; Somorjai, G. A. Copper Nanocrystals Encapsulated in Zr-Based Metal-Organic Frameworks for Highly Selective CO_2 Hydrogenation to Methanol. *Nano Lett.* **2016**, *16* (12), 7645–7649.

(66) Osterrieth, J. W. M.; Wright, D.; Noh, H.; Kung, C. W.; Vulpe, D.; Li, A.; Park, J. E.; Van Duyne, R. P.; Moghadam, P. Z.; Baumberg, J. J.; et al. Core-Shell Gold Nanorod@Zirconium-Based Metal-Organic Framework Composites as in Situ Size-Selective Raman Probes. *J. Am. Chem. Soc.* **2019**, *141* (9), 3893–3900.

(67) Cao, L. M.; Lu, D.; Zhong, D. C.; Lu, T. B. Prussian Blue Analogues and Their Derived Nanomaterials for Electrocatalytic Water Splitting. *Coord. Chem. Rev.* **2020**, *407*, 213156.

(68) Maurin-Pasturel, G.; Long, J.; Guari, Y.; Godiard, F.; Willinger, M. G.; Guerin, C.; Larionova, J. Nanosized Heterostructures of Au@Prussian Blue Analogues: Towards Multifunctionality at the Nanoscale. *Angew. Chemie - Int. Ed.* **2014**, *53* (15), 3872.

(69) Catala, L.; Mallah, T. Nanoparticles of Prussian Blue Analogs and Related Coordination Polymers: From Information Storage to Biomedical Applications. *Coord. Chem. Rev.* **2017**, *346*, 32–61.

(70) Verdaguer, M.; Girolami, G. S. *Magnetic Prussian Blue Analogues*; **2005**; Vol. 36.

(71) Simonov, A.; De Baerdemaeker, T.; Boström, H. L. B.; Ríos Gómez, M. L.; Gray, H. J.; Chernyshov, D.; Bosak, A.; Bürgi, H. B.; Goodwin, A. L. Hidden Diversity of Vacancy Networks in Prussian Blue Analogues. *Nature* **2020**, *578* (7794), 256–260.

(72) Evangelisti, M.; Manuel, E.; Affronte, M.; Okubo, M.; Train, C.; Verdaguer, M. Vacancy-Driven Magnetocaloric Effect in Prussian Blue Analogues. *J. Magn. Magn. Mater.* **2007**, *316*, 569–571.

(73) Yu, Z. Y.; Duan, Y.; Liu, J. D.; Chen, Y.; Liu, X. K.; Liu, W.; Ma, T.; Li, Y.; Zheng, X. S.; Yao, T.; et al. Unconventional CN Vacancies Suppress Iron-Leaching in Prussian Blue Analogue Pre-Catalyst for Boosted Oxygen Evolution Catalysis. *Nat. Commun.* **2019**, *10* (1), 2799.

(74) Fitta, M.; Prima-Garcia, H.; Czaja, P.; Korzeniak, T.; Krupiński, M.; Wojtyniak, M.; Bałanda, M. Magnetic and Magneto-Optical Properties of Nickel Hexacyanoferrate/Chromate Thin Films. *RSC Adv.* **2017**, *7* (3), 1382–1386.

(75) Zhou, P.; Xue, D.; Luo, H.; Chen, X. Fabrication, Structure, and Magnetic Properties of Highly Ordered Prussian Blue Nanowire Arrays. *Nano Lett.* **2002**, *2* (8), 845–847.

(76) Felts, A. C.; Slimani, A.; Cain, J. M.; Andrus, M. J.; Ahir, A. R.; Abboud, K.; Meisel, M. W.; Boukheddaden, K.; Talham, D. R. Control of the Speed of a Light–Induced Spin Transition through Mesoscale Core-Shell Architecture. *J. Am. Chem. Soc.* **2018**, *140*, 5814–5824.

(77) Qin, Z.; Li, Y.; Gu, N. Progress in Applications of Prussian Blue Nanoparticles in Biomedicine. *Adv. Healthc. Mater.* **2018**, *7* (20), 1800347.

(78) Ferlay, S.; Mallah, T.; Ouahès, R.; Veillet, P.; Verdaguer, M. A Room-Temperature Organometallic Magnet Based on Prussian Blue. *Nature* **1995**, *378* (6558), 701–703.

(79) Garde, R.; Villain, F.; Verdaguer, M. Molecule-Based Room-Temperature Magnets: Catalytic Role of V(III) in the Synthesis of Vanadium-Chromium Prussian Blue Analogues. *J. Am. Chem. Soc.* **2002**, *124* (35), 10531–10538.

(80) Sato, O.; Iyoda, T.; Fujishima, A.; Hashimoto, K. Photoinduced Magnetization of a Cobalt-Iron Cyanide. *Science* **1996**, *272* (5262), 704–705.

(81) Paolella, A.; Faure, C.; Timoshevskii, V.; Marras, S.; Bertoni, G.; Guerfi, A.; Vijh, A.; Armand, M.; Zaghib, K. A Review on Hexacyanoferrate-Based Materials for Energy Storage and Smart Windows: Challenges and Perspectives. *J. Mater. Chem. A* **2017**, *5* (36), 18919–18932.

(82) Morant-Giner, M.; Sanchis-Gual, R.; Romero, J.; Alberola, A.; García-Cruz, L.; Agouram, S.; Galbiati, M.; Padial, N. M.; Waerenborgh, J. C.; Martí-Gastaldo, C.; et al. Prussian Blue@MoS_2 Layer Composites as Highly Efficient Cathodes for Sodium- and Potassium-Ion Batteries. *Adv. Funct. Mater.* **2018**, *28*, 1706125.

(83) Han, L.; Tang, P.; Reyes-Carmona, Á.; Rodríguez-García, B.; Torréns, M.; Morante, J. R.; Arbiol, J.; Galan-Mascaros, J. R. Enhanced Activity and Acid PH Stability of

Prussian Blue-Type Oxygen Evolution Electrocatalysts Processed by Chemical Etching. *J. Am. Chem. Soc.* **2016**, *138* (49), 16037–16045.

(84) Fu, G.; Liu, W.; Feng, S.; Yue, X. Prussian Blue Nanoparticles Operate as a New Generation of Photothermal Ablation Agents for Cancer Therapy. *Chem. Commun.* **2012**, *48* (94), 11567.

(85) Sato, O. Reversible Photoinduced Magnetization. *J. Electrochem. Soc.* **1997**, *144* (1), L11.

(86) Crespilho, F. N.; Zucolotto, V.; Brett, C. M. A.; Oliveira, O. N.; Nart, F. C. Enhanced Charge Transport and Incorporation of Redox Mediators in Layer-by-Layer Films Containing PAMAM-Encapsulated Gold Nanoparticles. *J. Phys. Chem. B* **2006**, *110* (35), 17478–17483.

(87) Xue, M. H.; Xu, Q.; Zhou, M.; Zhu, J. J. In Situ Immobilization of Glucose Oxidase in Chitosan-Gold Nanoparticle Hybrid Film on Prussian Blue Modified Electrode for High-Sensitivity Glucose Detection. *Electrochem. commun.* **2006**, *8* (9), 1468–1474.

(88) Li, N. B.; Park, J. H.; Park, K.; Kwon, S. J.; Shin, H.; Kwak, J. Characterization and Electrocatalytic Properties of Prussian Blue Electrochemically Deposited on Nano-Au/PAMAM Dendrimer-Modified Gold Electrode. *Biosens. Bioelectron.* **2008**, *23* (10), 1519–1526.

(89) Kumar, S. S.; Joseph, J.; Phani, K. L. Novel Method for Deposition of Gold-Prussian Blue Nanocomposite Films Induced by Electrochemically Formed Gold Nanoparticles: Characterization and Application to Electrocatalysis. *Chem. Mater.* **2007**, *19* (19), 4722–4730.

(90) Qiu, J. D.; Peng, H. Z.; Liang, R. P.; Li, J.; Xia, X. H. Synthesis, Characterization, and Immobilization of Prussian Blue-Modified Au Nanoparticles: Application to Electrocatalytic Reduction of H_2O_2. *Langmuir* **2007**, *23* (4), 2133–2137.

(91) Hong, C.; Yuan, R.; Chai, Y.; Zhuo, Y. Amperometric Immunosensor for the Determination of 1-Fetoprotein Based on Core-Shell-Shell Prussian Blue-BSA-Nanogold Functionalized Interface. *Electroanalysis* **2008**, *20* (20), 2185–2191.

(92) Dou, Y.; Li, X.; Yang, W.; Guo, Y.; Wu, M.; Liu, Y.; Li, X.; Zhang, X.; Chang, J. PB@Au Core−satellite Multifunctional Nanotheranostics for Magnetic Resonance and Computed Tomography Imaging in Vivo and Synergetic Photothermal and Radiosensitive Therapy. *ACS Appl. Mater. Interfaces* **2017**, *9* (2), 1236–1272.

(93) Fu, G.; Liu, W.; Li, Y.; Jin, Y.; Jiang, L.; Liang, X.; Feng, S.; Dai, Z. Magnetic Prussian Blue Nanoparticles for Targeted Photothermal Therapy under Magnetic Resonance Imaging Guidance. *Bioconjug. Chem.* **2014**, *25* (9), 1655–1663.

(94) Larionova, J.; Maurin-Pasturel, G.; Long, J.; Palacios, M. A.; Guérin, C.; Charnay, C.; Willinger, M.-G.; Trifonov, A. A.; Guari, Y. Engineered Au Core@Prussian Blue Analogues Shell Nanoheterostructures: Their Magnetic and Optical Properties. *Chem. - A Eur. J.* **2017**, *23* (31), 7483–7496.

(95) Maurin-Pasturel, G.; Mamontova, E.; Palacios, M. A.; Long, J.; Allouche, J.; Dupin, J. C.; Guari, Y.; Larionova, J. Gold@Prussian Blue Analogue Core-Shell Nanoheterostructures: Their Optical and Magnetic Properties. *Dalt. Trans.* **2019**, *48* (18), 6205–6216.

(96) Kahn, O.; Kröber, J.; Jay, C. Spin Transition Molecular Materials for Displays and Data Recording. *Adv. Mater.* **1992**, *4* (11), 718–728.

(97) Kahn, O. Spin-Crossover Molecular Materials. *Curr. Opin. Solid State Mater. Sci.* **1996**, *1* (4), 547–554.

(98) Hogue, R. W.; Singh, S.; Brooker, S. Spin Crossover in Discrete Polynuclear Iron(Ii) Complexes. *Chem. Soc. Rev.* **2018**, *47* (19), 7303–7338.

(99) Prins, F.; Monrabal-Capilla, M.; Osorio, E. A.; Coronado, E.; Van Der Zant, H. S. J. Room-Temperature Electrical Addressing of a Bistable Spin-Crossover Molecular System. *Adv. Mater.* **2011**, *23* (13), 1545–1549.

(100) Pinilla-Cienfuegos, E.; Parra, J.; Brimont, A.; Olivares, I.; Sanchis-Gual, R.; Torres-Cavanillas, R.; Sanchis, P. New Molecular-Based Materials for Enabling Electro-Optical Bistability in the Silicon Photonics Platform. *Int. Conf. Transparent Opt. Networks* **2019**, *2019-July*..

(101) Molnár, G.; Salmon, L.; Nicolazzi, W.; Terki, F.; Bousseksou, A. Emerging Properties and Applications of Spin Crossover Nanomaterials. *J. Mater. Chem. C* **2014**, *2* (8), 1360–1366.

(102) Coronado, E.; Giménez-Marqués, M.; Mínguez Espallargas, G.; Rey, F.; Vitórica-Yrezábal, I. J. Spin-Crossover Modification through Selective CO2 Sorption. *J. Am. Chem. Soc.* **2013**, *135* (43), 15986–15989.

(103) Garcia, Y.; Niel, V.; Carmen Muñoz, M.; Real, J. A. Spin Crossover in 1D, 2D and 3D Polymeric Fe(II) Networks. *Top. Curr. Chem.* **2004**, *233*, 229–257.

(104) Muñoz, M. C.; Real, J. A. Thermo-, Piezo-, Photo- and Chemo-Switchable Spin Crossover Iron(II)-Metallocyanate Based Coordination Polymers. *Coord. Chem. Rev.* **2011**, *255* (17–18), 2068–2093.

(105) Muñoz, M. C.; Real, J. A.; Halcrow, M. A. Polymeric Spin-Crossover Materials. In *Spin-Crossover Materials Properties and Applications*; Wiley, **2013**; 121–138.

(106) Galán-Mascarós, J. R.; Coronado, E.; Forment-Aliaga, A.; Monrabal-Capilla, M.; Pinilla-Cienfuegos, E.; Ceolin, M. Tuning Size and Thermal Hysteresis in Bistable Spin Crossover Nanoparticles. *Inorg. Chem.* **2010**, *49* (12), 5706–5714.

(107) Giménez-Marqués, M.; García-Sanz de Larrea, M. L.; Coronado, E. Unravelling the Chemical Design of Spin-Crossover Nanoparticles Based on Iron(Ii)–Triazole Coordination Polymers: Towards a Control of the Spin Transition. *J. Mater. Chem. C* **2015**, *3* (30), 7946–7953.

(108) Quintero, C. M.; Félix, G.; Suleimanov, I.; Costa, J. S.; Molnár, G.; Salmon, L.; Nicolazzi, W.; Bousseksou, A. Hybrid Spin-Crossover Nanostructures. *Beilstein J. Nanotechnol.* **2014**, *5* (1), 2230–2239.

(109) Forestier, T.; Mornet, S.; Daro, N.; Nishihara, T.; Mouri, S. I.; Tanaka, K.; Fouché, O.; Freysz, E.; Létard, J. F. Nanoparticles of Iron(II) Spin-Crossover. *Chem. Commun.* **2008**, No. 36, 4327–4329.

(110) Tobon, Y. A.; Etrillard, C.; Nguyen, O.; Létard, J. F.; Faramarzi, V.; Dayen, J. F.; Doudin, B.; Bassani, D. M.; Guillaume, F. Resonance Raman Study of Spin-Crossover $[Fe(Htrz)_2(Trz)](BF_4)\cdot H_2O$ Particles Coated with Gold. *Eur. J. Inorg. Chem.* **2012**, *2* (35), 5837–5842.

(111) Suleimanov, I.; Sánchez Costa, J.; Molnár, G.; Salmon, L.; Bousseksou, A. The Photo-Thermal Plasmonic Effect in Spin Crossover@silica–Gold Nanocomposites. *Chem. Commun.* **2014**, *50* (86), 13015–13018.

(112) Qiu, D.; Gu, L.; Sun, X. L.; Ren, D. H.; Gu, Z. G.; Li, Z. $SCO@SiO_2@Au$ Core-Shell Nanomaterials: Enhanced Photo-Thermal Plasmonic Effect and Spin-Crossover Properties. *RSC Adv.* **2014**, *4* (106), 61313–61319.

(113) Moulet, L.; Daro, N.; Mornet, S.; Vilar-Vidal, N.; Chastanet, G.; Guionneau, P. Grafting of Gold onto Spin-Crossover Nanoparticles: SCO@Au. *Chem. Commun.* **2016**, *52* (90), 13213–13216.

(114) Li, Z.-H.; Wang, Y.-X.; Han, W.-K.; Zhu, W.; Li, T.; Li, Z.; Ren, X.; Gu, Z.-G. Integrating

Spin-Crossover Nanoparticles with Silver Nanowires: Toward Magnetic and Conductive Bifunctional Nanomaterials. *New J. Chem.* **2017**, *41* (18), 10062–10068.

(115) Palluel, M.; Tran, N. M.; Daro, N.; Buffière, S.; Mornet, S.; Freysz, E.; Chastanet, G. The Interplay between Surface Plasmon Resonance and Switching Properties in Gold@Spin Crossover Nanocomposites. *Adv. Funct. Mater.* **2020**, *30* (17), 2000447.

(116) Zhou, H. C.; Long, J. R.; Yaghi, O. M. Introduction to Metal-Organic Frameworks. *Chem. Rev.* **2012**, *112* (2), 673–674.

(117) Baumann, A. E.; Burns, D. A.; Liu, B.; Thoi, V. S. Metal-Organic Framework Functionalization and Design Strategies for Advanced Electrochemical Energy Storage Devices. *Commun. Chem.* **2019**, *2* (1), 86.

(118) Anik, Ü.; Timur, S.; Dursun, Z. Metal Organic Frameworks in Electrochemical and Optical Sensing Platforms: A Review. *Microchim. Acta* **2019**, *186* (3), 18–24.

(119) Mason, J. A.; Veenstra, M.; Long, J. R. Evaluating Metal-Organic Frameworks for Natural Gas Storage. *Chem. Sci.* **2014**, *5* (1), 32–51.

(120) Liu, Y.; He, L.; Liu, Y.; Liu, J.; Xiong, Y.; Zheng, J.; Tang, Z. Core-Shell Noble-Metal@metal-Organic-Framework Nanoparticles with Highly Selective Sensing Property. *Angew. Chem. Int. Ed.* **2013**, *52* (13), 3741–3745.

(121) Nh, U.-; Hinde, C. S.; Webb, W. R.; Chew, B. K. J.; Tan, R.; Zhang, W.; Andy, T. S.; Raja, R. For Selective Tandem Catalytic Reactions. *Chem. Commun.* **2016**, *52*, 6557–6560.

(122) Koh, C. S. L.; Lee, H. K.; Han, X.; Sim, H. Y. F.; Ling, X. Y. Plasmonic Nose: Integrating the MOF-Enabled Molecular Preconcentration Effect with a Plasmonic Array for Recognition of Molecular-Level Volatile Organic Compounds. *Chem. Commun.* **2018**, *54* (20), 2546–2549.

(123) Lin, W.; Murphy, C. J. A Demonstration of Le Chatelier's Principle on the Nanoscale. *ACS Cent. Sci.* **2017**, *3* (10), 1096–1102.

(124) Hermes, S.; Schröter, M. K.; Schmid, R.; Khodeir, L.; Muhler, M.; Tissler, A.; Fischer, R. W.; Fischer, R. A. Metal@MOF: Loading of Highly Porous Coordination Polymers Host Lattices by Metal Organic Chemical Vapor Deposition. *Angew. Chem. Int. Ed.* **2005**, *44* (38), 6237–6241.

(125) Jiang, H. L.; Liu, B.; Akita, T.; Haruta, M.; Sakurai, H.; Xu, Q. Au@ZIF-8: CO Oxidation over Gold Nanoparticles Deposited to Metal-Organic Framework. *J. Am. Chem. Soc.*

2009, *131* (32), 11302–11303.

(126) Gu, X.; Lu, Z. H.; Jiang, H. L.; Akita, T.; Xu, Q. Synergistic Catalysis of Metal-Organic Framework-Immobilized Au-Pd Nanoparticles in Dehydrogenation of Formic Acid for Chemical Hydrogen Storage. *J. Am. Chem. Soc.* **2011**, *133* (31), 11822–11825.

(127) Meilikhov, M.; Yusenko, K.; Esken, D.; Turner, S.; Van Tendeloo, G.; Fischer, R. A. Metals@MOFs - Loading MOFs with Metal Nanoparticles for Hybrid Functions. *European Journal of Inorganic Chemistry*. **2010**, 3701–3714.

(128) Hu, P.; Morabito, J. V.; Tsung, C. K. Core-Shell Catalysts of Metal Nanoparticle Core and Metal-Organic Framework Shell. *ACS Catal.* **2014**, *4* (12), 4409–4419.

(129) He, L.; Liu, Y.; Liu, J.; Xiong, Y.; Zheng, J.; Liu, Y. Core – Shell Noble-Metal @ Metal-Organic-Framework Nanoparticles with Highly Selective Sensing Property. Angewandte. *Angew. Chemie Int. Ed.* **2013**, *52*, 3741–3745.

(130) Khaletskaya, K.; Reboul, J.; Meilikhov, M.; Nakahama, M.; Diring, S.; Tsujimoto, M.; Isoda, S.; Kim, F.; Kamei, K. I.; Fischer, R. A.; et al. Integration of Porous Coordination Polymers and Gold Nanorods into Core-Shell Mesoscopic Composites toward Light-Induced Molecular Release. *J. Am. Chem. Soc.* **2013**, *135* (30), 10998–11005.

(131) Hu, P.; Zhuang, J.; Chou, L. Y.; Lee, H. K.; Ling, X. Y.; Chuang, Y. C.; Tsung, C. K. Surfactant-Directed Atomic to Mesoscale Alignment: Metal Nanocrystals Encased Individually in Single-Crystalline Porous Nanostructures. *J. Am. Chem. Soc.* **2014**, *136* (30), 10561–10564.

(132) Zheng, G.; de Marchi, S.; López-Puente, V.; Sentosun, K.; Polavarapu, L.; Pérez-Juste, I.; Hill, E. H.; Bals, S.; Liz-Marzán, L. M.; Pastoriza-Santos, I.; et al. Encapsulation of Single Plasmonic Nanoparticles within ZIF-8 and SERS Analysis of the MOF Flexibility. *Small* **2016**, *12*, 3935–3943.

(133) Osterrieth, J. W. M.; Wright, D.; Noh, H.; Kung, C. W.; Vulpe, D.; Li, A.; Park, J. E.; Van Duyne, R. P.; Moghadam, P. Z.; Baumberg, J. J.; et al. Core-Shell Gold Nanorod@Zirconium-Based Metal-Organic Framework Composites as in Situ Size-Selective Raman Probes. *J. Am. Chem. Soc.* **2019**, *141* (9), 3893–3900.

(134) Hinman, J. G.; Turner, J. G.; Hofmann, D. M.; Murphy, C. J. Layer-by-Layer Synthesis of Conformal Metal-Organic Framework Shells on Gold Nanorods. *Chem. Mater.* **2018**, *30* (20), 7255–7261.

Chapter 2

Magneto-plasmonic nanostructures based on Prussian Blue nanocrystals decorated with Au nanoparticles

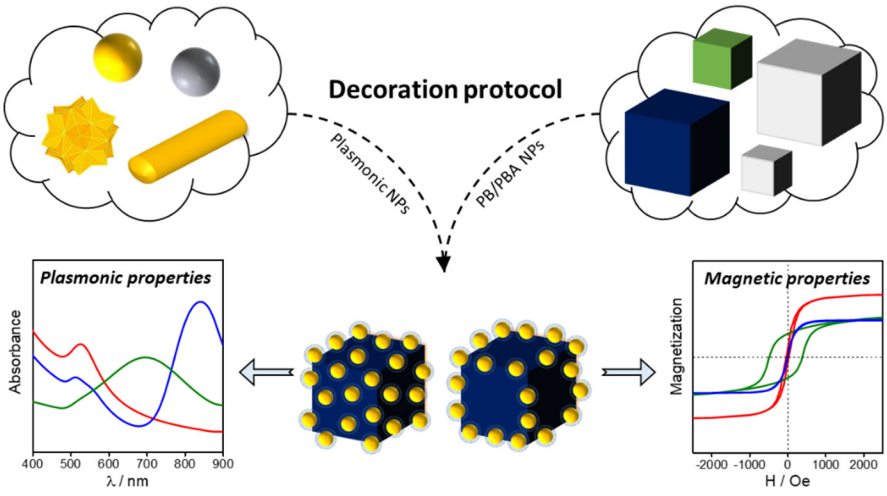

2.1 Introduction

Magneto-plasmonic nanoparticles (NPs) are one of the emerging multifunctional materials in the fields of physics[1] and nanomedicine.[2] Still, most of the works in this topic have been focused on the design of core@shell NPs formed by an inorganic magnetic core (typically a metal oxide) and an Au plasmonic shell. In this line, an exciting possibility is that of using as the magnetic component a molecule-based magnet instead of a pure inorganic one since the former can provide some advantages in terms of chemical versatility, tunability of the properties and optical transparency.[3] In spite of these features, this possibility has remained so far almost unexplored.

As already mentioned in Chapter 1, Prussian Blue Analogues (PBAs) are materials that have gained attention especially due to their interesting magnetic properties.[3–5] PBAs offer several advantages with respect to other conventional inorganic materials and semiconductors because of their processability and chemical versatility that permits a high tunability of their magnetic and optical properties.[3] Their magnetic and optical properties in combination with their optical transparency in the visible region make them excellent candidates for magneto-optical (MO) applications.[6]

MO effect is based on the interaction between light and the optical absorption properties of magnetically ordered materials. Specifically, a MO effect is a phenomenon where an electromagnetic wave interacts and/or propagates through a magnetic surface at different speeds as the permittivity changes corresponding to left and right rotating elliptical polarizations. Accordingly, the light changes its polarization when interacting with the surface of the magnetic material. Typically, when a beam of light propagates through a material, the electric field of the light will induce a motion of the electrons in the medium. In the absence of an external magnetic field, the right and left circularly polarized light drives the electrons into respective left and right circular motions with the same radius. Taking into account that the electric dipole moment is proportional to the radius of the circular orbit, no difference between dielectric constant for each type of circularly polarized electromagnetic waves is detected. In this situation, no MO effect shows up. On the contrary, in the presence of an external magnetic field, an additional Lorentz force

act on each electron, inducing a different radius for each circularly polarized component. Consequently, a MO response then shows up.[7,8] Notice that the MO effect is named differently depending on whether the light is being reflected or transmitted through the sample. Therefore, if the light is being reflected, the effect is called the magneto-optical Kerr effect and if the light is transmitted, it is called the Faraday effect.[1]

In this context, plasmonic materials lead to an important enhancement of the MO activity thanks to the plasmon-induced phase modification of the reflected or transmitted light.[9] Interestingly, LSPR effects are so strong that it has been possible to measure a substantial MO activity in plasmonic nanostructures of pure noble metals due to the increment of the magnetic Lorentz force induced by the large collective movement of the conduction electrons in the nanostructures after the LSPR excitation.[10,11] Considering the fact that the general requirement for maximizing the LSPR enhancement effect on the MO activity is the coupling of the plasmon band with the dielectric (more specifically, the MO) response of the magnetic material,[12] the wise selection of both the plasmonic NP and the magnetic PBA compound is crucial.

The most popular example of magneto-plasmonic NPs based on a PBA nanostructure can be formulated as Au@PB. However, the chemical approach required to prepare the core@shell hybrid nanostructures is quite limited since it is restricted to use as shell the PB (FeFe), or the reduced form of the NiFe and CoFe PBA derivatives, only.[13–16] These derivatives are weakly magnetic since they undergo long-range magnetic ordering at low temperatures only (T_c below 5 K). Hence, they are quite limited to investigate the enhanced MO properties that may arise in these systems as a result of the coupling of the magnetic component with the plasmonic one.[11,12] To overcome this limitation, other PBAs exhibiting high-T_c values need to be grown directly on the Au core. Nevertheless, this requires the insertion of a NiFe layer in between the Au and the PBA magnetic shell. Obviously, this strongly limits the interaction of this magnetic layer with the plasmonic core, thus reducing the intensity of the magneto-plasmonic effects.[17] A second limitation of this procedure is that it is restricted to spherical Au NPs since anisotropic shapes (such as nanorods or nanostars) have shown to be too reactive towards the cyanide molecule. Still, these limitations have not been too problematic for using this kind of

nanostructures in biomedicine (dual function NPs for imaging, photothermal therapy, or biosensing)[18,19] and electrocatalysis.[20,21]

Hereby, we propose a simple and versatile approach that allows synthesizing hybrid Au-PBA nanostructures, which are different from the core@shell one. These nanostructures are formed by a PBA cubic NP surrounded by Au NPs of different shapes and connected to the PBA surface through a bridging molecule. Owing to the possibility of using different plasmonic NPs, the developed protocol allows tuning the plasmon band position in the whole range of the visible spectrum. Here these possibilities will be illustrated by using as magnetic PBA component the $Ni^{II}Cr^{III}$ derivative. These results have been published in Chemical Communication.[22]

2.2 Results and discussion

The synthetic strategy for the obtention of the Au-PBA heterostructures using NPs of the NiCr magnetic PBA derivative is illustrated in Figure 2.1. These PBA NPs are negatively charged, stable in water in the absence of any coating agent and may have a T_C as large as 90 K in its bulk form.[23] Additionally, they are colorless which permits a better study of the plasmonic properties once the heterostructure is formed. These PBAs were obtained by slowly mixing the corresponding precursors (equimolar 10^{-3} M aqueous solutions of $K_3[Cr(CN)_6]$ and $NiCl_2 \cdot (H_2O)_6$) under vigorous stirring at room temperature. Cubic shape NPs of $K_{0.07}Ni[Cr(CN)_6]_{0.69}$ were obtained with a mean size of 140 ± 40 nm and a negative ζ-potential value of -37 ± 11 mV. We chose this size as they are big enough to clearly observe the Au decoration while they exhibit high colloidal stability which facilitates the reaction.

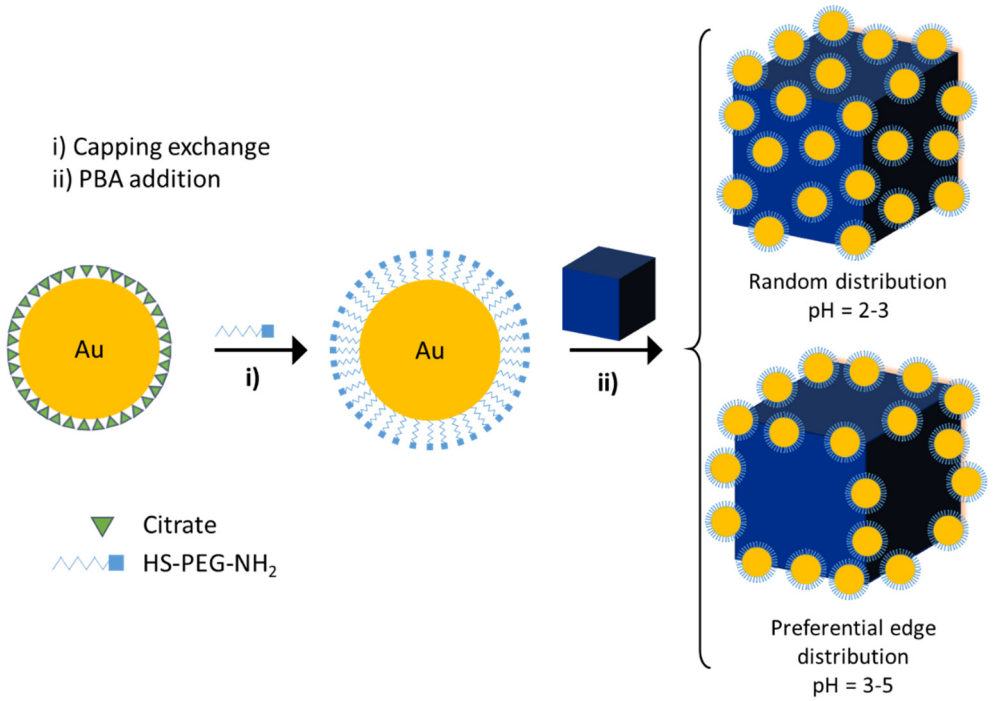

Figure 2.1 Schematic illustration for the preparation of a heterostructure formed by Au nanospheres decorating PBA NPs. The first step involves a capping substitution and the second step is related to the attachment of the Au onto the PBA surface. Two different Au decorations can be achieved by adjusting the pH solution: a random and a preferential edge distribution.

Regarding the synthesis, the magneto-plasmonic heterostructures were obtained through two different steps:

- The first step consists of exchanging, in aqueous solution the citrate molecules that coat the Au NPs, by the heteroditopic thiol-polyethyleneglycol-amine (HS-PEG-NH_2) ligand.
- In a second step, the as-obtained Au NPs are anchored to the PBA NPs suspended in water. Such a decoration takes place due to: i) the strong affinity of the thiol group to the metal particle surface[24] and ii) the strong interaction between the amino group and the negatively charged PBA NPs.

It is worth noting that the formation of the final hybrid nano-objects is not possible using the citrate-stabilized Au NPs due to the electrostatic repulsion between the two systems because they are both negatively charged (see Figure 2.2). That is why the first step requires a ligand exchange of the starting citrate-stabilized Au NPs of 12.4 ± 1.0 nm (see Figure 2.3)[25] with HS-PEG-NH_2. This ligand exchange was monitored by ζ-potential (see Table 2.1) and by attenuated total reflectance Fourier-transform infrared (ATR-FTIR, Figure 2.4).

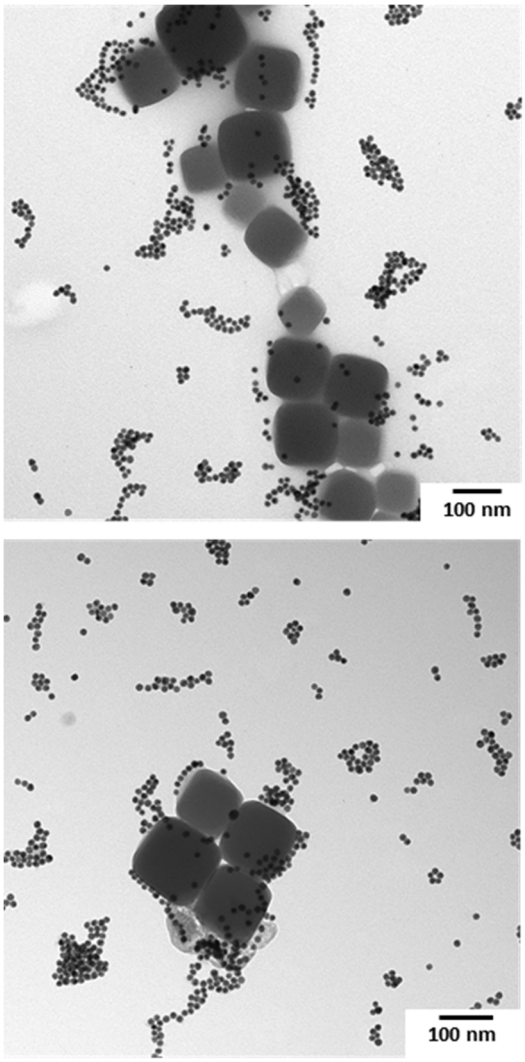

Figure 2.2 a) TEM images of citrate-stabilized Au NPs decorated PBA NPs.

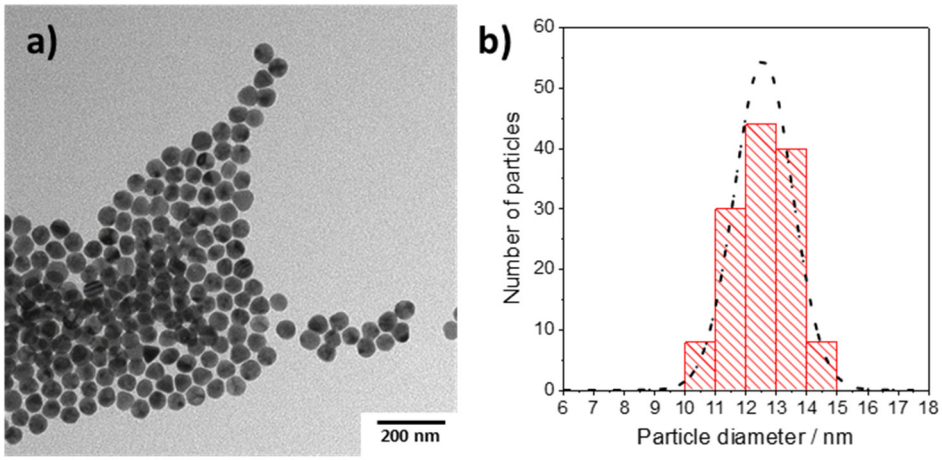

Figure 2.3 a) TEM image of citrate-stabilized spherical Au NPs and b) number-based particle size distribution measured by manual counting.

Table 2.1: ζ-potential values of the different Au and Ag NPs stabilized with different capping agents at pH near to 7.

	ζ-potential / mV		
	Citrate	CTAB	HS-PEG-NH_2
Au NPs	-40 ± 6	/	10 ± 3
AuNRs	/	35 ± 7	12 ± 4
AuNSs	/	/	12 ± 4
Ag NPs	-35 ± 10	/	11 ± 5

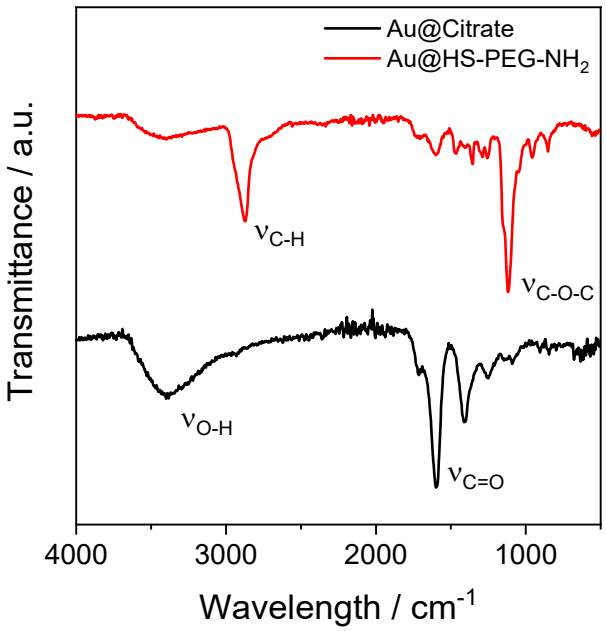

Figure 2.4 Infrared spectra of citrate stabilized and HS-PEG-NH_2 stabilized Au nanospheres.

ζ-potential is a common technique to characterize colloidal dispersions in order to provide information about the surface charge. In our Au NPs, the ζ-potential varies from a negative value, corresponding to the citrate capping, to a positive value, related to the HS-PEG-NH_2 molecule. In addition, the appearance in the ATR-FTIR measurements of new bands corresponding to C-H and C-O-C vibration modes of the PEG molecule and the decrease of the intensity of the citrate bands indicate a major substitution of citrate by the heteroditopic ligand.

In a further step, the solution of Au NPs stabilized with HS-PEG-NH_2 was adjusted at pH between 2 and 4 in order to protonate the dangling amino group (ζ-potential values vary from 9 ± 6 mV to > 20 mV). Mixing this solution with PBA NPs resulted in the decoration of the PBA NPs by the Au NPs. pH plays a crucial role in the whole process because at low pH (below 2) the Au NPs tend to aggregate (strong ionic force), while at high pH (above 5) a poor decoration of the PBA NPs is observed (weak electrostatic interaction because the weak positively charged Au NPs) (Figure 2.5). Hence, to optimize the decoration, the pH value was kept in the range of 2-5.

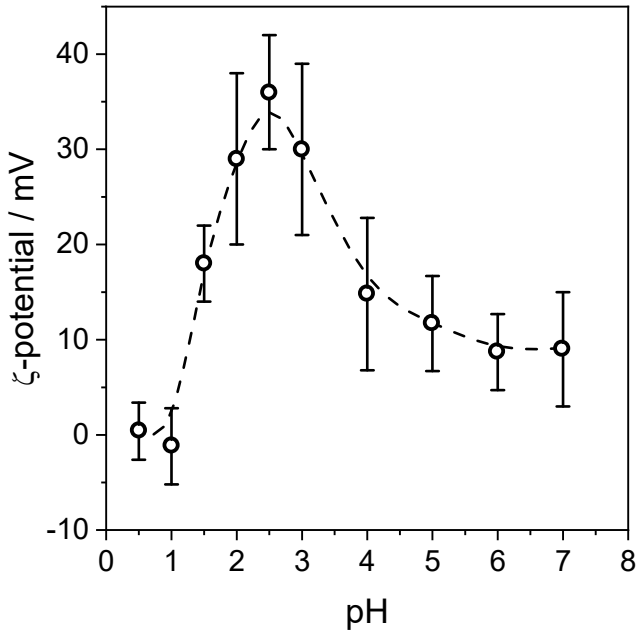

Figure 2.5 ζ-potential measurements of Au nanospheres stabilized with HS-PEG-NH_2 performed in water at different pH.

When the pH is in the 2-3 range, a random decoration of the PBA-NPs by Au is obtained, as demonstrated by Transmission Electron Microscopy (TEM) imaging. (Figure 2.6). An increase of the pH value (3-5) leads to a preferential binding of the Au NPs along the edges of the PBA cube (Figure 2.6). TEM images of the preferential edge decoration taken at different incidence angles are shown in Figure 2.7.

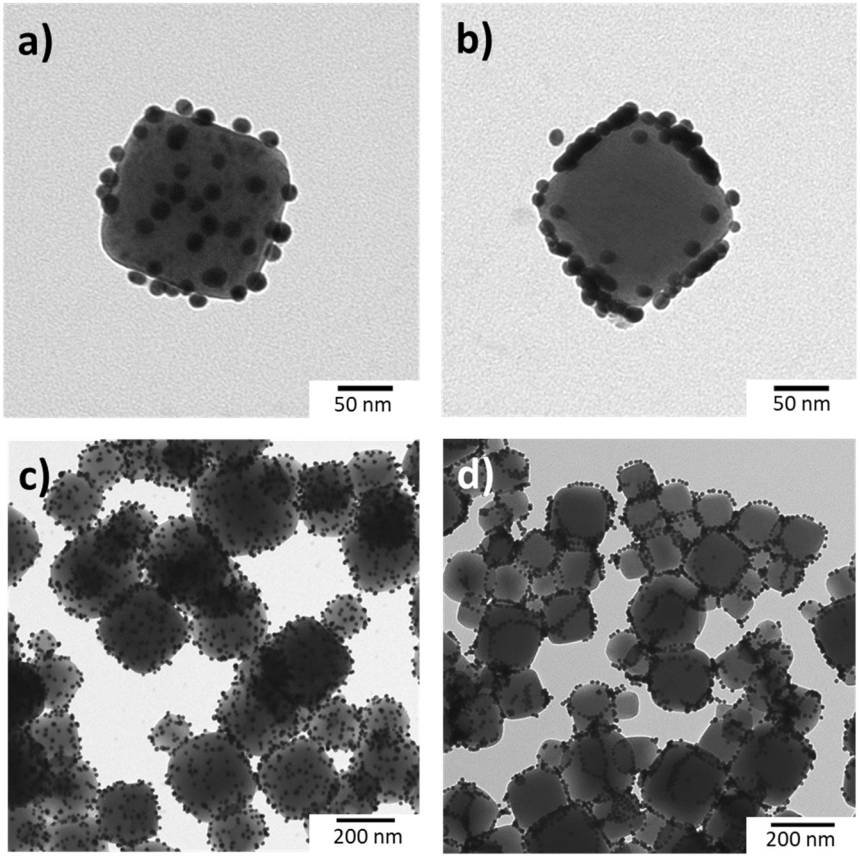

Figure 2.6 TEM images of the heterostructure of Au NPs with (a,c) random and (b,d) preferential edge decoration onto NiCr PBA.

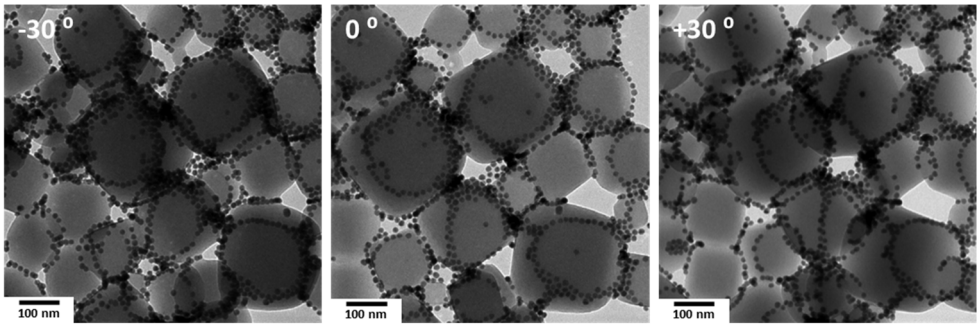

Figure 2.7 High-Resolution TEM images of Au-PBA heterostructure at different angles: (left) -30º, (center) 0º and (right) 30º.

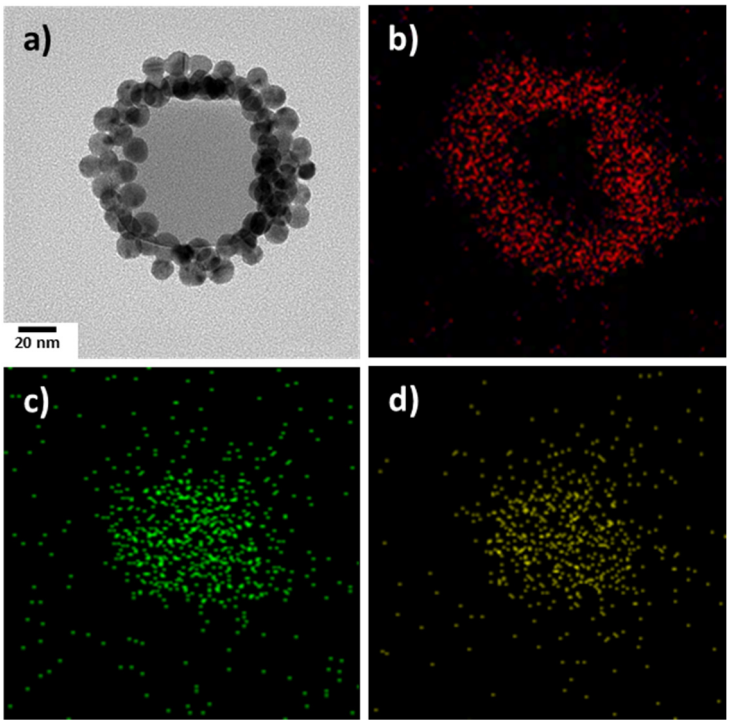

Figure 2.8 a) High-Resolution TEM image b-d) EDS Mapping of the metals present in the heterostructure (red: gold, green: nickel and yellow: iron).

Energy-dispersive X-ray spectroscopy mapping (Figure 2.8) confirms the presence of Cr and Ni at the center of the NP and Au at its edges. The selective decoration of the PBA-NPs edges at a pH ranging 3-5 is due to the larger negative charge density on (and near) the NPs edges than on their faces. Indeed, as it can be observed from its crystalline structure (presented in Chapter 1), on the particles' surface, each $Cr(CN)_6^{3-}$ species is surrounded by 5 Ni^{2+} (four belonging to the surface and one inside the NP), while on the edges each hexacyanometalate is surrounded by only four Ni^{2+} (two belonging to the surface and two to the particles' edge). At a pH of 3-5, the positive charge density of the Au NPs is weaker, therefore, privileging electrostatic interaction with the PBA-NPs edges where the negative charge density is larger. This effect is enhanced because of the possible presence

of a larger amount of defects in the vicinity of the NPs edges than on their faces. It is worth mentioning that the Au decoration (and thus the electrostatic interaction) is maintained after redispersing the hybrid in water at neutral pH (Figure 2.9).

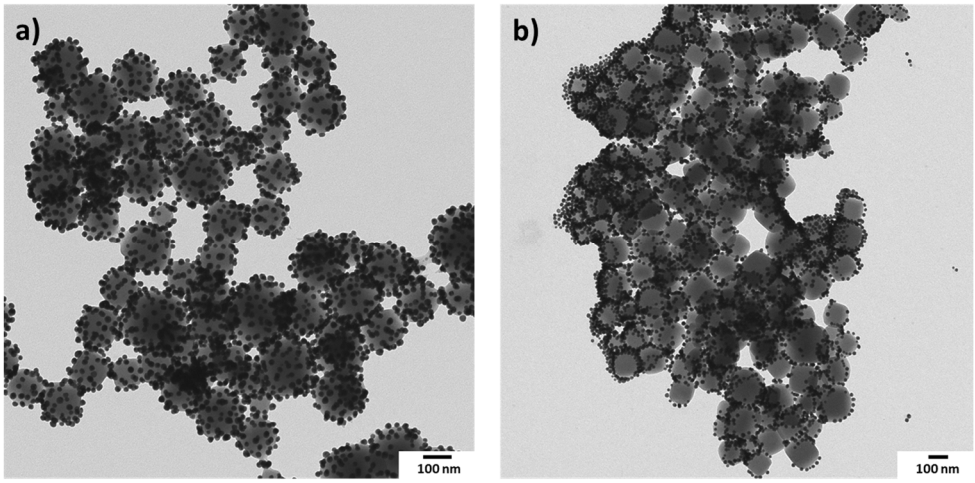

Figure 2.9 TEM images of the heterostructure of Au NPs with (a) random and (b) preferential edge decoration onto NiCr PBA after centrifuging and redispersing in water at neutral pH.

An optimum decoration of the PBA NPs can be achieved by tuning the ratio (Au/PBA) of the two components for the two pH ranges. For the low pH range (2-3, random distribution), we carried the experiments with Au/PBA molar ratio in the range 0.31 to 0.50. In this range, the higher the ratio is, the higher the decoration is (Figure 2.10). For high pH range (3-5, edge distribution), we investigated three different ratios, namely 0.28, 0.41 and 1.12. TEM imaging seems to indicate that the best results are obtained with the molar ratio of 0.41 (Figure 2.11). In order to assess the efficiency of the interaction between the two types of NPs, we determined the molar ratio of two thoroughly washed powder samples obtained with Au/PBA = 0.51 (low pH range) and 0.41 (high pH range) using inductively coupled plasma (ICP) measurements. Values of the Au/PBA ratio of 0.43 and 0.26 were obtained for the former and latter cases, respectively, allowing the determination of the optimum ratio for the two pH ranges.

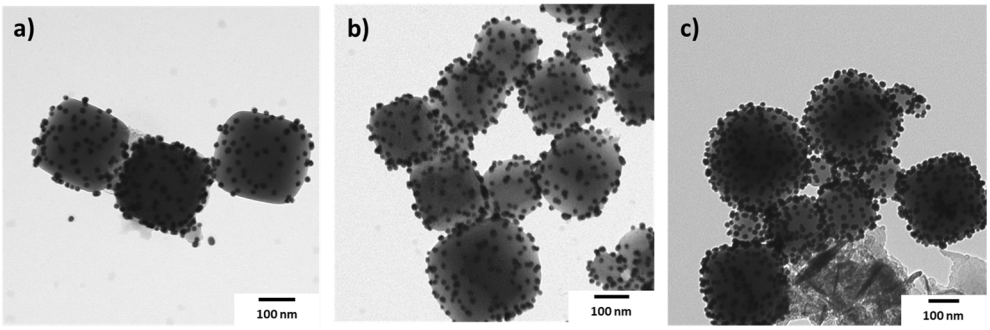

Figure 2.10 TEM image of decorated Au NPs onto PBA low pH 2-3 with ratio Au/PBA of (a) 0.31:1, b) 0.40:1 and c) 0.50:1.

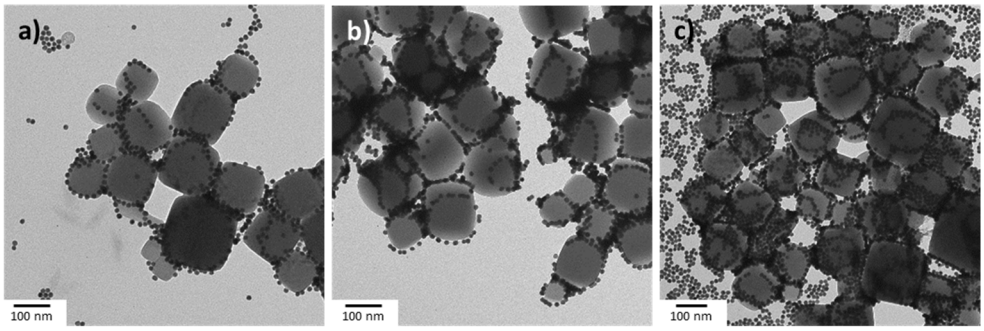

Figure 2.11 TEM image of decorated spherical Au NPs onto PBA with ratio Au/PBA of a) 0.28:1, b) 0.41:1 and c) 1.12:1.

We have presented a new synthetic approach that allows an optimum selective decoration (random *vs.* preferential) of PBA NPs with Au NPs. Let us now discuss the plasmonic and magnetic properties of these hybrid nanostructures.

The optical properties of Au NPs arise from the Localized Surface Plasmon Resonance (LSPR). Hence, the plasmon band is expected to be sensitive to the interaction between Au and PBA NPs. In Figure 2.12, we observe that the UV-vis absorption spectrum is dominated by the plasmon band.

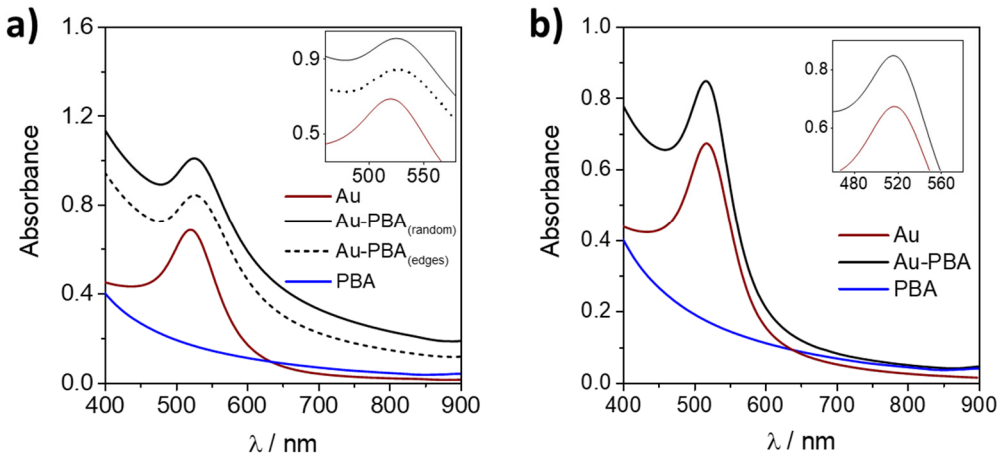

Figure 2.12 a) Spectra in the visible region of Au NPs and Au-PBA heterostructure decorated randomly and preferentially on the PBA edges. b) Spectra in the visible region of the attempt to obtain the heterostructure using citrate-stabilized Au NPs. Insets: magnified image of the plasmon bands.

For the functionalized Au-PEG NPs, the maximum of this band is located at 520 nm and shifts to 526 nm when Au-PEG is attached to the PBA NPs, independently of the type of decoration. The plasmon band shift is related to the change of the dielectric properties and, in particular, to the local refractive index at the surface of the plasmonic NPs.[26,27] It is worth noting that no shift is observed in the control experiment where the HS-PEG-NH_2 molecule was not used. Therefore, this shift is a clear indication of the PBA NPs decoration by the functionalized Au NPs. However, we also observe a progressive decay of the absorbance of the plasmonic band after 2 hours that becomes large after 48 h (Figure 2.13).

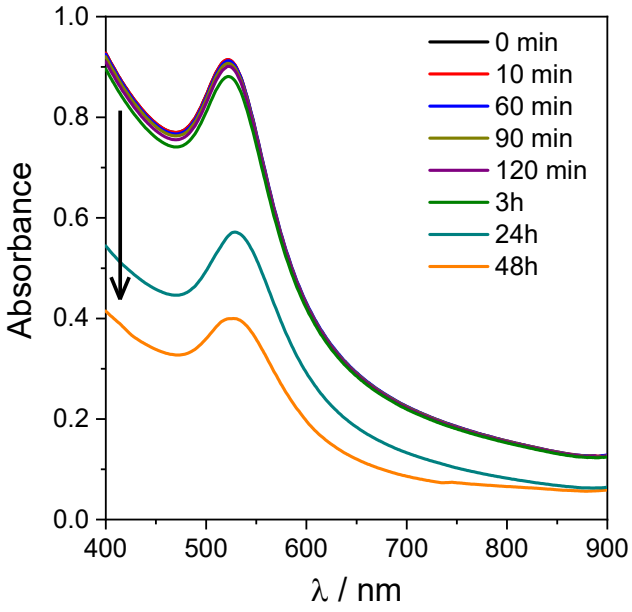

Figure 2.13 Study of the stability by recording the spectra in the visible region of the Au-PBA heterostructure in aqueous solution at room temperature.

A decrease of intensity of the plasmonic band is usually associated with the aggregation of the colloidal suspension but may also be due to Au degradation in the present case. Indeed, cyanide dissolution of spherical Au colloids usually takes place quickly;[28] thus, in order to check the chemical stability of the hybrid materials, powder X-ray diffraction (PXRD) study was performed on the pure PBA NPs and the hybrid material after leaving the suspensions to stand 1 week in water (see Figure 2.14). The detection of the characteristic Au diffraction peaks (at 38.2 and 44.3 degrees), together with unaltered PBA peaks indicate that the decrease of the intensity of the plasmonic band is due to the aggregation of the colloidal suspension with time and not to chemical degradation of the hybrid materials.

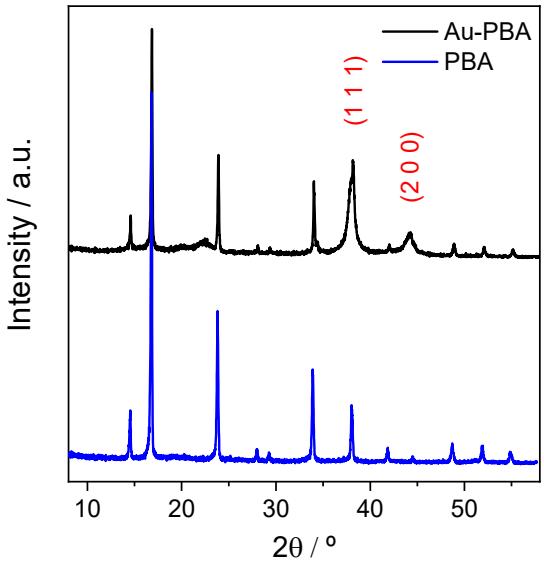

Figure 2.14 Room temperature PXRD for PBA NPs and Au-PBA heterostructure. Au peaks are indicated in red.

As far as the magnetic properties of the hybrid nanostructures are concerned, we observe that they are almost identical to those measured for pristine NiCr PBA NPs (Figures 2.15).[29] Thus, a ferromagnetic behavior below 68 K and a weak hysteresis in the magnetization of *ca.* 60 Oe at 2 K is observed, in agreement with the soft character of this PBA derivative. The only noticeable difference between hybrid and pristine NPs is the lower value for the saturation magnetization. This is due to the contribution of Au to the total weight of the nanostructure. In fact, if the presence of Au is corrected using the estimated amount of Au extracted from ICP measurements, such a difference disappears.

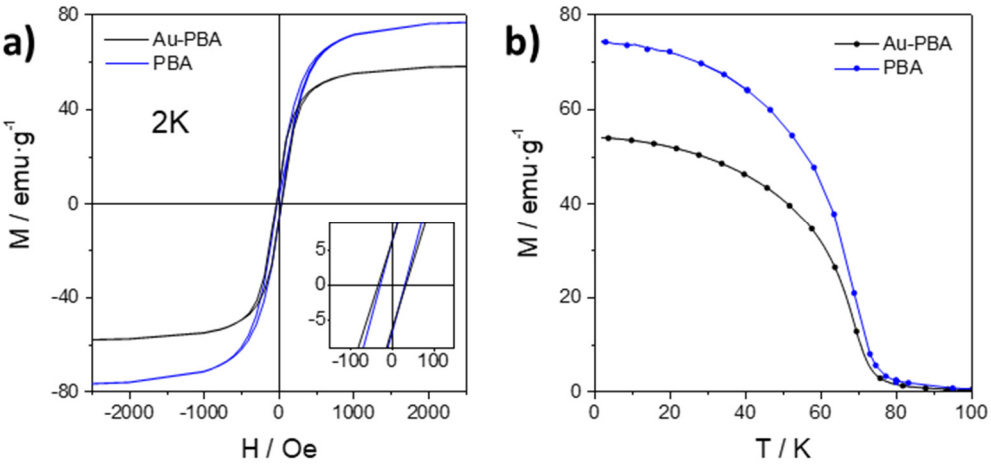

Figure 2.15 a) Hysteresis loop at 2K of PBA and Au-PBA with Au decorated preferentially on the PBA edges. b) Temperature dependence of field cooling magnetization of PBA and the heterostructure Au-PBA.

The generality of this approach is further illustrated by the fact that any plasmonic NP able to form thiol bonds with HS-PEG-NH_2 in acid conditions can be potentially used. This possibility opens the door to tune at will the plasmonic properties of the hybrid nanostructure simply by choosing the appropriate plasmonic NP. The different plasmonic NPs that were prepared are presented in Figures 2.16 – 2.18.

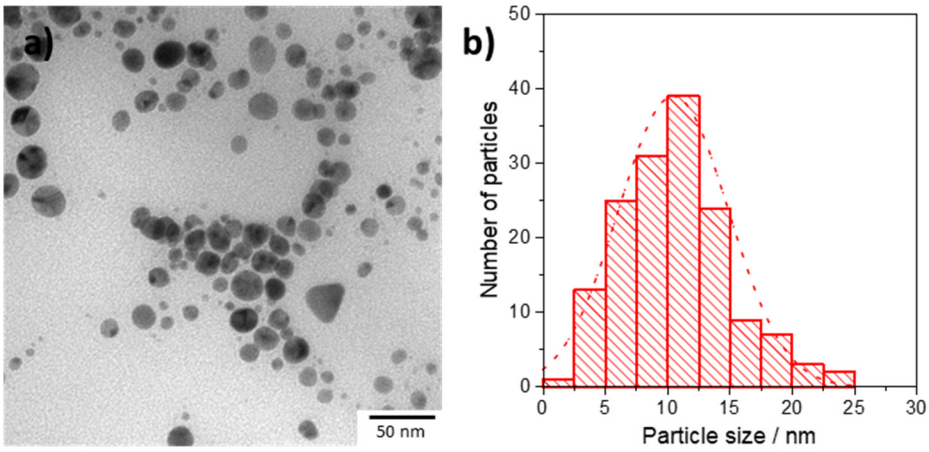

Figure 2.16 a) TEM image of citrate-stabilized spherical Ag NPs and b) number-based particle size distribution measured by manual counting.

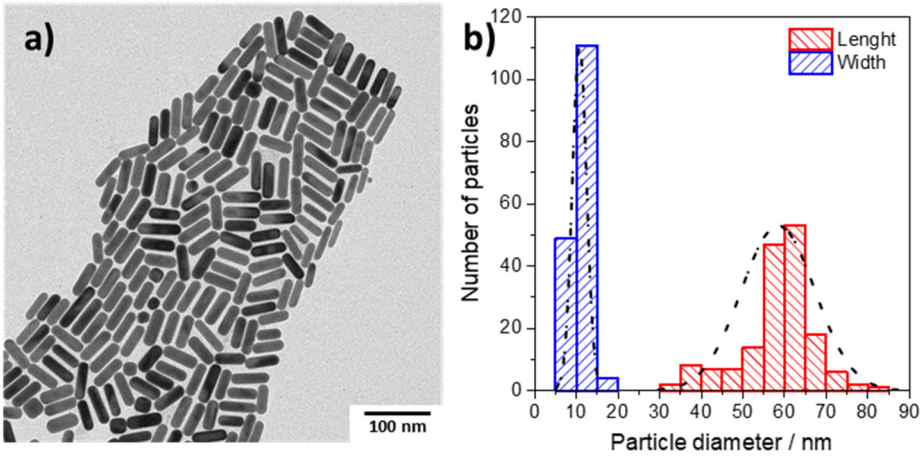

Figure 2.17 a) TEM image of CTAB stabilized AuNRs and b) Number-based particle size distribution measured by manual counting.

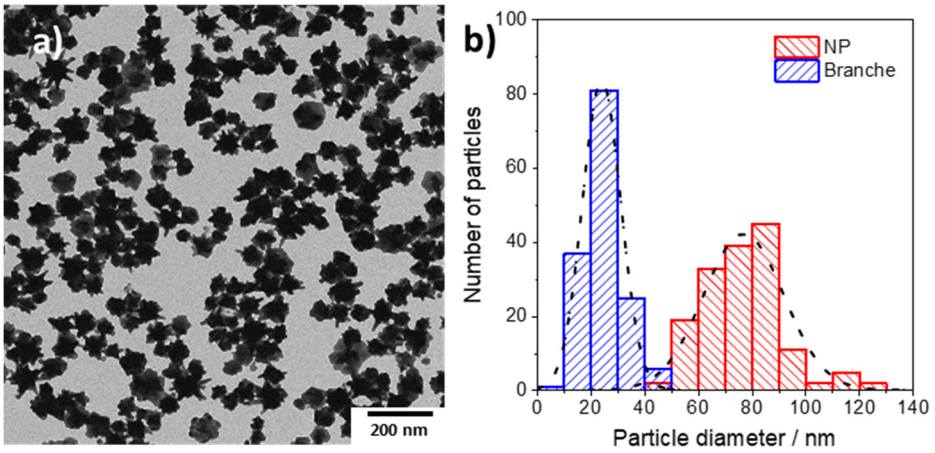

Figure 2.18 a) TEM image of HS-PEG-NH_2 stabilized AuNSs and b) Number-based particle size distribution measured by manual counting.

In this manner, citrate-stabilized spherical Ag NPs were used instead of Au NPs following the same experimental procedure in the pH range of 3-5. The obtained results are shown in Figure 2.19. The plasmon band of the Ag NPs is now located at 410 nm (to be compared with 520 for the Au NPs) and exhibits a red-shift of *ca.* 7 nm. This shift is similar to that observed in Au NPs, as it mainly depends on the shape of the NP, being independent of the metal.[30] Other Au NP with different shapes can also be used to decorate the NiCr PBA. Thus, we have chosen anisotropic Au NPs (NRs and NSs) which exhibit an intense plasmon band located at *ca.* 800 nm and *ca.* 700 nm, respectively. In these cases, the plasmon band can be tuned in a broad range by changing the ratio length/width in the AuNRs,[31] and the size of the branches and the core for the AuNSs.[32] In these two cases, the optimal ratio of Au/PBA changes with respect to that of the Au spheres, being 0.55:1 and 1.25:1 for AuNRs-PBA and AuNSs-PBA, respectively. This variation can be attributed to the different contact areas obtained for the different structures.

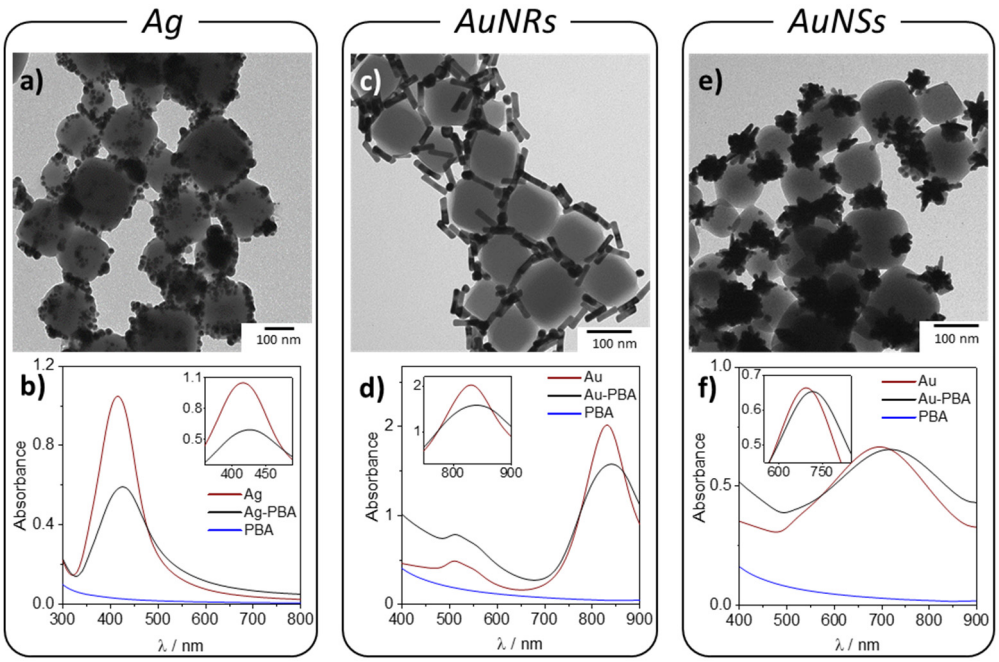

Figure 2.19 TEM images obtained for the following heterostructures: Ag-PBA (a), AuNRs-PBA (c) and AuNSs-PBA. UV-Vis spectra recorded for the heterostructures: Ag-PBA (b), AuNRs-PBA (d) and AuNSs-PBA (f). The insets show a zoom of the plasmon band shift. These heterostructures were obtained at pH 3-5 (preferential edge distribution).

Figure 2.19 shows the resulting nanostructures and plasmonic properties. As in the previous case, the synthesis was followed by UV-Vis spectra, searching for the plasmon shift as a proof of the interaction between Au and PBA NPs. In both cases, a shift in the plasmon band was noticed. Nevertheless, these shifts were more pronounced than the ones observed for the Au spheres due to the higher sensibility of these plasmons.[26,27] Concretely, AuNRs and AuNSs hybrid nanostructures show plasmon red-shifts of *ca.* 9 nm and 22 nm, respectively.

Furthermore, it is possible to control the decoration (*i.e.* the distribution) of the AuNRs on the cubic PBA surface. As commented above, a pH of 2-3 gives rise to a random decoration while a pH of 3-5 leads to a preferential edge distribution (Figure 2.20). Nevertheless, it is important to remark that the AuNSs decoration cannot be controlled possibly due to the high reactivity of these NPs.

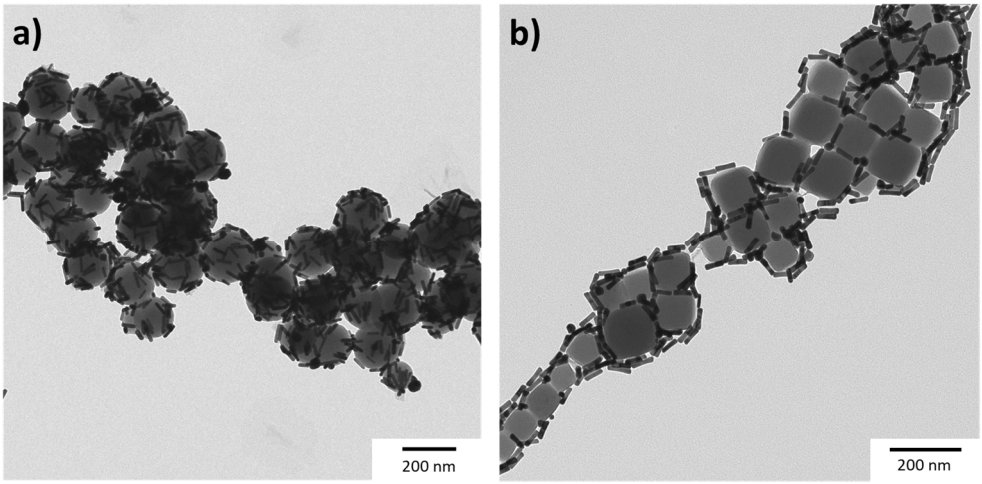

Figure 2.20 TEM images of AuNRs-PBA obtained at pH a) 2-3 (random decoration) and b) 3-5 (preferential edge distribution).

Finally, it can be noted that this procedure can also be extended to other PBA NPs. For example, NiCr can be changed by PB (FeFe), which was obtained as NPs with a size of 110 ± 20 nm and a ζ-potential value of -34 ± 4 mV. Figures 2.21a and 2.21b show the nanostructures achieved, as well as the corresponding shift in the UV-Vis spectrum of *ca.* 6 nm. Therefore, following this approach it is possible to attach Au NPs in any negatively charged PB or PBA NPs without capping agents, such as NiFe or CuCr. These nanostructures can be observed in Figure 2.21. Notice however that the colloidal stability of these systems is limited by the size of the PBA NPs since, if they are too small (below 25 nm), the NPs tend to aggregate (Figure 2.22) and if they are too big (above 300 nm) the processability is compromised as their colloidal stability is lower. Still, the heterostructures can be obtained by modifying the PBA size.

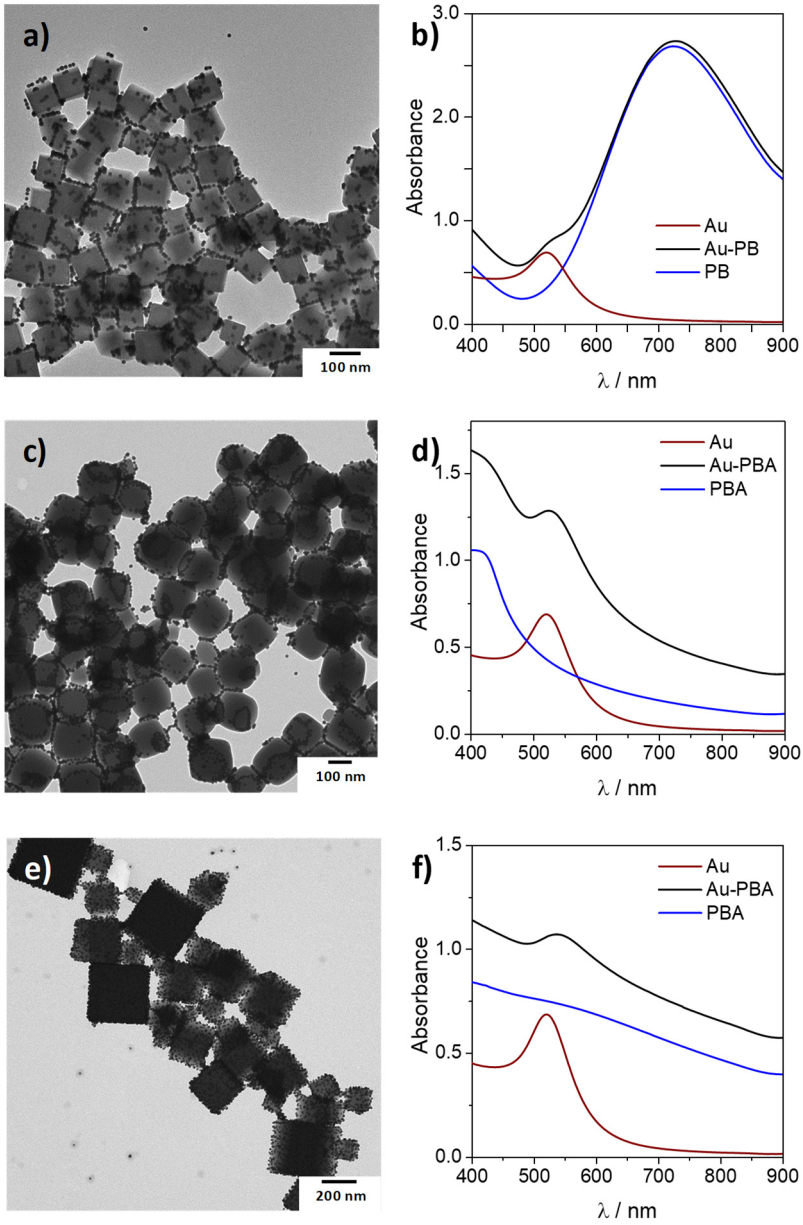

Figure 2.21 a) b) TEM image and UV-Vis spectrum of Au NPs decorated onto FeFe-PB NPs, c) d) decorated onto NiFe-PBA NPs and e) f) onto CuCr-PBA NPs (e) (f).

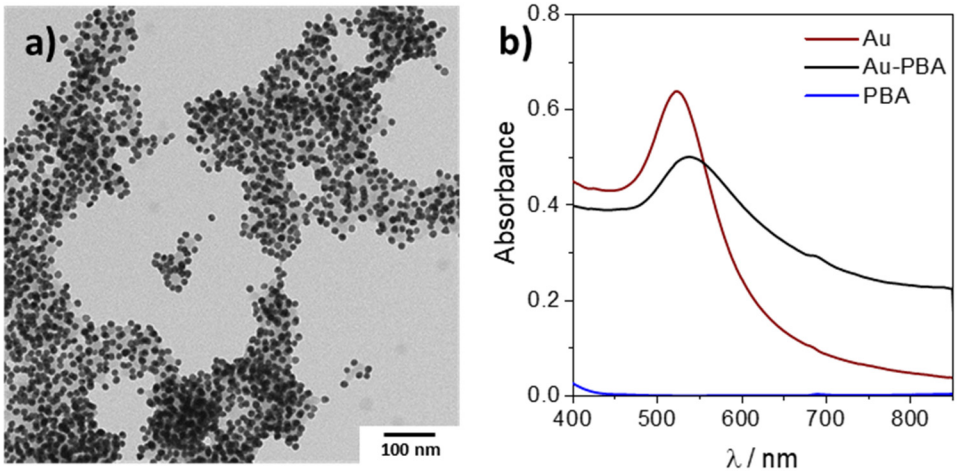

Figure 2.22 a) TEM image of spherical Au NPs decorated onto 20 nm NiCr-PBA NPs b) UV-Vis spectrum of spherical Au NPs decorated onto 20 nm NiCr-PBA NPs.

Besides, to further develop practical MO devices, Au NPs were attached to NiCr PBA NPs previously anchored on a silicon substrate.[33] Further details of the preparation of the self-assembly monolayers of PBA are available below, in the experimental part. Atomic Force Microscopy (AFM) images were taken after the addition of Au NPs stabilized with the HS-PEG-NH_2 molecule. These images show cubic morphologies corresponding to the PBA surrounded by spherical particles of Au, similar to the hybrid structure formed in solution proving the heterostructure formation (see Figures 2.23). Additionally, the Au addition onto the PBA monolayer gives rise to the appearance of the characteristic peaks of Ni, Cr, and Au in X-ray photoelectron spectroscopy, indicating the presence of Au NPs on the substrate (see Figure 2.24).

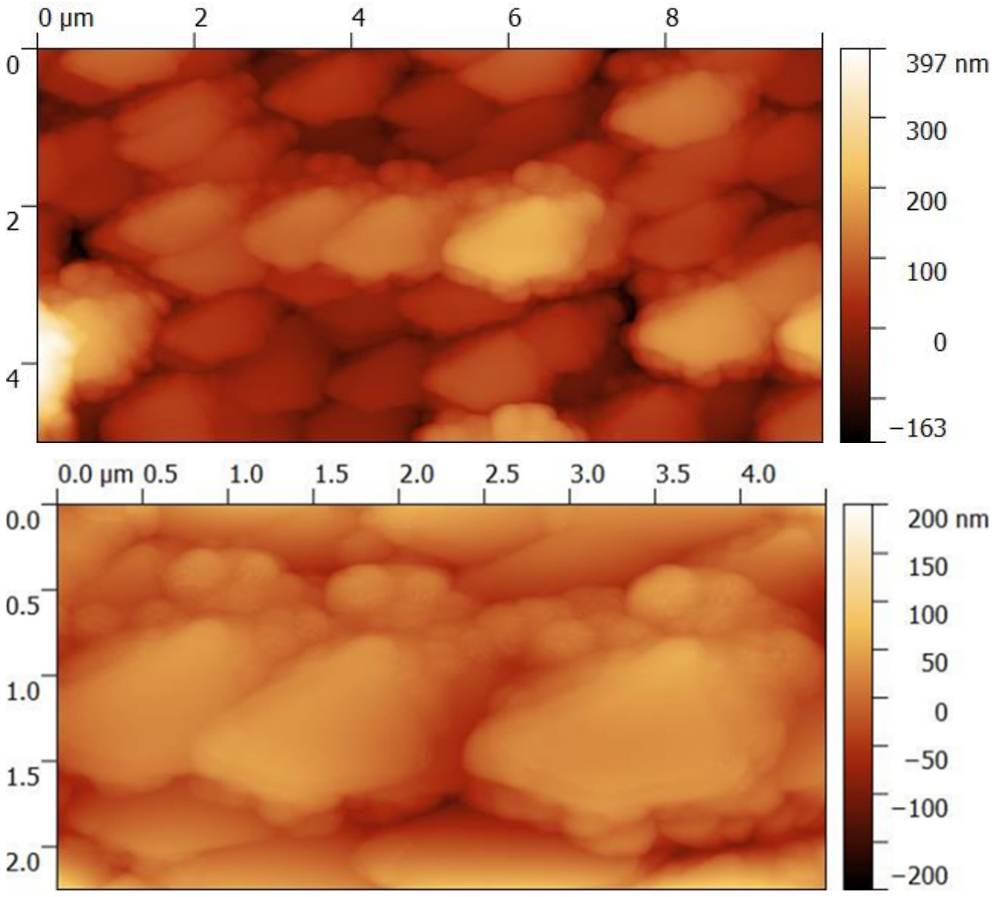

Figure 2.23 AFM images of a representative area of Au nanospheres decorated on a monolayer of NiCr-PBA on a SiO_2 substrate.

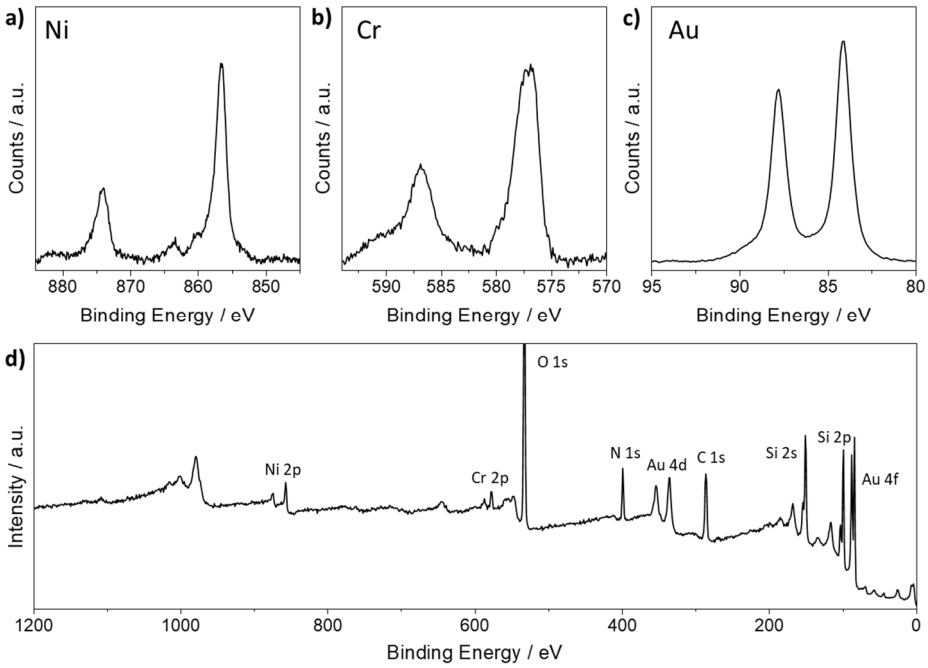

Figure 2.24 XPS spectra of a) Ni, b) Cr, c) Au and d) Survey for Au-PBA monolayers.

In future work, different PBAs will be measured to determine the wavelength where the maximum MO activity is reached as well as the optimal conditions for measuring. Then, a monolayer of the heterostructure with the suitable plasmonic NP will be synthesized. The magneto-optical Kerr effect of two different monolayers formed by PBA and Au-PBA will be carried out and compared in order to analyze the plasmon enhancement. Monolayers will be used to retain as much as possible the plasmon band properties that could be modified due to NP aggregation (*e.g.* in powder or pellets).

2.3 Conclusions and perspectives

In summary, we have developed a general and straightforward synthetic procedure to prepare, in aqueous solution, hybrid magneto-plasmonic nanostructures formed by metallic NPs decorated onto negatively charged magnetic NPs based on Prussian Blue Analogues by electrostatic attraction. By adjusting the pH, it is possible to control the positioning of Au over the Prussian Blue Analogue cubic NP. Indeed, Au can be attached randomly or preferentially on the edges of the cubes. This methodology, first tested with spherical Au, was extended in a second step to different plasmonic NPs of various shapes. This has permitted to tune the plasmon band position in a broad range of the visible spectrum. Finally, a similar procedure was carried out to attach Au on Prussian Blue Analogue monolayers obtaining the hybrid heterostructure successfully. Thus, this synthetic protocol provides appropriate hybrids to investigate the enhancement of the magneto-optical properties of the hybrids thanks to their coupling with the plasmonic properties.

2.4 Experimental details

2.4.1 Synthesis

All chemical reagents were purchased and used without further purification. Silver nitrate was purchased from Alfa Aesar. Chloroauric acid, L-ascorbic acid, potassium iodide, sodium citrate tribasic dihydrate, hexadecyltrimethylammonium bromide (CTAB), sodium borohydride, thiol polyethyleneglycole amine (HS-PEG3.5K-NH_2) and (3-aminopropyl)triethoxysilane (APTES) were purchased from Sigma-Aldrich. Ultra-pure water (18.2 MΩ) was used in the following synthesis.

Synthesis of plasmonic nanoparticles

Au Nanospheres: The synthesis was performed following the standard Turkevich's method.[25] The reduction of a gold hydrochlorate solution was achieved by adding the sodium citrate to the boiling solution with constant stirring in order to maintain a homogenous solution. A faint gray color was observed in the solution approximately one minute and in a period of 2–3 minutes later, it further darkening to deep wine and red color. Note that the color-changing is a clear visual indication that the colloidal Au is being produced.

Ag Nanospheres: These NPs were synthesized *via* a citrate reduction protocol.[34] Firstly, 1 mL of an aqueous solution of sodium citrate (1 wt %) and 0.25 mL of an aqueous solution of $AgNO_3$ (1 wt %) were dropped into 1.25 mL of water under stirring at room temperature. KI was added to the mixture to set a concentration of 0.06 µL. The mixture was incubated for 5 min prior to use. 50 µL of an aqueous solution of ascorbic acid (0.10 mM) was added into 47.5 mL of boiling water, followed by boiling for an additional 1 min. After the 5 min incubation, the mixture solution was introduced into the boiling water under vigorous stirring. After its color changed from colorless to yellow, the reaction solution was further boiled for 1 h under stirring.

Au Nanorods: AuNRs were obtained through a seed-mediated growth method.[35] After adding 25 µL of 50 mM $HAuCl_4$ solution to 4.7 mL of CTAB 0.1 M, the mixture was slowly stirred for 5 min. Then, 300 µL of a freshly prepared $NaBH_4$ 10 mM solution was rapidly injected under vigorous stirring. After 10 s stirring was stopped and the obtained seeds were let undisturbed for 1 hour at 30 °C. After the addition of 190 µL of HCl 1M and 100 µL of gold hydrochlorate 50 mM solution to 10 mL of CTAB 0.1 M, the mixture was shaken for 5 min. Subsequently, 120 µL of $AgNO_3$ 0.01 M solution was added to the mixture, which was then shaken for a few seconds. Quickly, 80 µL of ascorbic acid 0.1 M solution was then added to the growth solution and thoroughly shaken, turning colorless in few seconds. Finally, 24 µL of seeds were added to the mixture, and the solution was vigorously shaken and then left undisturbed at 30 °C for 2 hours. AuNRs were centrifuged and redispersed in water twice in order to remove the excess of surfactant.

Au Nanostars: Au NPs with star-like shapes were obtained by a seeded-growth process,[36] using citrate-stabilized spherical Au NPs as seeds. For the preparation of the growth solution, hydrochloric acid (10 µl, 1 M) was added to a gold hydrochlorate solution (10 mL, 0.25 mM). Afterward, aqueous solutions of ascorbic acid (50 µL, 0.1 M) and $AgNO_3$ (100 µL, 3 mM) were added, followed by the addition of 100 µL of seed solution (0.5 mM). Finally, HS-PEG-NH_2 was added as capping agent (1 mL, 1 $mg \cdot mL^{-1}$). After 30 minutes of incubation, AuNSs were ready for further use.

Synthesis of PB and PBA nanoparticles

$Ni^{II}Cr^{III}$ PBA: at room temperature, aqueous solutions of $NiCl_2 \cdot 6H_2O$ (5 mM, 10 mL) and $K_3[Cr(CN)_6]$ (5.65 mM, 10 mL) were added simultaneously to 100 mL of pure water at 2 $mL \cdot h^{-1}$ rate. After completion of the addition, the mixture was stirred for one hour before being centrifuged at 11000 rpm for 20 min. The supernatant was removed, and the white powder was redispersed in 10 mL of water.

20 nm $Ni^{II}Cr^{III}$ PBA: small NPs were synthesized by the mixture of $NiCl_2 \cdot 6H_2O$ 0.2 mM and $K_3[Cr(CN)_6]$ 0.2 mM aqueous solutions under stirring for 2 hours.

$Fe^{II}Fe^{III}$ PB: at room temperature, aqueous solutions of $FeCl_3 \cdot 6H_2O$ (5 mM, 10 mL) and $K_4[Fe(CN)_6]$ (5.65 mM, 10 mL) were added simultaneously to 100 mL of pure water at 2 $mL \cdot h^{-1}$ rate. After completion of the addition, the mixture was stirred for one hour before being centrifuged at 11000 rpm for 20 min. The supernatant was removed, and the NPs blue powder was redispersed in 10 mL of water.

$Ni^{II}Fe^{III}$ PBA: at room temperature, aqueous solutions of $NiCl_2 \cdot 6H_2O$ (5 mM, 10 mL) and $K_3[Fe(CN)_6]$ (5.65 mM, 10 mL) were added simultaneously to 100 mL of pure water at 2 $mL \cdot h^{-1}$ rate. After completion of the addition, the mixture was stirred for one hour before being centrifuged at 11000 rpm for 20 min. The supernatant was removed, and the yellowish powder was redispersed in 10 mL of water.

$Cu^{II}Cr^{III}$ PBA: at room temperature, aqueous solutions of $CuCl_2 \cdot 6H_2O$ (5 mM, 10 mL) and $K_3[Cr(CN)_6]$ (5.65 mM, 10 mL) were added simultaneously to 100 mL of pure water at 2 $mL \cdot h^{-1}$ rate. After completion of the addition, the mixture was stirred for one hour before being centrifuged at 11000 rpm for 20 min. The supernatant was removed, and the green powder was redispersed in 10 mL of water.

Au/Ag-PB/PBA Decoration

Firstly, 15 mL of a 0.33 $mg \cdot mL^{-1}$ HS-PEG-NH_2 solution was added to 15 mL of a $5 \cdot 10^{-4}$ M plasmonic NPs solution and let undisturbed overnight. The resulting capped NPs were centrifuged and redispersed to obtain a final concentration of $1.9 \cdot 10^{-4}$ M. Then, 5 mL of the aforementioned solution was adjusted to a pH between 2 and 5 (depending on the Au decoration), and immediately 0.5 mL of PB/PBA was added under magnetic stirring.

Au-PBA Monolayers

Firstly, thin films of NiCr PBA were prepared following a procedure developed by our group.[33] Substrates of silicon (dimension 1 × 1 cm) were washed three times with basic piranha and sonicated for 10 min each time. The next step was the functionalization of substrates by their immersion in a 1 mM APTES ethanolic solution for 45 min. Afterwards, they were washed and sonicated in ethanol for 10 min. Finally, the substrates were immersed in HCl 1 M for 7 min and dried under nitrogen flux. Furthermore, thin films of NiCr PBA were prepared by dropping a few drops of NiCr solution onto the substrate and after 2 min they were rinsed with water and dried. For the preparation of Au-PBA heterostructure, a grafting of spherical Au over a NiCr film was performed. A few drops of spherical Au NPs stabilized with HS-PEG-NH_2 at pH 3-4 were added to the NiCr previously prepared film for 2 min. After, the substrate was rinsed and dried under nitrogen flux.

2.4.2 Characterization

UV/Vis Spectroscopy: UV-vis absorption spectra were recorded on a Jasco V-670 spectrophotometer in baseline mode from 300 to 900 nm range, using 1.000-cm-optical-path plastic cuvettes.

Transmission Electron Microscopy (TEM): TEM studies were carried out on a JEOL JEM 1010 microscope operating at 100 kV, and Technai G2 F20 microscope operating at 200 kV. Samples were prepared by dropping suspensions on lacey formvar/carbon copper grids (300 mesh).

Inductively Coupled-Plasma Mass Spectrometry (ICP-MS): The ICP-MS analysis were conducted at the Universidad de Valencia (Sección de Espectrometría Atómica y Molecular). Samples were digested in an acid medium at 220 ºC using a microwave oven.

ζ-Potential measurements: ζ-potential measurements were performed at room temperature with a Zetasizer Nano ZS instrument (Malvern Instruments Ltd.).

Attenuated total reflectance Fourier-transform infrared (ATR-FTIR): spectra were collected in an Agilent Cary 630 FTIR spectrometer in the 4000−500 cm^{-1} range in the absence of KBr pellets.

Magnetic Measurements: Magnetic data were collected with a Quantum Design MPMS XL-5 susceptometer equipped with a SQUID sensor. dc FC magnetization measurements were performed under a magnetic field applied of 1000 Oe. Magnetization studies were performed between -0.3 and +0.3 T at a constant temperature of 2 K

Powder X-Ray Diffraction (PXRD): PXRD patterns were collected in a PANalytical Empyrean diffractometer using copper radiation (Cu $K_{\alpha\lambda}$= 1.5418 Å) with an PIXcel detector, operating at 40 mA and 45 kV at room temperature.

X-ray Photoelectron Spectroscopy (XPS): Samples were analyzed ex-situ at the X-ray Spectroscopy Service at the Universidad de Alicante using a K-ALPHA Thermo Scientific spectrometer. All spectra were collected using Al Kα radiation (1486.6 eV), monochromatized by a twin crystal monochromator, yielding a focused X-ray spot (elliptical in shape with a major axis length of 400 μm) at 30 mA and 2 kV. The alpha hemispherical analyzer was operated in the constant energy mode with survey scan pass energies of 200 eV to measure the whole energy band and 50 eV in a narrow scan to selectively measure the particular elements. XPS data were analyzed with Avantage software. A smart background function was used to approximate the experimental backgrounds. Charge compensation was achieved with the system flood gun that provides low energy electrons and low energy argon ions from a single source.

Atomic Force Microscopy (AFM): The substrates were imaged with a Digital Instruments Veeco Nanoscope IVa AFM microscope in tapping mode, using silicon tips with a resonance frequency of 300 kHz and with an equivalent constant force of 40 $N \cdot m^{-1}$. AFM images were treated with Gwyddion and WSxM softwares.

2.5 References

(1) Maksymov, I. S. Magneto-Plasmonic Nanoantennas: Basics and Applications. *Rev. Phys.* **2016**, *1*, 36–51.

(2) Nguyen, T. T.; Mammeri, F.; Ammar, S. Iron Oxide and Gold Based Magneto-Plasmonic Nanostructures for Medical Applications : A Review. *Nanomaterials* **2018**, *8* (3), 149.

(3) Verdaguer, M.; Girolami, G. S. *Magnetic Prussian Blue Analogues*; **2005**; Vol. 36.

(4) Coronado, E.; Makarewicz, M.; Prieto-Ruiz, J. P.; Prima-García, H.; Romero, F. M. Magneto-Optical Properties of Electrodeposited Thin Films of the Molecule-Based Magnet $Cr_{5.5}(CN)_{12}\cdot 11.5H_2O$. *Adv. Mater.* **2011**, *23* (37), 4323–4326.

(5) Pajerowski, D. M.; Gardner, J. E.; Andrus, M. J.; Datta, S.; Gomez, A.; Kycia, S. W.; Hill, S.; Talham, D. R.; Meisel, M. W. Magnetic Anisotropy in Thin Films of Prussian Blue Analogues. *Phys. Rev. B - Condens. Matter Mater. Phys.* **2010**, *82* (21), 214405.

(6) Ohkoshi, S. ichi; Mizuno, M.; Hung, G. jye; Hashimoto, K. Magnetooptical Effects of Room Temperature Molecular-Based Magnetic Films Composed of Vanadium Hexacyanochromates. *J. Phys. Chem. B* **2000**, *104* (40), 9365–9367.

(7) Qiu, Z. Q.; Bader, S. D. Surface Magneto-Optic Kerr Effect (SMOKE). *J. Magn. Magn. Mater.* **1999**, *200* (1–3), 664–678.

(8) Qiu, Z. Q.; Bader, S. D. Surface Magneto-Optic Kerr Effect. *Rev. Sci. Instrum.* **2000**, *71* (3), 1243–1255.

(9) López-ortega, A.; Takahashi, M.; Maenosono, S.; Vavassori, P. Plasmon Induced Magneto-Optical Enhancement. *Nanoscale* **2018**, *10* (2), 18672–18679.

(10) Sepúlveda, B.; González-Díaz, J. B.; García-Martín, A.; Lechuga, L. M.; Armelles, G. Plasmon-Induced Magneto-Optical Activity in Nanosized Gold Disks. *Phys. Rev. Lett.* **2010**, *104* (14), 147401.

(11) Armelles, G.; Cebollada, A.; García-Martín, A.; González, M. U. Magnetoplasmonics: Magnetoplasmonics: Combining Magnetic and Plasmonic Functionalities. *Adv. Opt. Mater.* **2013**, *1* (1), 10–35.

(12) Caminale, M.; Anghinolfi, L.; Magnano, E.; Bondino, F.; Canepa, M.; Mattera, L.; Bisio, F. Tuning the Magneto-Optical Response of Iron Oxide Nanocrystals in Au- and Ag-

Based Plasmonic Media. *ACS Appl. Mater. Interfaces* **2013**, *5* (6), 1955–1960.

(13) Maurin-Pasturel, G.; Long, J.; Guari, Y.; Godiard, F.; Willinger, M. G.; Guerin, C.; Larionova, J. Nanosized Heterostructures of Au@Prussian Blue Analogues: Towards Multifunctionality at the Nanoscale. *Angew. Chem. Int. Ed.* **2014**, *53* (15), 3872–3876.

(14) Cheng, L.; Gong, H.; Zhu, W.; Liu, J.; Wang, X.; Liu, G.; Liu, Z. PEGylated Prussian Blue Nanocubes as a Theranostic Agent for Simultaneous Cancer Imaging and Photothermal Therapy. *Biomaterials* **2014**, *35* (37), 9844–9852.

(15) Yin, Y.; Li, Q.; Ma, S.; Liu, H.; Dong, B.; Yang, J.; Liu, D. Prussian Blue as a Highly Sensitive and Background-Free Resonant Raman Reporter. *Anal. Chem.* **2017**, *89* (3), 1551–1557.

(16) Qiu, J. D.; Peng, H. Z.; Liang, R. P.; Li, J.; Xia, X. H. Synthesis, Characterization, and Immobilization of Prussian Blue-Modified Au Nanoparticles: Application to Electrocatalytic Reduction of H_2O_2. *Langmuir* **2007**, *23* (4), 2133–2137.

(17) Shemer, G.; Markovich, G. Enhancement of Magneto-Optical Effects in Magnetite Nanocrystals near Gold Surfaces. *J. Phys. Chem. B* **2002**, *106* (36), 9195–9197.

(18) Jing, L.; Liang, X.; Deng, Z.; Feng, S.; Li, X.; Huang, M. Biomaterials Prussian Blue Coated Gold Nanoparticles for Simultaneous Photoacoustic / CT Bimodal Imaging and Photothermal Ablation of Cancer. *Biomaterials* **2014**, *35* (22), 5814–5821.

(19) Maurin-Pasturel, G.; Rascol, E.; Busson, M.; Sevestre, S.; Lai-Kee-Him, J.; Bron, P.; Long, J.; Chopineau, J.; Devoisselle, J.-M.; Guari, Y.; et al. ^{201}Tl-Labeled Prussian Blue and Au@Prussian Blue Nanoprobes for SPEC-CT Imaging: Influence of the Size, Shape and Coating on the Biodistribution. *Inorg. Chem. Front.* **2017**, *4* (10), 1737–1741.

(20) Crespilho, F. N.; Zucolotto, V.; Brett, C. M. A.; Oliveira, O. N.; Nart, F. C. Enhanced Charge Transport and Incorporation of Redox Mediators in Layer-by-Layer Films Containing PAMAM-Encapsulated Gold Nanoparticles. *J. Phys. Chem. B* **2006**, *110* (35), 17478–17483.

(21) Xue, M. H.; Xu, Q.; Zhou, M.; Zhu, J. J. In Situ Immobilization of Glucose Oxidase in Chitosan-Gold Nanoparticle Hybrid Film on Prussian Blue Modified Electrode for High-Sensitivity Glucose Detection. *Electrochem. commun.* **2006**, *8* (9), 1468–1474.

(22) Sanchis-Gual, R.; Susic, I.; Torres-Cavanillas, R.; Arenas-Esteban, D.; Bals, S.;

Mallah, T.; Coronado-Puchau, M.; Coronado, E. The Design of Magneto-Plasmonic Nanostructures Formed by Magnetic Prussian Blue-Type Nanocrystals Decorated with Au Nanoparticles. *Chem. Comm.* **2021**.

(23) Gadet, V.; Mallah, T.; Castro, I.; Verdaguer, M.; Veillet, P. High-TcMolecular-Based Magnets: A Ferromagnetic Bimetallic Chromium(III)-Nickel(II) Cyanide with Tc= 90 K. *J. Am. Chem. Soc.* **1992**, *114* (23), 9213–9214.

(24) Häkkinen, H. The Gold-Sulfur Interface at the Nanoscale. *Nat. Chem.* **2012**, *4* (6), 443–455.

(25) Turkevich, J. Colloidal Gold. Part I. *Gold Bull.* **1985**, *18* (4), 125–131.

(26) Mayer, K. M.; Hafner, J. H. Localized Surface Plasmon Resonance Sensors. *Chem. Rev.* **2011**, *111* (6), 3828–3857.

(27) Chen, H.; Kou, X.; Yang, Z.; Ni, W.; Wang, J. Shape-and Size-Dependent Refractive Index Sensitivity of Gold Nanoparticles. *Langmuir* **2008**, *24*, 5233–5237.

(28) Jana, N. R.; Gearheart, L.; Obare, S. O.; Murphy, C. J. Anisotropic Chemical Reactivity of Gold Spheroids and Nanorods. *Langmuir* **2002**, *18* (3), 922–927.

(29) Dumont, M. F.; Knowles, E. S.; Guiet, A.; Pajerowski, D. M.; Gomez, A.; Kycia, S. W.; Meisel, M. W.; Talham, D. R. Photoinduced Magnetism in Core/Shell Prussian Blue Analogue Heterostructures of $K_jNi_k[Cr(CN)_6]L{\cdot}nH_2O$ with $Rb_aCo_b[Fe(CN)_6]C{\cdot}\ MH_2O$. *Inorg. Chem.* **2011**, *50* (10), 4295–4300.

(30) Lee, K. S.; El-Sayed, M. A. Gold and Silver Nanoparticles in Sensing and Imaging: Sensitivity of Plasmon Response to Size, Shape, and Metal Composition. *J. Phys. Chem. B* **2006**, *110* (39), 19220–19225.

(31) Yu; Chang, S.-S.; Lee, C.-L.; Wang, C. R. C. Gold Nanorods: Electrochemical Synthesis and Optical Properties. *J. Phys. Chem. B* **1997**, *101* (34), 6661–6664.

(32) Barbosa, S.; Agrawal, A.; Rodríguez-Lorenzo, L.; Pastoriza-Santos, I.; Alvarez-Puebla, R. A.; Kornowski, A.; Weller, H.; Liz-Marzán, L. M. Tuning Size and Sensing Properties in Colloidal Gold Nanostars. *Langmuir* **2010**, *26* (18), 14943–14950.

(33) Coronado, E.; Forment-Aliaga, A.; Pinilla-Cienfuegos, E.; Tatay, S.; Catala, L.; Plaza, J. A. Nanopatterning of Anionic Nanoparticles Based on Magnetic Prussian-Blue Analogues. *Adv. Funct. Mater.* **2012**, *22* (17), 3625–3633.

(34) Li, H.; Xia, H.; Wang, D.; Tao, X. Simple Synthesis of Monodisperse, Quasi-Spherical, Citrate-Stabilized Silver Nanocrystals in Water. *Langmuir* **2013**, *29* (16), 5074–5079.

(35) Nikoobakht, B.; El-Sayed, M. A. Preparation and Growth Mechanism of Gold Nanorods (NRs) Using Seed-Mediated Growth Method. *Chem. Mater.* **2003**, *15* (10), 1957–1962.

(36) Wang, Y.; Serrano, A. B.; Sentosun, K.; Bals, S.; Liz-Marzán, L. M. Stabilization and Encapsulation of Gold Nanostars Mediated by Dithiols. *Small* **2015**, *11* (34), 4314–4320.

Chapter 3

Chemical design of Au and Prussian Blue Analogue heterostructures for oxygen evolution reaction electrocatalysis

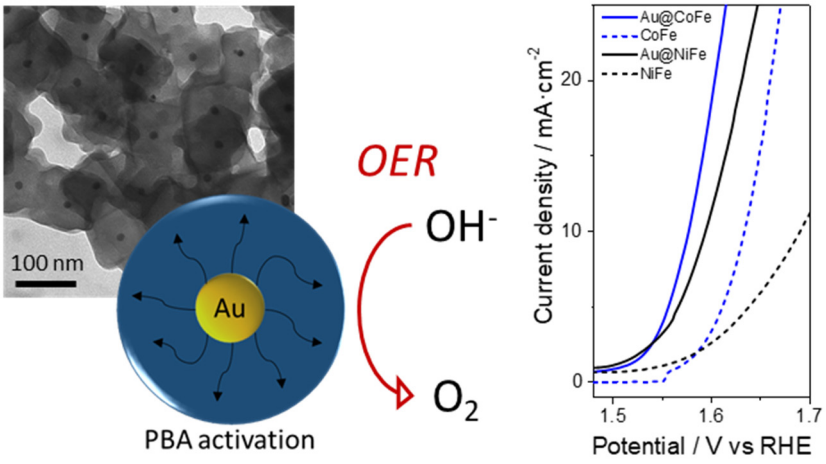

3.1 Introduction

The electrolysis of water to generate hydrogen and oxygen offers the exciting possibility of storing energy whose importance is out of question today. However, this process requires high voltages mainly due to the slow kinetics of the oxygen evolution reaction (OER). This reaction represents a significant efficiency loss in water-splitting systems and often requires an anode catalyst to reduce the energy barriers of the OER. In this context, earth-abundant electrocatalysts have been extensively studied in alkaline media.[1,2] First-row transition metal oxides of Co, Fe, or Ni show extremely high activities but only at very high pH (above 13), where the corresponding half-cell reduction reaction (for example, the hydrogen production) is more problematic. Nonetheless, at low pH, most of the catalysts suffer corrosion. Thus, an efficient catalyst for OER at acidic or near-neutral solution based on earth-abundant metals remains a significant challenge and highly desirable goal. In such conditions, benchmark materials are principally based on Ru or Ir oxides, affecting the cost of this technology considerably.[3,4]

In this context, Prussian Blue Analogues (PBA) are interesting materials since they are robust, chemically tunable and based on earth-abundant metals.[5] In fact, they have recently been investigated as an interesting implementation in multifunctional materials for many energy-related fields, such as supercapacitors, sodium-ion batteries and electrocatalysts.[6–9] Moreover, well-stabilized PBAs are effective and stable in an extensive pH range exhibiting catalytic activities comparable to those of metal oxides for OER.[9] However, PBAs exhibit low electrical conductivities, which increase the required overpotentials in water splitting.[10] For this reason, the combination of PBA with other nanomaterials has attracted considerable attention in order to further improve their electrocatalytic activity.[9,11] This activity must be a function of the concentration of electrocatalytic active sites in the material. Nonetheless, scarce attention has been paid to the number of electroactive sites of the electrocatalyst when this enhancement occurs.

Recent studies have shown that electrocatalysts based on Co, Ni and Fe are oxidized before the onset of oxygen evolution, being the oxidized metals the active species in the pathway for O_2 evolution.[12–14] Thus, a possibility to enhance the

electrocatalytic activity could be done by combining efficient electrocatalysts with highly electronegative metals. In this line, Au is the highest electronegative metal and thus it can drain electrons from the catalyst.[15,16] Besides, in combination with the electrocatalyst, it may contribute to improve the electrocatalytic performance thanks to the increase in the conductivity of the resulting material.[17–19] To this aim, in this work, we have explored the preparation of hybrid materials combining PBAs with Au. In particular, we have focused on nanoparticles (NPs) since they are usually the preferred form of catalysts due to the large number of electroactive sites provided by their high surface areas. Among them, the core@shell structure has been extensively used to obtain hybrid materials at the nanometer scale.[20,21] Still, Au@PBA heterostructure remains an unexplored hybrid material for electrocatalysis. Thus, Au@PBA heterostructures have been mostly focused on the pure Prussian Blue compound.[22–26] Only recently, heterostructures with other metallic compositions such as NiFe and CoFe, which are interesting for OER, have been reported.[27,28]

In this work, we have studied how the chemical design influences the specific density of electroactive sites in different Au-PBA nanostructures. To do so, we have synthesized and fully characterized a variety of well-formed core@shell NPs of Au@PBA (PBA of $Ni^{II}Fe^{II}$ and $Co^{II}Fe^{II}$) with an Au core diameter of around 15 nm and different shell sizes. The electrocatalytical activity of such NPs was systematically evaluated and compared to the pristine PBA and other Au-PBA heterostructures by studying the OER. By means of coulovoltammetry and electrochemical impedance spectroscopy, we noticed that the presence of 5-10 % of Au in the core@shell NPs leads to i) an enhancement of the intrinsic catalytic activity of the PBA centers and ii) an increment in the electroactive mass able to be reduced or oxidized and thus, to a higher number of sites able to take part in the OER. These effects decrease the onset potential significantly. At the same time, the Tafel slope remains unchanged, possibly indicating that Au reduces the limiting potential of the catalyst with no variation in the kinetics of the reaction. These improvements are a consequence of the high contact between both systems and the protective shell that prevents from Au oxidation. Therefore, these results make evident the existence of a strong synergistic effect between the core and the shell.

3.2 Results and discussion

The preparation of core@shell NPs of Au@PBA involves a two-step protocol in which $KAu(CN)_2$ reacts with KBH_4 in aqueous solution, reducing Au(I) to metallic Au, to afford Au NPs stabilized by cyanide groups (Au@CN NPs), followed in a second step by a dropwise addition of the PBA precursors to overgrow the PBA around the Au surface.[27,28]

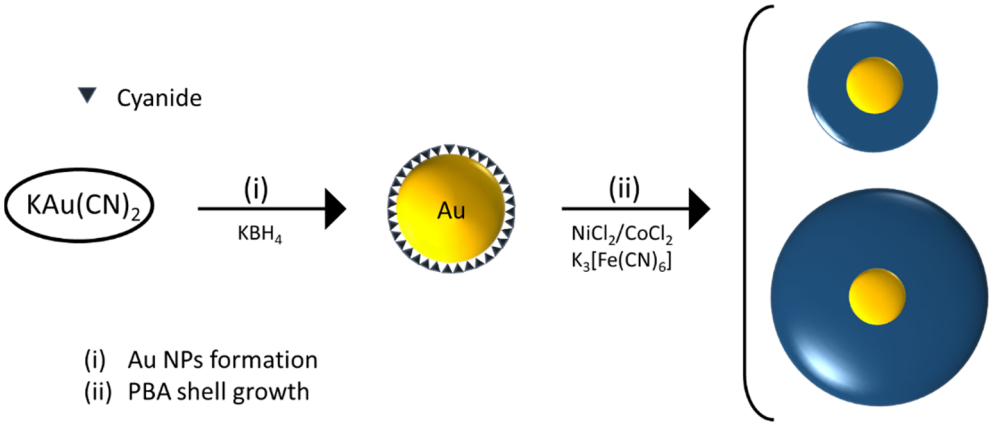

Figure 3.1 Schematic illustration of the preparation of Au@PBA NPs.

Still, this protocol needs further optimization to fulfill the requirements that are needed to make these hybrid Au@PBA NPs useful for electrocatalysis: (i) the amount of Au should be minimized with respect to that of the electroactive PBA shell since one needs to have the maximum number of electroactive sites while maintaining the beneficial properties of the Au core in terms of conductivity and activation of the shell (see below); (ii) a good coverage of the Au by the PBA shell to avoid its oxidation and dissolution during the electrochemical process; (iii) a good monodispersity in the size of the hybrid NPs to ensure the reproducibility in the electrochemical measurements.

Keeping these considerations in mind, the first step in the preparation of Au@PBA NPs has been carried out at low temperature (around 10 ºC). This temperature was set to induce the formation of smaller Au NPs and, consequently, to increase the surface area and the contact between Au and PBA. These NPs are in an equilibrium between borohydride (reducing agent) and cyanide (capping but also oxidizing agent). Furthermore, since KBH_4 leads to hydrogen bubbles that destabilize the Au NPs as a consequence of the water reduction,[29] in our protocol, the $Au(CN)_2$:KBH_4 molar ratio was increased with respect to the original synthesis (from 0.08 to 0.25) to improve the Au monodispersity. This smaller NP size distribution was proved by the width of the Au plasmon band (see below). On the other hand, in the specific case of Au@CoFe NPs, some additional changes need to be introduced to improve the CoFe coverage. Indeed, in this growth process, CoFe has a stronger tendency to self-nucleate than NiFe, as a consequence of the different kinetics.[30] For this reason, following the original protocol afforded an incomplete coverage of the Au NP by the overgrown shell (Figure 3.1a). To solve this problem, the precursors were added at lower rates in order to give enough time to the CoFe shell to grow better over Au (Figure 3.2b). Although a core@shell morphology is achieved at this point, a further improvement was still by varying the time delay (time between Au NPs formation and the beginning of the addition of the precursors). Thus, a higher time delay promotes the formation of single CoFe NPs (Figure 3.2c). In contrast, no time delay prevents the formation of well-stabilized Au@CN NPs (Figure 3.2d). A time delay of 10-20 min in combination with an addition rate of 0.5 $mL \cdot h^{-1}$ appears to be the most optimal conditions to get well stabilized Au NPs and thus, a well-defined shell growth around the metallic surface. Furthermore, PBA shell thickness can be controlled by varying the total PBA precursor volume. Thus, after optimizing the protocol, different PBA shells were obtained to evaluate the Au/PBA ratio on the electrochemical performance (Figure 3.3).

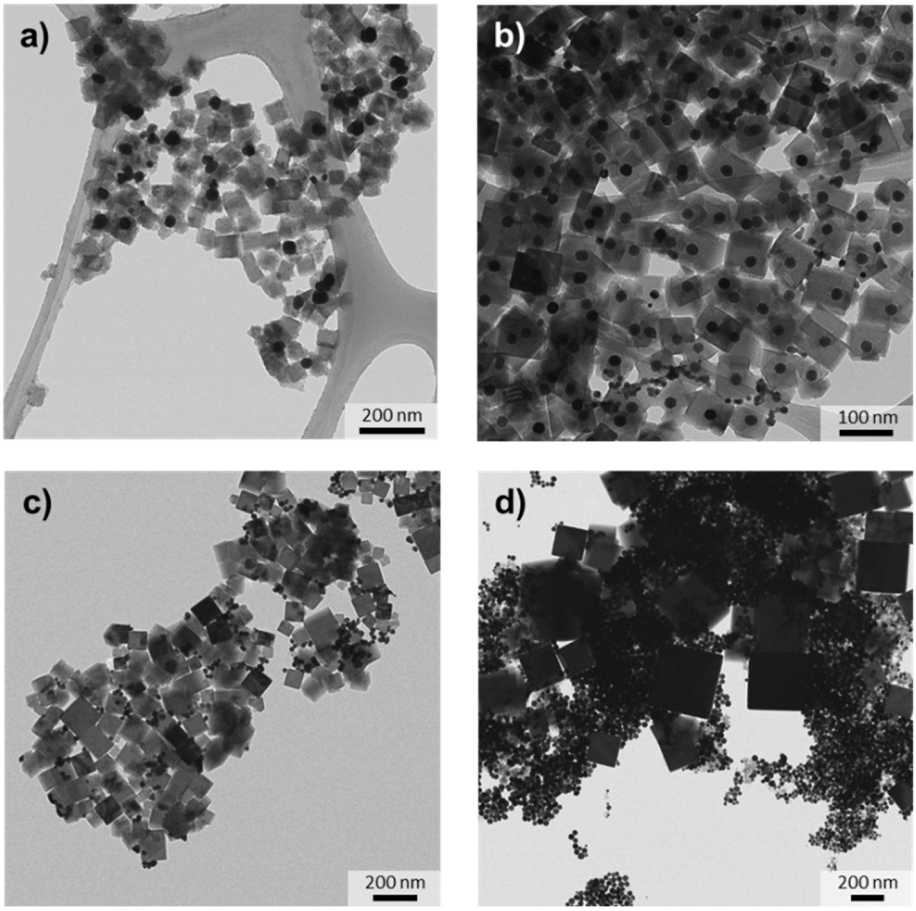

Figure 3.2 TEM images of the NPs obtained through the Au@CoFe protocol and applying the following parameters: a) addition rate of 2 $mL \cdot h^{-1}$ and time delay of 20-30 min. b) addition rate of 0.5 $mL \cdot h^{-1}$ and time delay of 20-30 min. c) addition rate of 0.5 $mL \cdot h^{-1}$ and time delay of 45 min. d) addition rate of 0.5 $mL \cdot h^{-1}$ and time delay of 0 min.

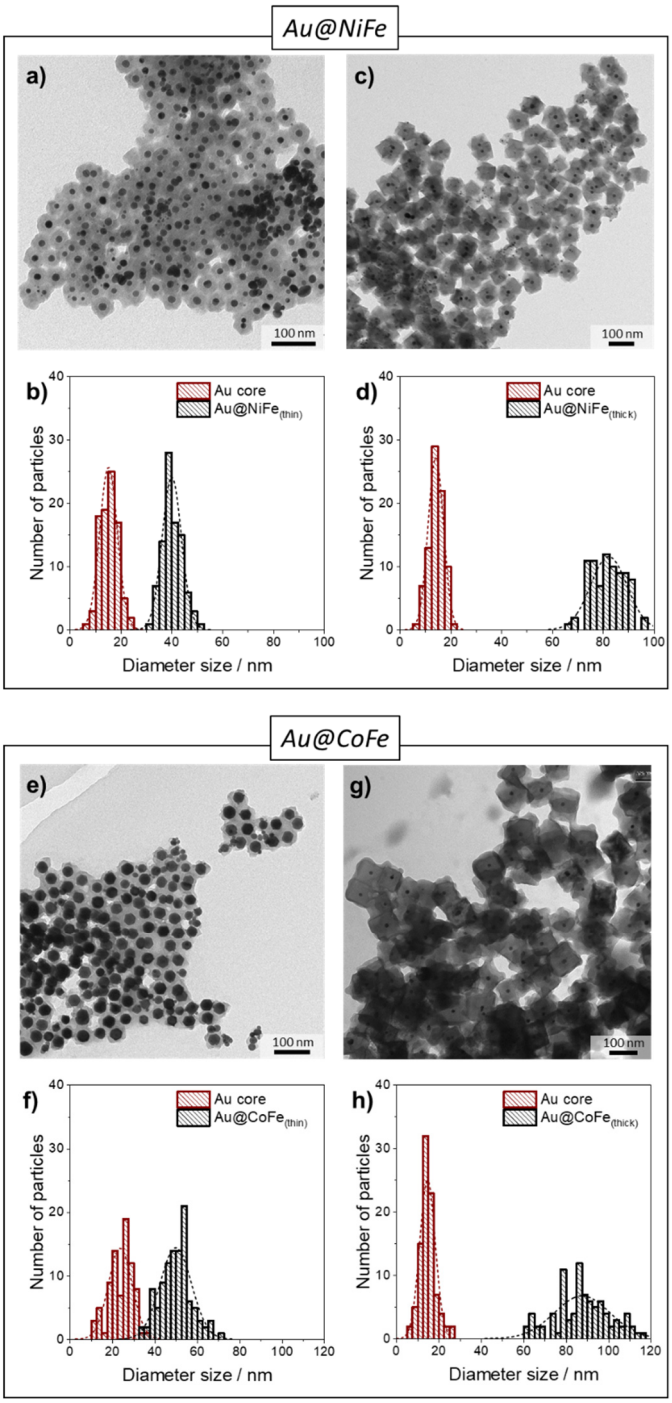

Figure 3.3 TEM images and histograms of the size distribution for Au@NiFe NPs with thinner (a, b) and thicker shells (c, d) and for Au@CoFe with thinner (e, f) and thicker shells (g, h).

Transmission Electron Microscopy (TEM) images of the hybrid NPs show a core@shell morphology formed by an Au core and a well-defined PBA shell (Figure 3.3). For NiFe, hybrid NPs with shell thicknesses of 12 ± 2 and 30 ± 3 nm were prepared, while maintaining a constant size of about 15 nm for the Au core (Figure 3.3a to 3.3d). For CoFe, shell thicknesses of 13 ± 3 and 35 ± 6 nm have been obtained, but, in contrast to those of NiFe, the size of the Au core varies from 22 to 15 nm, respectively (Figure 3.3e to 3.3h). This core size difference could be due to the major difficulties encountered in the CoFe shell synthesis for growing the PBA layer around Au.

Interestingly, the Localized Surface Plasmon Resonance (LSPR) of the Au NPs is progressively red-shifted during shell formation (Figure 3.4). It can be attributed to the progressive change in the dielectric constant around the Au surface upon the continuous overgrowth of the shell.[31,32] Such a shift of the plasmon band occurs upon the addition of the precursor salts indicating the formation of the PBA around the metallic Au surface. It is expected that NiFe and CoFe exhibit quite similar values for the dielectric constant. Indeed, by comparing the red-shift shown by Au@PBA NPs with different shell thicknesses, one can notice that for those having a 12-13 nm shell, a shift of *ca.* 21 nm is observed, while for those having a 30-35 nm shell this shift turns out to be of *ca.* 28 nm. In addition, the full width at half maximum (FWHM) of the plasmon band is slightly reduced after the PBA overgrowth. In point of fact, the modification in the dielectric constant also leads to an increase in the plasmon band intensity that decreases the FWHM (Figure 3.4). Moreover, the absence of other plasmon bands together with the small width of these bands point toward a narrow size distribution for the Au NPs. These plasmonic properties could be also beneficial for increasing the catalytic performance by light irradiation since the increase in the local temperature could reduce even more the onset potential and enhance the reaction rate.[33,34]

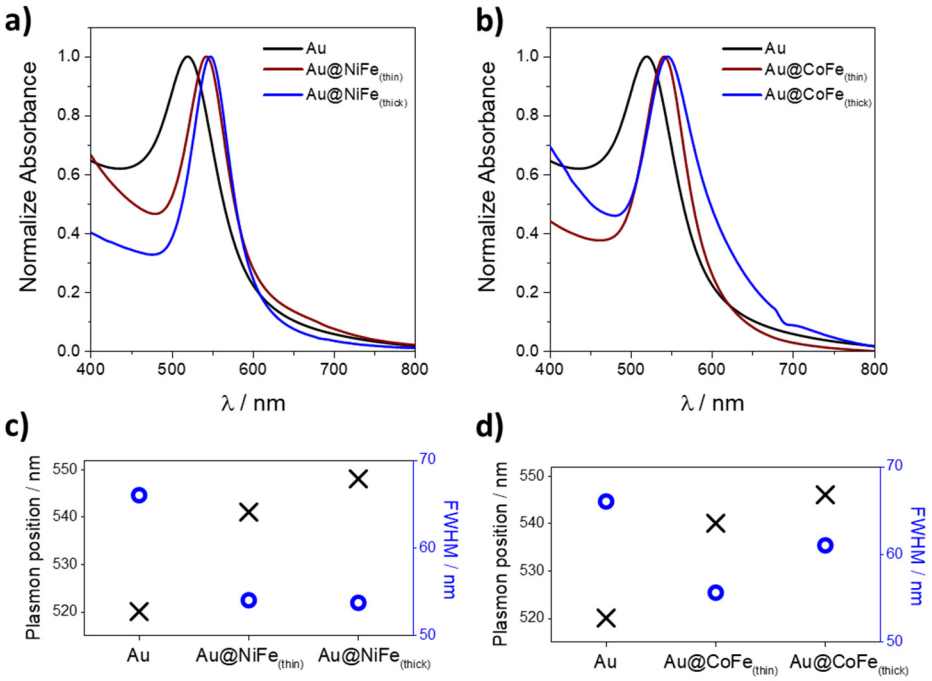

Figure 3.4 a) b) UV-Vis spectra of Au and the different Au@PBA NPs. c) d) Plasmon position and plasmon FWHM calculated for the different NPs.

Energy-dispersive X-ray spectroscopy (EDX) was carried out to ensure a homogeneous distribution of iron and nickel as well as iron and cobalt over the Au NPs (see Figures 3.5 and 3.6). The estimated Au content for the thinner and thicker shells is *ca.* 40 % and *ca.* 8%, respectively (see Table 3.1). The molecular formulas estimated by Inductively Coupled-Plasma Optical Emission Spectrometry (ICP-MS) can be found in Table 3.2. It is important to note that these PBAs do not contain many vacancies (thus, few structural defects are present[35]) since the KBH_4 provides the solution with a high amount of potassium cations.

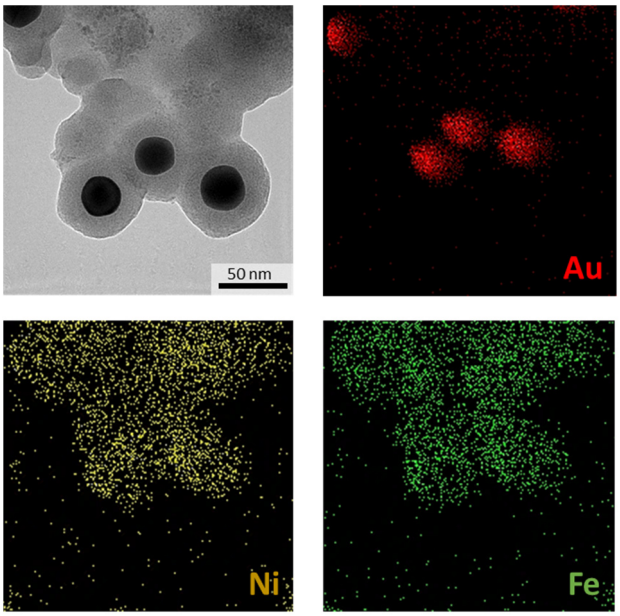

Figure 3.5 EDX mapping of the metals present in the Au@NiFe(thin). Au, Ni and Fe are represented in red, yellow and green, respectively.

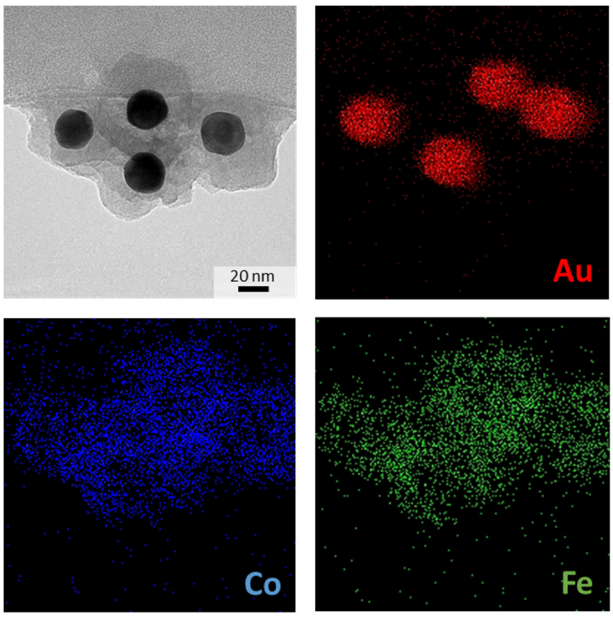

Figure 3.6 EDX mapping of the metals present in the Au@CoFe(thin). Au, Co and Fe are represented in red, blue and green, respectively.

Table 3.1 Percentage of Au (in weight) estimated for the different NPs.

Sample	*% Au (w/w)*
$Au@NiFe^{II}_{(thin)}$	39
$Au@NiFe^{II}_{(thick)}$	9
Au-NiFe	29
Au+NiFe	30
$Au@CoFe^{II}_{(thin)}$	46
$Au@CoFe^{II}_{(thick)}$	6
Au-CoFe	31
Au+CoFe	30

Table 3.2 Molecular formula estimated for the different NPs.

Sample	*Molecular formula*
$Au@NiFe^{II}_{(thin)}$	$Au_{0.88}@K_{1.60}Ni[Fe(CN)_6]_{0.90}$
$Au@NiFe^{II}_{(thick)}$	$Au_{0.13}@K_{1.44}Ni[Fe(CN)_6]_{0.86}$
NiFe	$K_{0.20}Ni[Fe(CN)_6]_{0.72}$
$NiFe^{II}$	$K_{1.04}Ni[Fe(CN)_6]_{0.76}$
$Au@CoFe^{II}_{(thin)}$	$Au_{1.10}@K_{1.52}Co[Fe(CN)_6]_{0.88}$
$Au@CoFe^{II}_{(thick)}$	$Au_{0.05}@K_{1.56}Co[Fe(CN)_6]_{0.89}$
CoFe	$K_{0.19}Co[Fe(CN)_6]_{0.73}$
$CoFe^{II}$	$K_{1.12}Co[Fe(CN)_6]_{0.78}$

X-ray photoelectron spectroscopy (XPS) was performed on a powder of these NPs to characterize the oxidation state of the metals contained in both PBA shells.

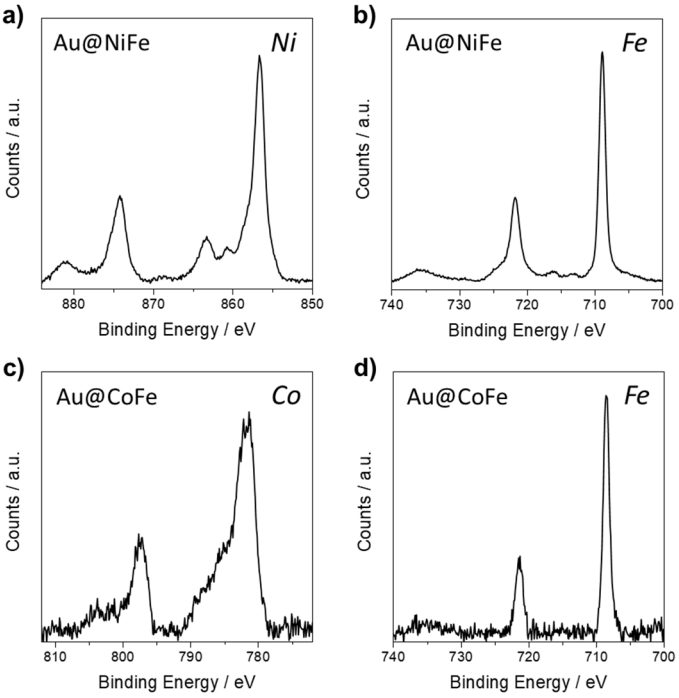

Figure 3.7 XPS spectra of Au@NiFe (up) and Au@CoFe (down).

For Au@NiFe NPs, as shown in Figure 3.7, nickel is present as Ni^{II} but iron is reduced from Fe^{III} to Fe^{II}. This is in good agreement with previous works reported in the literature[27] and with the magnetic measurements. Indeed, while the pure $Ni^{II}Fe^{III}$ PBA behaves as a magnet below *ca.* 20 K,[36] the Au@NiFe NPs stay paramagnetic down to 2 K (Figure 3.8). Similarly, while the pristine $Co^{II}Fe^{III}$ PBA possesses a magnetic ordering below 14 K,[36] Au@CoFe (*i.e.* $Co^{II}Fe^{II}$) remains paramagnetic at lower temperatures (Figure 3.8). These magnetic differences result from the reduction of Fe^{III} (with S = ½) to low spin Fe^{II} (with S = 0) in the core@shell systems. Such a reduction is promoted by the remaining KBH_4 used to reduce Au^{I} to metallic Au, which is still present in the solution. Indeed, a high concentration of this strong reductant is required to reach an equilibrium between the Au reduction and the oxidation by the cyanide. Lower amounts lead to non-stabilized Au NPs that can precipitate, avoiding the PBA shell overgrowth.

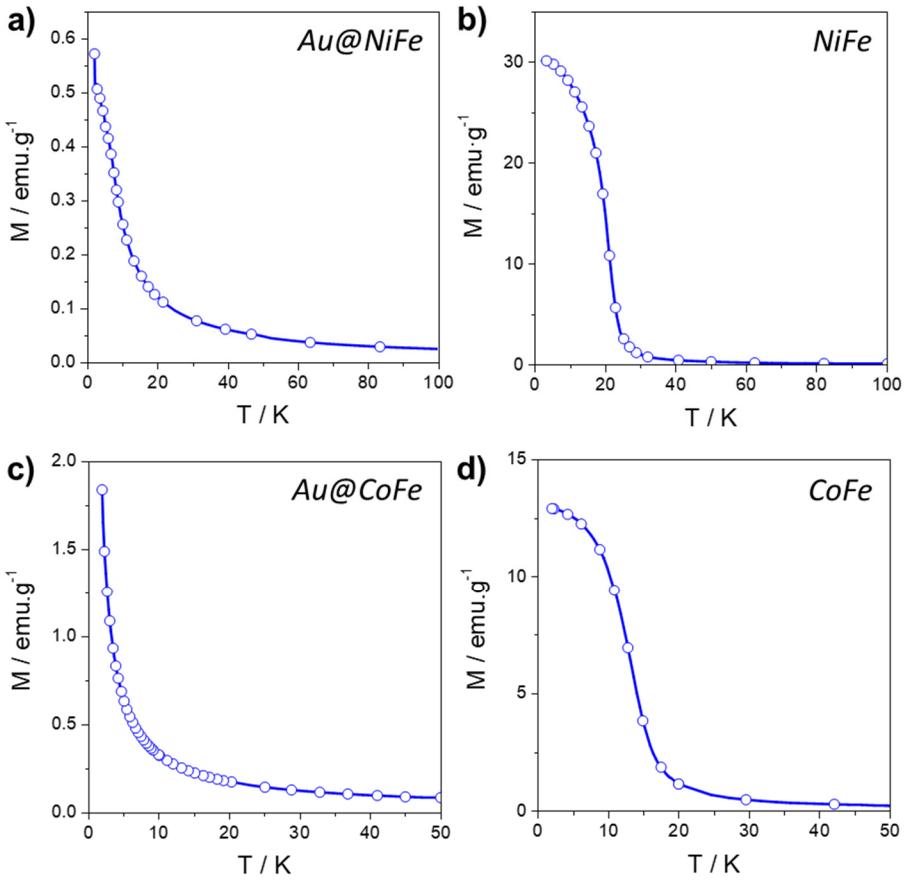

Figure 3.8 Magnetization vs. temperature curve performed for Au@NiFe and NIFe-PBA (up) and Au@CoFe and CoFe-PBA (down) NPs with an applied field of 1000 Oe.

Even though the presence of Fe^{II}, the Au@PBA heterostructures maintain the characteristic PB cubic structure in the powder X-ray diffraction (PXRD) data and the expected cyanide vibration in the Raman spectra, located at *ca.* 2150 cm^{-1} (see Figure 3.9).

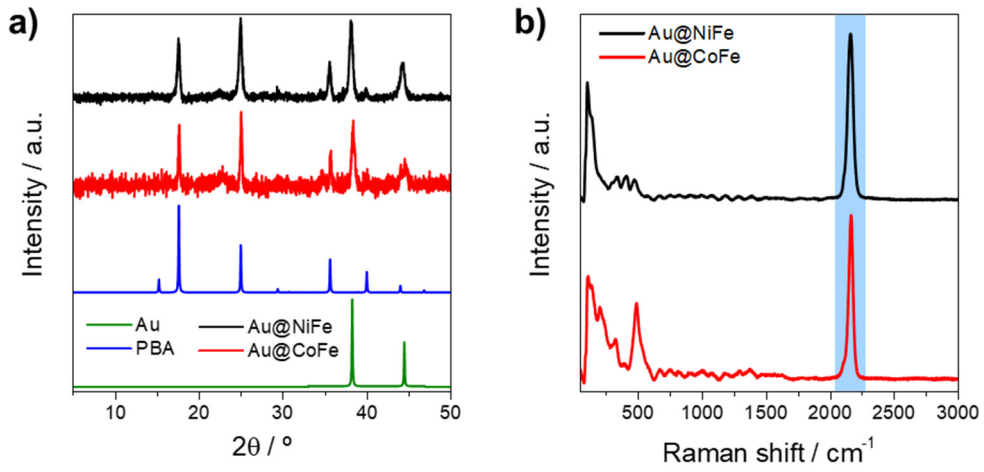

Figure 3.9 a) PXRD and b) Raman spectrum of the core@shell NPs. The cyanide vibration peak is highlighted in blue.

To verify the influence of Au on the electrochemical performance and the benefits of this sort of core@shell heterostructure, four kinds of NPs were also prepared: i) PBA NPs ($NiFe^{III}$ and $CoFe^{III}$) containing many defects (*i.e.* many vacancies) since they give rise to higher electrocatalytic performance,[37] ii) PBA with reduced Fe^{II} ($NiFe^{II}$ and $CoFe^{II}$) iii) PBA NPs decorated with Au NPs on its surface (Au-PBA)[38] and PBA NPs physically mixed with Au NPs (Au+PBA). TEM images of these systems and their respective histograms can be found in Figures 3.10 - 3.13. PBA NPs with a lot of defects were synthesized in order to get worthy references for the comparison.

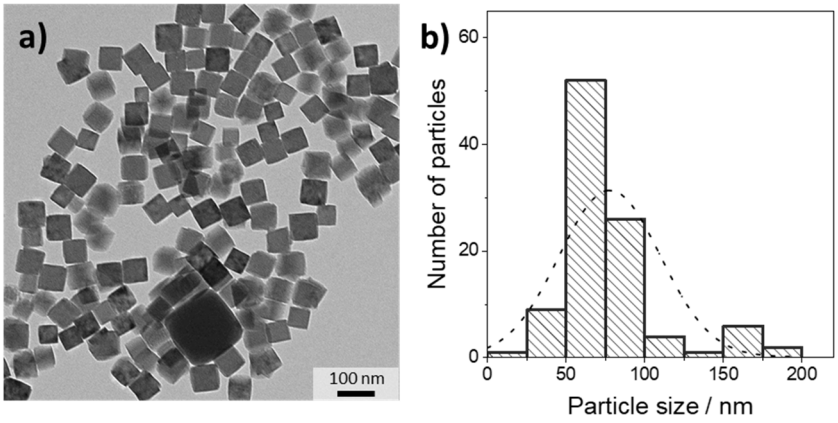

Figure 3.10 PBA-NiFe^{II} NPs and their corresponding histogram.

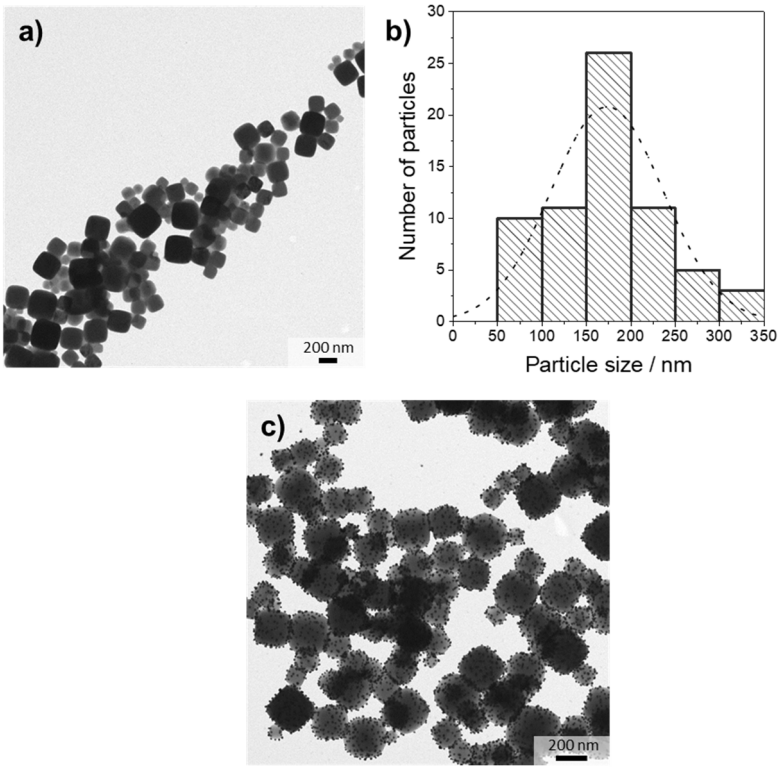

Figure 3.11 a) b) PBA-NiFe NPs and their corresponding histogram. c) Au-decorated PBA-NiFe NPs.

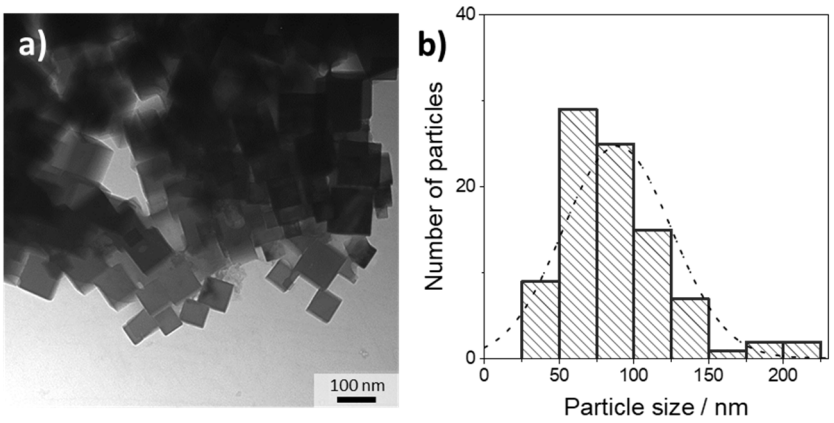

Figure 3.12 PBA-CoFe^{II} NPs and their corresponding histogram.

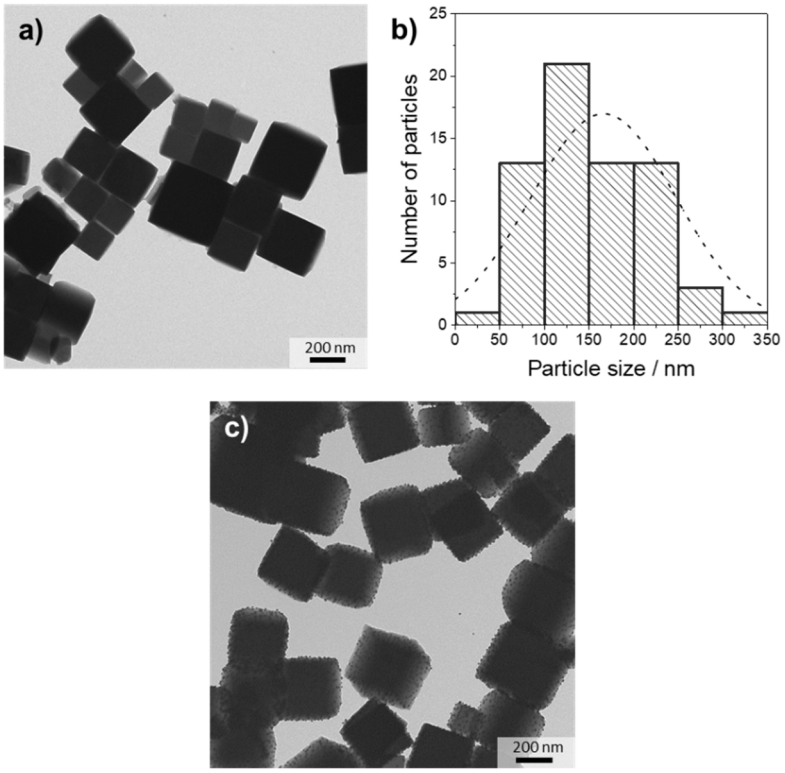

Figure 3.13 a) b) PBA-CoFe NPs and their corresponding histogram. c) Au-decorated PBA-CoFe NPs.

The different obtained NPs were tested as OER electrocatalysts. Prior to that, Cyclic Voltammetry (CV) curves were examined to analyze the redox processes. The Au@NiFe NPs exhibit redox peaks in a similar position as those observed for PBA-NiFe NPs of similar size (around 1.2 – 1.5 V), which are related to Ni processes (Figure 3.14).[39] In the CoFe compound, for all NPs it can be found a small redox couple between 1.2 and 1.4 V which can be assigned to Co redox process (Figure 3.15).[40]

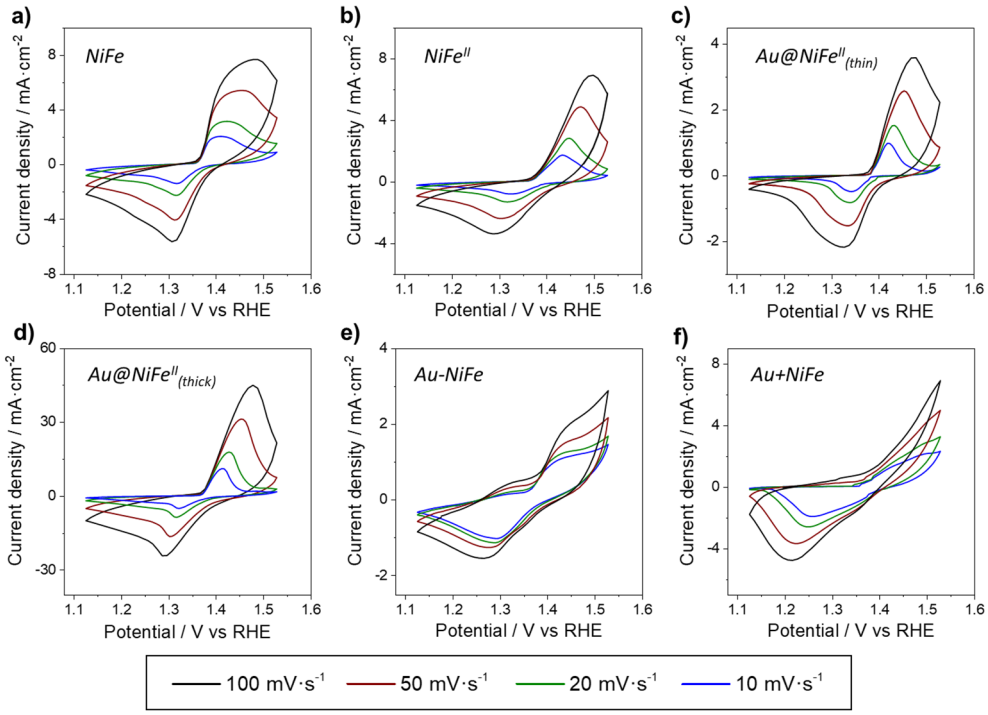

Figure 3.14 CVs performed at different scan rates in 1 M KOH aqueous solution for different NiFe NPs: a) PBA, b) PBA with Fe^{II}, c) Au@PBA (thin shell), d) Au@PBA (thick shell), e) Au decorated PBA NPs and f) physical mixture of Au and PBA NPs.

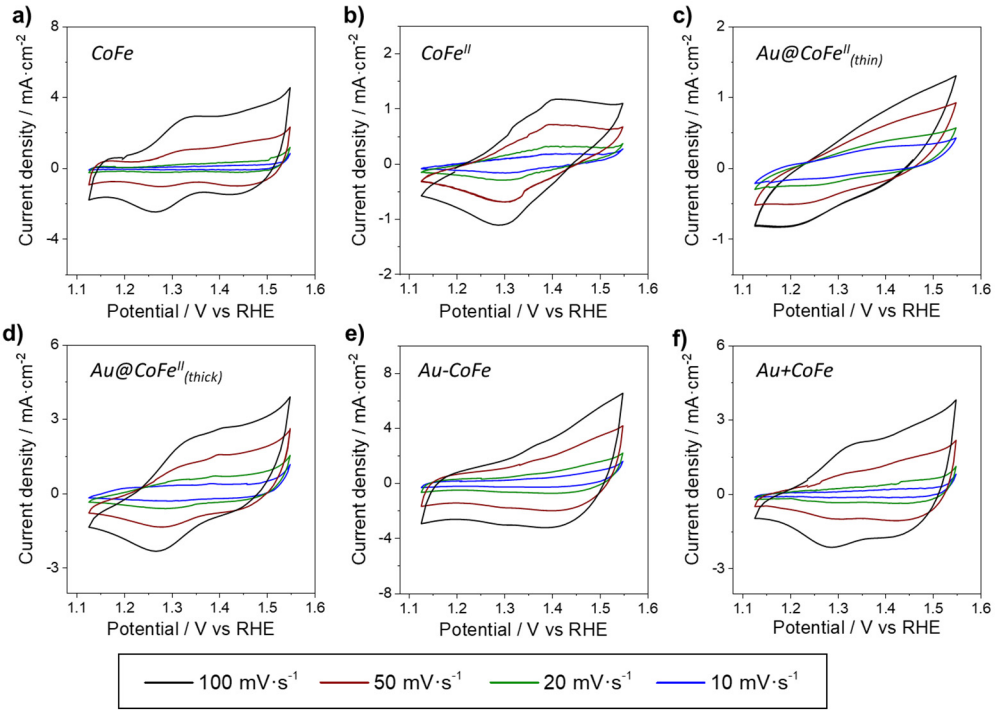

Figure 3.15 CVs performed at different scan rates in 1 M KOH aqueous solution for different CoFe NPs: a) PBA, b) PBA with Fe^{II}, c) Au@PBA (thin shell), d) Au@PBA (thick shell), e) Au decorated PBA NPs and f) physical mixture of Au and PBA NPs.

Observing the dependence of the charge on the applied potential, it can be noticed that NiFe compounds (Figure 3.16) display almost reversible peaks (closed coulovoltammetric loops[41,42]) whereas, in CoFe compounds, an excess anodic charge (open coulovoltammetric loops[41,42]) was detected (Figure 3.17). This irreversible charge is a consequence of the low onset potential of the OER that leads to the irreversible formation of O_2. To the best of our knowledge, this is the first time that coulovoltammetry is used to study irreversible electrocatalytic reactions. As it is demonstrated here, this is a useful technique since it brings the possibility to separate charges consumed by electrodic redox processes from charges expended by irreversible electrocatalytic processes, as oxygen evolution here, when both processes overlap in the same potential range. Therefore, this technique can provide

a deeper study of both, the onset OER potential and the evolution of the oxygen production. In this work, coulovoltammetry has been used to extract and analyze the reversible charges of the different compounds.

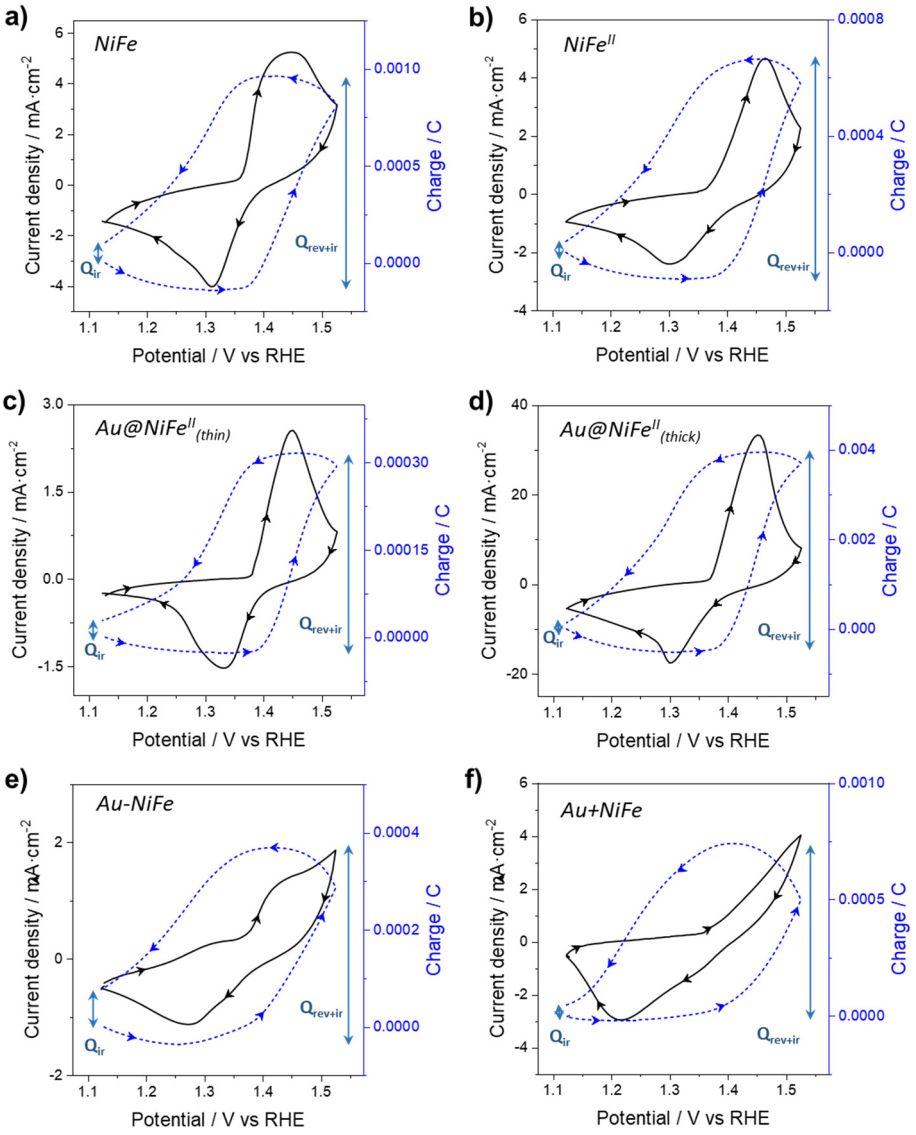

Figure 3.16 Evolution of the consumed charge parallel to the voltammetric response to the CV performed at 50 mV·s^{-1} in 1 M KOH aqueous solution for NiFe compounds.

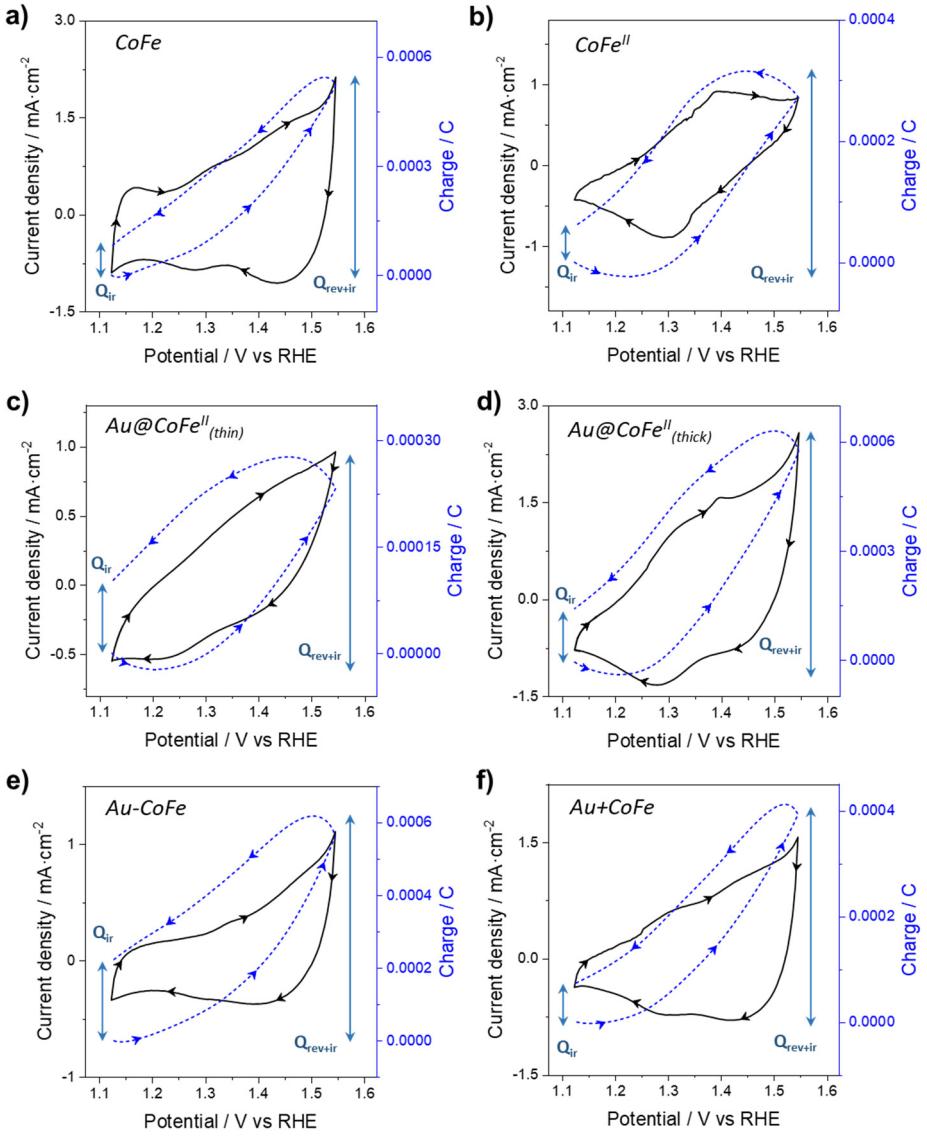

Figure 3.17 Evolution of the consumed charge during the voltammetric response to potential cycles performed at 50 $mV \cdot s^{-1}$ in 1 M KOH aqueous solution for CoFe compounds.

Remarkably, important differences in the current density and reversible charge are observed in the NPs, especially for the NiFe systems (Figures 3.14 - 3.17). Thus, compared to the pristine $NiFe^{III}$ and $NiFe^{II}$, the system Au@NiFe with a thin shell

displays lower current density values, possibly due to the low content of electroactive NiFe material, which represents *ca.* 60% of the total mass. In fact, if one takes into account the electroactive mass for these three cases, the current density and the total charge coming from these redox processes are quite similar (see Figure 3.18), suggesting that the density values are controlled by the percentage of electroactive PBA. Interestingly, this rule is not followed for Au@NiFe NPs with a thick shell. Then, with around 90 % (in weight) of NiFe, the current densities are about 5 times greater for the core@shell NPs as compared with those of the $NiFe^{II}$ NPs and even with those of the pristine $NiFe^{III}$ NPs.

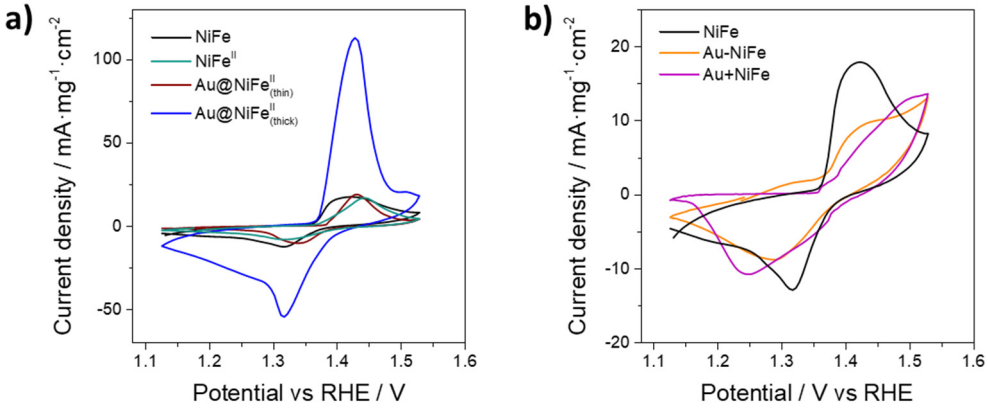

Figure 3.18 CVs performed at 20 $mV \cdot s^{-1}$ in 1 M KOH aqueous solution for NiFe compound compared to: a) $NiFe^{II}$ and the electroactive species of Au@NiFe(thin) and Au@NiFe(thick); and b) the electroactive species of Au-NiFe and Au+NiFe.

This strong and anomalous enhancement in the current density could be related to the increase in the conductivity of the hybrid material (compared with that of pristine PBA NPs), as well as with the number of electroactive sites. In this line, using Faraday's law of electrochemical reactions (Equation 3.1) and the redox charges extracted from Figures 3.16 and 3.17, the total PBA mass involved in the redox processes was estimated.

$$m = \frac{Q}{F} \cdot \frac{M}{z} \qquad \textbf{(Equation 3.1)}$$

In this equation, m is referred to the mass (g), Q to the charge corresponding to the reversible redox process, M to the molecular weight of the sample and z to the total number of electrons taking part in the redox process. Q was calculated by subtracting the total charge involving both reversible and irreversible reactions (Q_{rev+ir}) and the charge consumed by the irreversible oxygen evolution, (Q_{ir}) calculated in Figures 3.16 and 3.17. The reversible charge allows the calculations of the number of electroactive metal atoms. The redox processes of NiFe compounds are associated with the oxidation/reduction of Ni. Here, the initial Ni^{II} is firstly oxidized to a mixed valance state of Ni^{III}/Ni^{IV}. Therefore, for these materials, calculations were carried out considering one (z = 1) or two (z = 2) electrons involved in the reaction. For the CoFe compounds, the redox processes associated with the reaction of Co^{II} and Co^{III} involve only one electron (z = 1).

Table 3.3 Amount of PBA material being oxidized or reduced in cyclovoltamperometry.

Samples	PBA mass (mg/cm^2)	z = 1		z = 2	
		PBA e.a. mass (mg/cm^2)	PBA e.a. (%)	PBA e.a. mass (mg/cm^2)	PBA e.a. (%)
NiFe	0.25	0.049	19.2	0.025	9.6
$NiFe^{II}$	0.25	0.031	10.9	0.015	5.5
$Au@NiFe^{II}_{(thin)}$	0.14	0.017	13.6	0.008	6.8
$Au@NiFe^{II}_{(thick)}$	0.23	0.174	72.0	0.087	36.0
Au-NiFe	0.17	0.012	6.5	0.006	3.3
Au+NiFe	0.17	0.210	12.4	0.105	6.7
CoFe	0.25	0.016	6.3		
$CoFe^{II}$	0.25	0.012	4.5		
$Au@CoFe^{II}_{(thin)}$	0.12	0.0074	5.4		
$Au@CoFe^{II}_{(thick)}$	0.24	0.031	13.1		
Au-CoFe	0.18	0.013	6.9		
Au+CoFe	0.17	0.011	6.4		

e.a. = electroactive

For pristine PBA, the PBA of Fe^{II} and Au@PBA(thin), it was found that the reduced or oxidized PBA mass is below 20 % of the total PBA electrodic mass (See Table 3.3), suggesting that only the surface of the PBA material is electrochemically

active. Higher electroactive percentages of the PBA mass were estimated for the core@shell heterostructures with a thick shell. Indeed, compared to the PBA of Fe^{II}, in the case of Au@NiFe(thick), an increment in the mass of electroactive species of around 600 % was calculated, while for the Au@CoFe(thick) system, this increment was found to be around 300 %. These results are in good agreement with the increase of the electrochemical surface area (ECSA) found for these compounds (Figure 3.19). The ECSA represents the number of electroactive sites in the catalyst and some studies have indicated that Au contributes remarkably to the enhancement of this parameter.[43] Thus, it is reasonable to assume that a higher ECSA implies a better material because it implies that more electrocatalyst sites are available for the electrochemical reaction, here the OER. In our case and compared to the respective PBAs of Fe^{II}, an increment in the number of electroactive species of around 350 % was calculated for Au@NiFe(thick), while this increment was found to be around 500 % for the Au@CoFe(thick) system. Here the role of Au is the activation of the PBA shell, facilitating the interaction between the oxidized/reduced species and the electrolyte thanks to the close contacts established in this kind of core@shell heterostructure between the Au core and the PBA shell. This fact is corroborated by comparing these results with the lower current densities obtained in systems where the contacts between the two components are much weaker (PBA NPs decorated with Au NPs, Au-PBA) or inexistent (physical mixture of both NPs, Au+PBA) (see Figures 3.14, 3.15 and 3.18). These compounds display ECSA values considerably higher than that of the PBA NPs because Au exhibits a huge ECSA by itself (value of 0.18 $\mu F \cdot cm^{-2}$) when it is exposed to the electrolyte. Thus, these larger and activated PBA sites from the core@shell heterostructures could be exploited in order to increase the number of sites contributing to electrocatalytic reactions such as the OER.[44]

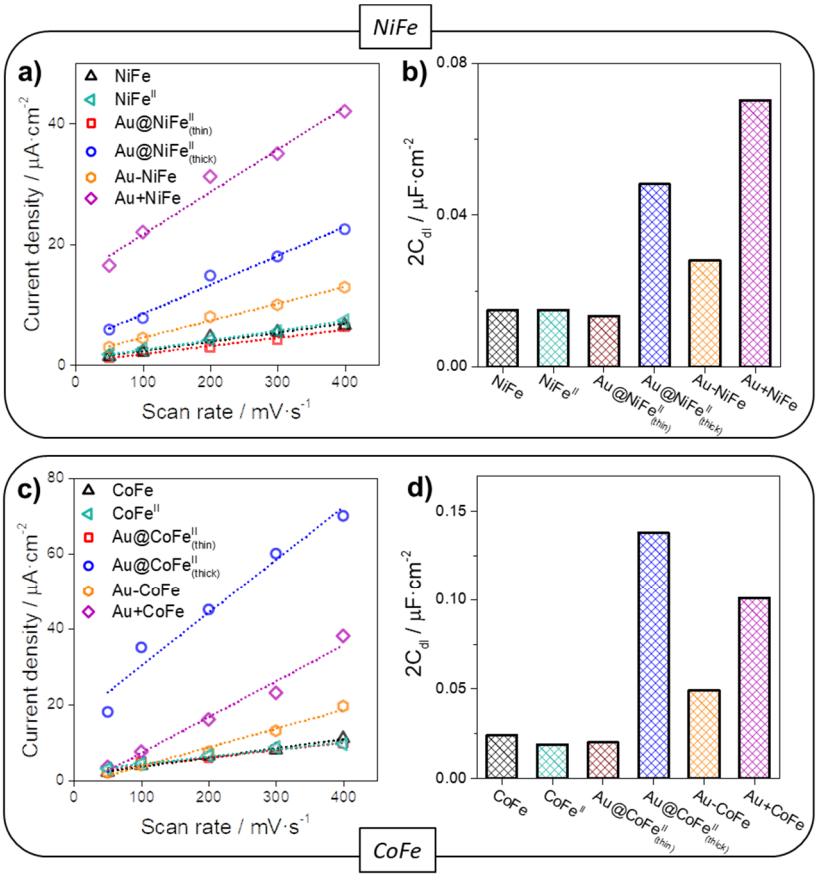

Figure 3.19 Linear slopes representing the ECSA calculated from CVs performed in a non-faradaic region at different scan rates for NiFe (a) and CoFe (c) PBA compounds. ECSA values of the different NPs of NiFe (b) and CoFe (d) PBA compounds.

Electrocatalytic activities of different NPs, with and without Au, were tested and compared by measuring Linear Sweep Voltammetry (LSV) performed at a slow scan rate to minimize the capacitive current (see Figures 3.20a and 3.21A). Figures 3.20b and 3.21b display a zoom of the starting catalytic region to evidence the electrocatalytic differences. It is important to remark that these curves were not corrected with the solution resistance (*iR*, R value of 3 ± 1 Ω) to make a fair comparison of the intrinsic electrocatalytic behavior of each sample. When we compare the polarization curves to the PBA NPs of Fe^{II}, it can be easily observed that both Au@PBA (with a thick and a thin shell) display lower onset potentials.

Furthermore, the lowest onset potentials are reached with a thicker shell, obtaining values even better than the pristine PBA with many defects (NiFe and CoFe). On the other hand, both, Au-PBA and Au+PBA do not result advantageous in terms of electrocatalysis. In these two cases, Au is exposed to the electrolyte, oxidizing at higher overpotentials in such a way that their LSV resembles the one recorded for Au. At this point, it is essential to mention that in the case of PBA NPs decorated with Au NPs, a polymer is used to connect both systems. Then, the polymer matrix surrounding Au NPs decreases the conductivity of the heterostructure leading to a lower electrocatalytic performance compared to that observed in the physical mixture (Au+PBA). To analyze the electrocatalytic behavior, some key parameters were compared:

(1) The overpotential required at 10 $mA \cdot cm^{-2}$ (horizontal dotted lines, Figures 3.20a and 3.21a). The overpotential required at 10 $mA \cdot cm^{-2}$ was chosen because it is the approximate current density expected for a 10% efficient solar-to-fuels conversion device under 1 sun illumination.[45]

(2) The current density recorded at an overpotential of 350 mV, corresponding to the vertical dotted lines (Figures 3.20b and 3.21b).

(3) The Tafel slopes. This parameter indicates how much it is necessary to increase the overpotential to rise the reaction rate (thus, the current density) by an order of magnitude.

Figures 3.20c and 3.21c evidence that a thin shell leads to lower overpotentials but increasing the shell thickness significantly conduces to a further decrease of these values. Indeed, this parameter is reduced from 465 mV to 426 and then to 375 mV for $NiFe^{II}$, Au@NiFe(thin) and Au@NiFe(thick), respectively. For $CoFe^{II}$, Au@CoFe(thin) and Au@CoFe(thick), the overpotential is decreased from 405 mV to 380 and then to 357 mV, respectively. A similar trend was observed for the current densities flowing at a fixed overpotential of 350 mV (Figures 3.20d and 3.21d). Here, the current density is increased for Au@NiFe(thick) from 1.6 to 5.1 $mA \cdot cm^{-2}$ (*i.e.* an improvement of 320 %) and for Au@CoFe(thick) from 1.9 to 8.1 $mA \cdot cm^{-2}$ (*i.e.* an improvement of 420 %). Besides, the results obtained for Au@PBA with a thick shell exceed considerably the performance recorded for a highly defective pristine PBA

(NiFe and CoFe). On the other hand, when Au is exposed to the electrolyte (Au-PBA and Au+PBA samples), the heterostructure does not seem to be electrocatalytic at these overpotentials (Figures 3.20a and 3.21a) even if they display superior ECSA (Figure 3.19). Therefore, the electrocatalytic enhancement is originated thanks to the presence of a larger number of activated PBA sites as it occurs in a thick PBA layer surrounding Au.

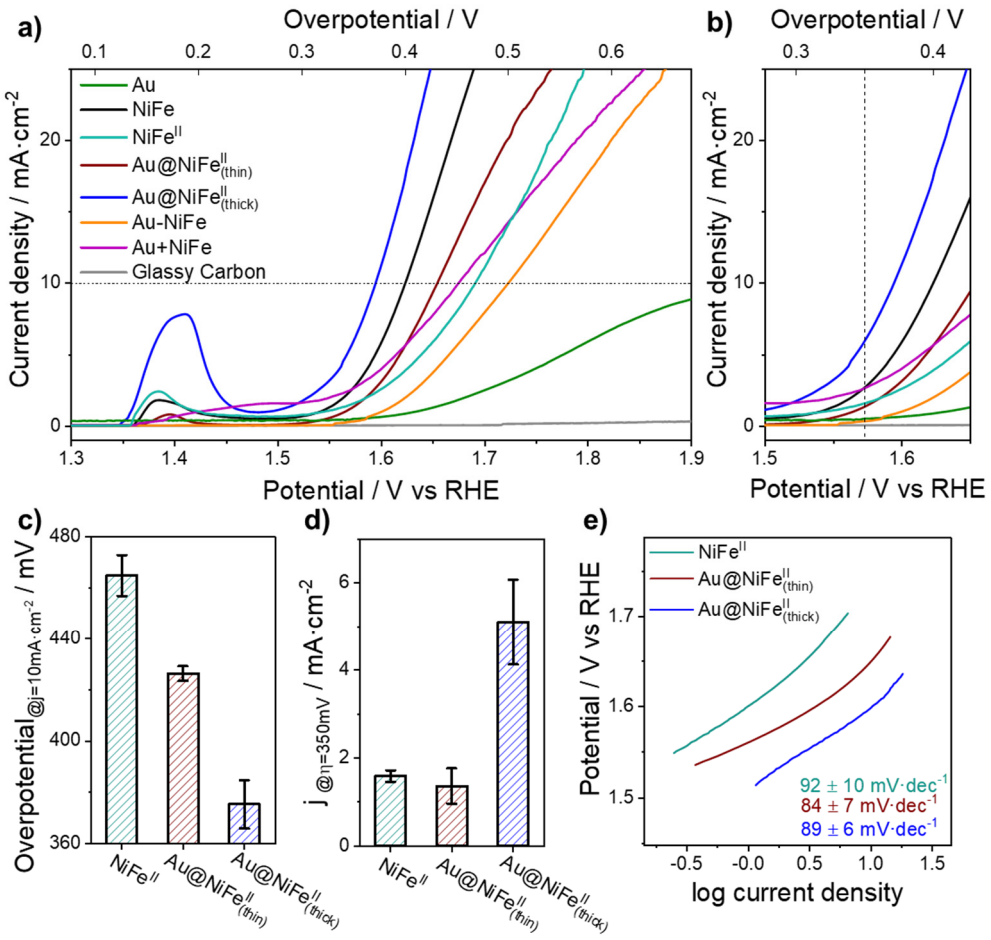

Figure 3.20 a) Linear Sweep Voltammetry of the different NiFe NPs measured at 5 $mV \cdot s^{-1}$ in 1 M KOH aqueous solution. b) Zoom of Figure 3.20a exhibiting the beginning of the OER. c) Overpotential required for a current density of 10 $mA \cdot cm^{-2}$ for NiFe NPs. d) Current density obtained at an overpotential of 350 mV for NiFe NPs. e) Tafel slopes calculated from LSV data for NiFe NPs.

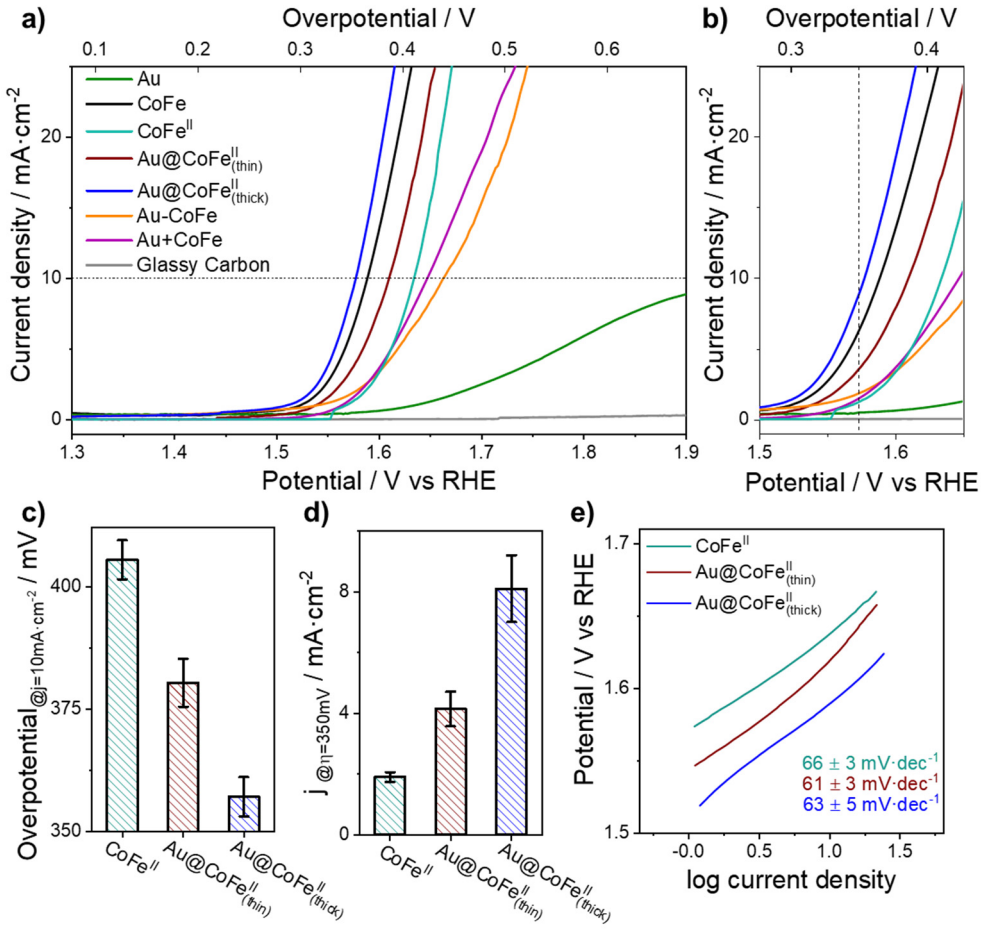

Figure 3.21 a) Linear Sweep Voltammetry of the different CoFe NPs measured at 5 $mV \cdot s^{-1}$ in 1 M KOH aqueous solution. b) Zoom of Figure 3.21a exhibiting the beginning of the OER. c) Overpotential required for a current density of 10 $mA \cdot cm^{-2}$ for CoFe NPs. d) Current density obtained at an overpotential of 350 mV for CoFe NPs. e) Tafel slopes calculated from LSV data for CoFe NPs.

To investigate the intrinsic catalytic activity of the PBA sites, turnover frequency (TOF) values were calculated at an overpotential of 350 mV (Figure 3.22). Considering de total number of PBA centers, Au@PBA nanostructures with thick shells exhibit the highest values. This result is not unexpected since these heterostructures display the best OER performance. Nevertheless, if the TOF is calculated considering only the electroactive PBA centers previously estimated (Table 3.3), Au@PBA with thin shells show the highest values. In fact, the proximity of the Au core and the PBA centers enhances their intrinsic activity. In this way, these hybrids have the lowest number of PBA centers, but they are more active, giving rise to better performance than the PBA of Fe^{II}. Still, in a thick PBA shell, Au is able to slightly activate the PBA centers. Therefore, Au can increase the total number of electroactive sites but also enhances their intrinsic activity. Additionally, it is worth mentioning that Au+PBA physical mixtures exhibit large variability in the TOF values. The reason is that only the catalytic activity of PBA centers close to the Au NPs is enhanced and this is difficult to control due to the preparation procedure. In this sense, the physical mixture of Au NPs and PBA (Au+PBA) does not result to be suitable electrocatalysts.

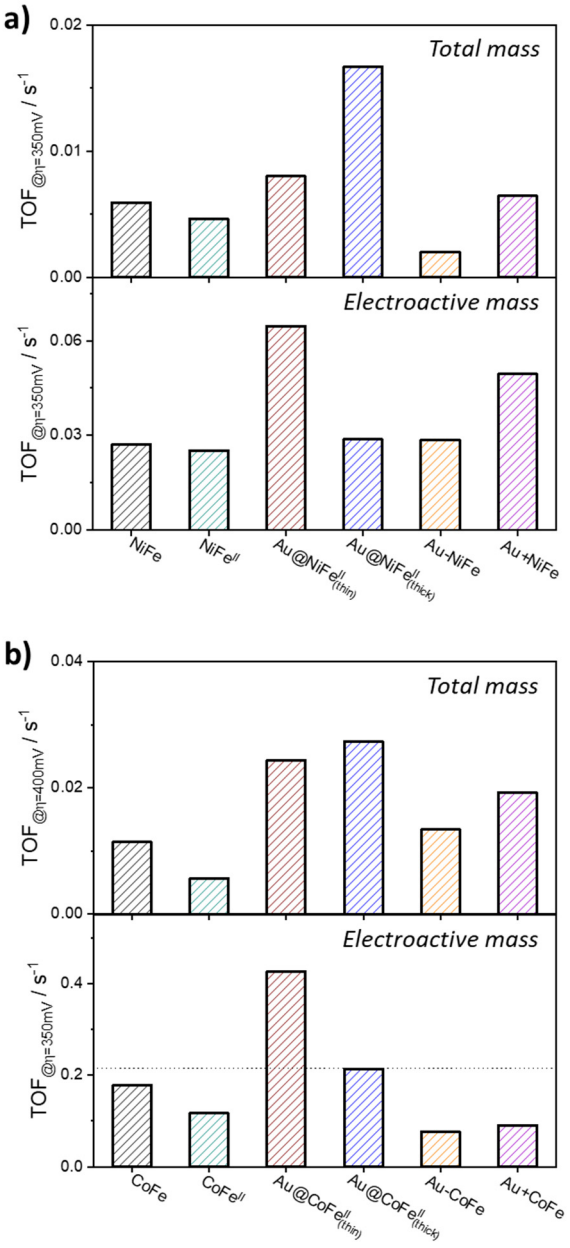

Figure 3.22 Turnover frequencies calculated at 0.35 V overpotential for NiFe compounds (a) and CoFe compounds (b). TOF values were calculated using the total PBA mass or the electroactive PBA mass previously obtained considering z = 1 (see Table 3.3).

Regarding the kinetics, Figures 3.20e and 3.21e show the Tafel slope values calculated from the LSV data for NiFe and CoFe compounds, respectively. Interestingly, when Au oxidation is not taking place (either the absence of Au or the core@shell structure) the NPs exhibit quite similar slopes in agreement with the fact that in the core@shell NPs, the PBA is the only electroactive species exposed to the electrolyte solution. Therefore, it is expected that all NPs would behave kinetically very similar. In fact, the addition of Au decreases the onset potential significantly but it does not affect the Tafel slope, possibly indicating that Au reduces the limiting potential of the catalyst with no variation in the reaction kinetics. These results are in good agreement with those reported for other core@shell structures based on an Au core[15,46], suggesting that this kind of nanostructure has a strong synergistic effect between the core and the shell. To confirm this point, Electrochemical Impedance Spectroscopy (EIS) measurements were performed (Figures 3.23a and 3.23b).

EIS is a technique based on the analysis of electrical circuits and describes the response of a circuit to an AC current or an AC voltage. Interestingly, the different electrochemical processes taking place in an electrode can be represented by different electrical components (*e.g.* resistors, capacitors or inductors) which networks are called equivalent circuits. The technique consists of measuring the AC current response, the phase shift and the amplitude changes over an extensive frequency range after applying a small AC potential (*e.g.* less than 10 mV) to an electrode. Examining the current response over a range of frequencies allows the separation of processes which occur on different timescales, making it an ideal tool for separating the different electrochemical processes.

Impedance expands the concept of resistance to AC circuits. Indeed, when working at DC, the resistance is defined by Ohm's law as V = IR. However, when the frequency is not zero (*i.e.* AC), the equation turns out to be V = IZ. Z corresponds to the impedance, which exhibits the same units as the resistance (ohm). As the resistance, the impedance is the opposition that a circuit presents to a current when a voltage is applied. However, depending on the applied frequency, capacitors and inductors can also interfere with the electrons flow, contributing to the impedance value. Thus, Z is a complex number composed of a real part, Z', and an imaginary part, Z" (Equation 3.2).

$$Z = Z' + iZ''$$ (**Equation 3.2**)

The real part (Z') is related to the electronic resistivity, while the imaginary part (Z") is mainly associated with capacitive effects. The representation of Z" as a function of Z' at different frequencies (Nyquist plot) permits to distinguish the electrochemical processes such as the resistance of the redox reactions.[47,48]

The equivalent circuits used to fit the EIS data are shown in Figures 3.23e and 3.23f. Constant phase elements (CPEs), which are non-ideal capacitances, were introduced to provide a good match with the experimental data because of the possible surface roughness, physical non-uniformity and the non-uniform distribution of the electroactive sites. When PBA is the only species interacting with the electrolyte, the equivalent circuit is composed of a resistance coming from the ionic transport through the solution and the current collectors (R_s) connected in series with a first parallel branch (R_{int} and CPE_{int}) corresponding to the interfacial contact between the NPs and the Glassy Carbon. These three elements are observed in the high-frequency region. In the low-frequency region, OER processes occurring on the PBA surface are represented by a second parallel branch (R_{PBA} and CPE_{PBA}). As observed in Figures 3.23c and 3.23d, R_{PBA} is significantly decreased due to the existence of defects in the PBA NPs, but an extraordinary drop is observed for the Au@NiFe heterostructures, leading to an enhancement of the electrocatalytic properties. As expected, a thinner PBA shell gives rise to lower resistance. Still, the incorporation of 5-10 % (in weight) of Au is enough to reduce this resistance by 4 for the NiFe and by 3 in the CoFe.

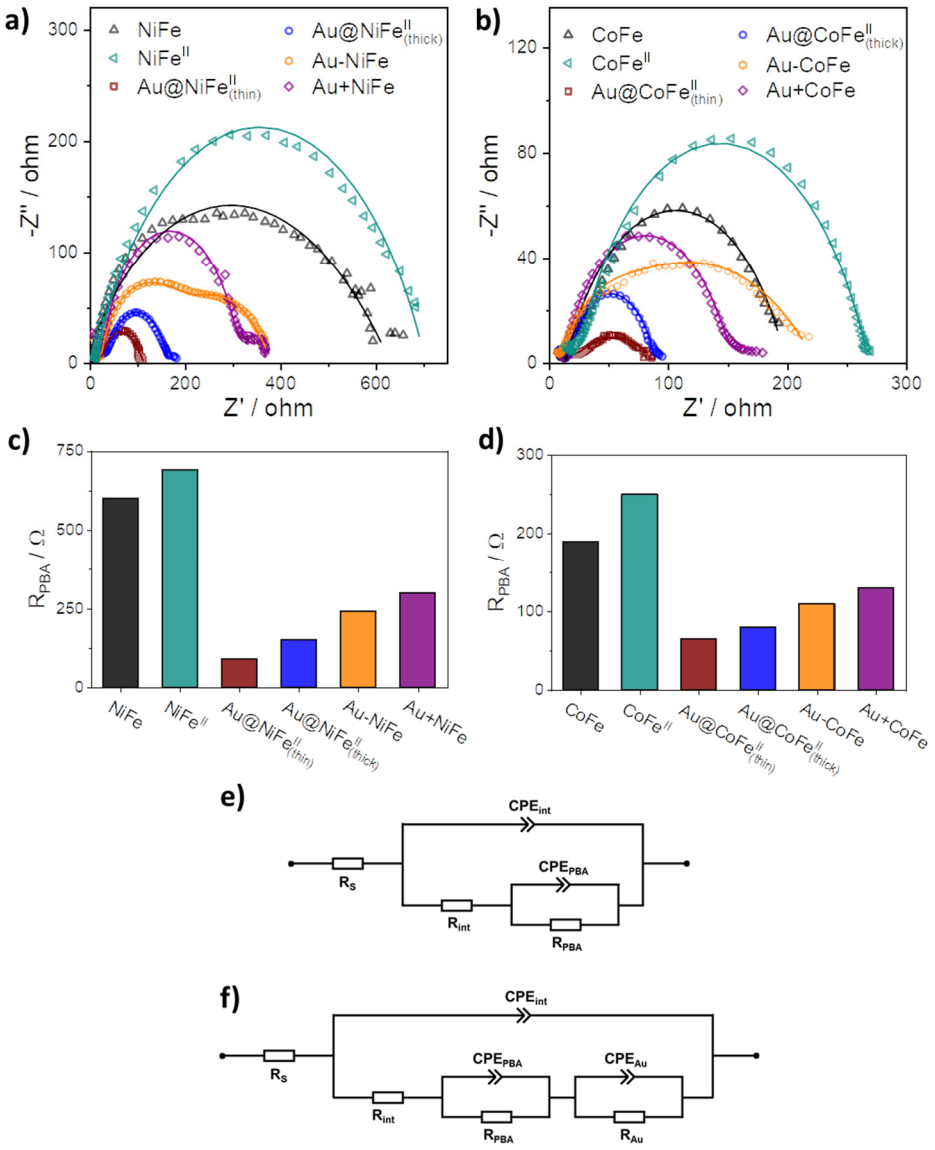

Figure 3.23 a) b) Nyquist plots of the different samples recorded at an overpotential of 0.4 V. Points correspond to experimental data, and lines are curves fitted with the equivalent circuit. Resistance values of the PBA associated with the OER process for c) NiFe compounds and d) CoFe compounds. These resistance values were calculated from the equivalent circuit. e) Equivalent circuit used for the two PBA NPs, Au@PBA(thin) and Au@PBA(thick). f) Equivalent circuit used for Au-PBA and Au+PBA.

Summarizing, by comparing the different systems exhibiting the same Au loading (*i.e.* Au@PBA(thin), Au-PBA and Au+PBA), one can conclude that the appropriate design of the heterostructure is crucial in order to maximize the electrocatalytic activity. In fact, Au activates the PBA sites and increases the conductivity of the hybrid but must be protected to prevent its oxidation. In this case, the Au@PBA system turns out to be the most suitable nanoarchitecture. Here, a thick PBA layer further improves the catalytic performance thanks to the larger number of activated PBA sites acting on the OER and the still important increment in conductivity.

Compared with previously reported OER electrocatalysts where their electrical conductivity was improved following different strategies in order to decrease the onset potential, our strategy turns out to be very useful (Table 3.4). Indeed, the introduction of small amounts of Au in a core@shell structure gives rise to a higher reduction of the voltage than using reduced graphene oxide (rGO). In addition to this, the overpotentials at 10 $mA \cdot cm^{-2}$ match the values obtained for IrO_2 and are comparable to other reported electrocatalysts (Table 3.5). Furthermore, our electrocatalysts still display room for improvement since the electrochemical activity can be further improved by using other supporting electrodes (such as Ni foam) and by subjecting the heterostructures to different thermal and physical pre-treatments (such as plasma activation).

Table 3.4 Comparison of overpotential improvement for the OER using previously reported strategies to increase the electrical conductivity of the electrocatalyst.

Sample comparison		Overpotential decrease at 10 $mA \cdot cm^{-2}$ (mV)	Reference
Au@NiFe PBA	NiFe PBA	92	This work
Au@CoFe PBA	CoFe PBA	51	This work
Au@Co_3O_4	Co_3O_4	50	15
$ZnCo_2O_4$/Au/CNTs	$ZnCo_2O_4$/CNTs	31	43
Au@NiO	NiO	90	46
Au@$CoFeO_x$	$CoFeO_x$	39	46
CNTs-Au@Co_3O_4	CNTs@Co_3O_4	50	49
Au/NiFe LDH	NiFe LDH	30	50
Ag+$Co(OH)_2$	$Co(OH)_2$	30	51
Ag@$Co(OH)_2$	$Co(OH)_2$	100	51
NiFe-rGO LDH	NiFe LDH	30	52
NiO-$NiFe_2O_4$/rGO	NiO-$NiFe_2O_4$	75	53
$Co(OH)_2$/SWNT	$Co(OH)_2$	40	54
$FeCoYO_x$ – Ni foam	$FeCoYO_x$ – GC	27	55

GC= Glassy Carbon

Table 3.5 Comparison of the electrocatalytic activity with previous reported OER electrocatalysts.

Sample	Overpotential at 10 mA·cm^{-2} (V vs RHE)	Solution	iR correction	Electrode	Reference
Au@NiFe	1.59	1M KOH	no	GC	This work
Au@CoFe	1.57	1M KOH	no	GC	This work
Au@Co_3O_4	1.61	0.1 M KOH	yes	GC	15
Au@$CoFeO_x$	1.55	1M KOH	yes	GC	46
Au@NiO	1.63	1M KOH	yes	GC	46
CoFe LDH	1.65	1M KOH	no	GC	44
NiFe LDH	1.58	1M KOH	yes	GC	56
IrO_2	1.57	1M KOH	yes	GC	56
CNTs-Au@Co_3O_4	1.58	1M KOH	no	GC	49
NiFe-v_{CN-} PBA	1.513	1M KOH	yes	RDE GC	37
CoFe-v_{CN-} PBA	1.599	1M KOH	yes	RDE GC	37
$ZnCo_2O_4$/Au/CNTs	1.67	1M KOH	no	RDE GC	43
NiO-$NiFe_2O_4$/rGO	1.53	1M KOH	no	RDE GC	53
CoFe oxide	1.54	1M KOH	yes	Ni foam	57
CoFe film PBA	1.66	0.1M KOH	no	FTO glass	8
Au/NiFe LDH	1.467	1M KOH	yes	Ti mesh	50
Ag@$Co(OH)_2$	1.48	1M KOH	no	Carbon cloth	51
Ag+$Co(OH)_2$	1.55	1M KOH	no	Carbon cloth	51

RDE = Rotating Disk Electrode ; GC= Glassy Carbon

Last but not least, the long-term stability of $NiFe^{II}$ and $CoFe^{II}$ with and without Au were compared for 24 hours under oxygen evolution at a constant current density of 20 mA·cm^{-2} (Figure 3.24). Note that Ni foam was used to avoid the detachment of the electrocatalyst from the electrode surface during the O_2 formation. The reaction overpotentials are lower than those expected from Figures 3.20 and 3.21 for the same current density due to the porous structure of the substrate used to support the NPs in these measurements (Ni foam foil).[58] The best electrocatalytic stability

was observed when introducing 5-10 % in weight of Au. Thus, after 24 hours of OER, the overpotential increment is 50 % lower in the core@shell NPs than when the Au is absent. It seems that Au gives rise to lower overpotentials which favors the long term stability of the PBA during the OER. It is worth noting that Au-PBA nanostructures exposing Au to the electrolyte exhibit a progressive voltage increase caused by Au oxidation and dissolution.

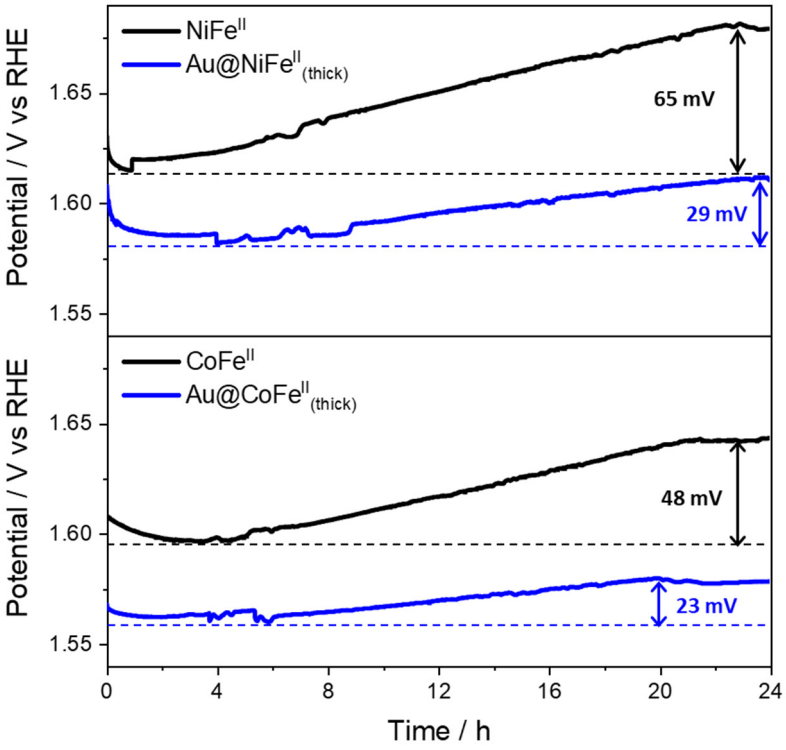

Figure 3.24 Stability of $NiFe^{II}$ and $CoFe^{II}$ with (in a core@shell structure) and without Au under a constant current density of 20 $mA \cdot cm^{-2}$ for 24 h.

Coulovoltametric responses before and after the stability test can be analyzed to calculate the electroactive mass involved in the redox processes (including Ni foam). A reduction of the electroactive mass of around 32 % for $NiFe^{II}$ but only 20 % for the Au@NiFe(thick) sample was found (Figure 3.25). For CoFe these values are 25 %

and 15 %, respectively (Figure 3.26). These results indicate a high stability, which could be improved in the future by different treatments. The increment of the reaction overpotential is likely a consequence of the loss of electroactive mass caused by the physical detachment or the progressive inactivity of these electroactive centers. The higher electrochemical stability could be a consequence of the lower required overpotentials in the Au@PBA that occurs as a result of the larger number of active sites taking part in the reaction. In this way, by applying lower voltages, the number of parasitic reactions (*i.e.* further oxidation of the electrocatalyst, the acetylene black, the Nafion and/or the Ni foam) is minimized.[59]

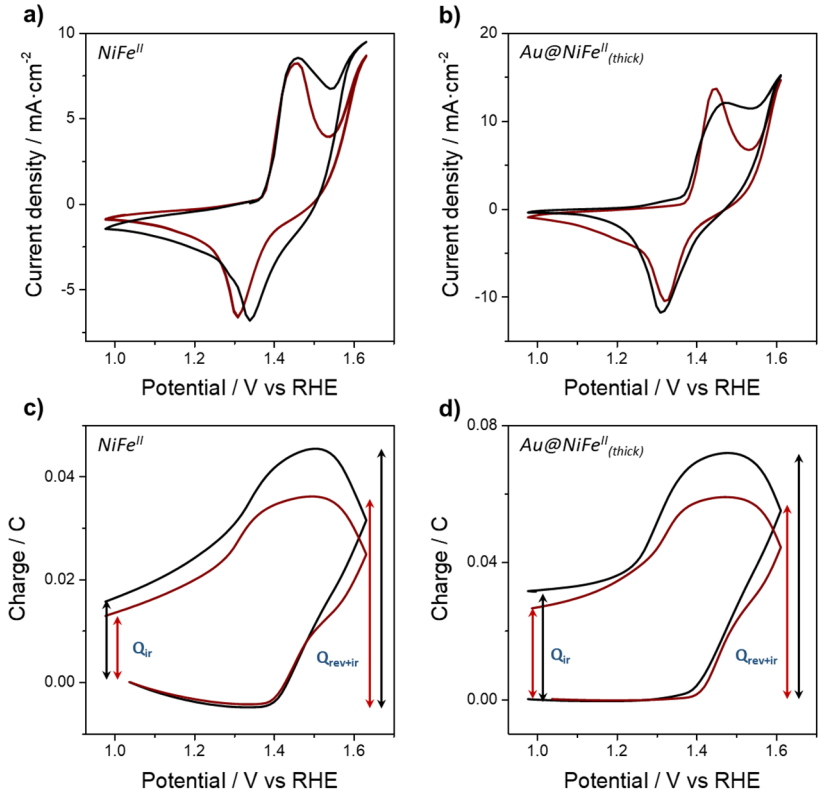

Figure 3.25 a) b) CVs performed at 50 mV·s^{-1} in 1 M KOH aqueous solution and c) d) evolution of the consumed charge (coulovoltammetric response) parallel to the voltammetric response to the CV performed at 50 mV·s^{-1} for NiFe^{II} and Au@NiFe(thick) compounds before and after stability test. Black colors are referred to measurements done before the stability test and red colors are referred to measurements done after the stability test.

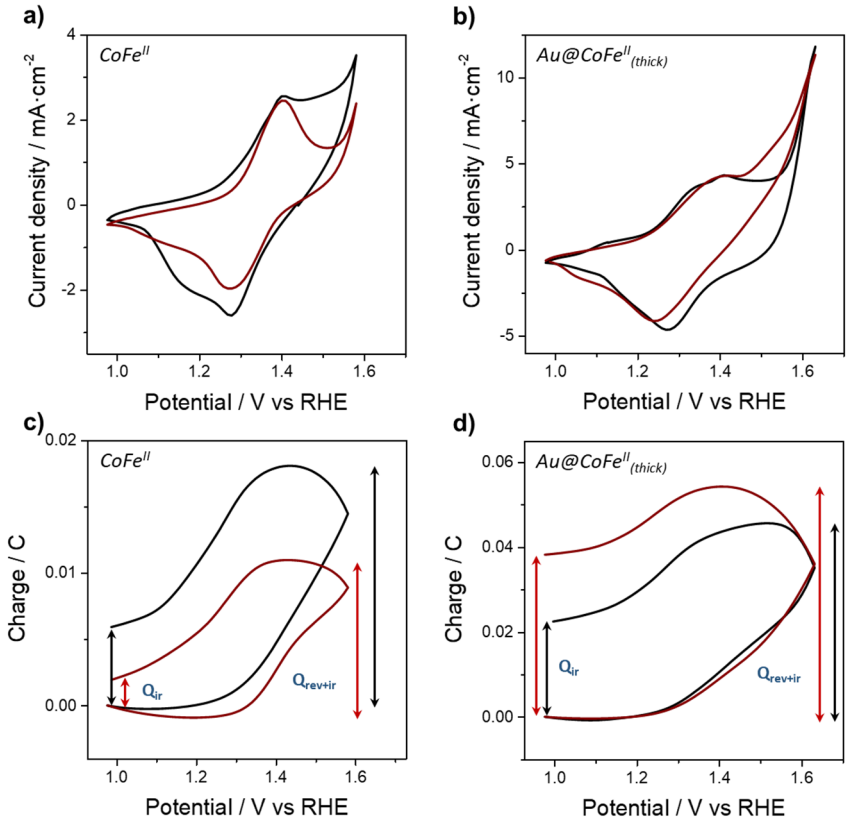

Figure 3.26 a) b) CVs performed at 50 mV·s^{-1} in 1 M KOH aqueous solution and c) d) evolution of the consumed charge (coulovoltammetric response) parallel to the voltammetric response to the CV performed at 50 mV·s^{-1} for CoFe^{II} and Au@CoFe(thick) compounds before and after stability test. Black colors are referred to measurements done before the stability test and red colors are referred to measurements done after the stability test.

Accordingly, these results prove that a proper Au incorporation greatly enhances the electrochemical activity of the electroactive PBA shell, improving at the same time its electrochemical stability. Along this front, a core@shell heterostructure with a good Au coverage is necessary to prevent its oxidation and thus, to achieve this synergistic effect between the core and the shell.

3.3 Conclusions and perspectives

In summary, we have reported here a variety of narrow-size distributed core@shell NPs of Au@PBA (PBA = Prussian Blue Analogues of $Ni^{II}Fe^{II}$ and $Co^{II}Fe^{II}$) formed by an Au core and a PBA shell of different thicknesses. The electrocatalytical activity of such NPs has been evaluated and compared to some PBA and other Au-PBA nanostructures. Compared to the PBA without Au, it was found that the introduction of small amounts of Au (5-10 % in weight) in the core@shell structure gives rise to a reduction of the overpotentials at 10 $mA \cdot cm^{-2}$ up to 100 mV and an increase up to 420 % of the current density recorded at an overpotential of 350 mV compared to the PBA without Au. Moreover, these voltage decreases are higher than the ones using reduced graphene oxide. Additionally, the Tafel slope remains unaffected, indicating that Au reduces the limiting potential of the catalyst with no variation in the kinetics of the reaction.

By means of coulovoltammetry, it was detected for these heterostructures i) an important increment in the electroactive mass able to be reduced or oxidized and thus, being able to participate in the OER and ii) and enhancement of the intrinsic catalytic activity of the PBA sites. These effects in combination with the higher conductivity of the hybrid, as observed by impedance, lead to an enhancement of the electrocatalytic activity that improves at the same time its electrochemical stability. Indeed, by applying lower voltages, the number of parasitic reactions is reduced, leading to the higher preservation of the activity of the electroactive centers. It should be noted that these effects are not observed in the other Au-PBA nanostructures mainly due to the lower contact between both compounds and the oxidation of Au.

Therefore, a core@shell heterostructure with a good Au coverage is required in order to get a protective and electroactive layer of PBA. These improvements are a consequence of the strong synergistic effect between the core and the shell of the Au@PBA nanostructures, which is facilitated by the close contact between both components. This work illustrates the importance of the chemical design for preparing PBA-based nanostructures exhibiting not only better electrocatalytic performances but also higher electrochemical stabilities likely caused by the

reduction of parasitic reactions. In subsequent studies both, the electrochemical activity and stability of these materials will be further improved by different thermal and physical pre-treatments. This will be facilitated, for example, by exploiting the plasmonic properties of Au, which will allow us to induce a photo-thermal effect in these nanostructures.

3.4 Experimental details

3.4.1 Synthesis

Materials:

All chemical reagents were purchased and used without further purification. Potassium ferricyanide, gold (I) potassium cyanide, nickel (II) chloride hexahydrate, cobalt (II) chloride hexahydrate, potassium borohydride, Chloroauric acid, sodium citrate tribasic dehydrate, thiol polyethyleneglycole amine ($HS\text{-}PEG_{3.5K}\text{-}NH_2$), potassium hydroxide (99.99%) and Nafion (117 solution) were purchased from Sigma-Aldrich. Carbon black, acetylene 50% compressed, was obtained from Alfa Aesar (99.9%). Milli-Q water was obtained from a Millipore Milli-Q equipment.

Nanoparticles synthesis

To prepare Au@NiFe NPs, 0.20 mmol of potassium borohydride (KBH_4) was added to 100 mL of an aqueous 0.5 mM solution of $K[Au(CN)_2]$ under vigorous stirring at around 10 ºC. After 20-30 min, aqueous solutions of $K_3[Fe(CN)_6]$ (5.7 mM) and $NiCl_2{\cdot}6H_2O$ (5.0 mM) were added simultaneously at a constant rate of 2 $mL{\cdot}h^{-1}$ to the Au NPs solution under vigorous stirring. After the total addition, the solution was vigorously stirred for half an hour. In order to prepare Au@CoFe NPs, 0.20 mmol of KBH_4 was added to 100 mL of an aqueous 0.5 mM solution of $K[Au(CN)_2]$ under vigorous stirring at around 10 ºC. 10-15 minutes after the solution turns red, aqueous solutions of $K_3[Fe(CN)_6]$ (5.7 mM) and $CoCl_2{\cdot}6H_2O$ (5.0 mM) were added simultaneously at an addition rate of 0.5 $mL{\cdot}h^{-1}$ to the Au NPs solution under

vigorous stirring. After the total addition, the solution was vigorously stirred for half an hour. Core@shell NPs were washed with water (11000 rpm for 20 minutes) and finally were dried under vacuum. A thinner and a thicker shell were achieved by adding respectively 2 and 10 mL of each precursor solution. $K[Au(CN)_2]$ reduction was carried out in an ice bath in order to produce smaller Au cores.

PBA-NiFe NPs of around 150 nm were synthesized at room temperature by adding, to 100 mL aqueous solution at 2 $mL \cdot h^{-1}$ rate, aqueous solutions of $CoCl_2 \cdot 6H_2O$ (5.0 mM, 7 mL) and $K_3[Fe(CN)_6]$ (5.7 mM, 7 mL) were added simultaneously. PBA-CoFe NPs of around 180 nm were also synthesized at room temperature by adding, to 100 mL aqueous solution at 2 $mL \cdot h^{-1}$ rate, aqueous solutions of $NiCl_2 \cdot 6H_2O$ (5.0 mM, 8 mL) and $K_3[Fe(CN)_6]$ (5.7 mM, 8 mL). After completion of the addition, the mixtures were stirred for half an hour before being centrifuged at 11000 rpm for 20 min. The supernatants were removed, and the powders were let dried under vacuum. PBA-$NiFe^{II}$ and PBA-$CoFe^{II}$ were prepared using the same synthetic procedure but adding 0.4 mmol of potassium borohydride (KBH_4) to promote the reduction of Fe^{III}.

Au NPs stabilized by citrate capping agent were synthesized following the well-known Turkevich method.[60] Physical mixture (Au+PBA) was prepared by joining in weight 30 % of Au NPs and 70 % of PBA NPs.

The decoration of Au on PBA NPs was carried out by connecting each NP by a polymer containing a thiol and an amine group (HS-PEG-NH_2) following the protocol described in chapter 2.

3.4.2 Characterization

Electrode preparation

For the electrode preparation, a dispersion composed of 1 mg of powder material, 0.5 mg of acetylene black, 200 µL of water and ethanol (1:1) and 8 µL of Nafion (10 %) was prepared and sonicated in order to obtain a well-dispersed suspension. Then, 3.6 µL was drop-casted in a previously polished (sequentially with 1.0, 0.3 and 0.05 µm alumina powder) 3 mm Glassy Carbon electrode. Afterwards, the solvent was let evaporated at room temperature. The electrode mass loading achieved was around 0.25 $mg \cdot cm^{-2}$.

Electrochemical measurements

Electrochemical tests were performed in a typical three-electrode cell equipped with Glassy Carbon acting as the working electrode and a platinum wire as the counter electrode. As the reference electrode, a silver-silver chloride (versus Ag/AgCl (3 M KCl)) was used. All potentials were converted referring to the oxygen evolution overpotential or the reversible hydrogen electrode (RHE). The measurements were performed at least three times for every sample using different electrodes on an Autolab PGSTAT 128N potentiostat/galvanostat. Linear sweep voltammetry (LSV) measurements were carried out at 5 $mV \cdot s^{-1}$ in a previously N_2 purged 1 M KOH aqueous solution. Prior to this, CVs were performed at different scan rates (100, 50, 20 and 10 $mV \cdot s^{-1}$).

Electrochemical Surface Area (ECSA) was acquired by measuring the current associated with double-layer capacitance from the scan rate dependence of CVs. The potential range used for the CVs was from -0.2 to 0.1 V versus Ag/AgCl (3 M KCl). The scan rates were 400, 300, 200, 100 and 50 mVs^{-1}. The double layer capacitance was estimated by plotting the (ja–jc) (anodic versus cathodic currents) at -0.05 V versus Ag/AgCl (3 M KCl) against the scan rate. The ECSA was measured on the working electrodes after performing an activation process consisting of 5 CVs at 50 $mV \cdot s^{-1}$ around their redox processes.

The turnover frequencies (TOF) were calculated from the following equation:

$$TOF = \frac{jA}{4Fn} \qquad \textbf{(Equation 3.3)}$$

where j is the current density at a given overpotential of 0.35 V, A is the surface area of the working electrode, F is the Faraday constant, and n is the total number of moles of PBA or the elctroactive number of moles of PBA.

Electrochemical impedance spectroscopy (EIS) measurements were carried out using a Gamry 1000E potentiostat/galvanostat controlled by Gamry software by applying an AC amplitude of 10 mV in the frequency range of 10^{-1}–10^{5} Hz at an overpotential of 0.4 V. EIS data were analyzed and fitted by means of Gamry Echem Analyst v. 7.07 software.

Stability tests were performed under a constant current density of 20 mA·cm^{-2} for 24 h using Ni foam foil (which area is 0.6 cm^2) as the working electrode containing 0.25 mg·cm^{-2} of electrocatalyst mass.

Physical characterization

UV/Vis Spectroscopy: UV-vis absorption spectra were recorded on a Jasco V-670 spectrophotometer in baseline mode from 300 to 900 nm range, using 1.000-cm-optical-path plastic cuvettes.

Inductively Coupled-Plasma Mass Spectrometry (ICP-MS): The ICP-MS analysis were conducted at the Universidad de Valencia (Sección de Espectrometría Atómica y Molecular). Samples were digested in an acid medium at 220 ºC using a microwave oven.

Transmission Electron Microscopy (TEM): TEM studies were carried out on a JEOL JEM 1010 microscope operating at 100 kV, and Technai G2 F20 microscope operating at 200 kV. Samples were prepared by dropping suspensions on lacey formvar/carbon copper grids (300 mesh).

Magnetic Measurements: Magnetic data were collected with a Quantum Design MPMS XL-5 susceptometer equipped with a SQUID sensor. Field Cooling

magnetization measurements were performed under a magnetic field applied of 1000 Oe.

Raman Spectroscopy: Raman spectra were acquired with a Raman Emission Horiba-MTB Xplora Spectrometer in ambient conditions. NPs were measured with a laser wavelength of 532 nm by drop-casting the samples onto silicon substrates.

Powder X-Ray Diffraction (PXRD): X-ray powder diffraction (PXRD) patterns were obtained with a PANalytical X'Pert diffractometer using the copper radiation (Cu-Ka = 1.54178 Å) in the 5–50 region.

X-ray Photoelectron Spectroscopy (XPS): Samples were analyzed using a K-ALPHA Thermo Scientific spectrometer. All spectra were collected using Al Kα radiation (1486.6 eV), monochromatized by a twin crystal monochromator, yielding a focused X-ray spot (elliptical in shape with a major axis length of 400 μm) at 30 mA and 2 kV. The alpha hemispherical analyzer was operated in the constant energy mode with survey scan pass energies of 200 eV to measure the whole energy band and 50 eV in a narrow scan to selectively measure the particular elements. XPS data were analyzed with Avantage software. A smart background function was used to approximate the experimental backgrounds. Charge compensation was achieved with the system flood gun that provides low energy electrons and low energy argon ions from a single source.

3.5 References

(1) Song, F.; Bai, L.; Moysiadou, A.; Lee, S.; Hu, C.; Liardet, L.; Hu, X. Transition Metal Oxides as Electrocatalysts for the Oxygen Evolution Reaction in Alkaline Solutions: An Application-Inspired Renaissance. *J. Am. Chem. Soc.* **2018**, *140* (25), 7748–7759.

(2) Wu, Z. P.; Lu, X. F.; Zang, S. Q.; Lou, X. W. Non-Noble-Metal-Based Electrocatalysts toward the Oxygen Evolution Reaction. *Adv. Funct. Mater.* **2020**, *30* (15), 1910274.

(3) Shi, Z.; Wang, X.; Ge, J.; Liu, C.; Xing, W. Fundamental Understanding of the Acidic Oxygen Evolution Reaction: Mechanism Study and State-of-the-Art Catalysts. *Nanoscale* **2020**, *12* (25), 13249–13275.

(4) Lyu, F.; Wang, Q.; Choi, S. M.; Yin, Y. Noble-Metal-Free Electrocatalysts for Oxygen Evolution. *Small* **2019**, *15* (1), 1804201.

(5) Verdaguer, M.; Girolami, G. S. *Magnetic Prussian Blue Analogues*; **2005**; Vol. 36.

(6) Morant-Giner, M.; Sanchis-Gual, R.; Romero, J.; Alberola, A.; García-Cruz, L.; Agouram, S.; Galbiati, M.; Padial, N. M.; Waerenborgh, J. C.; Martí-Gastaldo, C.; et al. Prussian Blue@MoS_2 Layer Composites as Highly Efficient Cathodes for Sodium- and Potassium-Ion Batteries. *Adv. Funct. Mater.* **2018**, *28*, 1706125.

(7) Zhao, F.; Wang, Y.; Xu, X.; Liu, Y.; Song, R.; Lu, G.; Li, Y. Cobalt Hexacyanoferrate Nanoparticles as a High-Rate and Ultra-Stable Supercapacitor Electrode Material. *ACS Appl. Mater. Interfaces* **2014**, *6* (14), 11007–11012.

(8) Han, L.; Tang, P.; Reyes-Carmona, Á.; Rodríguez-García, B.; Torréns, M.; Morante, J. R.; Arbiol, J.; Galan-Mascaros, J. R. Enhanced Activity and Acid PH Stability of Prussian Blue-Type Oxygen Evolution Electrocatalysts Processed by Chemical Etching. *J. Am. Chem. Soc.* **2016**, *138* (49), 16037–16045.

(9) Cao, L. M.; Lu, D.; Zhong, D. C.; Lu, T. B. Prussian Blue Analogues and Their Derived Nanomaterials for Electrocatalytic Water Splitting. *Coord. Chem. Rev.* **2020**, *407*, 213156.

(10) Chung, D. Y.; Park, S.; Lopes, P. P.; Stamenkovic, V. R.; Sung, Y.-E.; Markovic, N. M.; Strmcnik, D. Electrokinetic Analysis of Poorly Conductive Electrocatalytic Materials. *ACS Catal.* **2020**, *10* (9), 4990–4996.

(11) Zhao, D.; Lu, Y.; Ma, D. Effects of Structure and Constituent of Prussian Blue Analogs

on Their Application in Oxygen Evolution Reaction. *Molecules* **2020**, *25*, 2304.

(12) Dionigi, F.; Strasser, P. NiFe-Based (Oxy) Hydroxide Catalysts for Oxygen Evolution Reaction in Non-Acidic Electrolytes. *Adv. Energy Mater.* **2016**, *6*, 1600621.

(13) Friebel, D.; Louie, M. W.; Bajdich, M.; Sanwald, K. E.; Cai, Y.; Wise, A. M.; Cheng, M. J.; Sokaras, D.; Weng, T. C.; Alonso-Mori, R.; et al. Identification of Highly Active Fe Sites in (Ni,Fe)OOH for Electrocatalytic Water Splitting. *J. Am. Chem. Soc.* **2015**, *137* (3), 1305–1313.

(14) McAlpin, J. G.; Surendranath, Y.; Dincã, M.; Stich, T. A.; Stoian, S. A.; Casey, W. H.; Nocera, D. G.; Britt, R. D. EPR Evidence for Co(IV) Species Produced during Water Oxidation at Neutral PH. *J. Am. Chem. Soc.* **2010**, *132* (20), 6882–6883.

(15) Zhuang, Z.; Sheng, W.; Yan, Y. Synthesis of Monodispere Au@Co_3O_4 Core-Shell Nanocrystals and Their Enhanced Catalytic Activity for Oxygen Evolution Reaction. *Adv. Mater.* **2014**, *26* (23), 3950–3955.

(16) Yeo, B. S.; Bell, A. T. Enhanced Activity of Gold-Supported Cobalt Oxide for the Electrochemical Evolution of Oxygen. *J. Am. Chem. Soc.* **2011**, *133* (14), 5587–5593.

(17) Zou, S.; Burke, M. S.; Kast, M. G.; Fan, J.; Danilovic, N.; Boettcher, S. W. Fe (Oxy)Hydroxide Oxygen Evolution Reaction Electrocatalysis: Intrinsic Activity and the Roles of Electrical Conductivity, Substrate, and Dissolution. *Chem. Mater.* **2015**, *27* (23), 8011–8020.

(18) Ng, J. W. D.; García-Melchor, M.; Bajdich, M.; Chakthranont, P.; Kirk, C.; Vojvodic, A.; Jaramillo, T. F. Gold-Supported Cerium-Doped NiO x Catalysts for Water Oxidation. *Nat. Energy* **2016**, *1,* 16053.

(19) Torres-Cavanillas, R.; Sanchis-Gual, R.; Dugay, J.; Coronado-Puchau, M.; Giménez-Marqués, M.; Coronado, E. Design of Bistable Gold@Spin-Crossover Core–Shell Nanoparticles Showing Large Electrical Responses for the Spin Switching. *Adv. Mater.* **2019**, *31* (27), 1900039.

(20) Gawande, M. B.; Goswami, A.; Asefa, T.; Guo, H.; Biradar, A. V.; Peng, D. L.; Zboril, R.; Varma, R. S. Core-Shell Nanoparticles: Synthesis and Applications in Catalysis and Electrocatalysis. *Chem. Soc. Rev.* **2015**, *44* (21), 7540–7590.

(21) Gong, S.; Zhang, Y. X.; Niu, Z. Recent Advances in Earth-Abundant Core/Noble-Metal Shell Nanoparticles for Electrocatalysis. *ACS Catal.* **2020**, *10* (19), 10886–10904.

(22) Jing, L.; Liang, X.; Deng, Z.; Feng, S.; Li, X.; Huang, M. Biomaterials Prussian Blue Coated Gold Nanoparticles for Simultaneous Photoacoustic / CT Bimodal Imaging and Photothermal Ablation of Cancer. *Biomaterials* **2014**, *35* (22), 5814–5821.

(23) Yin, Y.; Li, Q.; Ma, S.; Liu, H.; Dong, B.; Yang, J.; Liu, D. Prussian Blue as a Highly Sensitive and Background-Free Resonant Raman Reporter. *Anal. Chem.* **2017**, *89* (3), 1551–1557.

(24) Qiu, J. D.; Peng, H. Z.; Liang, R. P.; Li, J.; Xia, X. H. Synthesis, Characterization, and Immobilization of Prussian Blue-Modified Au Nanoparticles: Application to Electrocatalytic Reduction of H 2O2. *Langmuir* **2007**, *23* (4), 2133–2137.

(25) Fu, G.; Liu, W.; Feng, S.; Yue, X. Prussian Blue Nanoparticles Operate as a New Generation of Photothermal Ablation Agents for Cancer Therapy. *Chem. Commun.* **2012**, *48* (94), 11567.

(26) Lu, X.; Li, Y.; Zhang, X.; Du, J.; Zhou, X.; Xue, Z.; Liu, X. A Simple and an Efficient Strategy to Synthesize Multi-Component Nanocomposites for Biosensor Applications. *Anal. Chim. Acta* **2012**, *711*, 40–45.

(27) Maurin-Pasturel, G.; Long, J.; Guari, Y.; Godiard, F.; Willinger, M. G.; Guerin, C.; Larionova, J. Nanosized Heterostructures of Au@Prussian Blue Analogues: Towards Multifunctionality at the Nanoscale. *Angew. Chemie - Int. Ed.* **2014**, *53* (15), 3872–3876.

(28) Maurin-Pasturel, G.; Mamontova, E.; Palacios, M. A.; Long, J.; Allouche, J.; Dupin, J. C.; Guari, Y.; Larionova, J. Gold@Prussian Blue Analogue Core-Shell Nanoheterostructures: Their Optical and Magnetic Properties. *Dalt. Trans.* **2019**, *48* (18), 6205–6216.

(29) Liu, B. H.; Li, Z. P. A Review: Hydrogen Generation from Borohydride Hydrolysis Reaction. *J. Power Sources* **2009**, *187* (2), 527–534.

(30) Liang, J.; Li, C. H.; Talham, D. R. Growth Mechanisms of Mesoscale Prussian Blue Analogue Particles in Modifier-Free Synthesis. *Cryst. Growth Des.* **2020**, *20* (4), 2713–2720.

(31) Miller, M. M.; Lazarides, A. A. Sensitivity of Metal Nanoparticle Surface Plasmon Resonance to the Dielectric Environment. *J. Phys. Chem. B* **2005**, *109* (46), 21556–21565.

(32) Mayer, K. M.; Hafner, J. H. Localized Surface Plasmon Resonance Sensors. *Chem. Rev.* **2011**, *111* (6), 3828–3857.

(33) Wang, C.; Ranasingha, O.; Natesakhawat, S.; Ohodnicki, P. R.; Andio, M.; Lewis, J. P.; Matranga, C. Visible Light Plasmonic Heating of Au–ZnO for the Catalytic Reduction of CO_2. *Nanoscale* **2013**, *5* (15), 6968–6974.

(34) Zhang, X.; Chen, Y. L.; Liu, R. S.; Tsai, D. P. Plasmonic Photocatalysis. *Reports Prog. Phys.* **2013**, *76* (4), 046401.

(35) Buser, H. J.; Ludi, A.; Schwarzenbach, D.; Petter, W. The Crystal Structure of Prussian Blue: $Fe_4[Fe(CN)_6]_3 \cdot xH_2O$. *Inorg. Chem.* **1977**, *16* (11), 2704–2710.

(36) Juszczyk, S.; Johansson, C.; Hanson, M.; Ratuszna, A.; Malecki, G. Ferromagnetism of the Me_3 [Fe (CN)& H_2O Compounds , Where Me = Ni and CO. *J. Phys. Condens. Matter* **1994**, *6*, 5697–5706.

(37) Yu, Z. Y.; Duan, Y.; Liu, J. D.; Chen, Y.; Liu, X. K.; Liu, W.; Ma, T.; Li, Y.; Zheng, X. S.; Yao, T.; et al. Unconventional CN Vacancies Suppress Iron-Leaching in Prussian Blue Analogue Pre-Catalyst for Boosted Oxygen Evolution Catalysis. *Nat. Commun.* **2019**, *10* (1), 2799.

(38) Sanchis-Gual, R.; Susic, I.; Torres-Cavanillas, R.; Arenas-Esteban, D.; Bals, S.; Mallah, T.; Coronado-Puchau, M.; Coronado, E. The Design of Magneto-Plasmonic Nanostructures Formed by Magnetic Prussian Blue-Type Nanocrystals Decorated with Au Nanoparticles. *Chem. Comm.* **2021**, 57, 1903-1906.

(39) Su, X.; Wang, Y.; Zhou, J.; Gu, S.; Li, J.; Zhang, S. Operando Spectroscopic Identification of Active Sites in NiFe Prussian Blue Analogues as Electrocatalysts: Activation of Oxygen Atoms for Oxygen Evolution Reaction. *J. Am. Chem. Soc.* **2018**, *140* (36), 11286–11292.

(40) Pintado, S.; Goberna-Ferrón, S.; Escudero-Adán, E. C.; Galán-Mascarós, J. R. Fast and Persistent Electrocatalytic Water Oxidation by Co-Fe Prussian Blue Coordination Polymers. *J. Am. Chem. Soc.* **2013**, *135* (36), 13270–13273.

(41) Otero, T. F.; Alfaro, M.; Martinez, V.; Perez, M. A.; Martinez, J. G. Biomimetic Structural Electrochemistry from Conducting Polymers: Processes, Charges, and Energies. Coulovoltammetric Results from Films on Metals Revisited. *Adv. Funct. Mater.* **2013**, *23* (31), 3929–3940.

(42) Otero, T. F. Coulovoltammetric and Dynamovoltammetric Responses from Conducting Polymers and Bilayer Muscles as Tools to Identify Reaction-Driven Structural Changes. A Review. *Electrochim. Acta* **2016**, *212*, 440–457.

(43) Cheng, H.; Su, C. Y.; Tan, Z. Y.; Tai, S. Z.; Liu, Z. Q. Interacting $ZnCo_2O_4$ and Au Nanodots on Carbon Nanotubes as Highly Efficient Water Oxidation Electrocatalyst. *J. Power Sources* **2017**, *357*, 1–10.

(44) Carrasco, J. A.; Harvey, A.; Hanlon, D.; Lloret, V.; McAteer, D.; Sanchis-Gual, R.; Hirsch, A.; Hauke, F.; Abellán, G.; Coleman, J. N.; et al. Liquid Phase Exfoliation of Carbonate-Intercalated Layered Double Hydroxides. *Chem. Commun.* **2019**, *55* (23), 3315–3318.

(45) Mccrory, C. C. L.; Jung, S.; Ferrer, I. M.; Chatman, S. M.; Peters, J. C.; Jaramillo, T. F. Benchmarking Hydrogen Evolving Reaction and Oxygen Evolving Reaction Electrocatalysts for Solar Water Splitting Devices. *J. Am. Chem. Soc.* **2015**, *137*, 4347–4357.

(46) Strickler, A. L.; Escudero-Escribano, M.; Jaramillo, T. F. Core-Shell Au@Metal-Oxide Nanoparticle Electrocatalysts for Enhanced Oxygen Evolution. *Nano Lett.* **2017**, *17* (10), 6040–6046.

(47) Ciureanu, M.; Mikhailenko, S. D.; Kaliaguine, S. PEM Fuel Cells as Membrane Reactors : Kinetic Analysis by Impedance Spectroscopy. **2003**, *82*, 195–206.

(48) Ellis, C. L. C.; Smith, E.; Javaid, H.; Berns, G.; Venkataraman, D. *Ion Migration in Hybrid Perovskites*; Elsevier Inc., 2018.

(49) Fang, Y.; Li, X.; Hu, Y.; Li, F.; Lin, X.; Tian, M.; An, X.; Fu, Y.; Jin, J.; Ma, J. Ultrasonication-Assisted Ultrafast Preparation of Multiwalled Carbon Nanotubes/Au/Co_3O_4 Tubular Hybrids as Superior Anode Materials for Oxygen Evolution Reaction. *J. Power Sources* **2015**, *300*, 285–293.

(50) Zhang, J.; Liu, J.; Xi, L.; Yu, Y.; Chen, N.; Sun, S.; Wang, W.; Lange, K. M.; Zhang, B. Single-Atom Au/NiFe Layered Double Hydroxide Electrocatalyst: Probing the Origin of Activity for Oxygen Evolution Reaction. *J. Am. Chem. Soc.* **2018**, *140* (11), 3876–3879.

(51) Zhang, Z.; Li, X.; Zhong, C.; Zhao, N.; Deng, Y.; Han, X.; Hu, W. Spontaneous Synthesis of Silver□Nanoparticle□Decorated Transition□Metal Hydroxides for Enhanced Oxygen Evolution Reaction. *Angew. Chem. Int. Ed.* **2020**, *59* (18), 7245.

(52) Long, X.; Li, J.; Xiao, S.; Yan, K.; Wang, Z.; Chen, H.; Yang, S. A Strongly Coupled Graphene and FeNi Double Hydroxide Hybrid as an Excellent Electrocatalyst for the Oxygen Evolution Reaction. *Angew. Chem. Int. Ed.* **2014**, *126* (29), 7714–7718.

(53) Zhang, G.; Li, Y.; Zhou, Y.; Yang, F. NiFe Layered□double□hydroxide□derived NiO□ $NiFe_2O_4$/Reduced Graphene Oxide Architectures for Enhanced Electrocatalysis of Alkaline Water Splitting. *ChemElectroChem* **2016**, *3* (11), 1927–1936.

(54) McAteer, D.; Godwin, I. J.; Ling, Z.; Harvey, A.; He, L.; Boland, C. S.; Vega-Mayoral, V.; Szydłowska, B.; Rovetta, A. A.; Backes, C.; et al. Liquid Exfoliated $Co(OH)_2$ Nanosheets as Low-Cost, Yet High-Performance, Catalysts for the Oxygen Evolution Reaction. *Adv. Energy Mater.* **2018**, *8* (15), 1702965.

(55) Zhang, Q.; Liu, N.; Guan, J. Charge-Transfer Effects in Fe–Co and Fe–Co–Y Oxides for Electrocatalytic Water Oxidation Reaction. *ACS Appl. Energy Mater.* **2019**, *2* (12), 8903–8911.

(56) Song, F.; Hu, X. Exfoliation of Layered Double Hydroxides for Enhanced Oxygen Evolution Catalysis. *Nat. Commun.* **2014**, *5*, 4477.

(57) Chuang, C.-H.; Hsiao, L.-Y.; Yeh, M.-H.; Wang, Y.-C.; Chang, S.-C.; Tsai, L.-D.; Ho, K.-C. Prussian Blue Analogue-Derived Metal Oxides as Electrocatalysts for Oxygen Evolution Reaction: Tailoring the Molar Ratio of Cobalt to Iron. *ACS Appl. Energy Mater.* **2020**, *3* (12), 11752–11762.

(58) Zheng, W.; Liu, M.; Lee, L. Y. S. Best Practices in Using Foam-Type Electrodes for Electrocatalytic Performance Benchmark. *ACS Energy Lett.* **2020**, *5* (10), 3260–3264.

(59) Zhang, P.; Ding, M.; Li, X.; Li, C.; Li, Z.; Yin, L. Challenges and Strategy on Parasitic Reaction for High-Performance Nonaqueous Lithium–Oxygen Batteries. *Adv. Energy Mater.* **2020**, *10* (40), 2001789.

(60) Turkevich, J. Colloidal Gold. Part I. *Gold Bull.* **1985**, *18* (4), 125–131.

Chapter 4

Electrical switching in hybrid core@shell nanoparticles based on Au surrounded by smart Coordination Polymers

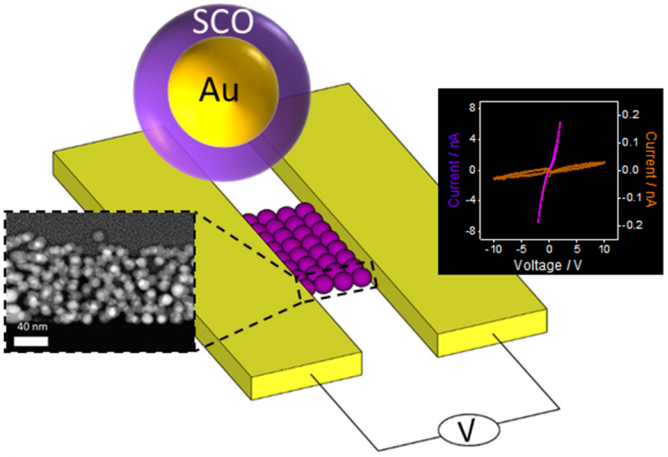

4.0 Previous considerations

This chapter is devoted to the development of core@shell nanoparticles formed by a plasmonic core surrounded by a smart Coordination Polymer with the aim of improving the electrical detection of the switching properties in these nanostructures thanks to the presence of the metallic core and a thin shell. Firstly, we present the development of a synthetic protocol for covering different metallic cores with a Spin-Crossover (SCO) compound, which can undergo a spin transition upon varying the temperature. After that, with the purpose of extending this procedure to other systems, we introduce our preliminary attempts of combining an Au core with porous Coordination Polymers (Metal-Organic Frameworks; MOFs). The final goal, in this case, is to use the sorption/release of guest molecules as an external stimulus to trigger an electrical change. It is important to remark that this is still an ongoing work. It is also important to point out that the chemical design of the Au@MOF nanostructures has been supervised by Dr. Monica Giménez-Marqués. Regarding the electrical measurements, Dr. Julien Dugay and Ramón Torres-Cavanillas have been in charge.

4.1 Introduction

One of the most appealing perspectives in molecular chemistry is to take advantage of molecular systems for information processing and electronic applications. In this context, molecular bistable systems are particularly engaging as they can switch between two different stable electronic states triggered by a broad range of external stimuli. An example of molecular switching is provided by Spin-Crossover (SCO) compounds. Of particular interest are those SCO materials displaying a hysteretic behavior in their spin transition since they can be useful as components of non-volatile memory devices.[1–3] With the aim of reading-out the spin state in these devices, materials with large electrical responses, preferably displaying hysteretic spin transitions occurring near room temperature, are required. However, the SCO electronic devices reported to date, based on micrometric particles, have typically shown a gradual hysteresis in the conductance as well as very low electrical responses due to the insulating character of the SCO material.[4,5] This situation becomes even more complex when the SCO system is downscaled to the nanometer or single molecule range since, under these circumstances, the hysteretic behavior observed in bulk is usually lost.[6–8]

A plausible investigated strategy to overcome these limitations in switching electronic devices consists of the combination of SCO entities and metallic NPs in hybrid heterostructures typically following a grafting protocol.[9–13] Although these SCO-metal composite materials have been successfully obtained, their impact on the physical properties is still ineffective. To improve this result, a careful chemical of the hybrid heterostructure is mandatory. The requirements are: i) to use SCO nanostructures as small as possible to maintain the molecular bistability and ii) to incorporate metallic nanoparticles (NPs) in order to improve the conducting properties, while keeping them separate to avoid short circuits.

According to these requirements, the preparation of core@shell NPs formed by a metallic Au core and a SCO shell seems to be a suitable choice. Despite the extensive works performed on core@shell NPs,[14–16] nanostructures formed by a metallic core and a molecular SCO shell are not common. In addition, as compared to previous examples that contain simple SCO entities deposited or contacted to Au

surfaces/electrodes,[9–13,17–19] the core@shell configuration reported here is expected to combine in a single nanostructure the metallic behavior of the core with the insulating behavior of the SCO shell. In these hybrid nanostructures, the appropriate selection of the SCO material should warrant the maintenance of a cooperative spin transition at the nanoscale, while the metallic core is expected to make these novel nanostructures electrically more conductive. As SCO material the chosen system has been the well-known iron(II)-triazole Coordination Polymer (CP) of formula $[Fe(Htrz)_2(trz)](BF_4)$ (Htrz = 1,2,4-triazole).[20,21] This SCO material exhibits large and abrupt thermal hysteresis occurring near room temperature. Furthermore, its well-established miniaturization protocol,[22–24] enables the maintenance of the cooperative spin transition features in NPs as small as 4 nm.[25] These NPs have already been integrated into electronic devices, showing a detectable conductivity change during the SCO transition. Thus, single NP devices (NP mean size of 10 nm) showed an ON/OFF ratio in the conductivity of ≈2. This performance is significantly improved in electronic devices based on two-dimensional assemblies of SCO NPs for which the ON/OFF ratio increases up to a value of ≈300.[26] In this context, the only attempt to combine metallic Au NPs with SCO molecules for the fabrication of molecular devices resulted in 2D arrays of SCO-functionalized Au NPs exhibiting however minor switching performances.[27] Here, we will show that thanks to the improvement in the conductive properties of the core@shell NPs, the corresponding SCO-based devices show large electrical responses in the spin switching, with ON/OFF ratios of ≈5300. These results have been published in Advanced Materials.[28]

Besides, we were able to adapt this protocol in order to cover Au nanostars (AuNSs) and Ag nanospheres (addressed here as Ag NPs) with the $[Fe(Htrz)_2(trz)](BF_4)$ SCO polymer by slightly modifying the synthesis. In this way, the plasmonic NP can be selected. Thus, the Localized Surface Plasmon Resonance (LSPR) position can be controlled in a wide range of the visible spectrum. This was possible thanks to the simplicity and versatility of the synthetic method.

In a similar way, the integration of metallic NPs in core@shell nanostructures can also be a useful strategy to enhance the electrical response of porous CPs such as Metal-Organic Frameworks (MOFs) in order to detect the sorption/release of guest molecules by an electrical change. Indeed, electrically conductive and porous

solids displaying high surface area are two exciting properties for the development of novel electronic devices in the near future. However, as for the SCO compounds, the evolution of MOFs in electronic applications has been sluggish, especially due to its insulating nature that leads to a dearth of sophisticated molecular recognition and signal transduction capabilities for sensors.[29,30] That is why in recent years, different approaches have been used to obtain conductive MOFs exhibiting high conductivity as well as high porosity.[31] In this context, the development of Au@MOFs heterostructures with a MOF thin shell emerges as an interesting possibility to extrinsically incorporate conductivity. As commented in Chapter 1, in general, thick MOF shells have been overgrown around different Au nanoarchitectures due to the difficulties of having precise synthetic control. For the preparation of small MOF shells, layer-by-layer methods have emerged as an alternative that can provide greater control.[32] However, this protocol involves too many steps with centrifugation that can easily lead to some aggregation. Thus, it is relevant to promote new protocols to prepare core@shell heterostructures with metallic cores and thin MOF shells for their integration in electronic devices.

Therefore, we have extended the synthetic protocol developed for Au@SCO to obtain Au@MOF heterostructures exhibiting a thin shell. The MOFs grown around the Au were the MIL-100(Fe) or the MIL-88(Fe). However, these compounds do not exhibit any characteristic X-ray diffraction peak suggesting the CPs are amorphous. Interestingly, the obtained hybrids exhibit some colloidal stability, plasmonic properties and enhanced conductivity thanks to the incorporation of Au NPs.

4.2 Results and discussion

For the preparation of the core@shell NPs, a straightforward protocol that coats spherical Au NPs with a thin shell of $[Fe(Htrz)_2(trz)](BF_4)$ material has been carried out (Figure 4.1). At first, citrate-stabilized Au NPs of 12.4 ± 1.0 nm were synthesized following the well-known Turkevich method.[33] Then, the overgrowth of the SCO compound around the Au NP surface was performed following a two-step approach. It consists of a partial ligand substitution of the Au surface capping agent, citrate by the ligand triazole and the subsequent growth of the SCO polymer by controlled addition of the precursors (see below for experimental details).

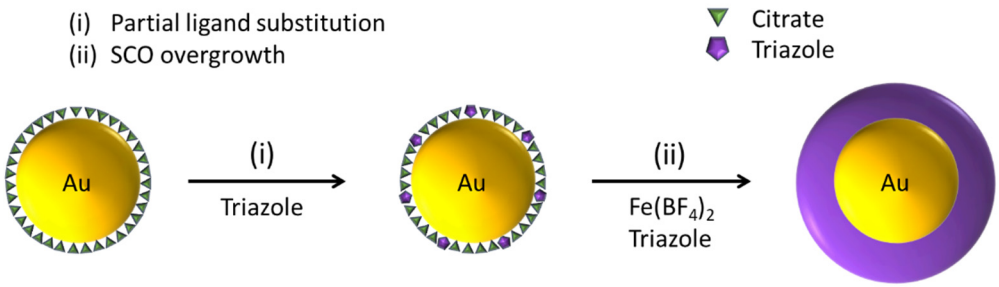

Figure 4.1 Schematic illustration of the steps involved in the preparation of Au@SCO NPs.

The first critical step occurs at the surface of stable Au NPs colloids, involving the partial ligand substitution of citrate capping agent by Htrz ligands. To do so, a diluted solution of Htrz ligand (0.5 mM) was added into a stable suspension of citrate-stabilized Au NPs (0.16 mM). As a result, a partial ligand exchange occurred on the NP surface, originating some nucleation sites that act as anchors for the subsequent growth of the SCO shell. Such a surface modification occurred thanks to the rather weak Au-citrate interaction[34] and needed to be partial to maintain the colloidal stability of the NPs. It should be noted that a complete surface ligand substitution with Htrz can be achieved by using larger amounts of Htrz ligand, although in this case the Au NPs were not effectively stabilized and tended to aggregate. Therefore, fine control of both the amount of Htrz ligands added as well as the reaction time were critical parameters to overgrow the shell while avoiding NP precipitation. This

ligand exchange process was checked by X-Ray photoemission spectroscopy (XPS), which showed the appearance of nitrogen atoms at the surface of the Au NPs after ligand exchange (Figure 4.2), in agreement with the presence of the triazole ligands.

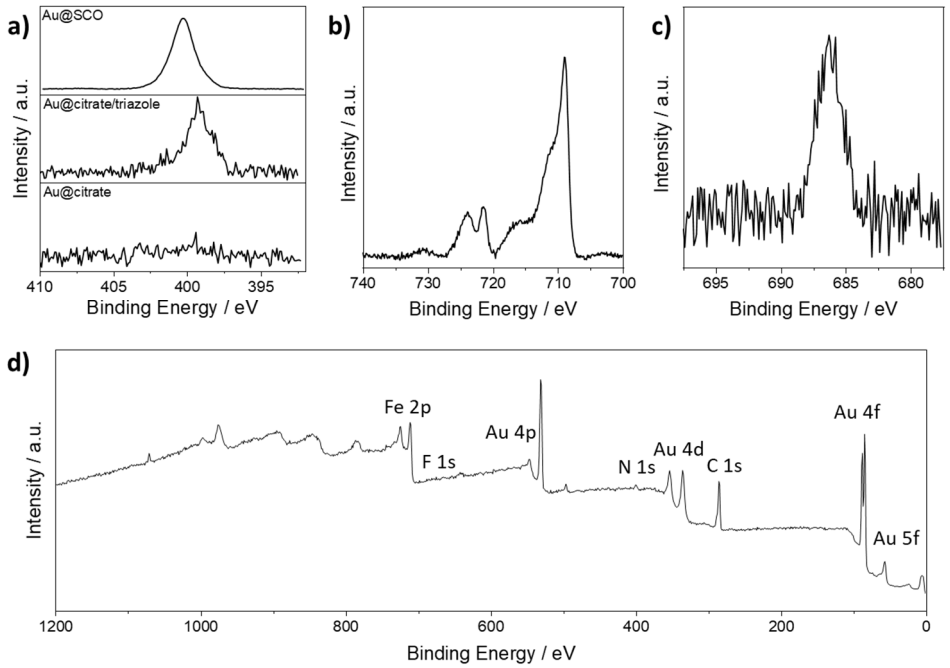

Figure 4.2 XPS spectra of a) N, b) Fe, c) F and d) Survey for Au@SCO NPs.

The second key step of the protocol comprises the continuous growth of the SCO complex onto the pre-modified surface of the Au NPs (Figure 4.1) upon the controlled addition of the precursors. Thus, an aqueous solution of the Fe^{II} precursor and the Htrz ligand were simultaneously added to the Au suspension at a constant rate (4 $mL \cdot h^{-1}$) and appropriate concentrations (0.16 and 0.5 mM, respectively), at room temperature and under stirring. It is worth mentioning that larger concentrations of either Au NPs or Fe^{II} precursors (>0.3 mM) results in NP aggregation. After the complete addition of reagents, colloidally stable Au@SCO core@shell NPs were

obtained. Interestingly and in contrast with the previously reported examples of SCO NPs, these Au@SCO NPs possess naked surfaces (*i.e.*, free from any organic moiety). Such surfactant-free configuration may turn out to be particularly convenient to enhance the interactions between the SCO shells of neighboring NPs or to conduct post-synthetic modification on the surface of these NPs. Transmission electronic microscopy (TEM) images evidenced uniform Au@SCO NPs with an overall diameter of 19.4 ± 1.9 nm and thin SCO shells of 3.6 ± 1.0 nm (Figure 4.3).

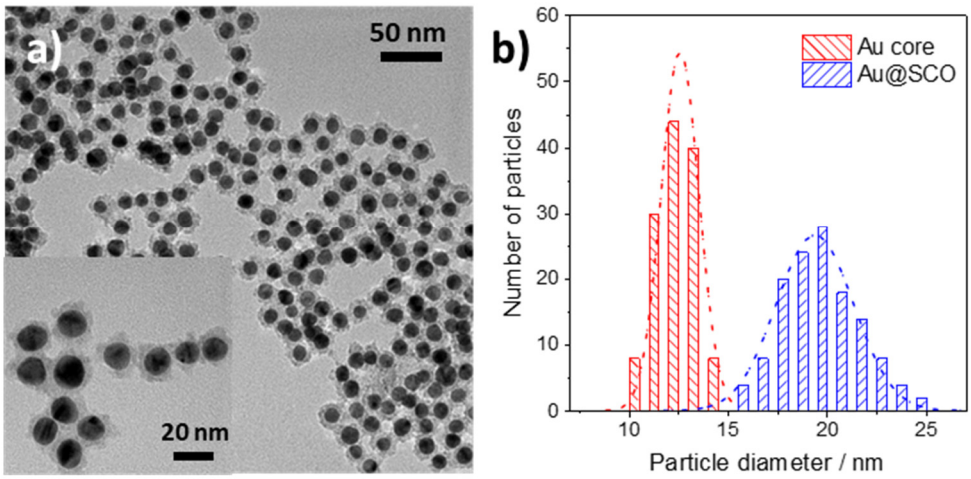

Figure 4.3 a) TEM image of Au@SCO NPs. Inset: HR-TEM image of Au@SCO NPs. b) Histograms of the size distributions for the Au core (red) and the overall core@shell NP diameter (blue).

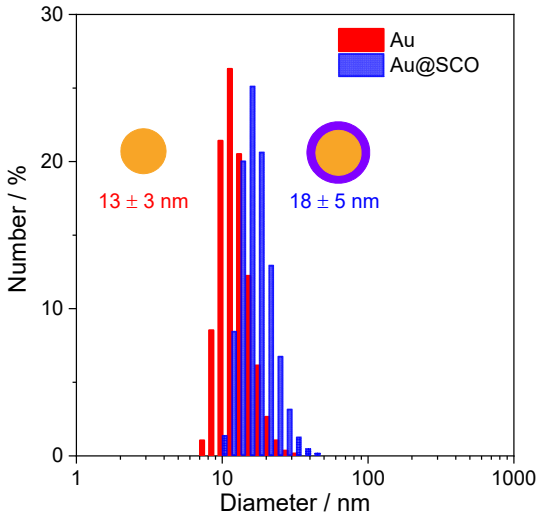

Figure 4.4 Dynamic Light Scattering plot for citrate-stabilized Au NPs and Au@SCO NPs.

An evident core@shell structure was distinguished in all the NPs, demonstrating the formation of individual coatings rather than a less controlled composite made of Au NPs embedded in a SCO matrix. This narrow size distribution was also confirmed by dynamic light scattering (DLS) measurements performed in water suspensions of Au@SCO NPs, which indicates a hydrodynamic diameter of 18 ± 5 nm, dismissing the presence of aggregates (Figure 4.4). ζ-potential analysis was used to assess the colloidal stability of the suspensions (Table 4.1), showing a strong modification from −40 ± 7 to −28 ± 4 mV for the Au@citrate and the Au@SCO NPs, respectively. Energy dispersive X-ray spectroscopy (EDX) was used to estimate the metallic composition of the Au@SCO NPs (Figure 4.5), showing a clear core@shell distribution with an estimated ratio of $Au/Fe_{0.58}$.

Table 4.1: ζ-potentials of Au@citrate NPs, Au@citrate/Htrz NPs and Au@SCO NPs.

Sample	ζ-potential / mV	pH
Au@citrate	- 40 ± 7	6.61
Au@citrate/Htrz	- 40 ± 8	6.77
Au@SCO	- 28 ± 4	6.52

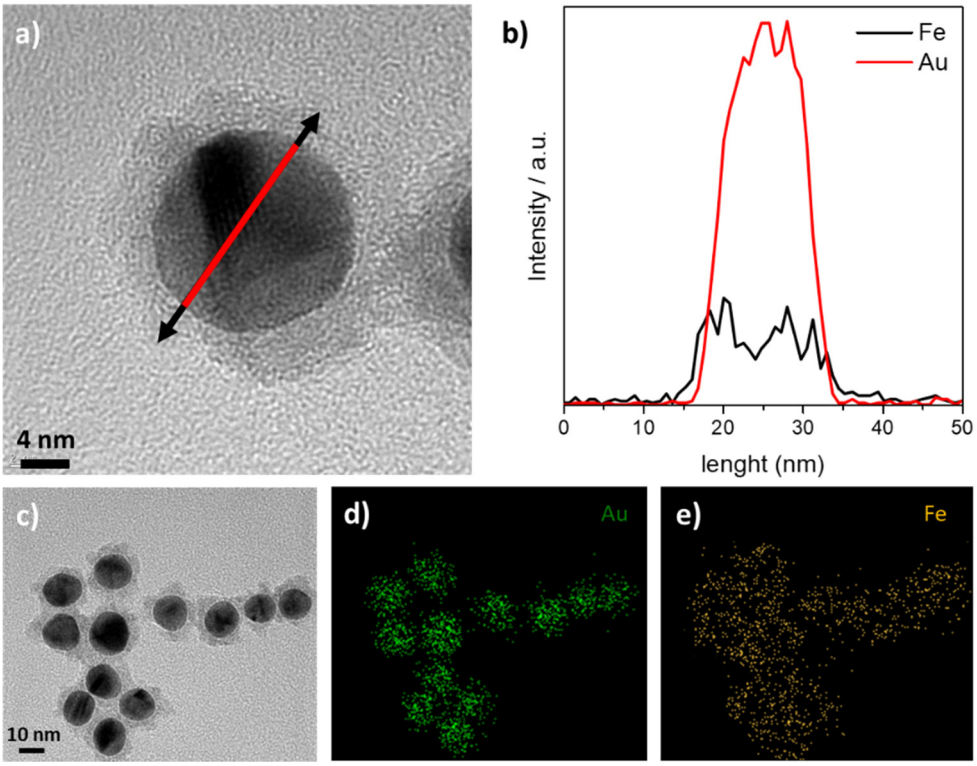

Figure 4.5 a) High-Resolution Transmission Electron Microscopy (HR-TEM) image and b) EDX profile showing the presence of Au and Fe on a single NP; c–e) EDX mapping of the metals present in the heterostructure.

A more accurate analysis of the metal content was performed by Inductively Coupled-Plasma Mass Spectrometry (ICP-MS), where the relative (atomic) amount was found to be $Au/Fe_{0.62}$. XPS and X-ray diffraction analysis of the powdered materials (Figure 4.6) were performed in an attempt to characterize the chemical composition of the shell. In the XPS spectra, peaks of iron, nitrogen, and fluorine were observed (Figure 4.2), which indicate the presence of metal, ligand, and counterion, thus supporting the formation of the spin-crossover compound. Nevertheless, the iron peak reveals the existence of an important fraction of iron (III) that could be caused by partial iron oxidation of the small SCO shell during the synthesis and/or during the XPS sample preparation.

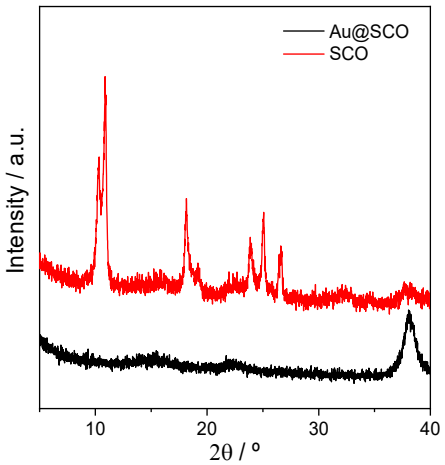

Figure 4.6 Room temperature PXRD for Au@SCO (black) and SCO (red) compounds.

The diffraction pattern of the Au@SCO NPs exhibited a unique peak at 38.2° characteristic of metallic Au, whereas the expected peaks for the $[Fe(Htrz)_2(trz)](BF_4)$ compound were not observed.[35] This absence could be due to the small thickness of the SCO shell, which may be beyond the detection limit of the X-ray diffractometer, as well as to the large electron density of the crystalline Au cores, which can screen the signal coming from the SCO compound.[9]

An important aspect during the synthesis of Au@SCO NPs results from the change in the optical properties due to the high sensitivity of the LSPR of the Au NPs. The optical properties of these hybrid NPs are reported in Figure 4.7 and compared with the bare Au NPs. It is observed that the LSPR of Au NPs, which exhibits a maximum at 518 nm, is gradually red-shifted during shell growth up to 530 nm in the Au@SCO NPs. This plasmon shift was visually detected by a color change in the suspension from red to pink, evidencing the high sensitivity of the LSPR to the presence of a dielectric SCO shell covering the Au NPs. In addition, a subsequent increase in the plasmon band intensity was also observed. Similar behavior has been recently reported on a system based on Au NPs decorated with SCO molecules ($[Fe(AcS\text{-}BPP)_2](ClO_4)_2$).[27] The mechanism at play may have its origin in the change of the dielectric properties at the Au NP surface upon the overgrowth of the SCO shells around.[36,37]

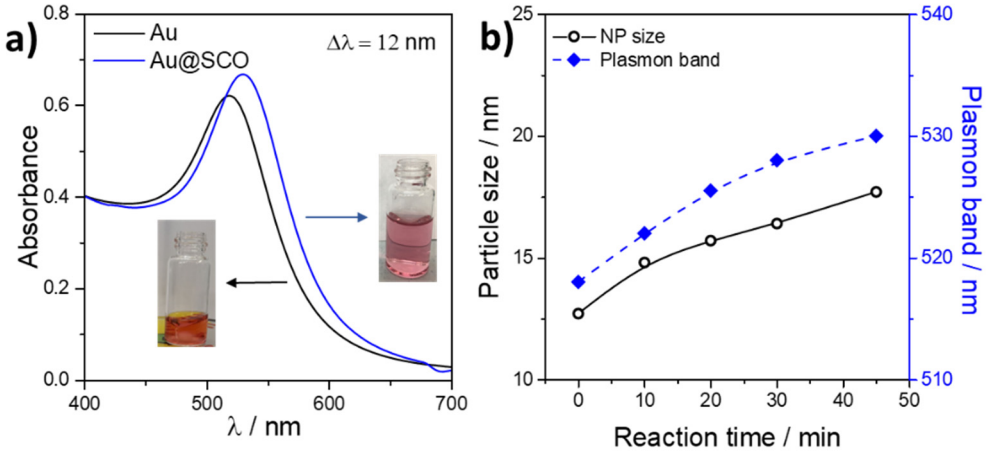

Figure 4.7 a) Spectra of Au and Au@SCO NPs in the visible region. b) Evolution of the mean particle size and plasmon band position upon the addition of the precursors during the Au@SCO synthesis.

On the other hand, by stopping the reaction before finishing, it can be achieved core@shell NPs with a thinner shell (Figure 4.8a). It is possible to obtain a thicker shell (of maximum *ca*. 5 nm) by slightly decreasing the initial Au concentration (from 0.16 to 0.12 mM) in order to reduce the total number of particles (Figure 4.8b). As aforementioned above, the plasmon shift depends on the shell overgrowth, allowing precise control of the SCO compound formation around the Au NP surfaces (Figure 4.8c and 4.8d).

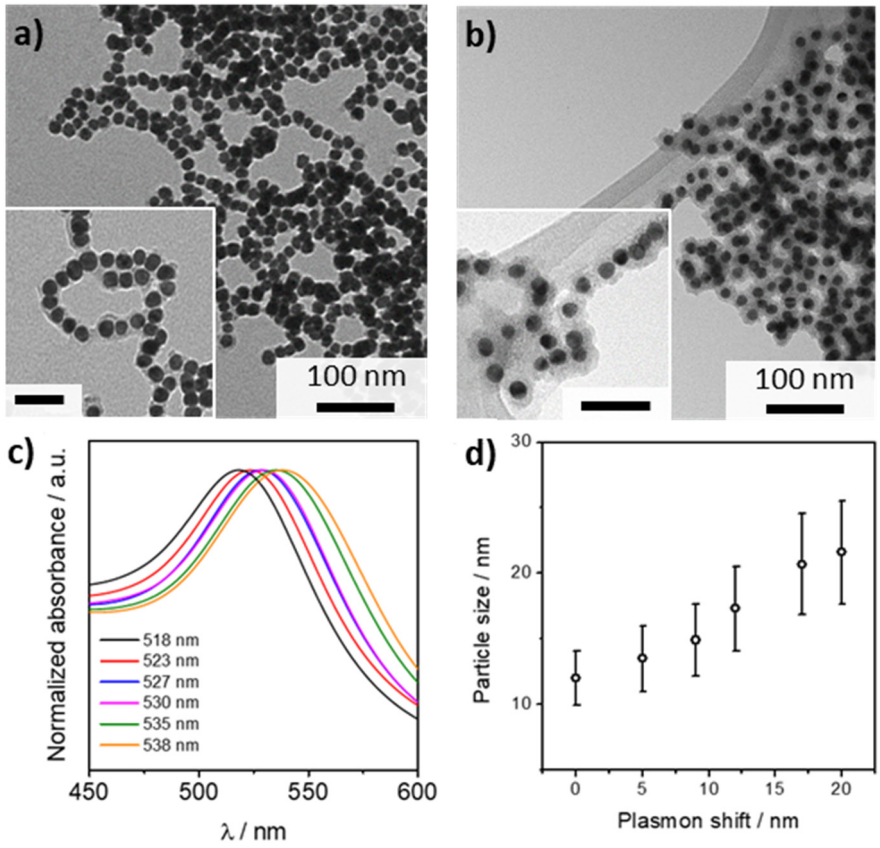

Figure 4.8 TEM images of Au@SCO NPs with a) thinner shell and b) thicker shell. Insets: magnified TEM images of the NPs. Bar scales represent 50 nm. c) Spectra of different size core@shell NPs in the visible region. d) Correlation of the mean particle size and plasmon band shift.

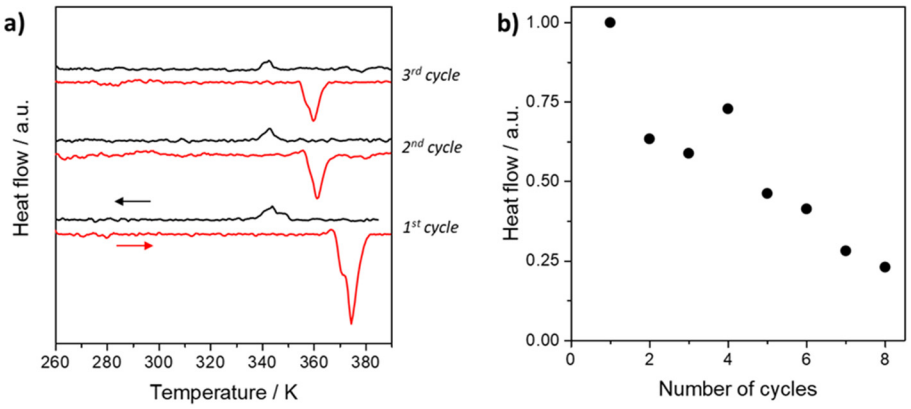

Figure 4.9 DSC curves of Au@SCO; the red line indicates the heating mode and the black line represents the cooling mode. b) Variation of the endothermic peak upon DSC cycles.

The occurrence of a spin transition in the hybrid NPs was unambiguously confirmed by differential scanning calorimetry (DSC) measurements that show two different peaks at 361 and 342 K in heating and cooling modes, respectively (Figure 4.9a). This result is in good agreement with the already reported spin transition values for 4 nm NPs of the same SCO compound estimated from magnetic susceptibility measurements (367 and 343 K in heating and cooling modes, respectively).[25] Eight temperature cycles were carried out to check the stability of the spin transition (Figure 4.9b). With the successive cycles, the material undergoes progressive fatigue that is especially visible in the exothermic peak. However, a remarkable hysteretic behavior remains in the core@shell nanostructure despite the reduced thickness of the SCO shell, thus proving the cooperativity of the spin transition. It is possible to take advantage of this cooperative spin transition to prepare memory devices in which the spin state is thermally addressed and electrically detected through temperature-dependent transport measurements. Thus, the hybrid Au@SCO NPs were deposited into electrical devices consisting of interpenetrated “fingers” (10 μm gap) following a previously reported dielectrophoretic deposition process.[4] Scanning electron microscopy (SEM) images (Figure 4.10) performed after deposition and transport measurements revealed a dense and thin assembly of NPs between the electrodes, which remain stable without evidence of coalescence.

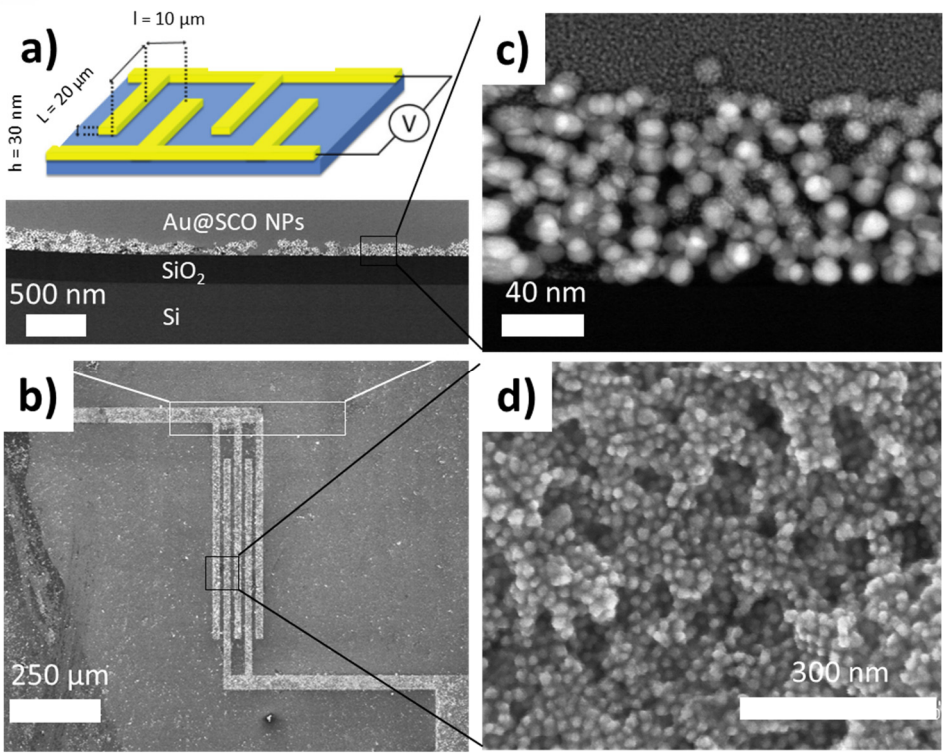

Figure 4.10 Left: Au finger-like electrode device used to measure the transport properties of an assembly of NPs. a) Scheme and dimensions of the electrodes (top); STEM transversal cross-section of the device (bottom). A zoom of this image to show the packing of the NPs is displayed in (c). b) SEM image of the device (top view). A zoom of this image is shown in (d).

Current–voltage (I–V) characteristics before and after Au@SCO NPs deposition in the device were first compared. After deposition, two out of twelve devices (*i.e.* 17%) displayed a clear increase in conductance as compared to the empty gap measurement (Figure 4.11), indicating that several particles in parallel were contacted between the electrodes in these devices. These results reflect that the deposition of the NPs (using a dielectrophoretic method) is the key step for the convenient preparation of the devices.

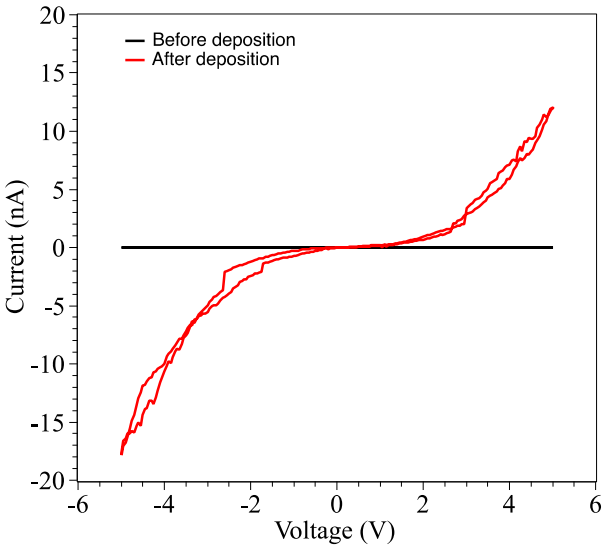

Figure 4.11 Comparison of the room temperature current-voltage characteristics before (black line) and after deposition (red curve). Changes in the transport-characteristics can then be attributed to the presence of hybrid Au@SCO NPs in the gap.

Then, temperature-dependent charge-transport measurements were performed on these devices recording the current at a fixed bias voltage of V = 2 V, while ramping the temperature (Figure 4.12). One observes a switching behavior in the conductance with two evident different values, which may be associated with the conductance of the two spin states, and a sharp transition between these two states. The relative change in conductance, as well as a small hysteretic effect (with a width of ≈ 5 K), are observed, evidencing a genuine switching/memory effect, in agreement with DSC measurements.

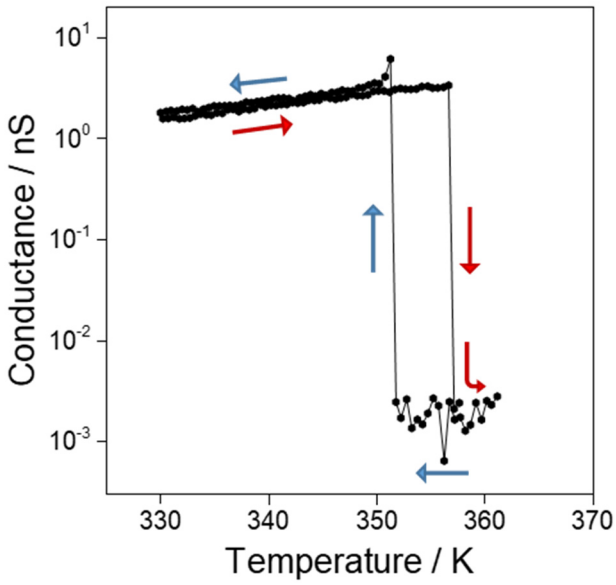

Figure 4.12 Thermal variation of the electrical current for an applied voltage of 2 V in the heating and cooling modes at 1 K·min^{-1} scan rate.

To prove that the change in the conductance is reproducible and independent of the scan rate, I–V curves at two fixed temperatures close to the spin transition were studied. A state with higher conductance was observed at T = 325 K, which has to be associated with the LS state, while a lower conductance state was observed at T = 355 K (measured in the cooling mode) for the HS state (Figure 4.13).

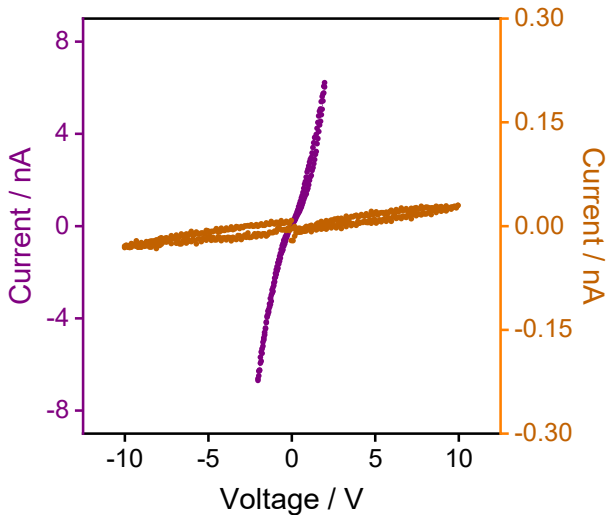

Figure 4.13. I–V curves of the high-conductive (purple) and low-conductive (orange) behaviors associated with the LS and HS states, respectively.

This result is in good agreement with previous studies performed in related SCO systems.[4,26,27,38] The unprecedented sharp transition in the conductance can be explained by considering the coexistence of several factors, namely i) the preservation of thermal bistability in small SCO NPs (4 nm) of the Fe-triazole series;[25] ii) a reinforcement of the elastic interactions occurring at the core@shell interfaces because of the reduced sizes of the NPs;[39] and iii) the excellent thermal conductivity of the Au NP center that is expected to provide a homogeneous and efficient heat transfer. All these aspects, operating either independently or synergistically, could render the observed fast and efficient spin transition.

Another remarkable feature is the relatively high conductance values observed in this Au@SCO-based device in the LS state, which are in the nS range despite the large electrode gap used (10 μm, Figure 4.10). These conductance values are well above the detection limit of the apparatus (in the pS range) and therefore can be measured with reasonable accuracy. In the HS state, the conductance values are in the pS range and, therefore, much less accurate and noisy. For comparison, an analogous device based on SCO NPs of 16 nm, stabilized by an organic surfactant and without the Au core was prepared. In this case, no electrical signal was recorded,

likely due to the insulating character of the sample. Such improvement in the conductance is attributed to the presence of the Au core, which does enhance the conductance of these core@shell NPs, thus facilitating the charge transport through the device. Table 4.2 shows a comparison of the conductance values of the present device with those exhibited by previous devices based on SCO NPs. It is observed that, despite the larger gap between electrodes, the conductance values in the present device are higher than those reported in previous works. An important consequence of this feature, as far as the device performance is concerned, is that the conductances associated with the two spin states exhibit ON/OFF ratios of about 5300 ± 200. These values are substantially larger than the previous record of 310 ± 80 reported by some of us in devices that use 2D assemblies of $[Fe(Htrz)_2(trz)](BF_4)$ NPs stabilized by an organic surfactant.[26] These exciting results may have their origin due to a different transport mechanism. In the present device, electrical pathways could be flowing through metallic dots separated by thin insulating shells instead of a hopping mechanism as proposed in the pristine SCO NPs.

Table 4.2 Summary of the already published conductance values of SCO NPs under similar conditions

Reference	NPs	Size / μm	Gap / μm	Voltage / V	E / V·μm^{-1}	G_{LS} / S *	G_{HS} / S *
This work	Au@SCO	0.02	10	2	0.2	$3\cdot10^{-9}$	$2\cdot10^{-12}$
40	SCO@AOT	0.01	0.01	0.4	40	$0.5\cdot10^{-9}$	$0.9\cdot10^{-9}$
40	SCO@AOT	0.01	0.01	0.4	40	$2\cdot10^{-11}$	$6\cdot10^{-11}$
4	SCO@AOT	*ca.* 0.030	0.1	10	100	$0.2\cdot10^{-9}$	$0.1\cdot10^{-9}$
4	SCO-rods	3	4	10	2.5	$0.5\cdot10^{-9}$	$0.3\cdot10^{-9}$
4	SCO-rods	0.25	4	10	2.5	$4\cdot10^{-12}$	$1\cdot10^{-12}$
26	SCO@AOT	0.025	0.05	15	300	$8\cdot10^{-11}$	$4\cdot10^{-12}$
41	SCO	> 0.1	-	0.5	-	10^{-12}	-
42	SCO-rods	2	4	20	5	$1\cdot10^{-12}$	$1\cdot10^{-13}$
43	SCO-rods	1	4	20	5	$1\cdot10^{-10}$	$5\cdot10^{-11}$

* All conductance values are estimated from the respective publications

Interestingly, the synthesis can also be carried out using other Au nanostructures. Among others, AuNSs offer great potential due to their hot spot created at the star branches. Moreover, as their optical properties result from the hybridization of plasmons focalized at the core and the tips of the NPs, they present a high plasmon tunability by the synthetic chemical modification of the NP.[44]

To prepare analogous core@shell NPs but employing AuNSs as the metallic core, the protocol was slightly modified. At first, Polyvinylpyrrolidone (PVP)-stabilized AuNSs of 74 ± 13 nm were synthesized by a seed-mediated growth method.[45] Similarly, a two-step procedure was carried out to achieve the growth of a SCO shell onto the nanosphere (see Figure 4.14).

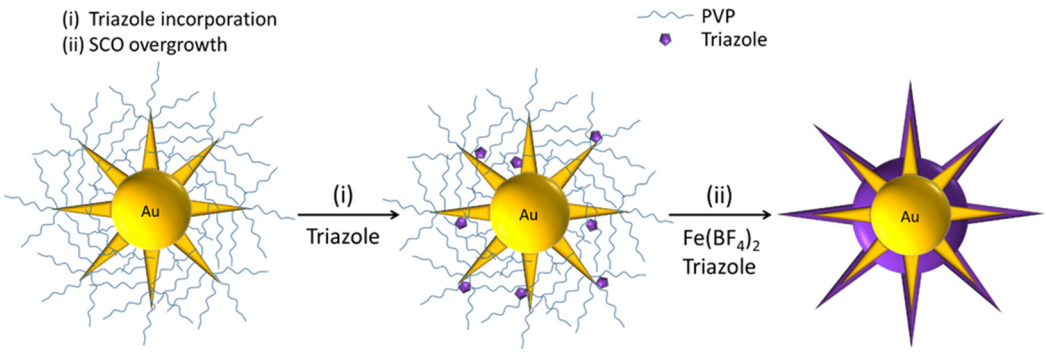

Figure 4.14 Schematic illustration of the steps involved in the preparation of AuNSs@SCO NPs.

Due to the use of a different capping agent surrounding the Au (PVP in this case) as well as the anisotropic shape of these NPs, some aspects have to be considered. Indeed, PVP is a high number polymer that sterically stabilizes the NP, mitigating any interaction with many ligands but also increasing the colloidal stability. Therefore, the incorporation/approximation time of triazole can be increased to one hour without compromising the colloidal suspension. However, the ligand presence cannot be appropriately checked by XPS because of the initial N corresponding to the PVP (see Figure 4.15a). It is important to remark that for AuNSs, this first step is not so essential as for the Au spheres. In fact, without this initial step, the resulting

NPs exhibit a core@shell structure but the shell is not well-formed. It could be that the greater reactivity of the branches leads to easier SCO growth. In any case, a pre-modification surface seems to permit a fine and more accurate overgrowth.

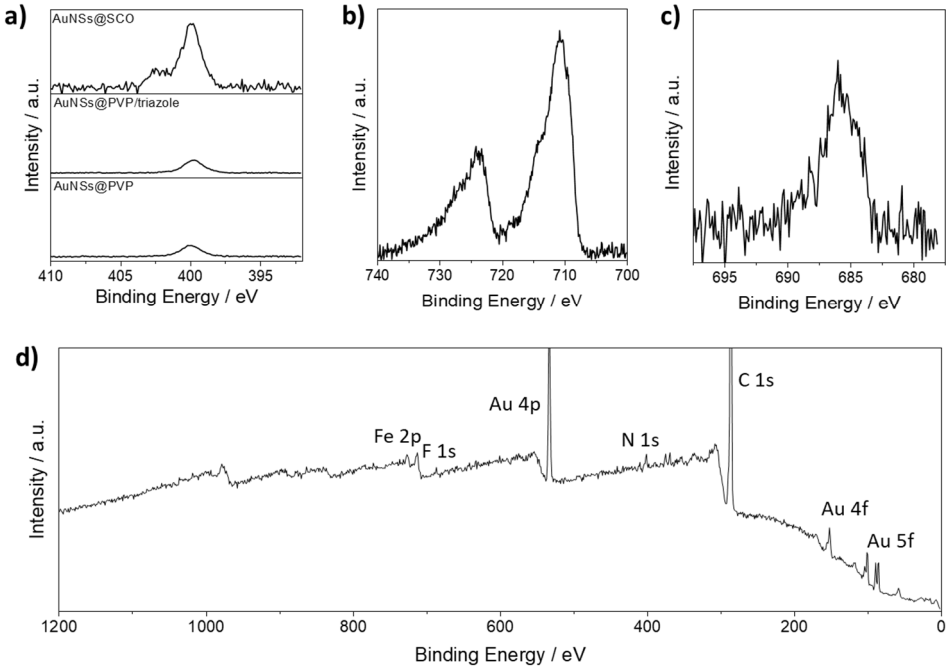

Figure 4.15 XPS spectra of a) N, b) Fe, c) F and d) Survey for AuNSs@SCO NPs.

Regarding the second step of the protocol, aqueous solutions of the Fe^{II} precursor and the Htrz ligand were dropwise added to the AuNSs suspension at a constant rate of 4 $mL \cdot h^{-1}$ at room temperature and under stirring. It is worth noting that, compared to the nanospheres, AuNSs are considerably bigger (12 *vs.* 74 nm) implying a substantially lower number of particles in the solution, a lower nanoparticle total area and a larger SCO volume for the resulting core@shell, assuming a 4 nm shell. Therefore, concentrations have to be revised in order to get a well-formed shell. Besides, taking advantage of the greater colloidal stability, concentrations can be increased, obtaining AuNSs@SCO with a thinner or thicker shell (*ca.* 4.8 nm and

ca. 14 nm, respectively; Figure 4.16). A thin SCO shell leads to a small variation of the obtained surface charge attaining a value high enough to have stable colloidal suspensions (Table 4.3 and Figure 4.17). On the other hand, the colloidal stability is partially lost for the core@shell with a thicker SCO shell where a combination of single and aggregated NPs can be found by TEM and DLS (Figures 4.16 and 4.17).

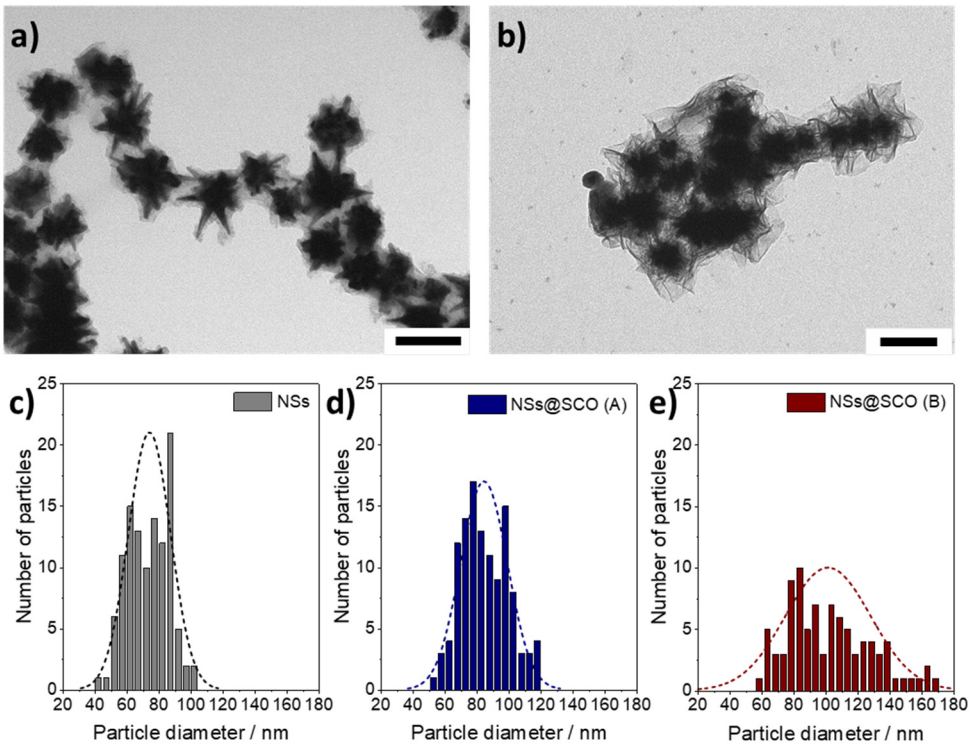

Figure 4.16 TEM images of AuNSs@SCO with a) a thinner shell and b) a thicker shell. Histograms of the size distributions for c) the AuNSs and d, e) the overall core@shell with a thin and thick shell, respectively.

Table 4.3: ζ-potentials of AuNSs@PVP, AuNSs@PVP/Htrz and AuNSs@SCO NPs.

Sample	ζ-potential / mV	pH
AuNSs@PVP	- 29 ± 8	6.42
AuNSs@PVP/Htrz	- 28 ± 11	6.70
AuNSs@SCO$_{(thin)}$	- 20 ± 9	6.53

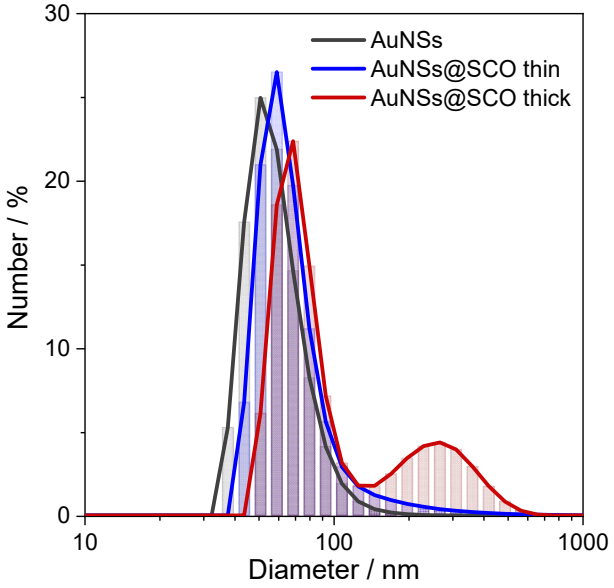

Figure 4.17 DLS plot for PVP-stabilized AuNSs, AuNSs with a thin SCO shell and AuNSs with a tick SCO shell.

To characterize the metallic composition, EDX was used (Figure 4.18) evidencing a defined core@shell distribution. Also, XPS spectra (Figure 4.15) display peaks of iron, nitrogen, and fluorine, indicating the presence of metal, ligand, and counterion, thus supporting the formation of the SCO compound.

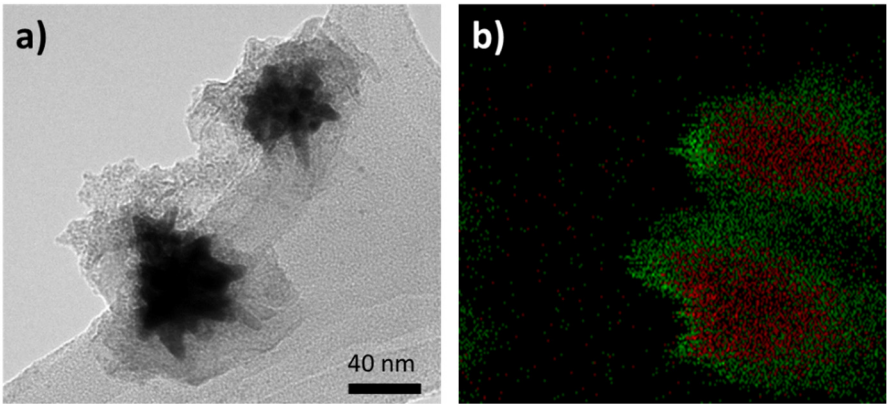

Figure 4.18 EDX mapping of the metals present in the AuNSs@SCO.

Figure 4.19 displays the diffraction pattern of the AuNSs@SCO; once again, a unique peak at 38.2°, characteristic of metallic Au, can be noticed. Again, the expected peaks for the $[Fe(Htrz)_2(trz)](BF_4)$ compound were not observed. For this measurement, the thickest shell was used (of around 14 nm). Therefore, the obtention of an SCO amorphous phase seems the most plausible reason. In any case, SCO formation was confirmed by the observation of its characteristic vibrational peaks (Figure 4.20) by means of attenuated total reflectance Fourier-transform infrared (ATR-FTIR).

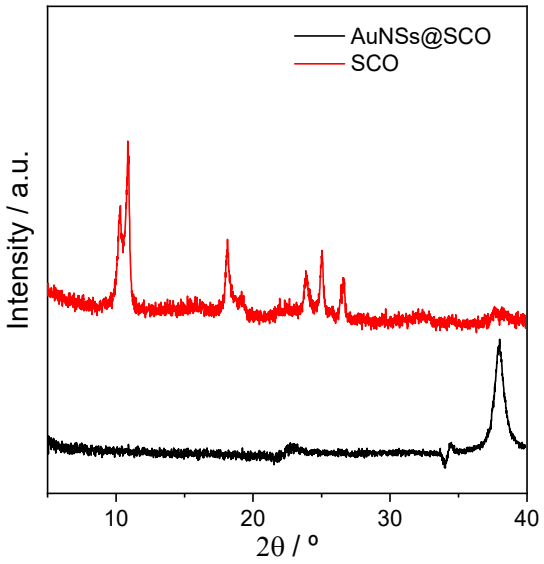

Figure 4.19 Room temperature PXRD for Au@SCO (black) and SCO (red) compounds.

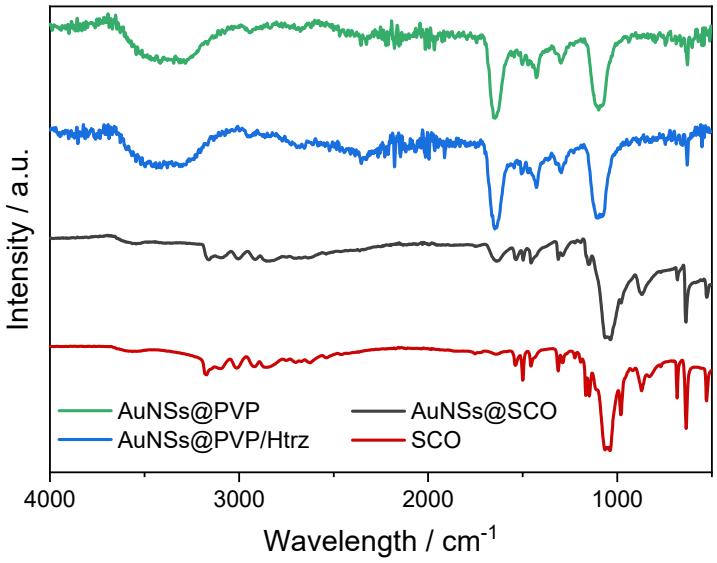

Figure 4.20 ATR-FTIR spectra of PVP-stabilized AuNSs before and after the Htrz addition.

Comparing the optical properties of these hybrids with the pristine Au (Figure 4.21), it is observed that the maximum at 697 nm, corresponding to the plasmon band, is shifted after the shell formation to 738 nm. This plasmon shift is considerably more pronounced than the one observed in the Au spheres (41 *vs.* 12 nm) as a consequence of the higher sensibility of the Au branches.[46,47]

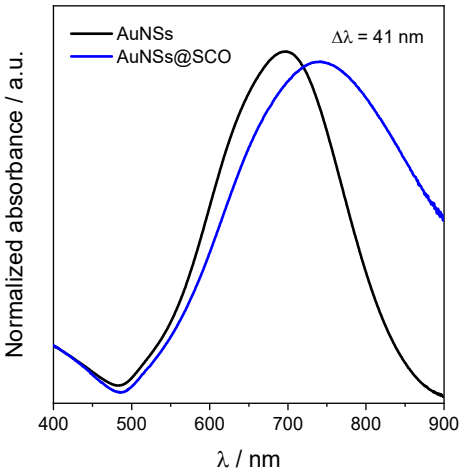

Figure 4.21 Spectra of AuNSs and AuNSs@SCO in the visible region.

On this occasion, the spin-transition was also confirmed by DSC measurements that exhibit two different peaks at 352 and 342 K in heating and cooling modes, respectively (Figure 4.22a). Nevertheless, smaller hysteresis and extreme differences between the intensities of endothermic (LS to HS) and exothermic (HS to LS) peaks are recorded. The observation of such smaller hysteresis could be associated with the presence of PVP that influences the SCO NP formation. On the other hand, the reduction of the endothermic peak indicates the appearance of an important and swift fatigue after the first spin-transition (Figure 4.22b). This strong reduction in the intensity of the spin-transition peaks could be due to a possible introduction of oxygen during the sample measurement. Therefore, these measurements must be repeated to extract further conclusions. Interestingly, by performing the synthesis under nitrogen atmosphere, a clear endothermic can be

discerned in the heating process, while, during the cooling mode, the LS recovery can evidence by an exothermic peak at 65ºC (Figure 4.22c). In this way, it seems that the preparation of these NPs under an inert atmosphere gives rise to more Fe^{II} centers able to switch their spin state. Observing the resulting NPs in TEM, they look analogous to the AuNSs@SCO shown in Figure 4.16. As future work, we will fully characterize and study this obtained heterostructure in order to further improve the synthetic protocol.

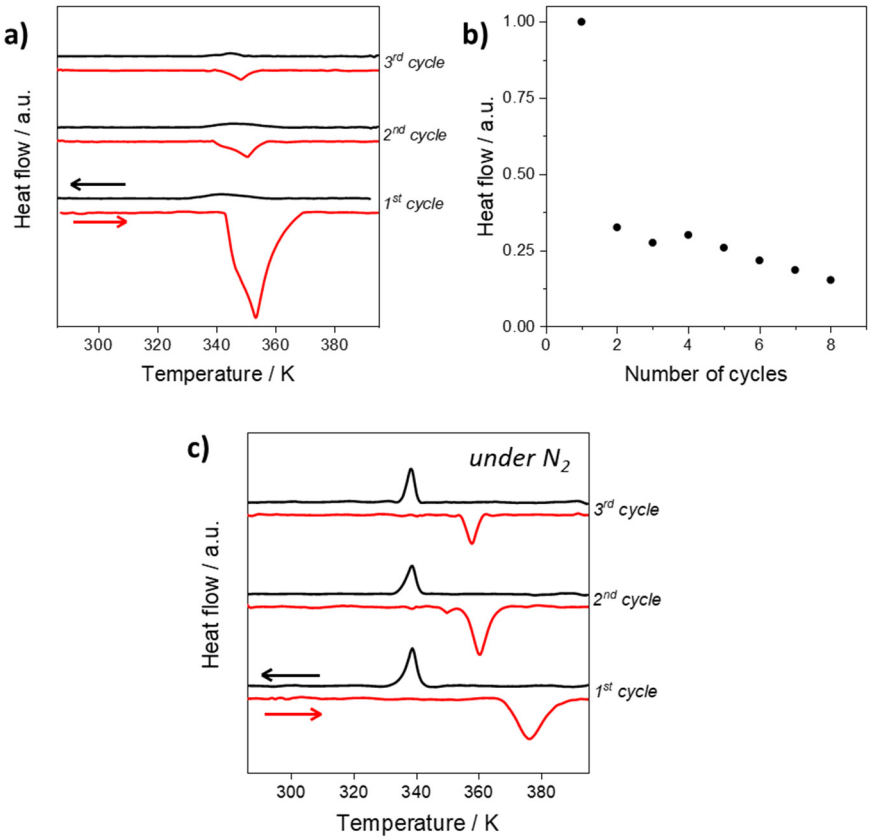

Figure 4.22 a) DSC curves of AuNSs@SCO obtained by scaling up the reaction; the red line indicates the heating mode and the black line represents the cooling mode. b) Variation of the endothermic peak upon DSC cycles. c) DSC curves of AuNSs@SCO obtained under nitrogen atmosphere.

Finally, the Au metallic composition of the core was changed to Ag by reproducing the same two-step approach used for the Au nanospheres coverage. Ag NPs were firstly synthesized following the seed-mediated growth Lee-Meisel method.[48] As the Ag NPs stabilized by citrate exhibited similar size, no modification of the procedure was required. Core@shell NPs of 23 ± 3 nm were obtained with an Ag core of 14 ± 3 nm and a shell size of about 4.5 nm (Figure 4.23). In addition to this, the resulting hybrid was colloidally stable (see Table 4.4), presenting a ζ-potential value of – 20 ± 9, quite similar to the other Au@SCO nanostructures. By EDX, a metal ratio of $Ag/Fe_{0.68}$ was estimated.

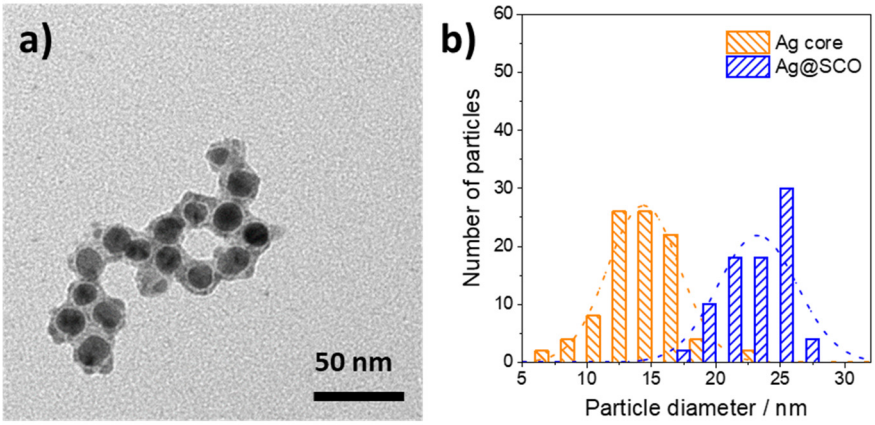

Figure 4.23 a) TEM image of Ag@SCO NPs. b) Histograms of the size distributions for the Ag core (orange) and the overall core@shell NP diameter (blue).

Table 4.4: ζ-potentials of Ag@citrate, Ag@citrate/Htrz and Ag@SCO NPs.

Sample	ζ-potential / mV	pH
Ag@citrate	- 29 ± 8	6.84
Ag@citrate/Htrz	- 27 ± 11	6.97
Ag@SCO	- 20 ± 9	6.64

Once again, the XPS spectra display peaks of iron, nitrogen, and fluorine (Figure 4.24), indicating the presence of metal, ligand, and counterion, suggesting the SCO formation

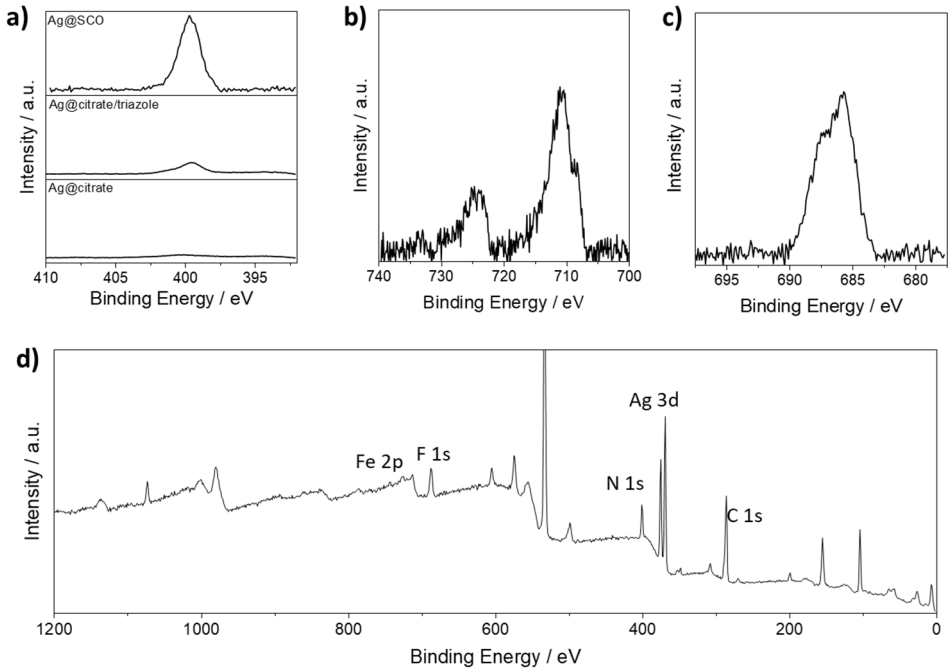

Figure 4.24 XPS spectra of a) N, b) Fe, c) F and d) Survey for Ag@SCO NPs.

Regarding the plasmonic properties for the Ag@SCO heterostructure (Figure 4.25), the plasmon is shifted 15 nm, comparable to the spherical Au shift (15 *vs.* 12 nm). This similarity is not unexpected considering the fact that plasmonic NPs with the same geometry have analogous sensitivity regardless of the metal composition.[49] On the other hand, spin transition peaks were found in DSC (Figure 4.26). Two different endothermic peaks were observed. Taking into account the influence of the size on the spin transition,[7,50] this could be a consequence of the additional formation of different NPs of SCO that could have self-nucleated during the synthesis and/or the partial oxidation of the thin SCO shell.

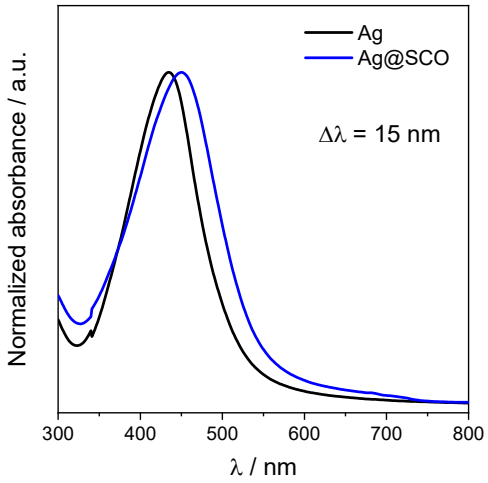

Figure 4.25 Spectra of Ag and Ag@SCO in the visible region.

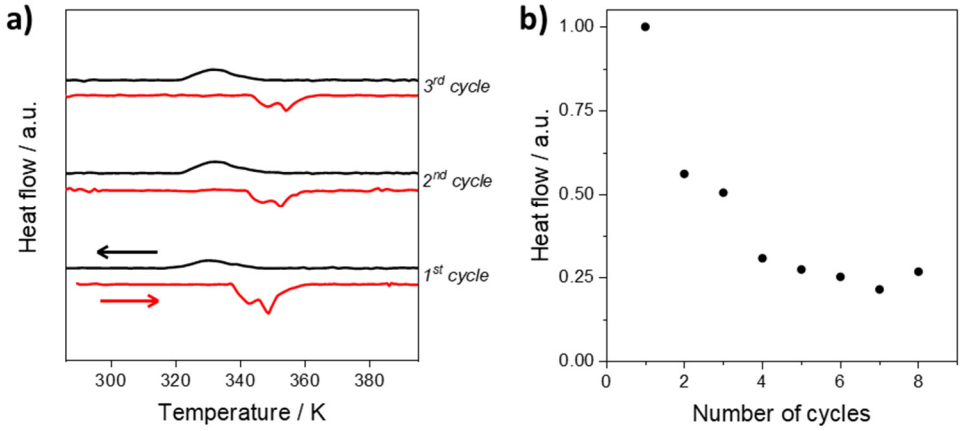

Figure 4.26 DSC curves of Ag@SCO obtained by scaling up the reaction; the red line indicates the heating mode and the black line represents the cooling mode. b) Variation of the endothermic peak upon DSC cycles.

In summary, core@shell heterostructures formed by metallic cores of different shapes and a SCO shell can be obtained. In these hybrid NPs, the plasmonic band can be tuned in a wide range of the visible spectrum by selecting the plasmonic NP. This possibility may be exciting in order to selectively induce the spin-transition by light irradiation of the appropriate wavelength.

As already mentioned, we have attempted to extend this procedure in order to develop some heterostructures of Au@MOF with the final aim of tuning their electrical properties by the presence of guest molecules. The notation MOF-like is used considering the possible synthesis of an amorphous CP based on MIL-100 and MIL-88. In this line, two different Au@MOF-like hybrids were obtained. However, only preliminary electrical characterization of one of them was carried out. Still, as an ongoing work, some future experiments will be proposed at the end of this part.

The selected MOFs to cover the Au NPs were MIL-100(Fe) and MIL-88(Fe) (addressed here as MIL-100 and MIL-88, respectively), well-known compounds that offer a great variety of applications. The structure of MIL-100 is a zeotype crystal composed of trimesic acid organic linkers and Fe(III) trimers. On the other hand, the structure of the MIL-88 is hexagonal and is built up from the connection of Fe(III) trimers, octahedrally interconnected through the dicarboxylates of fumaric acid.[51–54] Previously to the shell growing, spherical citrate-stabilized Au NPs of around 12 nm were synthesized following the well-known protocol reported by Turkevich.[33]

The procedure followed is illustrated in Figure 4.27. As it can be noticed, contrary to the Au@SCO heterostructures, a ligand exchange is not required. Citrate molecules anchored to the Au surface will act as a nucleation site for the MOF growth. In fact, citrate has similarities with the MOF ligands (fumaric and trimesic acid): all of them have carboxylic acid groups that can coordinate the Fe. Nevertheless, citrate molecules remaining in the solution can also act as nucleation sites. Therefore, before the shell overgrowth, Au NPs were washed to remove the excess of citrate but with remaining capping molecules located on the surface, as can be deduced from ζ-potential and ATR-FTIR measurements. A small amount of $FeCl_3$ was added to coordinate the Au@citrate NPs in order to act as anchoring sites. It has to be mentioned that by skipping this step, core@shell NPs can also be prepared. However, this step leads to a reproducibility improvement and a better shell formation. After the Fe stabilization, the continuous growth of the complex onto the Au NPs was performed upon the controlled addition of the precursors (*i.e.* $FeCl_3$ and trimesic/fumaric acid). The precursors were simultaneously added to the Au suspension at a constant rate (4 $mL \cdot h^{-1}$) at room temperature and under magnetic stirring. It is important to point out that the formation of a shell requires low particle

concentrations to endow the preservation of the colloidal suspension. Higher Au (> 0.5 mM) and precursor concentrations (> 0.18 and 0.12 mM for Fe and ligand, respectively) lead to severe NP aggregation. Despite this, the synthesis can be accomplished using higher concentrations (for instance, using double concentrated solutions) but the NPs do not present a core@shell structure. It seems that in these conditions the MOF compound grows at some facets instead of over the whole metal surface.

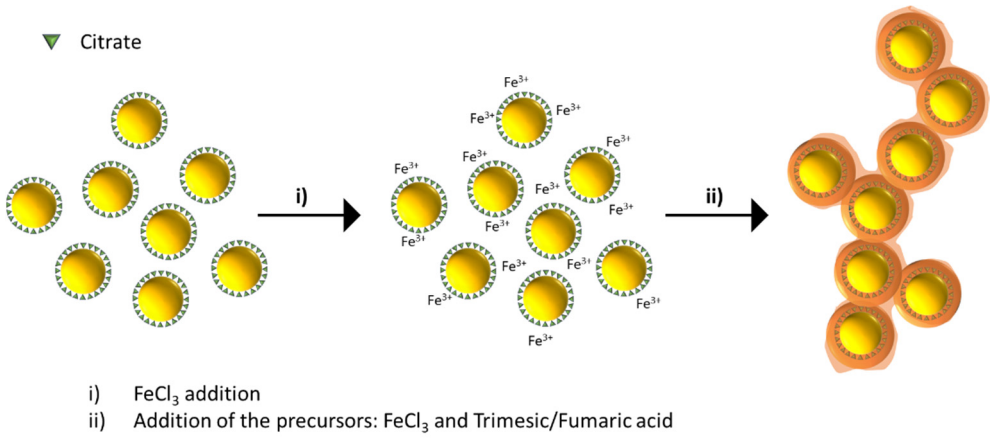

Figure 4.27 Schematic illustration of the protocol for preparing Au@MOF-like NPs of MIL-100 and MIL-88.

To further explore the synthesis of the hybrid composites, the addition rate and the Au/Fe ratio were modified. However, a faster addition rate gives rise to self-nucleated NPs, while a slower rate leads to Au aggregation. On the other hand, by decreasing the Au/Fe ratio (*i.e.* an increase in the Fe content), a thicker shell is formed but also plenty of self-nucleated NPs. Consequently, 4 $mL \cdot h^{-1}$ and the initial Au/Fe ratio of 2.8 are the optimal conditions to achieve a core@shell morphology without compromising the colloidal stability.

As it can be observed in Figure 4.28, TEM images evidence the existence of grapes of core@shell NPs (for both the MIL-100 and MIL-88). Once the synthesis is

completed, these core@shell grapes are principally formed by 100 nm aggregates (Figure 4.29). Gradually, they grow in size until the colloidal stability is lost. Consequently, after 48-72 hours, the system collapses.

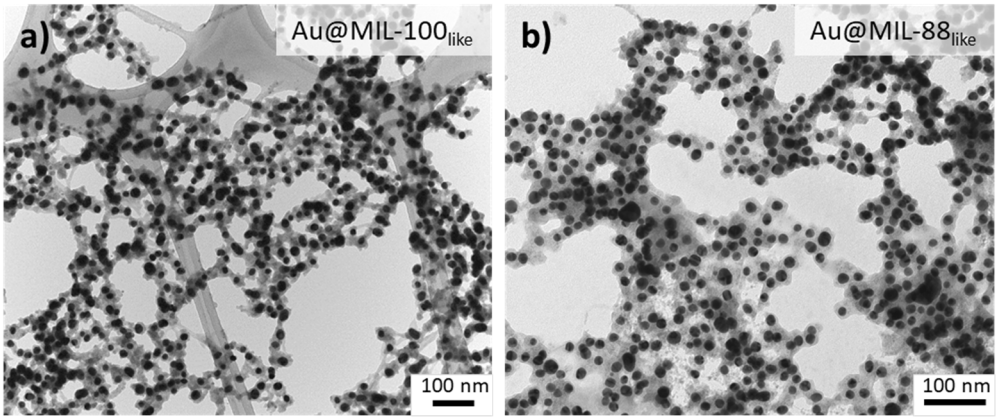

Figure 4.28 TEM images for the Au@MOFs-like: Au@MIL-100$_{like}$ (a) and Au@MIL-88 $_{like}$ (b) after the reaction being completed.

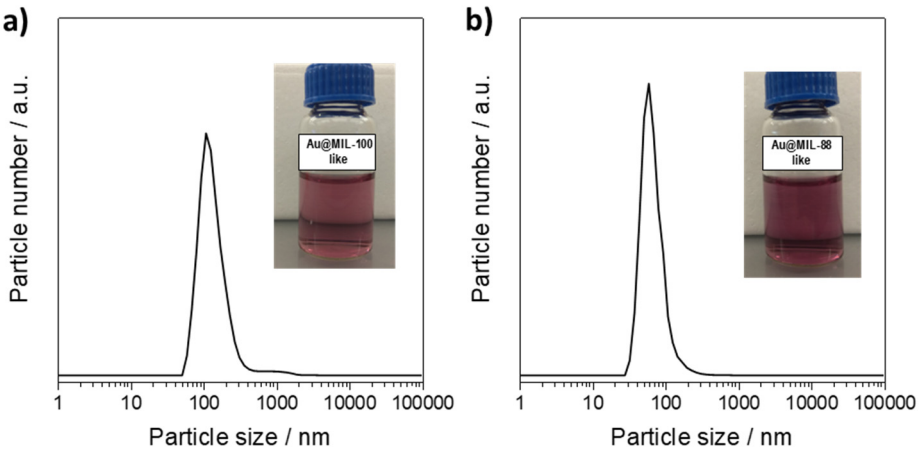

Figure 4.29 DLS of the Au@MOFs-like: Au@MIL-100 $_{like}$ (a) and Au@MIL-88 $_{like}$ NPs (b).

The resulting core@shell NPs were characterized by ATR-FTIR, where characteristic vibrational peaks were found (Figure 4.30). In particular, comparing with the MIL-100 system, it can be observed: C = O stretching located at 1620 cm^{-1}, C – O vibration at 1375 cm^{-1}, – OH vibration at 1445 cm^{-1}, C = O stretching coming from the uncoordinated trimesic acid at 1720 cm^{-1}, C – H stretching vibration of benzene ring at 760 and 711 cm^{-1}. Comparing with the MIL-88 compound, it can be noticed: C = O symmetric and asymmetric vibrations located at 1390 and 1600 cm^{-1}, C = O stretching coming from the uncoordinated fumaric acid at 1700 cm^{-1}, carbonyl vibrations at 675 and 640 cm^{-1}. In Figure 4.31, ATR-FTIR spectra before and after Au NPs washing are presented, showing: i) an effective removal of the excess citrate in the solution and ii) a persistence of the citrate vibrations coming from the molecules acting as capping agent. This fact is in good agreement with ζ-potential analysis displaying insignificant variation after the washing process.

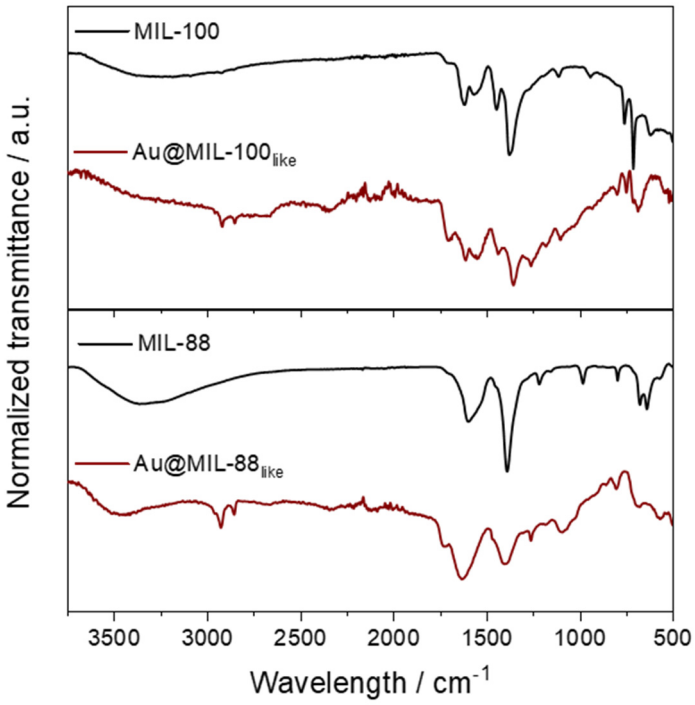

Figure 4.30 ATR-FTIR spectra of the MOF compounds and the Au@MOFs-like.

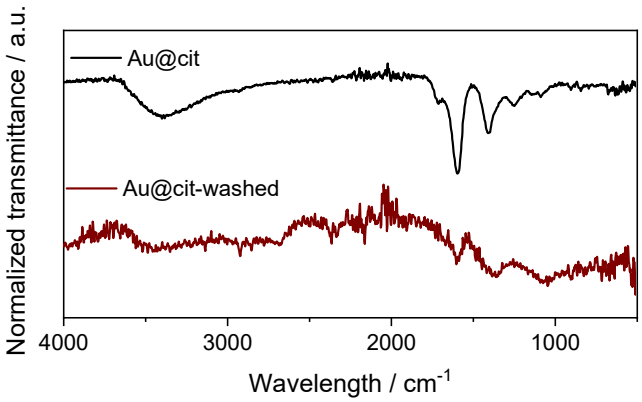

Figure 4.31 ATR-FTIR spectra of citrate-stabilized Au NPs before and after washing.

Interestingly, the X-ray diffraction patterns of the core@shell systems, shown in Figure 4.32, exhibit two peaks located at 38.2° and 44.3º related to the Au. Nevertheless, the peaks related to the MOFs were not observed. As in the Au@SCO heterostructure, this absence could be due to the small thickness of the shell, which may be beyond the detection limit of the X-ray diffractometer, the large electron density of the Au cores, which can screen the signal coming from the SCO component, or the existence of an amorphous shell around the Au. However, due to the high crystallinity that MOFs usually exhibit, the most likely reason is the presence of amorphous CPs formed by iron and trimesic acid (for MIL-100) and fumaric acid (for MIL-88). As future work, synthetic parameters will be further optimized in order to improve the crystallization of the MOF compound (*i.e.* increasing the reaction time, temperature, *etc.*). Also, porosity measurements will be carried out to ascertain the presence or not of high porosity in these heterostructures.

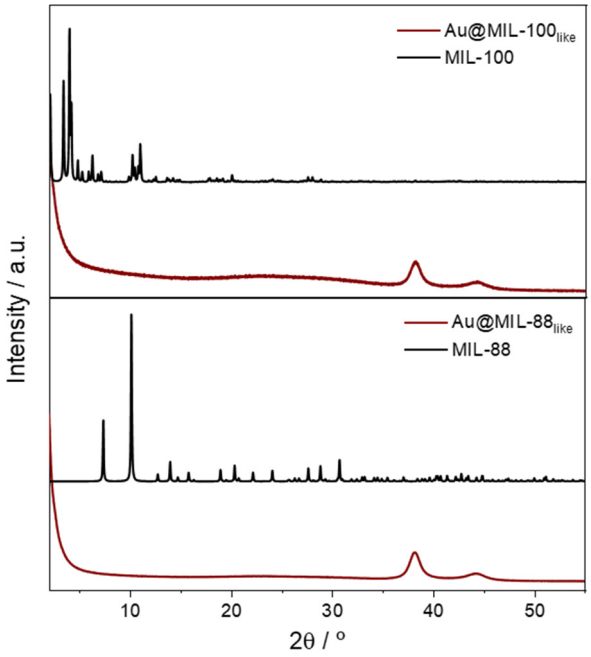

Figure 4.32 PXRD of the MOF compounds and the Au@MOFs-like NPs.

XPS was carried out to evidence the presence of Fe(III) in both cases (Figure 4.33). In parallel, EDX was carried out to identify the distribution of iron over the NPs. Figure 4.34 shows evident core@shell systems connected through a matrix to other NPs with an estimated Fe/Au ratio for both cases of around 0.4.

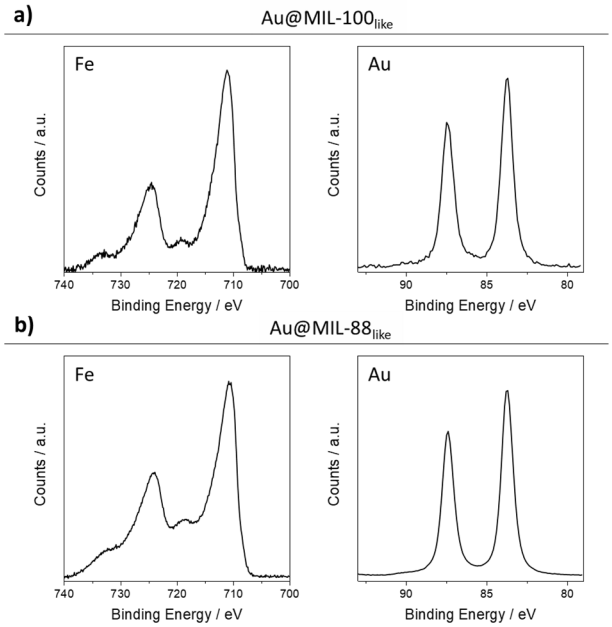

Figure 4.33 XPS spectra of the Au@MOFs-like NPs.

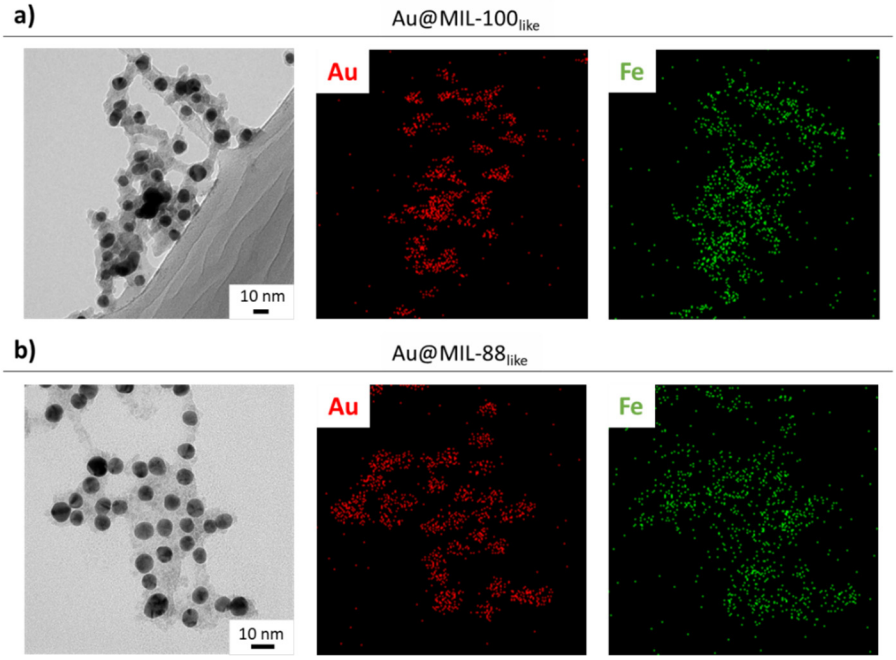

Figure 4.34 HR-TEM images and EDX mapping of the metals present in the heterostructures (red: Au; green: Fe).

Regarding the optical properties, the LSPR of Au NPs is progressively red-shifted during shell formation. Such a color change from red to pink is essentially occurring upon the addition of iron and ligand solutions suggesting the MOF-like formation around the Au surfaces. As in the Au@SCO system, the plasmon band shift has its origin in the change of the dielectric constant around the Au NP surface upon the continuous overgrowth of the shell.[36,37]

The kinetics of the reaction was followed by monitoring the plasmon band position during the synthesis. Besides, the full width at half maximum (FWHM) was calculated to estimate the NP aggregation. Indeed, a widening of the plasmon band and a diminution of its intensity are generally associated with aggregation.[55] Results for both core@shell systems are displayed in Figure 4.35. For the Au@MIL-100$_{like}$ heterostructure, it can be observed that the plasmon properties (position and FWHM) do not vary considerably before adding 1.0 mL of each precursor. After that, the plasmon position is considerably shifted with almost no change in its FWHM until 2.5 mL. Nevertheless, after adding 2.5 mL of each precursor there is a plasmon red-shift with a significant decrease in intensity. This is due to NP aggregation that leads to an increase in the plasmon peak width. NP aggregation was also noticed for Au@MIL-88$_{like}$. However, a significant plasmon band shift was observed after adding 1 mL of each precursor, suggesting a faster shell formation compared to the compound based on the MIL-100.

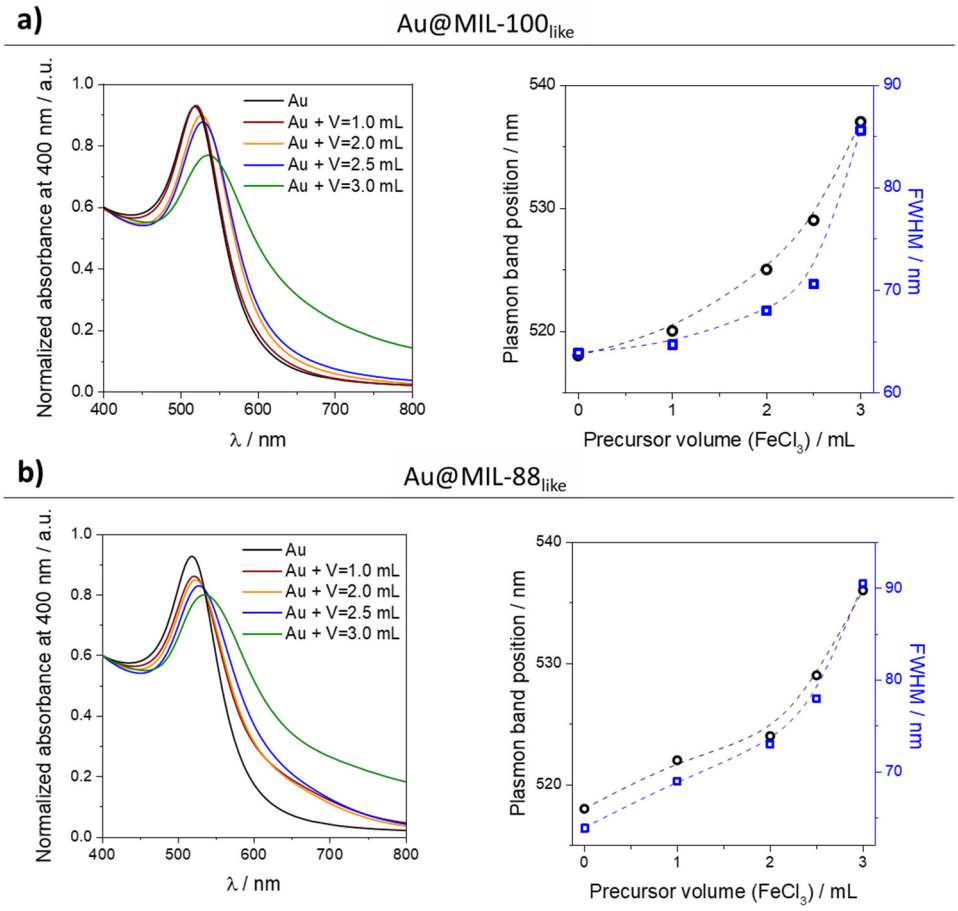

Figure 4.35 (Left) UV-Vis spectra at different reaction steps and (Right) plasmon band position and FWHM evolution during the reaction for a) Au@MIL-100$_{like}$ and Au@MIL-88$_{like}$ compounds.

Au@MIL-100$_{like}$ NPs were deposited into electrical devices consisting of interpenetrated “fingers” (2.5 µm gap) in order to study their electrical properties. Contrary to the Au@SCO device, a smaller electrode gap was used to improve the contact between the electrodes, thus increasing the reproducibility of the measurements. Indeed, after deposition, two out of four devices (*i.e.* 50%) displayed a clear increase in conductance as compared to the empty gap measurement.

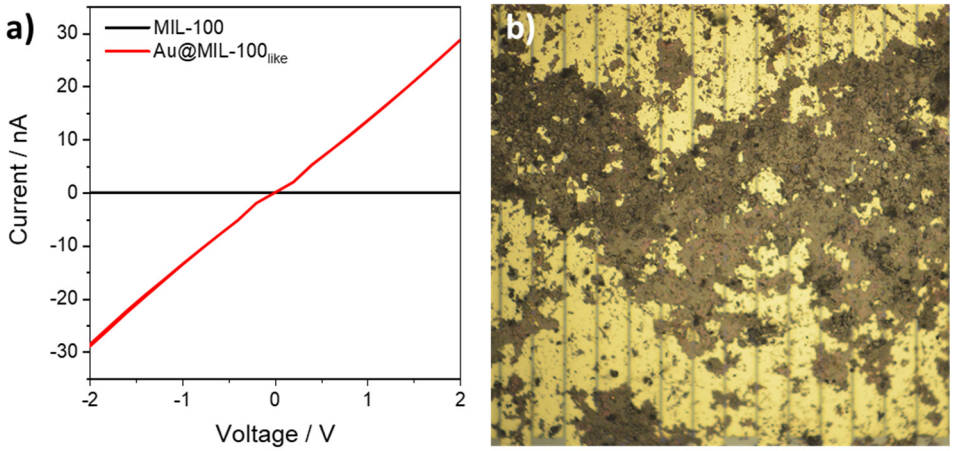

Figure 4.36 a) Comparison of the room temperature current-voltage measurements of the Au@MIL-100$_{like}$ and MIL-100 compounds. b) Optical image of the Au finger-like electrode device used to measure an assembly of Au@MIL-100$_{like}$ NPs.

I–V curve of the Au@MIL-100$_{like}$ NPs was compared with the MIL-100 compound where no electrical signal was recorded due to the insulating character of the sample (Figure 4.36). The core@shell system evidences an improvement in the conductance which is attributed to the presence of the Au cores. As observed in the Au@SCO heterostructure, Au is facilitating the charge transport through the device.

For future work, the synthetic protocol will be further optimized to improve the crystallinity of the MOF systems. Also, porosity measurements will be carried out and the adsorption of various gas molecules will be explored and analyzed. In addition to this, similar measurements will be carried out for the Au@MIL-88$_{like}$ hybrid and the MIL-88 compound to ascertain the conductivity improvement. We expect that, thanks to the increase of detection limit, a study on the influence of the electrical properties of the guest molecules inside the MOF pores will be possible *via* transport measurements under different gas atsmospheres. In this way, these hybrids could act as remarkable electrical gas sensors overcoming the insulating limitations of MOFs.

4.3 Conclusions and perspectives

A simple chemical protocol has been reported to prepare stable colloidal suspensions of core@shell NPs formed by a spherical metallic Au core of ≈12 nm surrounded by a thin shell of an insulating SCO CP, 4 nm thick. This procedure has allowed us to prepare Au@SCO NPs having a naked surface, in sharp contrast with previous examples that required the presence of a capping agent in the surface (surfactant molecules or SiO_2 shell) to limit the growth of the SCO NP. Through DSC measurements it has been proved that these hybrid NPs undergo a cooperative spin transition in the range 340–360 K, in full agreement with the values reported for 4 nm NPs of the same SCO compound. Thanks to the metallic core and the naked surface of the ultrathin SCO shell, these core@shell NPs are more conductive than the pristine SCO NPs when contacted to electrodes. As a consequence, these SCO devices exhibit a significant improvement in the electrical detection of the spin state, with values for the ON/OFF ratio, which are an order of magnitude better than the best ones obtained in previous devices based on SCO NPs.

This chemical protocol is also adapted to nanostars (AuNSs) that present higher sensitivity and could help to develop highly sensitive switching devices based on the SCO phenomenon, being also possible to extend it to other metallic components such as Ag. Additionally, by modifying the chemical protocol, it was possible to cover spherical Au NPs with two different CPs based on MOFs (the MIL-88 and the MIL-100). These resulting heterostructures are mainly formed by grapes of *ca.* 100 nm. As for the Au@SCO NPs, these heterostructures are also more conductive compared to the pristine MOF material. Thanks to that, in future work, the electrical detection of guest molecules will be explored.

A further development that can also be imagined for these heterostructures is that of taking advantage of the plasmon properties of the Au core. The Au@SCO heterostructures could be used to get a light-induced spin transition exactly at room temperature. In this case, the efficient absorption of light provided by the plasmonic NP should be sufficient to heat the SCO shell and to provoke the spin transition. Similarly, the plasmon can be used in Au@MOF systems to get photo-thermal desorption of molecules from the MOF shell due to the heating of the system.

Finally, the presented procedure is shown to be very effective in covering metallic NPs with a thin shell of SCO for improving the SCO electrical detection. In addition to this, it can be an effective strategy in order to grow other CPs such as MOF or even Hofmann clathrates.

4.4 Experimental details

4.4.1 Synthesis

All chemical reagents were purchased and used without further purification. Chloroauric acid, sodium citrate tribasic dihydrate, 1,2,4-triazole, iron tetrafluoroborate hexahydrate, L-ascorbic acid, iron trichloride hexahydrate, trimesic acid, fumaric acid and Polyvinylpyrrolidone-30K were purchased from Sigma-Aldrich. Silver nitrate was purchased from Alfa Aesar and ultra-pure water (18.2 MΩ).

Au@SCO synthesis.

Iron-triazole polymeric spin-crossover system was grown onto citrate-stabilized Au NPs of 12 nm freshly prepared following the well-known Turkevich method[33] and washed with water to remove the excess of citrate in the solution. To overgrow the SCO shell a preliminary step is essential, which consists of the partial triazole surface functionalization of the Au NPs. A triazole aqueous solution (200 µL, 0.5 mM) was added to Au NPs aqueous solution (3 mL, 0.16 mM) and the mixture is stirred for 30 minutes. Then, aqueous solutions of the precursors, iron tetrafluoroborate hexahydrate (3 mL, 0.16 mM) and triazole (3 mL, 0.5 mM), were simultaneously added at a continuous rate (4 $mL \cdot h^{-1}$) under stirring at room temperature. After completion of the addition, the aqueous colloidal suspension was washed with water at 8000 rpm for 30 minutes to collect the Au@SCO NPs. Thicker SCO shells were obtained by decreasing the Au concentration to 0.12 mM.

Additional note: the optimal triazole/gold ratio required in the preliminary triazole surface functionalization was established by adding different concentrations of

triazole onto a colloidal suspension of Au NPs of known concentration. For triazole/gold molar ratios > 1/3 ($1.5 \cdot 10^{-6}$ mol of triazole per $5.0 \cdot 10^{-6}$ mol of Au), Au NPs immediately collapse and aggregate, whereas, for lower values, the best colloidal stability of the resulting NPs was obtained by adding a molar ratio of 1/5 ($1.0 \cdot 10^{-7}$ mol of triazole) on the same Au dispersion.

AuNSs@SCO synthesis.

Au NPs with star-like shapes (AuNSs) were obtained by a seeded-growth process,[45] using citrate-stabilized AuNPs as seeds, obtained following the Turkevich method.[33] For the preparation of growth solution, hydrochloric acid (10 µL, 1 M) was added to a $HAuCl_4$ solution (10 mL, 0.25 mM). Afterward, aqueous solutions of ascorbic acid (50 µL, 0.1 M) and $AgNO_3$ (100 µL, 0.003 M) were added, followed by the addition of 100 µL of seed solution. Finally, PVP was added as capping agent (1 mL, 10 $g \cdot L^{-1}$). After 30 minutes of incubation, AuNSs were washed with water to remove the excess of PVP in the solution.

SCO system was grown onto PVP-stabilized AuNSs following a similar two-step approach. In a first step, a triazole aqueous solution (250 µL, 0.5 mM) was added into the previously prepared Au aqueous solution (3 mL, 0.16 mM) under continuous stirring in air for 60 minutes. In a second step, iron tetrafluoroborate hexahydrate (3 mL, 0.16 mM) and triazole (3 mL, 0.5 mM) aqueous solutions were simultaneously added (4 $mL \cdot h^{-1}$) under stirring in air at room temperature. The obtained core@shell AuNSs@SCO nanoparticles were then collected by centrifugation (3500 rpm, 15 min) and easily re-dispersed in different solvents (water, ethanol, acetone, and chloroform). Thicker SCO shells were obtained by changing the following concentrations: iron tetrafluoroborate hexahydrate (3 mL, 0.5 mM) and triazole (3 mL, 1.5 mM) and Au (3 mL, 0.4 mM).

Ag@SCO synthesis.

Iron-triazole polymeric spin-crossover system was grown onto citrate-stabilized Ag NPs of 10-20 nm prepared following the seed-mediated growth Lee-Meisel method[49] and washed with water to remove the excess of citrate in the solution. To overgrow the SCO shell, it was performed an experimental protocol similar to the Au@SCO synthesis.

Additional note: All aqueous solutions were purged with Ar before starting the synthesis.

Au@MOF$_{like}$ synthesis

A CP based on the MIL-100(Fe) was grown onto citrate stabilized Au NPs. Au was previously washed with water to remove the excess of citrate in the solution, obtaining 3 mL of 0.25 mM solution. To overgrow the "MIL-100" shell, aqueous solutions of the precursors, iron chloride hexahydrate (2.5 mL, 0.09 mM) and trimesic acid (2.5 mL, 0.06 mM), were simultaneously added at a continuous rate (4 mL·h^{-1}) under stirring at room temperature. After completion of the addition, the aqueous colloidal suspension was washed with water at 8 000 rpm for 30 minutes to collect the Au@MIL-100$_{like}$ NPs.

A CP based on the MIL-88(Fe) system was grown onto citrate stabilized Au NPs. Au was previously washed with water to remove the excess of citrate in the solution, obtaining 3 mL of 0.25 mM solution. To overgrow the MOF$_{like}$ shell, aqueous solutions of the precursors, iron chloride hexahydrate (2.0 mL, 0.09 mM) and fumaric acid (2.0 mL, 0.06 mM), were simultaneously added at a continuous rate (4 mL·h^{-1}) under stirring at room temperature. After completion of the addition, the aqueous colloidal suspension was washed with water at 8 000 rpm for 30 minutes to collect the Au@MIL-88$_{like}$ NPs.

4.4.2 Characterization

UV/Vis Spectroscopy: UV-vis absorption spectra were recorded on a Jasco V-670 spectrophotometer in baseline mode from 400 to 800 nm range, using 1.000-cm-optical-path plastic cuvettes.

High-resolution transmission electron microscopy (HRTEM) and transmission electron microscopy (TEM): HRTEM studies were carried out on a Technai G2 F20 microscope operating at 200 kV and TEM studies on a JEM-1010 operating at 100 kV. Samples were prepared by dropping suspensions on lacey formvar/carbon copper grids (300 mesh).

ζ-Potential (ZP) and Dynamic Light Scattering (DLS) measurements: ZP and DLS measurements were performed at room temperature with a Zetasizer Nano ZS instrument (Malvern Instruments Ltd.) of the as-synthesized suspension.

X-ray Photoelectron Spectroscopy (XPS): Samples were analyzed at the X-ray Spectroscopy Service at the Universidad de Alicante using a K-ALPHA Thermo Scientific spectrometer. All spectra were collected using Al Kα radiation (1486.6 eV), monochromatized by a twin crystal monochromator, yielding a focused X-ray spot (elliptical in shape with a major axis length of 400 μm) at 30 mA and 2 kV. The alpha hemispherical analyzer was operated in the constant energy mode with survey scan pass energies of 200 eV to measure the whole energy band and 50 eV in a narrow scan to selectively measure the particular elements. XPS data were analyzed with Avantage software. A smart background function was used to approximate the experimental backgrounds. Charge compensation was achieved with the system flood gun that provides low energy electrons and low energy argon ions from a single source.

Transport measurements: Au@SCO and SCO transport measurements have been performed using a two terminal device configuration in a temperature range of 10 to 380 K under a high vacuum. A Physical Properties Measurement System (Quantum Design PPMS-9). Electrical measurements have been performed in the PPMS chamber using a Keithley 2450 voltage source and a Keithley 6517b electrometer. Dielectrophoresis was used to trap Au@SCO NPs between the

electrodes by powering a sinusoidal signal of 10 kHz frequency and 10 V peak-to-peak potential to the electrodes. Au@MOF$_{like}$ and MOF transport measurements have been performed inside a glovebox under N_2 atmosphere at room temperature, using a Keithley 4200-SCS as voltage source and electrometer. The measurements were carried out in a two-probe configuration using commercial fingerprinted electrodes, with a gap of 2.5 μm. The NPs were organized in the electrodes gap by drop-casting a suspension of the material.

Inductively Coupled-Plasma Mass Spectrometry (ICP-MS): The ICP-MS analysis were conducted at the Universidad de Valencia (Sección de Espectrometría Atómica y Molecular). Samples were digested in an acid medium at 220 ºC using a microwave oven.

Powder X-Ray Diffraction (PXRD): X-ray powder diffraction (PXRD) patterns were obtained with a PANalytical X'Pert diffractometer using the copper radiation (Cu-Ka = 1.54178 Å) in the 5–40 region.

Differential Scanning Calorimetry (DSC): DSC scans were recorded in a Mettler Toledo DSC 821e model that operates in the temperature range -25 - 500ºC equipped with a liquid nitrogen cryostat and a 200 W furnace.

Attenuated total reflectance Fourier-transform infrared (ATR-FTIR): spectra were collected in an Agilent Cary 630 FTIR spectrometer in the 4000−500 cm^{-1} range in absence of KBr pellets.

4.5 References

(1) Kahn, O.; Jay Martinez, C. Spin-Transition Polymers: From Molecular Materials Toward Memory Devices. *Science.* **1998**, *279* (5347), 44–48.

(2) Lefter, C.; Rat, S.; Costa, J. S.; Manrique-Juárez, M. D.; Quintero, C. M.; Salmon, L.; Séguy, I.; Leichle, T.; Nicu, L.; Demont, P. Current Switching Coupled to Molecular Spin States in Large Area Junctions. *Adv. Mater.* **2016**, *28* (34), 7508–7514.

(3) Shalabaeva, V.; Ridier, K.; Rat, S.; Manrique-Juarez, M. D.; Salmon, L.; Séguy, I.; Rotaru, A.; Molnár, G.; Bousseksou, A. Room Temperature Current Modulation in Large Area Electronic Junctions of Spin Crossover Thin Films. *Appl. Phys. Lett.* **2018**, *112* (1), 013301.

(4) Rotaru, A.; Dugay, J.; Tan, R. P.; Guralskiy, I. A.; Salmon, L.; Demont, P.; Carrey, J.; Molnár, G.; Respaud, M.; Bousseksou, A. Nano-Electromanipulation of Spin Crossover Nanorods: Towards Switchable Nanoelectronic Devices. *Adv. Mater.* **2013**, *25* (12), 1745–1749.

(5) Kumar, K. S.; Ruben, M. Emerging Trends in Spin Crossover (SCO) Based Functional Materials and Devices. *Coord. Chem. Rev.* **2017**, *346*, 176–205.

(6) Molnár, G.; Rat, S.; Salmon, L.; Nicolazzi, W.; Bousseksou, A. Spin Crossover Nanomaterials: From Fundamental Concepts to Devices. *Adv. Mater.* **2018**, *30* (5), 1703862.

(7) Volatron, F.; Catala, L.; Rivie, E.; Gloter, A.; Ste, O.; Mallah, T. Spin-Crossover Coordination Nanoparticles. *Inorg. Chem.* **2008**, *47* (15), 6584–6586.

(8) Martinez, V.; Boldog, I.; Gaspar, A. B.; Ksenofontov, V.; Bhattacharjee, A.; Gütlich, P.; Real, J. A. Spin Crossover Phenomenon in Nanocrystals and Nanoparticles of [Fe(3-Fpy)$_2$M(CN)$_4$](M^{II}= Ni, Pd, Pt) Two-Dimensional Coordination Polymers. *Chem. Mater.* **2010**, *22* (14), 4271–4281.

(9) Qiu, D.; Gu, L.; Sun, X.-L.; Ren, D.-H.; Gu, Z.-G.; Li, Z. SCO@SiO_2@Au Core–Shell Nanomaterials: Enhanced Photo-Thermal Plasmonic Effect and Spin-Crossover Properties. *RSC Adv.* **2014**, *4*, 61313–61319.

(10) Moulet, L.; Daro, N.; Mornet, S.; Vilar-Vidal, N.; Chastanet, G.; Guionneau, P. Grafting

of Gold onto Spin-Crossover Nanoparticles: SCO@Au. *Chem. Commun.* **2016**, *52* (90), 13213–13216.

(11) Suleimanov, I.; Sánchez Costa, J.; Molnár, G.; Salmon, L.; Bousseksou, A. The Photo-Thermal Plasmonic Effect in Spin Crossover@silica–Gold Nanocomposites. *Chem. Commun.* **2014**, *50* (86), 13015–13018.

(12) Li, Z.-H.; Wang, Y.-X.; Han, W.-K.; Zhu, W.; Li, T.; Li, Z.; Ren, X.; Gu, Z.-G. Integrating Spin-Crossover Nanoparticles with Silver Nanowires: Toward Magnetic and Conductive Bifunctional Nanomaterials. *New J. Chem.* **2017**, *41* (18), 10062–10068.

(13) Tobon, Y. A.; Etrillard, C.; Nguyen, O.; Létard, J. F.; Faramarzi, V.; Dayen, J. F.; Doudin, B.; Bassani, D. M.; Guillaume, F. Resonance Raman Study of Spin-Crossover $[Fe(Htrz)_2(Trz)](BF_4)\cdot H_2O$ Particles Coated with Gold. *Eur. J. Inorg. Chem.* **2012**, *2* (35), 5837–5842.

(14) Catala, L.; Brinzei, D.; Prado, Y.; Gloter, A.; Stéphan, O.; Rogez, G.; Mallah, T. Core-Multishell Magnetic Coordination Nanoparticles: Toward Multifunctionality on the Nanoscale. *Angew. Chemie - Int. Ed.* **2009**, *48* (1), 183–187.

(15) Felts, A. C.; Slimani, A.; Cain, J. M.; Andrus, M. J.; Ahir, A. R.; Abboud, K.; Meisel, M. W.; Boukheddaden, K.; Talham, D. R. Control of the Speed of a Light–Induced Spin Transition through Mesoscale Core-Shell Architecture. *J. Am. Chem. Soc.* **2018**, *140*, 5814–5824.

(16) Maurin-Pasturel, G.; Long, J.; Guari, Y.; Godiard, F.; Willinger, M. G.; Guerin, C.; Larionova, J. Nanosized Heterostructures of Au@Prussian Blue Analogues: Towards Multifunctionality at the Nanoscale. *Angew. Chemie - Int. Ed.* **2014**, *53* (15), 3872–3876.

(17) Meded, V.; Bagrets, A.; Fink, K.; Chandrasekar, R.; Ruben, M.; Evers, F.; Bernand-Mantel, A.; Seldenthuis, J. S.; Beukman, A.; Van der Zant, H. S. J. Electrical Control over the Fe (II) Spin Crossover in a Single Molecule: Theory and Experiment. *Phys. Rev. B* **2011**, *83* (24), 245415.

(18) Frisenda, R.; Harzmann, G. D.; Celis Gil, J. A.; Thijssen, J. M.; Mayor, M.; van der Zant, H. S. J. Stretching-Induced Conductance Increase in a Spin-Crossover Molecule. *Nano Lett.* **2016**, *16* (8), 4733–4737.

(19) Gopakumar, T. G.; Matino, F.; Naggert, H.; Bannwarth, A.; Tuczek, F.; Berndt, R. Electron□Induced Spin Crossover of Single Molecules in a Bilayer on Gold. *Angew. Chemie Int. Ed.* **2012**, *51* (25), 6262–6266.

(20) Based, M.; Fe, M.; Htrz, F.; Bf, H.; Krober, J.; Audibre, J.; Claude, R.; Codjovi, E.; Kahn, O.; Grolibre, F.; Jay, C.; Bousseksou, A.; Linarbs, J.; Varret, F.; Gonthier-vassal, A. Spin Transitions and Thermal Hystereses in The. *Chem. Mater.* **1994**, *2* (3), 1404–1412.

(21) Haasnoot, J. G.; Vos, G.; Groeneveld, W. L. 1, 2, 4-Triazole Complexes, III Complexes of Transition Metal (II) Nitrates and Fluoroborates. *Zeitschrift für Naturforsch. B* **1977**, *32* (12), 1421–1430.

(22) Galán-Mascarós, J. R.; Coronado, E.; Forment-Aliaga, A.; Monrabal-Capilla, M.; Pinilla-Cienfuegos, E.; Ceolin, M. Tuning Size and Thermal Hysteresis in Bistable Spin Crossover Nanoparticles. *Inorg. Chem.* **2010**, *49* (12), 5706–5714.

(23) Coronado, E.; Galán-Mascarós, J. R.; Monrabal-Capilla, M.; García-Martínez, J.; Pardo-Ibáñez, P. Bistable Spin-Crossover Nanoparticles Showing Magnetic Thermal Hysteresis near Room Temperature. *Adv. Mater.* **2007**, *19* (10), 1359–1361.

(24) Moulet, L.; Daro, N.; Etrillard, C.; Létard, J.-F.; Grosjean, A.; Guionneau, P. Rational Control of Spin-Crossover Particle Sizes: From Nano-to Micro-Rods of $[Fe(Htrz)_2(Trz)](BF_4)$. *Magnetochemistry* **2016**, *2* (1), 10.

(25) Giménez-Marqués, M.; García-Sanz de Larrea, M. L.; Coronado, E. Unravelling the Chemical Design of Spin-Crossover Nanoparticles Based on Iron(II)–Triazole Coordination Polymers: Towards a Control of the Spin Transition. *J. Mater. Chem. C* **2015**, *3* (30), 7946–7953.

(26) Dugay, J.; Giménez-Marqués, M.; Kozlova, T.; Zandbergen, H. W.; Coronado, E.; Van Der Zant, H. S. J. Spin Switching in Electronic Devices Based on 2D Assemblies of Spin-Crossover Nanoparticles. *Adv. Mater.* **2015**, *27* (7), 1288–1293.

(27) Devid, E. J.; Martinho, P. N.; Kamalakar, M. V.; Šalitroš, I.; Prendergast, Ú.; Dayen, J. F.; Meded, V.; Lemma, T.; González-Prieto, R.; Evers, F.; Keyes, T. E.; Ruben, M.; Doudin, B.; Van Der Molen, S. J. Spin Transition in Arrays of Gold Nanoparticles and Spin Crossover Molecules. *ACS Nano* **2015**, *9* (4), 4496–4507.

(28) Torres□Cavanillas, R.; Sanchis□Gual, R.; Dugay, J.; Coronado□Puchau, M.; Giménez□Marqués, M.; Coronado, E. Design of Bistable Gold@Spin□Crossover Core–Shell Nanoparticles Showing Large Electrical Responses for the Spin Switching. *Adv. Mater.* **2019**, 1900039.

(29) Kreno, L. E.; Leong, K.; Farha, O. K.; Allendorf, M.; Van Duyne, R. P.; Hupp, J. T. Metal-Organic Framework Materials as Chemical Sensors. *Chem. Rev.* **2012**, *112* (2), 1105–1125.

(30) Sun, L.; Campbell, M. G.; Dincə, M. Electrically Conductive Porous Metal-Organic Frameworks. *Angew. Chemie - Int. Ed.* **2016**, *55* (11), 3566–3579.

(31) Xie, L. S.; Skorupskii, G.; Dincă, M. Electrically Conductive Metal-Organic Frameworks. *Chem. Rev.* **2020**, *120* (16), 8536–8580.

(32) Hinman, J. G.; Turner, J. G.; Hofmann, D. M.; Murphy, C. J. Layer-by-Layer Synthesis of Conformal Metal-Organic Framework Shells on Gold Nanorods. *Chem. Mater.* **2018**, *30* (20), 7255–7261.

(33) Turkevich, J. Colloidal Gold. Part I. *Gold Bull.* **1985**, *18* (4), 125–131.

(34) Park, J. W.; Shumaker-Parry, J. S. Structural Study of Citrate Layers on Gold Nanoparticles: Role of Intermolecular Interactions in Stabilizing Nanoparticles. *J. Am. Chem. Soc.* **2014**, *136* (5), 1907–1921.

(35) Urakawa, A.; Van Beek, W.; Monrabal-Capilla, M.; Galán-Mascarós, J. R.; Palin, L.; Milanesio, M. Combined, Modulation Enhanced X-Ray Powder Diffraction and Raman Spectroscopic Study of Structural Transitions in the Spin Crossover Material $[Fe(Htrz)_2(Trz)](BF_4)$. *J. Phys. Chem. C* **2011**, *115* (4), 1323–1329.

(36) Miller, M. M.; Lazarides, A. A. Sensitivity of Metal Nanoparticle Surface Plasmon Resonance to the Dielectric Environment. *J. Phys. Chem. B* **2005**, *109* (46), 21556–21565.

(37) Mayer, K. M.; Hafner, J. H. Localized Surface Plasmon Resonance Sensors. *Chem. Rev.* **2011**, *111* (6), 3828–3857.

(38) Holovchenko, A.; Dugay, J.; Giménez-Marqués, M.; Torres-Cavanillas, R.; Coronado, E.; van der Zant, H. S. J. Near Room-Temperature Memory Devices Based on Hybrid

Spin-Crossover@SiO_2 Nanoparticles Coupled to Single-Layer Graphene Nanoelectrodes. *Adv. Mater.* **2016**, *28* (33), 7228–7233.

(39) Mikolasek, M.; Félix, G.; Nicolazzi, W.; Molnár, G.; Salmon, L.; Bousseksou, A. Finite Size Effects in Molecular Spin Crossover Materials. *New J. Chem.* **2014**, *38* (5), 1834–1839.

(40) Prins, F.; Monrabal-Capilla, M.; Osorio, E. A.; Coronado, E.; Van Der Zant, H. S. J. Room-Temperature Electrical Addressing of a Bistable Spin-Crossover Molecular System. *Adv. Mater.* **2011**, *23* (13), 1545–1549.

(41) Rotaru, A.; Gural'skiy, I. A.; Molnár, G.; Salmon, L.; Demont, P.; Bousseksou, A. Spin State Dependence of Electrical Conductivity of Spin Crossover Materials. *Chem. Commun.* **2012**, *48* (35), 1–4.

(42) Lefter, C.; Tan, R.; Dugay, J.; Tricard, S.; Molnár, G.; Salmon, L.; Carrey, J.; Rotaru, A.; Bousseksou, A. Light Induced Modulation of Charge Transport Phenomena across the Bistability Region In. *Phys. Chem. Chem. Phys.* **2015**, *17* (Umr 5215), 5151–5154.

(43) Lefter, C.; Tan, R.; Tricard, S.; Dugay, J.; Molnár, G.; Salmon, L.; Carrey, J.; Rotaru, A.; Bousseksou, A. On the Stability of Spin Crossover Materials : From Bulk Samples to Electronic Devices. *Polyhedron* **2015**, *102*, 434–440.

(44) Barbosa, S.; Agrawal, A.; Rodríguez-Lorenzo, L.; Pastoriza-Santos, I.; Alvarez-Puebla, R. A.; Kornowski, A.; Weller, H.; Liz-Marzán, L. M. Tuning Size and Sensing Properties in Colloidal Gold Nanostars. *Langmuir* **2010**, *26* (18), 14943–14950.

(45) Wang, Y.; Serrano, A. B.; Sentosun, K.; Bals, S.; Liz-Marzán, L. M. Stabilization and Encapsulation of Gold Nanostars Mediated by Dithiols. *Small* **2015**, *11* (34), 4314–4320.

(46) Chen, H.; Kou, X.; Yang, Z.; Ni, W.; Wang, J. Shape-and Size-Dependent Refractive Index Sensitivity of Gold Nanoparticles. *Langmuir* **2008**, *24*, 5233–5237.

(47) Shiohara, A.; Langer, J.; Polavarapu, L.; Liz-Marzán, L. M. Solution Processed Polydimethylsiloxane/Gold Nanostar Flexible Substrates for Plasmonic Sensing. *Nanoscale* **2014**, *6* (16), 9817–9823.

(48) Wan, Y.; Guo, Z.; Jiang, X.; Fang, K.; Lu, X.; Zhang, Y.; Gu, N. Quasi-Spherical Silver

Nanoparticles: Aqueous Synthesis and Size Control by the Seed-Mediated Lee-Meisel Method. *J. Colloid Interface Sci.* **2013**, *394* (1), 263–268.

(49) Lee, K. S.; El-Sayed, M. A. Gold and Silver Nanoparticles in Sensing and Imaging: Sensitivity of Plasmon Response to Size, Shape, and Metal Composition. *J. Phys. Chem. B* **2006**, *110* (39), 19220–19225.

(50) Torres-Cavanillas, R.; Lima-Moya, L.; Tichelaar, F. D.; Zandbergen, H. W.; Giménez-Marqués, M.; Coronado, E. Downsizing of Robust Fe-Triazole@SiO_2 Spin-Crossover Nanoparticles with Ultrathin Shells. *Dalt. Trans.* **2019**, *48*, 15465–15469.

(51) Benítez, A.; Amaro-Gahete, J.; Esquivel, D.; Romero-Salguero, F. J.; Morales, J.; Caballero, Á. MIL-88A Metal-Organic Framework as a Stable Sulfur-Host Cathode for Long-Cycle Li-S Batteries. *Nanomaterials* **2020**, *10* (3), 424.

(52) Jeremias, F.; Khutia, A.; Henninger, S. K.; Janiak, C. MIL-100(Al, Fe) as Water Adsorbents for Heat Transformation Purposes - A Promising Application. *J. Mater. Chem.* **2012**, *22* (20), 10148–10151.

(53) Serre, C.; Mellot-Draznieks, C.; Surblé, S.; Audebrand, N.; Filinchuk, Y.; Férey, G. Role of Solvent-Host Interactions That Lead to Very Large Swelling of Hybrid Frameworks. *Science.* **2007**, *315* (5820), 1828–1831.

(54) Simon, M. A.; Anggraeni, E.; Soetaredjo, F. E.; Santoso, S. P.; Irawaty, W.; Thanh, T. C.; Hartono, S. B.; Yuliana, M.; Ismadji, S. Hydrothermal Synthesize of HF-Free MIL-100 (Fe) for Isoniazid-Drug Delivery. *Sci. Rep.* **2019**, *9*, 16907.

(55) Bastús, N. G.; Casals, E.; Ojea, I.; Varon, M.; Puntes, V. The Reactivity of Colloidal Inorganic Nanoparticles. In *The Delivery of Nanoparticles*; **2012**; 377–400.

General Conclusions

This thesis has been focused on the synthesis and characterization of hybrid nanomaterials formed by plasmonic nanoparticles (NPs) and Coordination Polymers (CPs). These hybrids have been designed to maximize the interaction between both nanosystems and thus to enhance some properties of the CPs thanks to the introduction of these plasmonic nanostructures. This thesis addresses the field of hybrid nanomaterials from three different perspectives: magneto-optics, electrocatalysis and electrical conductivity. In each application, different strategies have been carried out to prepare suitable heterostructures.

In chapter 2, we have developed and optimized a general synthetic procedure to obtain, in aqueous solution, hybrid systems formed by metallic NPs decorated onto any negatively charged Prussian Blue and its Analogues (PB and PBA) NPs by electrostatic attraction. By adjusting the pH, it is possible to control the Au decoration over the PBA NP surface. Indeed, Au can be attached randomly or preferentially on the edges. This methodology has been tested over isotropic NPs of Au with different PB/PBA obtaining reproducible heterostructures in each case. In addition, to demonstrate the robustness of this methodology, anisotropic Au NPs and isotropic Ag NPs were also used to decorate PBAs. Therefore, we have achieved different reproducible heterostructures that display different tunable plasmonic properties, with plasmon bands covering all the visible region. This tunable plasmon band position makes them suitable for future magneto-optical applications. Finally, a similar procedure was carried out to attach Au on a PBA monolayer obtaining the hybrid material. The resulting heterostructures also display plasmonic and magnetic properties.

In chapter 3, we have reported a variety of narrow-size distributed core@shell NPs of Au@PBA (PBA of $Ni^{II}Fe^{II}$ and $Co^{II}Fe^{II}$) formed by an Au core and different PBA shell sizes. The electrocatalytical activity of such NPs was evaluated and compared to some PBA without Au and other Au-PBA heterostructures by studying the oxygen evolution reaction (OER). In this chapter, the coulovoltammetry

technique has been applied in electrocatalysis for the first time. This technique provides information on the number of electroactive mass that is strongly related to the electrocatalytic sites, being able to participate in the OER. It was estimated that the introduction of small amounts of Au (5-10 %) in the core@shell structure leads to an increment in the electroactive mass. This greater amount of electroactive sites largely decreases the onset potential, while the Tafel slope remains unaffected. This enhancement of the catalytic activity is related to the increment of the number of electroactive sites and the great reduction of the resistance associated with the electrocatalytic process due to the improvement of the conductivity. These improvements are a consequence of the high contact between both systems and the protective shell that prevents Au oxidation. Therefore, these results evidence, in core@shell structures, a strong synergistic effect between the core and the shell that emerge as an excellent strategy to enhance the electrocatalytic performance and the electrochemical stability. In addition, plasmonic properties could also be beneficial for increasing the catalytic performance by light irradiation where the local temperature increase could reduce even more the onset potential.

In chapter 4, a simple chemical protocol has been reported to prepare stable colloidal suspensions of core@shell NPs formed by a spherical metallic Au core of ≈12 nm surrounded by a thin shell of an insulating Spin-Crossover (SCO) CP, 4 nm thick. This procedure has allowed us to prepare Au@SCO NPs having a naked surface, in sharp contrast with previous examples that required the presence of a capping agent in the surface (surfactant molecules or SiO_2 shell) to limit the growth of the SCO NP. These hybrid NPs undergo a cooperative spin transition in the range 340–360 K, in full agreement with the values reported for 4 nm NPs of the same SCO compound. Thanks to the metallic core and the naked surface of the ultrathin SCO shell, these core@shell NPs are more conductive than the pristine SCO NPs when contacted to electrodes. Consequently, these SCO devices exhibit a significant improvement in the electrical detection of the spin state, with values for the ON/OFF ratio, which are an order of magnitude better than the best ones obtained in previous devices based on SCO NPs. Interestingly, this chemical protocol was also adapted to Au nanostars that present higher sensitivity and could help to develop highly sensitive switching devices based on the SCO phenomenon. This synthetic route

can also be extended to other core@shell with different metallic components such as Ag. Accordingly, the plasmon band can be tuned in the visible spectrum permitting to induce the spin-transition by light irradiation of the appropriate wavelength. Additionally, by further modifying the chemical protocol, it was possible to cover spherical Au NPs with two different CPs based on two Metal-Organic Frameworks (MOFs): the MIL-88(Fe) and the MIL-100(Fe). As the Au@SCO NPs, these hybrids are also more conductive compared to the pristine MOF material. Thanks to that, the influence and the detection of guest molecules will be carried out in future work.

The most relevant overall conclusions that can be extracted are the following:

- The core@shell heterostructures have been proven as excellent platforms to ensure an intimate contact between both systems. It was observed that a plasmonic core, such as a metallic Au core, gives rise to an important enhancement of some properties (the conductivity or even the plasmonic properties of the resulting hybrid material). In this way, we can take advantage of it for electrocatalytic application or spin state detection.

- Core@shell NPs are usually prepared through non-versatile synthetic protocols where it is quite challenging to change the metallic core NP and to incorporate the functional molecular shell. Here we have developed more flexibles synthetic routes that have allowed an easy modification of the size, shape and composition of the resulting hybrids. This versatility is key for some applications like magneto-optics where the plasmon band control, as well as the interaction between the metallic and the molecular systems, are essential in order to improve the resulting properties

- Altogether this thesis has contributed to the development of novel plasmonic heterostructures based on CPs at the nanometer scale.

Resumen de la Tesis Doctoral

Introducción

Las nanopartículas (NPs) son una clase de materiales que por lo general incluyen partículas con dimensiones menores a 100 nm. Entre ellas, las nanopartículas de metales nobles son de gran interés. Y es que, cuando reducimos el tamaño de la partícula, surgen nuevas propiedades ópticas como resultado de la interacción entre la luz y los electrones situados en la superficie metálica. Este fenómeno es conocido como resonancia de plasmón localizada en la superficie (LSPR, por sus siglas en inglés). Diferentes factores tales como el tamaño, la forma y la constante dieléctrica del entorno afectan considerablemente. Por ello, la síntesis de nuevas NPs plasmónicas con diferentes morfologías (tales como nanoestrellas o nanocilindros) ha permitido un gran control de la posición del plasmón. De entre todos los metales nobles, el oro es posiblemente el que más interés ha despertado en el transcurso de la historia. En la escala nanométrica, dicho interés se incrementa exponencialmente debido a sus atractivas propiedades ópticas, su sencilla funcionalización, su alta estabilidad o su conductividad térmica y eléctrica. Por si fuera poco, el desarrollo de nuevos métodos sintéticos de NPs de oro ha permitido maximizar las propiedades del metal, controlar su morfología y también ha facilitado su integración en otros materiales.

Los nanomateriales híbridos han posibilitado la combinación de las propiedades intrínsecas de los componentes individuales, pero también en algunos casos ha conllevado la aparición de propiedades adicionales debido a la sinergia entre los materiales constituyentes. Es por ello que las NPs híbridas están recibiendo tanta atención por parte de la comunidad científica. La integración de NPs de oro en estos híbridos resulta muy atractivo, tanto es así que, en la última década, casi el 20 % de los materiales híbridos están formados por NPs de oro.

Las NPs de oro son muy sencillas de sintetizar y de funcionalizar lo que facilita la preparación de heteroestructuras. Hay diferentes nanosistemas que pueden obtenerse al combinar nanoestructuras de oro con otro material nanopartículado.

Las más relevantes son: nucleo@recubrimiento (core@shell en inglés), NPs recubiertas de oro, NPs de tipo Janus, NPs decoradas en la superficie de otra NP, etc. Cada heteroestructura tiene sus peculiaridades y, dependiendo de las propiedades deseadas o de la aplicación final, uno u otro material híbrido será más conveniente. De esta manera, el diseño químico de los materiales híbridos resulta esencial.

Los Polímeros de Coordinación (CPs, por sus siglas en inglés) son unos materiales poliméricos y organometálicos formados por la asociación de iones metálicos y ligandos orgánicos. La amplia variedad de cationes metálicos y ligandos permite un número enorme de posibles combinaciones. Generalmente, los metales de la primera serie de transición junto al Zn, Cd Hg, Ag, Au, Pd y Pt son los más usados ya que su reactividad química está muy estudiada. Por otra parte, la coordinación del ligando determina la estructura del CP, así como su dimensionalidad. Asimismo, el tamaño de las partículas obtenidas puede ser controlado en la nanoescala. Por todo ello, las propiedades que presentan dichos materiales son muy amplias: magnéticas, ópticas, electroquímicas, electrónicas, etc. Además, los CPs presentan grandes ventajas sobre otros materiales inorgánicos como son su fácil nanoprocesado o su variedad estructural. Por todo ello, la integración de NPs plasmónicas (especialmente de oro) en una heteroestructura es de gran interés para el desarrollo de nuevas propiedades y así extender la aplicación de estos materiales organometálicos. En esta tesis doctoral hemos trabajado con tres diferentes clases de CPs que se describen a continuación:

- Materiales análogos al Azul de Prusia (PBA, por sus siglas en inglés): Éstos compuestos se componen de una estructura cúbica donde centros metálicos de la primera serie de transición quedan coordinados octaédricamente a ligandos de tipo ciano en una red tridimensional. La fórmula de dichos compuestos es $A_aB_x[D(CN)_6]_y \cdot nH_2O$ (siendo A un catión alcalino mientras que B y C son cationes metálicos de la primera serie de transición). La principal ventaja de estos materiales es su variedad química, el gran control sintético de su tamaño y la posibilidad de obtener suspensiones coloidales estables. En los últimos años se han desarrollado algunas combinaciones de estos materiales con NPs de oro que se han enfocado principalmente para la electrocatálisis de agua

oxigenada y para aprovechar las propiedades plasmónicas en aplicaciones biomédicas (fototerapia).

- Materiales de transición de espín (SCO, por sus siglas en inglés): La transición de espín es un fenómeno que conlleva un cambio en el estado electrónico por medio de un factor externo como puede ser la temperatura, la luz o la presión. La transición ocurre al cambiar el estado del compuesto de bajo espín a alto espín provocando cambios en la distancia de enlaces entre metales y ligandos e induciendo cambios en sus propiedades magnéticas, ópticas y eléctricas. La integración de NPs plasmónicas en dichos compuestos se ha realizado especialmente para aprovechar el plasmón para que, por medio de la irradiación por luz, facilite la transición de espín por efecto fototérmico.

- Materiales de red metalorgánica (MOF, por sus siglas en inglés): Los MOFs son compuestos de red tridimensionales con alta cristalinidad, altísima porosidad y enorme área superficial. Es por ello que son unos materiales muy prometedores para el almacenamiento de gases, para la separación de compuestos y para catálisis. Se han realizado numerosos trabajos combinando MOFs con NPs de oro. En la mayoría de casos, la heteroestructura core@shell, siendo el oro el núcleo y el MOF el recubrimiento, es la más adecuada para aprovechar la sinergia de ambos compuestos. Por ejemplo, se ha aprovechado la capacidad del oro para incrementar la señal obtenida en Raman para detectar las moléculas adsorbidas por el MOF.

Objetivos

La tesis aquí descrita está motivada por el creciente interés en el campo de la ciencia de los materiales y, especialmente, por el avance en el desarrollo de materiales híbridos. El principal objetivo de esta tesis es el diseño y la preparación de heteroestructuras integradas por CPs y NPs plasmónicas (especialmente NPs de oro). Concretamente, los CPs que se han utilizado son materiales nanoparticulados multifuncionales de PBA, de SCO y de MOF. Los resultantes materiales híbridos han sido preparados para mejorar y optimizar diferentes propiedades y, por tanto, mejorar su posible implementación en dispositivos

magneto-ópticos, electroquímicos y electrónicos. Durante los diferentes capítulos se han analizado y se han discutido los protocolos sintéticos empleados, la caracterización de los híbridos, sus diferentes propiedades y porqué estas heteroestructuras resultan más adecuadas para dichas aplicaciones.

Metodología

Síntesis

Por lo general, las NPs de oro fueron obtenidas por medio de la conocida reacción de Turkevich, donde una sal de oro es reducida por moléculas de citrato que actúan también como agente estabilizador. Las diferentes formas (cilíndros y estrellas) se obtuvieron por un protocolo de crecimiento mediado por semillas. Con respecto a las NPs de plata, se obtuvieron usando citrato como agente reductor.

Para la preparación de NPs de PBA decoradas por NPs de oro se procedió cambiando el agente estabilizador de las NPs plasmónicas que fue reemplazado por un polímero con un grupo tiol y un grupo amino: HS-PEG-NH_2. Por otra parte, las partículas de PBA se prepararon por adición gota a gota de los precursores por medio de perfusores. Estas partículas no requieren de agente estabilizador, resultando estables coloidalmente con una carga negativa. Ajustando el pH y la concentración de ambas NPs se obtiene la heteroestructura. Curiosamnete, la decoración del oro es dependiente del pH. Un pH entre 2-3 conlleva una distribución aleatoria por el cubo del PBA mientras que un pH entre 3-5 da lugar a una decoración preferencial en las aristas del PBA. Este protocolo fue realizado con una gran variedad de PBA con diferentes tamaños. También se prepararon monocapas de dichas heteroestructuras. Para ello, se ancló (3-Aminopropil)trietoiysilano (APTES) a la superficie de silicio para funcionalizarla. Tras ello, se añadió secuencialmente y, a un pH adecuado, NPs de PBA y NPs plasmónicas.

Para sobrecrecer los PBA (concretamente, de NiFe(II) y el CoFe(II)) alrededor de NPs de oro, nos basamos en la síntesis reportada por Larionova. En este caso, partimos de una sal de oro y cianuro que, por medio de la adición de un potente reductor, forma NPs de oro estabilizadas por grupos ciano. A partir de este punto,

con unas condiciones adecuadas (concentraciones, velocidad de adición de los precursores del PBA) que optimizamos, es posible sobrecrecer estos PBAs con diferentes espesores. Para comparar las propiedades electrocatalíticas, otras NPs fueron obtenidas: PBAs con muchas vacantes (y por tanto muchos defectos), PBAs con Fe(II), PBAs con NPs de oro decorando su superficie y una mezcla física de NPs de oro y PBAs.

Las heteroestructuras de tipo core@shell formadas de SCO o de MOF fueron preparadas a través de un protocolo en dos etapas. Respecto al SCO, el compuesto de $[Fe(Htrz)_2(trz)](BF_4)$ (Htrz = 1,2,4-triazol) fue seleccionado debido a su temperatura de transición (situada por encima de temperatura ambiente) y la persistencia de sus propiedades incluso en NPs con un tamaño menor a 10 nm. En relación al MOF, los compuestos de MIL-100 y MIL-88 fueron escogidos debido a que están formados de Fe y de ligandos similares al citrato, resultando muy interesantes al permitir continuar con el método anterior aplicado para el crecimiento del SCO. Los dos CPs se sobrecrecen por adición de sus precursores: el metal y el ligando que, bajo condiciones adecuadas (concentraciones, velocidad de adición de los precursores, velocidad de agitación de la suspensión coloidal), se coordinan. Para favorecer el crecimiento de dichos materiales en la superficie del oro, en primer lugar, se añadió uno de los dos precursores para que se ancle en la superficie o coordine el citrato y, de esta manera, sirva como semilla de crecimiento. Tras ello, se adicionó secuencialmente gota a gota los precursores en unas concentraciones muy diluidas con el fin de evitar la agregación de la heteroestructura.

Caracterización

Los híbridos resultantes fueron caracterizados por diferentes técnicas. La morfología fue principalmente comprobada por microscopía electrónica de transmisión (TEM, por sus siglas en inglés) y por dispersión dinámica de luz. Las imágenes obtenidas por TEM fueron empleadas para realizar histogramas de las dimensiones de las diferentes NPs. Por medio de microscopía electrónica de transmisión en alta resolución (HR-TEM, por sus siglas en inglés) y Fluorescencia de rayos X por energía dispersiva (EDX, por sus siglas en inglés) se determinó la

distribución de los metales en las heteroestructuras de tipo core@shell. La presencia de las propiedades plasmónicas fue verificada mediante medidas de espectroscopia UV-Vis. Medidas de rayos X fueron realizadas para estudiar la estructura cristalina de los materiales. Por otra parte, la espectroscopia infrarroja y la espectroscopia Raman permitió ahondar acerca de la presencia de enlaces de coordinación. Medidas de potencial zeta resultaron muy útiles para estudiar la estabilidad coloidal de diferentes NPs.

Por otro lado, la espectroscopia de fotoelectrones emitidos por rayos X permitió conocer el estado de oxidación de los diferentes elementos. Las formulas moleculares se estimaron a través de medidas de espectrometría de masas con plasma acoplado inductivamente. Las imágenes de la monocapa de la heteroestructura de Au-PB/PBA fue tomada con un microscopio de fuerza atómica (AFM, por sus siglas en inglés).

Respecto a las medidas magnéticas, éstas se adquirieron por medio de medidas en SQUID (superconductores de interferencia cuántica). Concretamente, se midieron histéresis magnéticas a la temperatura de 2 K y la respuesta magnética frente a la variación de la temperatura bajo un campo aplicado de 1000 Oes.

La actividad electrocatalítica de las partículas Au@PBA fue estudiada por medio de la reacción de evolución de oxígeno. Se midió utilizando una celda de tres electrodos compuesta de un electrodo de carbono vítreo (electrodo de trabajo), un hilo de platino (electrodo auxiliar) y un electrodo de plata/cloruro de plata (electrodo de referencia). Todas las medidas fueron realizadas en una disolución acuosa de KOH 1 M que fue previamente purgada con nitrógeno. En cuanto a los experimentos llevados a cabo, se registraron voltamperometrías (tanto lineales como cíclicas) para estudiar el incremento de la densidad de corriente respecto al voltaje aplicado. Para comprender las diferencias obtenidas con respecto a las demás partículas preparadas, se estudió, por medio de diferentes técnicas (principalmente voltamperometrías cíclicas, coulovoltametrías e impedancia electroquímica) la masa de material susceptible de ser oxidada y reducida, el área electroquímicamente activa y las resistencias internas de cada proceso electroquímico.

Calorimetrías diferenciales de barrido fueron llevadas a cabo para caracterizar la transición de espín en las heteroestructuras elaboradas con diferentes NPs plasmónicas y el compuesto de SCO.

Las medidas de conductividad se llevaron a cabo en electrodos interdigitados donde previamente fueron depositadas las NPs ya sea dejando secar una gota vertida directamente de la suspensión (Au@MOF) o bien mediante dielectroforesis (Au@SCO).

Resultados y discusión

Anclaje de NPs plasmónicas en la superficie de NPs de PBA

Respecto a la decoración de NPs de PBA mediante NPs plasmónicas, la molécula utilizada (HS-PEG-NH_2) resultó ser clave para la unión de ambos nanosistemas. El grupo del tiol tiene una gran afinidad por metales como la plata y el oro mientras que el grupo amino, a un pH adecuado, es capaz de interaccionar electroestáticamente con los PBAs. Observamos que, variando el pH de la disolución, la decoración de la superficie del PBA era distinta. En cierto rango de pH (entre 2 y 3), la decoración se produce de forma aleatoria por toda la superficie del PBA pero, cambiando el rango de pH a 3-5, esta decoración tiene una mayor preferencia por los bordes y esquinas del CP. Este protocolo fue realizado con una gran variedad de PBA y utilizando diferentes tamaños, resultando muy eficaz en todos los casos. En particular, se probó con el clásico PB de FeFe y diferentes PBAs: NiCr, CoFe, CuCr y NiFe. Cabe resaltar que las propiedades magnéticas de los CPs se mantienen, así como las propiedades plasmónicas provenientes de la NP metálica. De hecho, la banda del plasmón se ve desplazada como consecuencia del cambio de índice de refracción causado por la presencia de NPs de PBA alrededor de la superficie del oro. Por otra parte, dependiendo de la NP plasmónica seleccionada es posible modificar y, así, controlar la posición de la banda del plasmón en el espectro visible e infrarrojo cercano (entre 400 y 1200 nm). Estos híbridos se han diseñado para incrementar la actividad magneto-óptica del compuesto magnético de PBA. Para ello, dicha actividad magneto-óptica y la posición de la banda del plasmón han de situarse en la misma longitud de onda. Es

por eso que este protocolo resulta tan conveniente: podemos escoger la NP plasmónica (luego, podemos modular la posición de la banda del plasmón) y la NP de PBA. Finalmente, también se pudo preparar monocapas de dichos híbridos que fueron caracterizadas por AFM y XPS. Para ello, se realizó un tratamiento de la superficie de silicio con APTES, provocando un enlace covalente entre el silano y el silicio y dejando el grupo amino libre. Mediante el uso de una disolución ácida (HCl 1 M) se protonó dicho amino para que se anclara a las NPs de PBA. Tras esto, se decoró NPs de oro añadiendo éstas con el HS-PEG-NH_2 y con su grupo amino protonado. Estas monocapas pueden resultar de gran utilidad para el estudio de la actividad magneto-óptica y el posible incremento causado por el plasmón.

Heteroestructuras de Au@PBA como electrocatalizadores de oxígeno

Las heteroestructuras de tipo core@shell (Au@PBA) fueron preparadas con un núcleo de oro de alrededor 15 nm mientras que se obtuvo un espesor del recubrimiento de PBA de 12 nm (recubrimiento más fino) y de unos 30 nm (recubrimiento más grueso). Para ambos casos, se sintetizaron heteroestructuras de NiFe y de CoFe ya que estos metales de transición resultan ser los más interesantes y eficientes para la electrocatálisis de la reacción de evolución de oxígeno. Los híbridos resultantes son coloidalmente estables, con un recubrimiento muy homogéneo (es decir, con una distribución de los metales homogénea), con una distribución de tamaños pequeña además de mantener las propiedades plasmónicas. De hecho, la banda del plasmón se ve una vez más desplazada como consecuencia del cambio de índice de refracción debido al sobrecrecimiento del PBA alrededor del oro. Debido a ser una estructura de tipo core@shell, dicho desplazamiento es mucho más mayor que en la decoración en la heteroestructura anteriormente mencionada. Sin embargo, estos recubrimientos se ven afectados debido al uso de borohidruro potásico durante la síntesis, ocasionando la reducción del Fe(III) a Fe(II). Este reductor es requerido para mantener el oro en un equilibrio entre el cianuro (que oxida el oro) y el borohidruro (que lo reduce). Sin embargo, la formación de Fe(II) conlleva importantes cambios en las propiedades magnéticas, dando lugar a diferentes temperaturas de ordenación magnética. Sin embargo, a pesar de ello, se comprobó por medio de difracción de rayos X y espectroscopia

Raman que la estructura cúbica típica de los compuesto cianometálicos se mantiene.

Para evaluar las propiedades electroquímicas de dichos híbridos, se prepararon otros compuestos: NPs de PBA sin oro, NPs de PBA con el Fe en estado de oxidación 2, NPs de PBA decoradas con oro y una mezcla física de NPs de PBA y oro. Se observó que, en las estructuras de tipo core@shell con un recubrimiento de PBA grueso, se produce una importante reducción de la sobretensión requerida para producir una densidad de corriente de 10 $mA \cdot cm^{-2}$. De la misma forma, la densidad de corriente producida es mucho mayor aplicando una sobretensión fija. Para comprender estos resultados se llevó a cabo el estudio de coulovoltamperometrías, el cálculo de la superficie electroquímicamente activa y medidas de impedancia electroquímica. Se apreció que la introducción de oro (5-10 % en peso) en la heteroestructura de tipo core@shell ocasiona una mayor cantidad de masa de PBA capaz de reaccionar electroquímicamente, una mayor superficie activa donde puede tener lugar la electrocatálisis y una reducción de la resistencia asociada a la formación de oxígeno, posiblemente debido al incremento de la conductividad del material. Finalmente, se analizó la estabilidad del PBA durante el proceso de evolución de oxígeno de los compuestos conteniendo y sin contener oro. De este modo, además de una notoria mejora en la actividad catalítica, también se observó una mayor estabilidad tras la introducción de una pequeña cantidad de oro en el sistema core@shell.

Heteroestructuras de Au@SCO y Au@MOF para aplicaciones eléctricas

Se desarrolló un protocolo sintético para sobrecrecer SCO en la superficie de nanoesferas, nanoestrellas de oro y nanoesferas de plata. Esta síntesis consiste en dos etapas: la sustitución de citratos coordinados al oro por triazoles y la adición controlada de los precursores ($Fe(BF_4)_2$ y triazoles). En el caso de las nanoesferas de oro, es importante recalcar que, si una gran cantidad de triazoles reemplazan los citratos, la estabilidad coloidal se pierde imposibilitando así el sobrecrecimiento del SCO. Una pequeña cantidad de triazol es suficiente de forma que los triazoles sirvan como germen de nucleación del compuesto en la siguiente etapa. La presencia de

estos ligandos se determinó por XPS al observar la aparición de un pico de nitrógeno. La adición de los precursores se llevó a cabo bajo unas condiciones muy concretas. En caso de incrementar la velocidad de adición o las concentraciones conlleva a la malformación del recubrimiento o, directamente, la formación del compuesto de SCO por su cuenta. Usando técnicas de microscopía, vimos la aparición de un recubrimiento muy fino (en torno a 4 nm de espesor) pero bastante homogéneo alrededor de la superficie de las nanoesferas de oro. Las propiedades plasmónicas nuevamente se ven afectadas con respecto a las propiedades iniciales del oro. El plasmon es desplazado como consecuencia del cambio de índice de refracción. Por rayos X solo pudo observarse los picos correspondientes al oro. Es posible que la ausencia de picos del SCO se deba al pequeño tamaño del recubrimiento, el enmascaramiento del oro o la formación de un compuesto amorfo. En cualquier caso, el híbrido mantiene también su transición de espín, con valores de temperatura muy similares al compuesto prístino de SCO. Sin embargo, se vio una importante fatiga del material al realizar muchos ciclos de transición de espín. Tras caracterizar el nanomaterial, se diseñó un dispositivo, en donde este híbrido fue depositado entre electrodos interdigitados, para evaluar los efectos causados por la transición de espín en las propiedades eléctricas. Al variar la temperatura se registró un importante cambio de la conductividad eléctrica en un rango de temperatura similar al registrado por calorimetría. Asimismo, se distinguieron dos estados eléctricos muy diferenciados relacionados con el estado de espín del compuesto de SCO: un estado más conductor (dentro del rango de los nS/cm) que coincide con el bajo espín y uno menos conductor (dentro del rango de los pS/cm) que coincide con el alto espín. Paralelamente, un compuesto análogo de SCO sin NPs de oro fue medido, pero no se pudo detectar señal debido al comportamiento aislante del material. Por tanto, la introducción de oro permite mejorar la detección del estado de espín del compuesto de SCO. Por otra parte, las propiedades plasmónicas pueden ser aprovechadas para inducir la transición de espín por medio de la irradiación de luz. La luz puede dar lugar al calentamiento del oro por efecto fototérmico, facilitando la transición del compuesto de SCO. Debido a esto, el diseño y la preparación de híbridos con mayores propiedades plasmónicas resulta de gran interés. Por ejemplo, las nanoesferas de plata presentan una banda de plasmón alrededor de 400 nm mientras que las nanoestrellas de oro tienen el plasmón

situado entre 600 y 1200 nm (dependiendo del tamaño de las puntas). Sobrecrecer el compuesto de SCO nos permite tener un híbrido con propiedades de transición de espín y con un gran control de las propiedades plasmónicas en toda la ventana del espectro visible. La preparación de estas NPs de core@shell se llevó a cabo de forma análoga, pero modificando parámetros tales como la concentración o el tiempo y volumen de adición. Y es que la estabilidad coloidal resulta nuevamente crucial. En caso de desestabilizarse la suspensión coloidal se imposibilita el sobrecrecimiento del recubrimiento de SCO alrededor de la superficie metálica.

Este protocolo fue modificado para hacer viable la síntesis de NPs de Au@MOF. Particularmente, se intentó formar los MOFs de MIL-100 y MIL-88 ya que el metal (hierro) es el mismo, salvo por el estado de oxidación, que el utilizado en el apartado anterior. Además, los ligandos de estos MOFs se parecen bastante al citrato (molécula que estabiliza las NPs de oro) al tener varios grupos carboxílicos, haciendo la síntesis más sencilla gracias a las semejanzas con la síntesis del Au@SCO. Sin embargo, debido a que la formación de estos MOFs está más favorecida con respecto al SCO, se obtuvo una malla con NPs de oro embebidas en ella, formando “racimos de uva” de unos 100 nm. Por otro lado, la ausencia de picos de difracción en rayos X relacionados con el MOF sugiere que podríamos haber obtenido polímeros de coordinación amorfos basados en el MIL-100 y el MIL-88. Por este motivo, en el futuro optimizaremos la síntesis para así mejorar la cristalinidad del material. Respecto a las propiedades ópticas, el híbrido posee propiedades plasmónicas y, como en los casos anteriores, el plasmón se ve afectado por el cambio en la constante dieléctrica. Por otra parte, se realizaron medidas de conductividad eléctrica utilizando electrodos interdigitados, observándose una mayor conducción eléctrica en este híbrido que el material prístino. De hecho, el material sin oro exhibe una corriente eléctrica que no supera el límite de detección del aparato empleado (del orden de los pA). Teniendo esto en cuenta, este híbrido resulta especialmente interesante para incrementar la respuesta eléctrica aumentando el límite de detección del compuesto. De esta forma, es posible aprovechar las propiedades del MOF para adsorber diferentes moléculas y poder así analizar la influencia de dichas moléculas en las propiedades eléctricas.

Conclusiones

En conclusión, la presente tesis doctoral aborda el campo de los materiales híbridos dentro de la escala nanométrica formados por NPs plasmónicas y polímeros de coordinación. Los materiales híbridos presentados a lo largo de este trabajo se han diseñado para maximizar la interacción entre ambos nanosistemas y, así, gracias a la presencia de las NPs plasmónicas mejorar las propiedades de los polímeros de coordinación para sus aplicaciones magneto-ópticas, electroquímicas y eléctricas. Las principales conclusiones del trabajo realizado se pueden resumir de la siguiente manera:

- Las heteroestructuras de tipo core@shell resultan muy favorables para aumentar al máximo las interacciones entre ambos nanosistemas. En este trabajo, comprobamos que la introducción de un núcleo de oro confiere al híbrido de una mayor conducción que puede ser beneficioso para incrementar la actividad electrocatalítica o la detección del estado de espín de compuestos de transición de espín.
- Por otra parte, las metodologías que suelen utilizarse para preparar las heteroestructuras de tipo core@shell son, por lo general, bastante rígidas haciendo muy complejo cambiar de NP plasmónica y más aún su morfología. Para ciertas aplicaciones (como es el caso de la magneto-óptica) la posición de absorción del plasmón resulta crucial por lo que este tipo de heteroestructura no resulta tan conveniente. Por consiguiente, desarrollamos un procedimiento más flexible que permite la decoración de NPs plasmónicas en la superficie de polímeros de coordinación negativamente cargados.
- El diseño químico es esencial para aprovechar las propiedades de las NPs plasmónicas. Por tal motivo, resulta imprescindible desarrollar y explorar nuevas rutas sintéticas que conduzcan a una mayor sinergia y una mejora en las propiedades del material híbrido resultante.

En su conjunto esta tesis representa un avance significativo en el desarrollo de nuevos materiales híbridos plasmónicos utilizando NPs metálicas y plasmónicas aportando nuevos resultados que puedan repercutir en un mayor conocimiento y desarrollo en este campo.

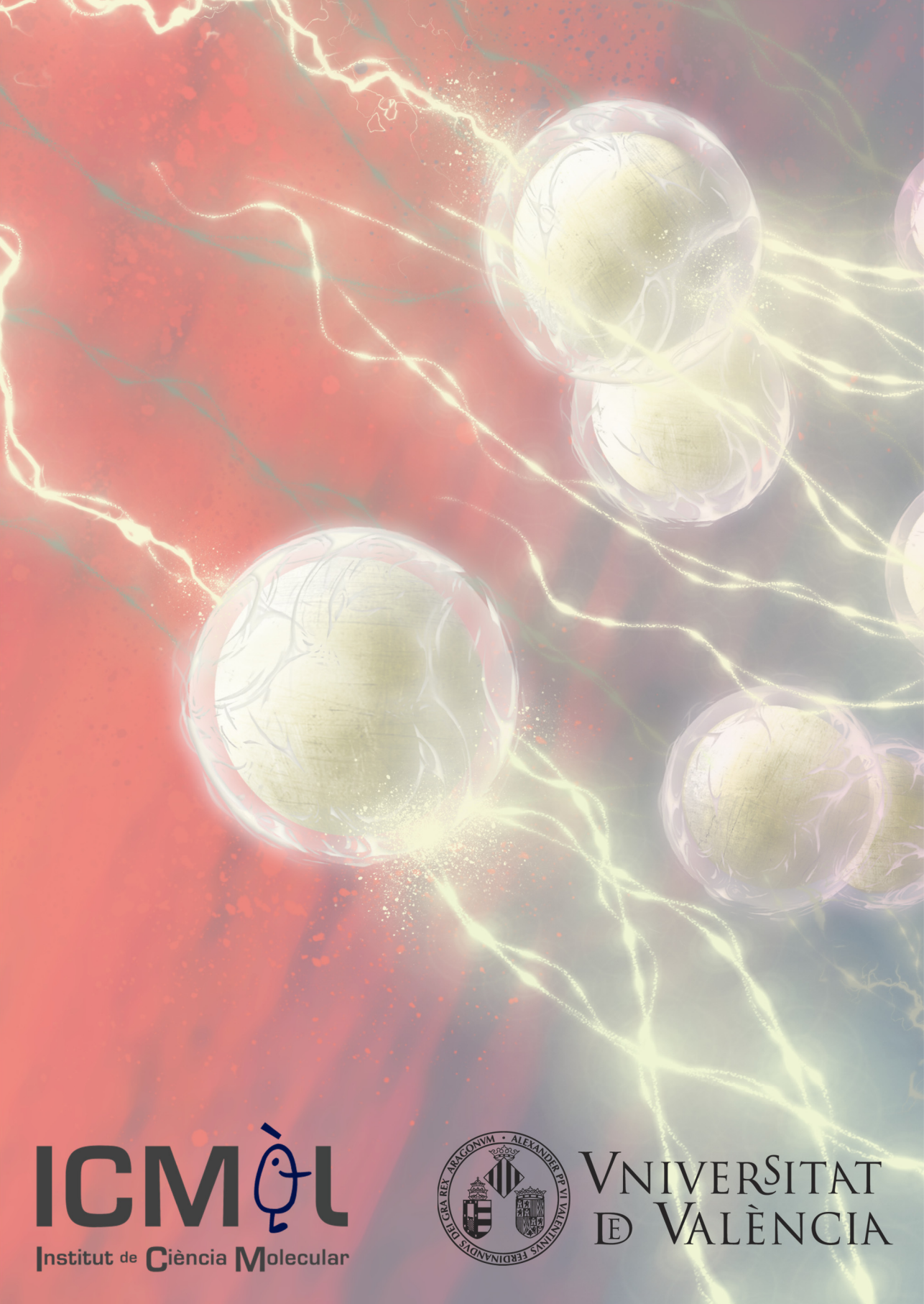

ICMOL

Institut de Ciència Molecular

VNIVERSITAT DE VALÈNCIA